



HAL
open science

Caractérisation et optimisation de structures treillis fabriquées par EBM

Mathieu Suard

► **To cite this version:**

Mathieu Suard. Caractérisation et optimisation de structures treillis fabriquées par EBM. Matériaux. Université Grenoble Alpes, 2015. Français. NNT : 2015GREAI055 . tel-01241583

HAL Id: tel-01241583

<https://theses.hal.science/tel-01241583>

Submitted on 10 Dec 2015

HAL is a multi-disciplinary open access archive for the deposit and dissemination of scientific research documents, whether they are published or not. The documents may come from teaching and research institutions in France or abroad, or from public or private research centers.

L'archive ouverte pluridisciplinaire **HAL**, est destinée au dépôt et à la diffusion de documents scientifiques de niveau recherche, publiés ou non, émanant des établissements d'enseignement et de recherche français ou étrangers, des laboratoires publics ou privés.

THÈSE

Pour obtenir le grade de

DOCTEUR DE L'UNIVERSITÉ GRENOBLE ALPES

Spécialité : **Science des matériaux**

Arrêté ministériel : 7 août 2006

Présentée par

Mathieu Suard

Thèse dirigée par **Rémy Dendievel, François Villeneuve**
et codirigée par **Frédéric Vignat**

préparée au sein des laboratoires **SIMaP et G-Scop**
dans l'**Ecole Doctorale IMEP2**

Characterization and Optimization of Lattice Structures made by Electron Beam Melting

**Caractérisation et Optimisation de structures
treillis fabriquées par EBM**

Thèse soutenue publiquement le **13 Novembre 2015**,
devant le jury composé de :

Stéphane Godet

Professeur, Université Libre de Bruxelles, Président

Patrice Peyre

Directeur de recherche, Arts et Métiers ParisTech, Rapporteur

Marc Thomas

Ingénieur-Docteur HDR, ONERA the french aerospace lab, Rapporteur

Rémy Dendievel

Professeur, Laboratoire SIMaP, Directeur de thèse

François Villeneuve

Professeur, Laboratoire G-Scop, Co-Directeur de thèse

Frédéric Vignat

Maître de conférence, Laboratoire G-Scop, Invité

Jean-Jacques Blandin

Directeur de recherche, Laboratoire SIMaP, Invité



Remerciements

Une thèse est un long voyage. La première année on fait ses bagages et on découvre un peu quel est l'état du chemin. On se demande si on va plutôt traverser le long désert en chameau ou prendre la route paisible bien assis dans son 4x4. Par curiosité ou défi sur soi-même, on choisi le désert. La deuxième année, on fait des rencontres dans le désert, on analyse, on engrange des résultats. Il se peut que notre chameau ne soit plus très vaillant et alors là, il nous faut continuer à pied pour atteindre l'oasis. Des fois, on croit que l'on est en train de l'atteindre mais on tombe sur un mirage. Enfin, après la tempête de sable des derniers mois de rédaction, on termine cette traversée. On retourne à la civilisation et on se rend compte qu'on est pas si différent mais que cette traversée du désert nous a quand même donnée une bonne leçon de vie.

Je n'aurais jamais pu faire ce voyage tout seul. Je tiens à remercier sincèrement mon directeur de thèse, Rémy Dendievel, pour m'avoir aidé à avancer, m'avoir indiqué les bonnes routes à suivre durant ces trois ans. J'ai énormément apprécié travailler avec toi au quotidien. Que ce soit sur le plan scientifique ou humain, je ne pouvais pas mieux tomber.

Je tiens aussi à remercier mes encadrants à G-Scop : François Villeneuve (co-directeur de thèse) et Frédéric Vignat (co-encadrant) pour m'avoir fait découvrir qu'il n'y avait pas que la science des matériaux dans la recherche. Leur expertise en conception m'ont apporté de nouvelles connaissances dans ce domaine.

Je remercie les rapporteurs de ce manuscrits Patrice Peyre et Marc Thomas d'avoir eu la lourde tâche de relire ce manuscrit. Un grand merci à Stéphane Godet pour avoir bien voulu être président de jury de ma soutenance et pour les nombreuses discussions scientifiques (ou non) que nous avons eu.

Je souhaite remercier aussi Jean-Jacques Blandin et Guilhem Martin qui ne faisaient pas parti de l'encadrement officiel mais qui ont participé activement à me faire avancer dans ce travail. Je pense que je me souviendrais longtemps de l'ambiance qui régnait dans les réunions ensemble! Entre Rémy qui cherche la *jolie histoire*, Guilhem le malade du *stylo rouge* et Jean-Jacques qui te dis : " Mais, *in fine*, tu cherche à faire quoi là ? ". La recherche a, pour moi, cela de bon qu'elle permet de lisser les hiérarchies.

J'ai vraiment apprécié le cadre de travail au SIMaP, et plus précisément au GPM2. Il permet des discussions poussées entre chercheurs et doctorants à la machine à café par exemple. Merci à Xavier pour avoir supporté mes sautes d'humeurs, à Camila pour partager son maté et à tout les autres doctorants du labo! Bon courage à tout les autres pour la fin de la thèse. Je tiens à remercier tout les personnes qui m'ont aidé que ce soit pour des aspects techniques (Charles, Franck, Xavier, Jef, Alain, Thierry) ou pour des aspects administratifs (Claire, Claude et Élisabeth)

J'ai passé beaucoup de temps au labo pendant ces trois années mais pas seulement. Mes amis ont fait parti intégrante de cette traversée du désert. Je n'ai pas assez de pages pour écrire à quel point vous êtes importants pour moi! Merci à mes trois colocataires successifs et amis Thib, Martoni et Jay pour les soirées à la Nat, les traditionnels visionnages de série, les énormes soirées où on réveille les séniles d'en face! Merci à Philémon pour être un pilier dans ma vie, une personne sur qui tu es sûr de pouvoir compter pour aller au bar ou pour partir faire du vélo à l'autre bout du monde. La liste est longue mais je tiens

à vous remercier tous de faire parti de ma vie et d'être venu pour la soutenance! Merci à Mathilde, Ched, Caro, Yo, Sandy, Mumu, Anais, Clément, Fanny, Charlotte, Gaspard, Sam, Nono, Yvan, Dragé... Merci aux Céciles. Merci aux colocataires actuels pour m'avoir supportés dans les dernier moments!

Merci à Kasia pour son amour, celui qui est beau et sincère. Kocham cie bardzo!

Sans vous je n'aurais pas pu faire cette thèse, merci à mes parents pour tout leur vie amour et avoir tout fait pour que je puisse étudier ce que je veux dans de bonnes conditions. C'est vraiment une chance! Je vous aime! Merci aussi à ma soeur Marion. Des guerres fraternelles aux joies de partager des passions communes, tu as toujours été importante dans ma vie. Ne t'inquiète pas je reviendrais vite dans nos régions!

Table des matières

French Summary - Résumé étendu en Français	1
---	----------

Introduction et revue bibliographique	3
1 Caractérisation du Ti-6Al-4V produit par EBM	9
1.1 Caractérisation microstructurale	9
1.1.1 Alliage Ti-6Al-4V conventionnel	9
1.1.2 Alliage Ti-6Al-4V produit par EBM	10
1.2 Caractérisation mécanique	11
1.2.1 Comparaison entre les propriétés mécaniques requises et celles fabriquées	11
1.2.2 Vers la compréhension des différences de résistance à la traction et de ductilité	11
2 Méthode pour la prédiction de la rigidité de structures treillis produites par EBM	13
2.1 Caractérisation structurale et mécanique de poutres unitaires	13
2.1.1 Apparence générale et porosité	13
2.1.2 Concept pour relier les caractéristiques géométriques et la prédiction mécanique	15
2.2 Prédiction des propriétés élastiques de la structure Octet-truss	15
2.3 Variation du diamètre mécaniquement équivalent avec le diamètre nominal et l'orientation des poutres	17
3 Optimisation des structures treillis	19
3.1 Optimisation de l'orientation d'une structure treillis pour sa fabrication par EBM	19
3.1.1 Démarche	19
3.1.2 Résultats	20
3.2 Optimisation paramétrique de structures treillis fabriquées par EBM	21
3.2.1 Démarche	21
3.2.2 Résultats	22
3.2.3 Développements futur	22
4 Amélioration de la précision géométrique et de la rugosité des poutres	23
4.1 Amélioration de la qualité de surface par des post-traitements	23
4.1.1 Démarche	23

4.1.2	Résultats	24
4.2	Amélioration de la précision géométrique par changement des paramètres de fabrication	25
4.2.1	Démarche	25
4.2.2	Résultats	26
Conclusion et perspectives		29
General Introduction		35

I	Generalities and Overview	39
<hr/>		
1	Lattice structures	43
1.1	Introduction	43
1.1.1	Architected materials	43
1.1.2	Properties of architected materials	44
1.2	Metallic lattice structures	45
1.2.1	Elastic properties of periodic lattice structures	46
1.2.2	Conventional manufacturing techniques	50
2	Metallic Additive Manufacturing	53
2.1	Current technologies and challenges	53
2.1.1	Direct Metal Deposition	54
2.1.2	Laser Beam Melting	55
2.2	Electron Beam Melting (EBM)	55
2.2.1	Description of the process	56
2.2.2	Description of the components	57
2.2.3	Description of the raw material	58
2.2.4	Process parameters and strategies	59
2.2.5	Manufacturing lattice structures by Electron Beam Melting	61
2.3	Limitations	63
3	Problematic raised and starting point of the work	65
3.1	Problematic of the PhD thesis	65
3.2	Strategy of the PhD	66

II	Characterization of the material properties	67
<hr/>		
4	Microstructural characterization	71
4.1	Conventional Titanium alloys	71
4.1.1	Metallurgy of Titanium alloys	71
4.1.2	Ti-6Al-4V alloy	73
4.2	Ti-6Al-4V produced by EBM	75
4.2.1	Materials and methods	76
4.2.2	Microstructures	76
4.2.3	Porosity	82
5	Mechanical properties	85
5.1	Mechanical properties of conventional Ti-6Al-4V alloy	85
5.2	Samples and experiments	86
5.2.1	Tensile test	86
5.2.2	Tensile samples	86
5.3	Mechanical properties of EBM-built Ti-6Al-4V alloy	87
5.3.1	Main Results	87
5.3.2	Origin of the high strength	90
5.3.3	Origin of the low elongation to failure	93

III	A methodology for the stiffness prediction of lattice structures produced by EBM	101
------------	---	------------

6	Review on geometrical and mechanical variability in AM of lattice structures	105
6.1	Electron Beam Melting	106
6.2	Other AM processes	107
6.2.1	Laser Beam Melting	107
6.2.2	Direct Metal Deposition	108
7	Structural and mechanical characterization of single struts	111
7.1	Materials and methods	111
7.1.1	Fabrication of 1 mm struts	111
7.1.2	X-Ray Tomography	113
7.1.3	Image Analysis	114
7.2	Structural characterization of struts	115
7.2.1	General Appearance	115
7.2.2	Porosity	115
7.2.3	Shape and size	116
7.2.4	Surface irregularities	118
7.3	Concepts to link geometrical features and mechanical prediction	120
7.3.1	Geometrical equivalent diameter D_{EQ}^{GEOM}	120
7.3.2	Numerical equivalent diameter D_{EQ}^{NUM}	121
7.3.3	Representative Volume Element	124
7.3.4	Comparison	125
7.3.5	Summary	125
8	Prediction of the elastic properties of the Octet-truss structure manufactured by EBM	127
8.1	The Octet-truss lattice	128
8.1.1	Generalities	128
8.1.2	Manufacturing by the EBM technology	128
8.1.3	RVE analysis	130
8.2	Compression Test	130
8.2.1	Testing configuration	130
8.2.2	Young's Modulus determination	131
8.3	Numerical Simulation	132
8.3.1	Homogenization and boundary conditions	132
8.3.2	Finite Element Modeling	133
8.3.3	Comparison between experiments and simulations	136
8.4	Validation of the equivalent diameter	136
8.4.1	FEM with equivalent diameters	136
8.4.2	Comparison with the experimental data	136

9	Variation of the mechanical equivalent diameter with strut size and orientation angle	139
9.1	Fabricated struts	139
9.2	Structural analysis of the struts	142
9.2.1	Comparison between "Net" and "Melt" themes for 1 mm diameter struts	142
9.2.2	Analytical equation of D_{EQ}^{NUM}	144

IV	Optimization of lattice structures	149
<hr/>		
10	Beam Simulation for the octet-truss structure	153
10.1	Methodology	153
10.1.1	Materials properties and cross-section parameters	153
10.2	Range of application	154
11	Optimal orientation of lattice structures within the EBM build	157
11.1	From lattice orientation to struts orientation	157
11.2	Results of the simulation	158
12	Parametric optimization of lattice structures made by EBM	161
12.1	Methodology and validation of the code	161
12.1.1	Scheme of the code	161
12.1.2	Validation of the code using the cantilever shape	162
12.2	"Realistic" Parametric Optimization of an octet-truss unit-cell	164
12.2.1	Parameters	164
12.2.2	Constraints	164
12.2.3	Objective function and initial parameters	165
12.2.4	Results of optimization	166
12.2.5	Further development	166

V Towards the improvement of strut's size and surface geometry	171
<hr/>	
13 Improvement of the surface roughness through post-treatments	175
13.1 Electro-Chemical Polishing	176
13.1.1 Parameters and methodology	176
13.1.2 Results	177
13.2 Chemical Etching	180
13.2.1 Parameters and methodology	180
13.2.2 Results	181
14 Improvement of the strut's size through the EBM process	183
14.1 Improvement of the size accuracy for a 1 mm vertical strut	183
14.1.1 Methodology	183
14.1.2 Results	185
14.2 Variation of the scan strategy for 5 mm-diameter struts	186
14.2.1 Methodology	186
14.2.2 Results	186
General conclusion and Future work	193
Appendices	213
A FFT simulation of heterogenous media	213
B Detailed example of Periodic Boundary Conditions for the beam simulation	215
C Comments on the relative density calculation	219
D Description of the lattice creator program	221

French Summary - Résumé en français

Cette partie est un résumé étendu de la thèse en français. Elle présente le contexte de la thèse, les principaux résultats ainsi que les perspectives qui en découlent. C'est avant tout une *vulgarisation des résultats obtenus*. Pour avoir accès à des résultats et une problématique plus rigoureuse, merci de se référer au manuscrit en anglais.

Introduction et revue bibliographique

Cette thèse commença avec l'arrivée à Grenoble INP d'une machine de Fabrication Additive de technologie *Electron Beam Melting (EBM)*. Dans ce manuscrit, les résultats présentés ont été obtenus avec la machine EBM A1.

Comme ces technologies de fabrications additives permettent de fabriquer des géométries très complexes, une application visée a été la fabrication de structures architecturées très difficiles à fabriquer de manière conventionnelle. En effet, depuis des années, il est possible de concevoir des géométries optimisées. Ces modèles résultant d'optimisations mécaniques sont maintenant fabricables par des technologies additives.

Structures treillis

Matériaux architecturés

Les matériaux monolithiques ne permettent plus de satisfaire des cahiers des charges industriels de plus en plus complexes. Afin de répondre à ces demandes multi-fonctionnelles, il est nécessaire d'architecturer les matériaux en combinant un matériau et de l'air ou plusieurs matériaux ensemble. Selon Mike Ashby, les matériaux architecturés sont une combinaison d'au moins deux matériaux ou d'un matériau et de l'air configurés afin d'avoir des caractéristiques que ne peuvent offrir chaque matériau seul [1].

La figure 1 montre différentes classes de matériaux architecturés. Ce travail de thèse se focalise sur les structures treillis (encadré en vert). Ces structures sont composées d'un réseau inter-connecté de poutres.

Structures treillis

Ces architectures sont majoritairement utilisées pour des applications mécaniques. Elles permettent de créer des pièces légères tout en gardant une rigidité élevée. Cette application est celle visée dans la thèse. Certaines géométries de structures treillis sont aussi utilisées pour des propriétés d'absorption d'énergie [2]. Elles peuvent aussi trouver leur place dans des domaines d'applications thermiques [3–5] ou acoustiques [6].

Les propriétés mécaniques de ces structures sont très dépendantes de la topologie de celle-ci. Le paramètre le plus important dans la topologie des structures treillis est la connectivité nodale. En fonction de cette connectivité, on peut distinguer des structures dont le mode de déformation est dominé par de la traction-compression et d'autres dont le mode dominant est la flexion [7, 8].

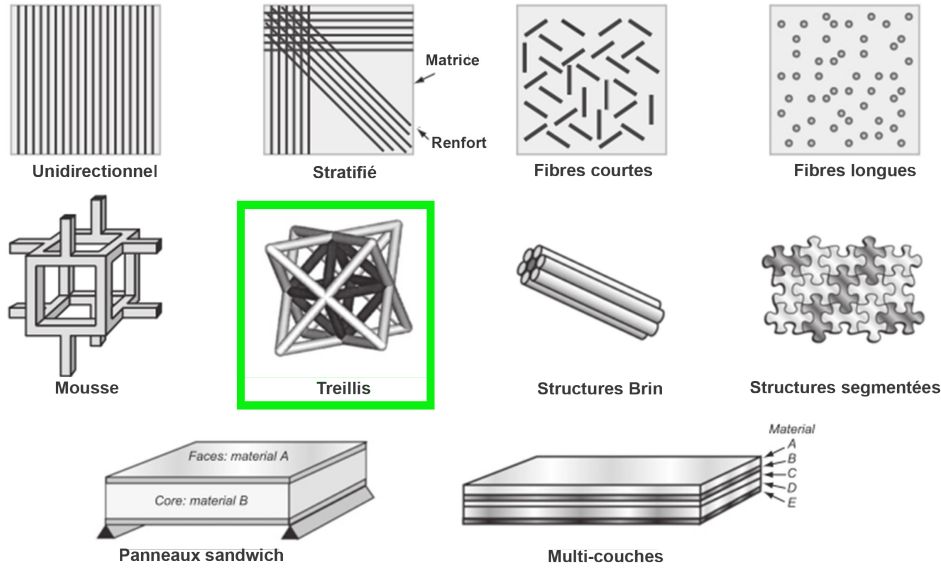


Figure 1 Exemples de matériaux architecturés. Image provenant de [1].

Gibson et Ashby [9] ont proposé des lois d'échelles permettant de prédire la rigidité et la limite d'élasticité de ces deux classes de structures (Tableau 1).

	Traction-compression	Flexion
Rigidité	$\frac{E}{E_S} \propto \left(\frac{\rho}{\rho_S}\right)$	$\frac{E}{E_S} \propto \left(\frac{\rho}{\rho_S}\right)^2$
Limite d'élasticité	$\frac{\sigma_{pl}}{\sigma_{y,s}} \propto \left(\frac{\rho}{\rho_S}\right)^{3/2}$	$\frac{\sigma_{pl}}{\sigma_{y,s}} \propto \left(\frac{\rho}{\rho_S}\right)$

Tableau 1 Lois d'échelles prédisant la rigidité et la limite d'élasticité de structures treillis.

Les structure se déformant par traction-compression sont, à densité égale, généralement plus rigides que celles se déformant par flexion. Durant ce travail de thèse nous allons nous intéresser à une structure se déformant par traction-compression (structure octet-truss, qui sera présentée plus tard).

Pour fabriquer ces structures treillis, des techniques basées sur le pliage et le découpage de tôles métalliques existent [3, 10–13]. En soudant les poutres entre elles, les structures deviennent plus rigides. Cependant, ces techniques sont lourdes à mettre en place et ne permettent pas de fabriquer toutes les géométries possibles.

La fabrication additive permet, elle, de créer des pièces avec une très grande liberté de géométrie. Pour créer des pièces métalliques par fabrication additive, trois technologies majeures existent. Les technologies *Laser Beam Melting* (LBM) et *Electron Beam Melting* (EBM) permettent de fondre couche par couche un lit de poudre métallique en utilisant un laser ou un faisceau d'électrons respectivement. La technologie de dépôt de matière *Direct Metal Deposition* (DMD) dépose de la poudre de métal sur un substrat.

Dans le cadre de la thèse, la technique de fabrication *Electron Beam Melting* a été utilisée.

La technologie Electron Beam Melting

Description générale

La technologie de Fabrication Additive Electron Beam Melting est représentée à travers le schéma de la figure 2. Elle permet de fondre de la poudre métallique couche par couche grâce à un faisceau d'électrons. Les électrons sont créés par une anode en tungstène puis accélérés grâce à une différence de potentiel de 60kV entre l'anode et la cathode. Dans le canon à électrons, les électrons sont focalisés et défléchis par des lentilles électromagnétiques. La lentille de déflexion permet au faisceau de balayer la surface de fabrication.

La poudre est déposée par couches de $50 \mu m$ d'épaisseur grâce à un râteau. La fabrication débute sur une plaque en acier inoxydable afin de supporter les premières couches.

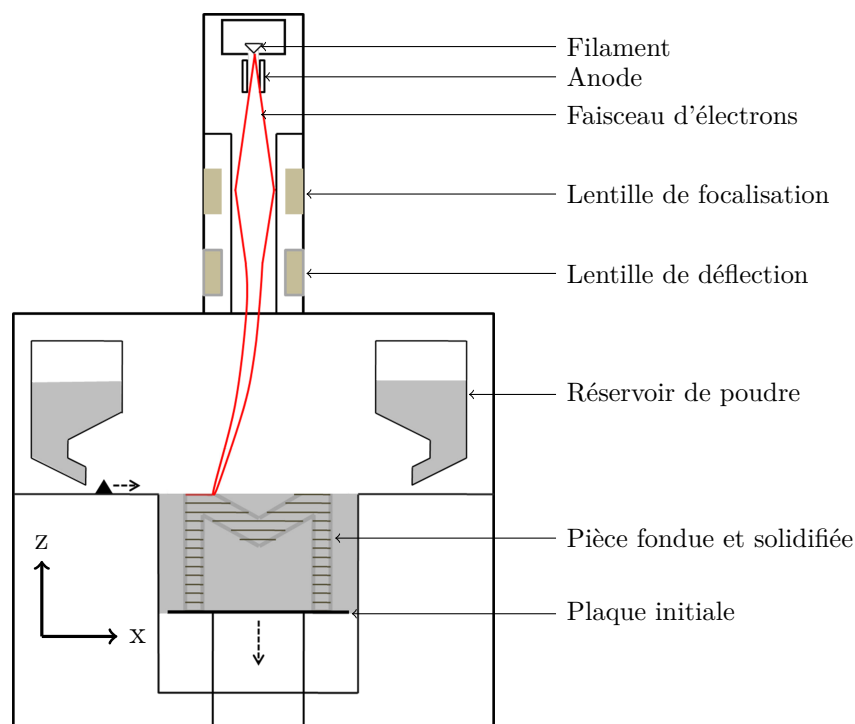


Figure 2 Schéma du procédé EBM.

Pour que les électrons arrivent à la surface, la chambre est maintenue sous vide secondaire (10^{-4} mbar). La taille maximale de pièce réalisable avec la machine EBM A1 est de 200 x 200 x 180 mm. Le faisceau d'électrons défléchi par une lentille électromagnétique permet de fondre à une vitesse très rapide (jusqu'à 8000 m/s).

Le faisceau d'électrons fond localement la poudre selon la géométrie voulue. L'ensemble de la surface de poudre déposée est chauffée avant sa fusion afin de créer des cous entre les particules pour augmenter la conductivité thermique et électrique du lit de poudre. Cette étape (appelée "Preheat") permet d'éviter des accumulations de charges locales pouvant engendrer des explosions électrostatiques de poudre (expliquées en détail dans la thèse de Tushar Mahale [14]). Cette étape de chauffage permet de maintenir une température d'environ $700 \text{ }^{\circ}\text{C}$ à la surface de la couche, contrairement à d'autres techniques de fabrication additive [15–17].

A la fin de la fabrication, la zone de fabrication ressemble à un "gâteau" de poudre consolidé dans lequel se trouve des pièces fondues et consolidées. Afin d'accéder à ces pièces, il faut casser les cous entre les particules frittées. Pour cela, le gâteau est mis dans une boîte à gants dans laquelle il est sablé avec de la poudre de même composition que celle utilisée pour la fabrication. Les pièces fondues sont extraites et la poudre est réutilisée pour une prochaine fabrication.

Matière première : poudre métallique

La matière première pour la fabrication additive par EBM est de la poudre métallique sphérique. Dans cette étude, l'alliage utilisé est le Ti-6Al-4V. C'est un alliage de titane utilisé couramment dans l'industrie aéronautique et biomédicale. La microstructure et les propriétés mécaniques de cet alliage fabriqué par EBM sont expliqués plus en détails dans le chapitre 1.

Le diamètre médian des poudres est de $62 \mu m$ pour les poudres neuves et augmente légèrement pour des poudres recyclées dû au fait que les petites poudres ne sont pas recyclées lors de l'étape de sablage.

Pour que les poudres puissent s'étaler facilement, les particules sont sphériques. Elles ont été obtenues par atomisation au gaz. Ce procédé d'obtention de poudre crée des porosités internes qui se retrouvent dans les pièces fabriquées par EBM. Cela a été largement étudié dans la littérature [18–21].

Problématique et point de départ du projet de thèse

Problématique

Ce sujet de thèse se focalise sur les structures treillis fabriquées par le procédé EBM. Bien que ce procédé permette d'atteindre de nouvelles formes à fabriquer, il apporte aussi de nouvelles contraintes de fabrication.

La stratégie de la thèse est résumée dans la figure 3.

Cette thèse va se focaliser sur les différences géométriques et mécaniques entre le modèle et la pièce fabriquée pour des structures treillis. Afin de faire le lien entre les propriétés "attendues" et les propriétés "réelles", un concept de "matière efficace" émerge. Ce concept peut finalement être utilisé dans des simulations et optimisations mécaniques qui prennent en compte les contraintes de fabrication. Les questions principales sont :

- Quel est l'écart entre la géométrie conçue et celle fabriquée (effet de l'orientation) ?
- Quel est l'impact des différences géométriques sur les propriétés mécaniques désirées ?
- Comment inclure ces contraintes de procédé dans les procédures d'optimisation et simulation ?
- Quelles sont les pistes pour diminuer ces différences ?

Stratégie de la thèse

Pour répondre à ces questions, la stratégie suivante a été adoptée :

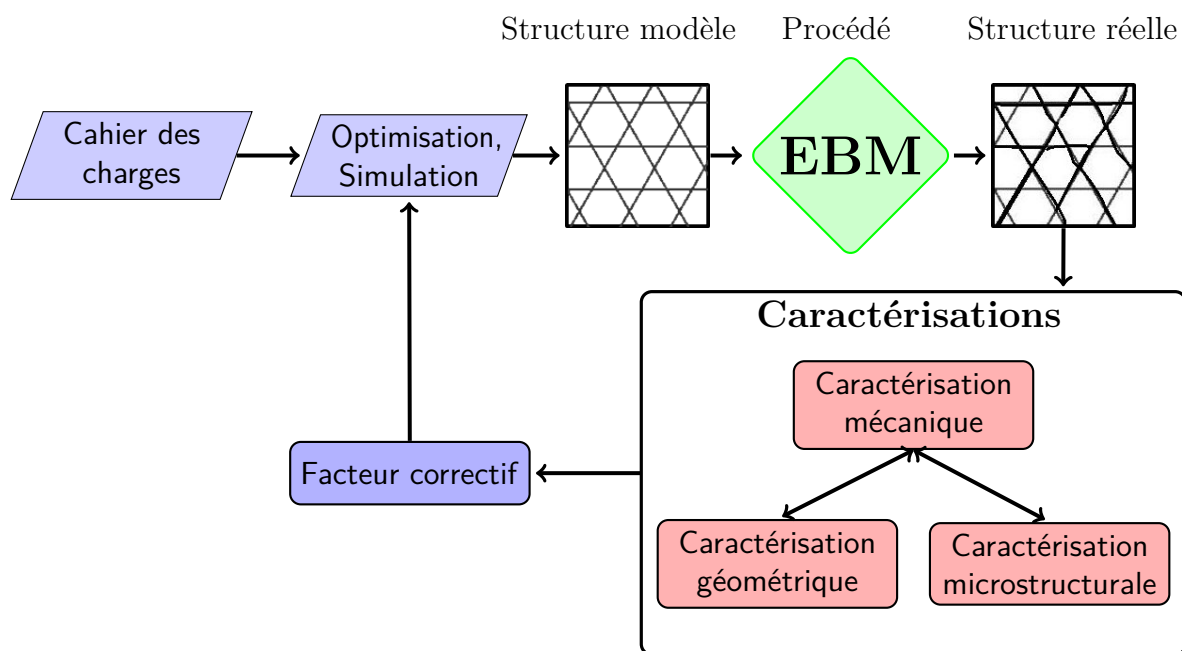


Figure 3 Problématique de la thèse

- 1. Caractérisation du Ti-6Al-4V produit par EBM :** Avant de s'intéresser aux structures treillis, il a fallu caractériser la microstructure et les propriétés mécaniques de pièces massives et fines fabriquées par EBM. L'influence de la taille des poutres sur la microstructure et les propriétés mécaniques a été évaluée.
- 2. Méthode pour la prédiction de la rigidité de structures treillis :** Connaissant les propriétés mécaniques du matériau constituant les poutres, les structures treillis fabriquées par EBM ont été caractérisées.
Des poutres unitaires de différentes tailles et orientations ont été caractérisées par tomographie aux rayons X pour en extraire leur forme et leur taux de porosité. Un concept général a été extrait : le diamètre mécaniquement équivalent.
Ce diamètre a été appliqué sur une structure treillis : l'Octet-truss. L'utilisation de ce concept a été validée en comparant la simulation avec des données expérimentales.
- 3. Optimisation des structures treillis :** Un code d'optimisation paramétrique de structures treillis a été conçu et appliqué à la structure Octet-truss. Ce code permet de prendre en compte les contraintes de fabrication par l'utilisation du diamètre mécaniquement équivalent.
- 4. Amélioration de la précision géométrique et de la rugosité des poutres :** Des techniques d'électro-polissage et d'attaques chimiques ont été utilisées sur des structures treillis réalisées par EBM afin de réduire les irrégularités de surface. Ces études ont été réalisées en collaboration avec l'École de Technologie Supérieure de Montréal (Canada) et l'Université Libre de Bruxelles (Belgique) respectivement.
Les paramètres du procédé ont été adaptés pour réduire le décalage géométrique entre les structures conçues et celle réalisées.



Chapitre 1

Caractérisation du Ti-6Al-4V produit par EBM

1.1 Caractérisation microstructurale

1.1.1 Alliage Ti-6Al-4V conventionnel

L'alliage utilisé durant ce travail de thèse est l'alliage à base titane Ti-6Al-4V grade 5. Il est composé majoritairement de titane avec 6 wt.% d'aluminium et 4 wt.% de vanadium. Selon la norme ASTM F1108 (pour les matériaux fondus), son taux d'oxygène doit être inférieur à 0.2 wt.%.

Cet alliage permet une coexistence des phase α et β à température ambiante. Le diagramme de phase pseudo-binaire de l'alliage est présenté en figure 1.1.

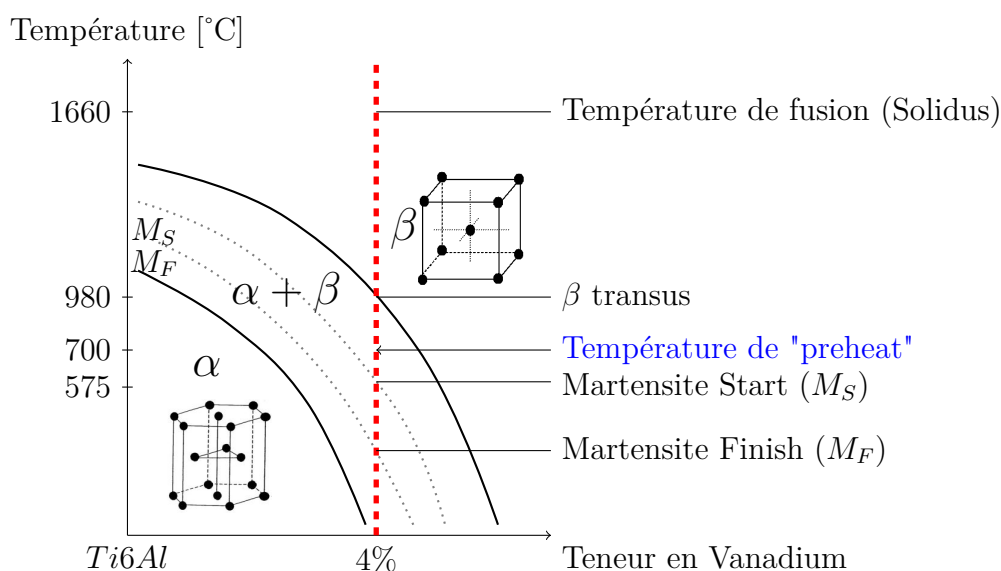


Figure 1.1 Diagramme de phase pseudo-binaire de l'alliage Ti-6Al-4V.

Le solidus de cet alliage se trouve à 1660 °C. En dessous de cette température et jusqu'à la température du β transus, l'alliage est en phase β . En dessous de cette température, il y a germination de la phase α . Comme mentionné dans l'introduction, une spécificité du procédé EBM est un maintien du lit de poudre à une température de 700 °C environ (température de "preheat"). De ce fait, la matière qui subit une fusion dans l'EBM voit

un premier refroidissement rapide jusqu'à la température de 700 °C environ, puis un refroidissement beaucoup plus lent de cette température jusqu'à la température ambiante. Selon la vitesse de refroidissement lors de cette seconde étape, il peut y avoir formation de martensite α' et $\alpha + \beta$ ou seulement de $\alpha + \beta$.

1.1.2 Alliage Ti-6Al-4V produit par EBM

Afin de connaître la microstructure constituant la matière des poutres fines, nous avons fait des analyses au Microscope Électronique à Balayage (MEB) sur des pièces massives et fines. La figure 1.2 représente des micrographies de surfaces parallèles à la direction de fabrication pour une pièce massive et pour une poutre de diamètre 1 mm.

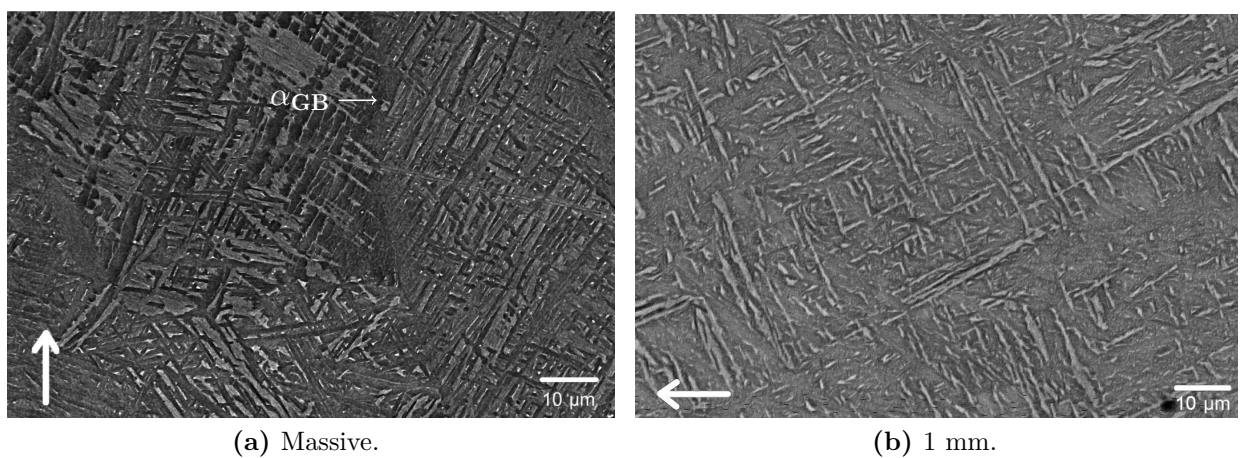


Figure 1.2 Micrographie MEB d'une coupe parallèle à la direction de fabrication pour une pièce massive et pour une poutre de 1 mm de diamètre. La direction de fabrication est représentée par des flèches blanches.

La phase α présente une structure lamellaire avec une microstructure très fine dans les deux cas. Elle est composée de lamelles dans une matrice β . La largeur des lamelles α est de l'ordre de 1 μm . Sur l'image représentant la pièce massive, on peut apercevoir la couche de phase α retenue dans les joints de grains β à haute température (α_{GB}).

Les grains parents β (à haute température) sont allongés et orientés selon la direction de fabrication. Cette orientation préférentielle des grains β à haute température est due à leur croissance épitaxiale tout au long de la fabrication [22–25]. La microstructure de la phase β est donc très anisotrope.

D'après ces observations, la microstructure semble similaire dans le cas des poutres fines et des pièces massives. Suite à des cartographies EBSD, il a été possible de remonter à des informations sur les grains β à haute température. Ces informations ont montré une légère diminution de la largeur de ces grains β de 150-200 μm pour les pièces massives à 70-100 μm pour des poutres fines.

La morphologie des pores rencontrés peut être divisée en deux catégories : sphérique ou non-sphérique. Les pores sphériques proviennent de porosité piégée dans la poudre initiale après le procédé d'atomisation à l'argon. Ce phénomène a été largement étudié dans la littérature [18, 20, 26, 27]. Les pores non-sphériques proviennent quant à eux d'une mauvaise fusion lors du procédé EBM.

1.2 Caractérisation mécanique

1.2.1 Comparaison entre les propriétés mécaniques requises et celles fabriquées

Afin de caractériser pleinement le matériau fabriqué par EBM, des essais de traction ont été réalisés. Dans un premier temps ces essais ont été réalisés sur des éprouvettes de même diamètre (6 mm) provenant de fabrications différentes afin d'évaluer la **reproductibilité** du procédé EBM. La figure 1.3a montre les courbes de traction de six éprouvettes de même géométrie.

Une très grande reproductibilité est visible. Les échantillons affichent un module d'Young de 114 GPa, une limite élastique de 1045 MPa et une contrainte maximale de 1100 MPa. Leur allongement à rupture est de 2.3 % en moyenne.

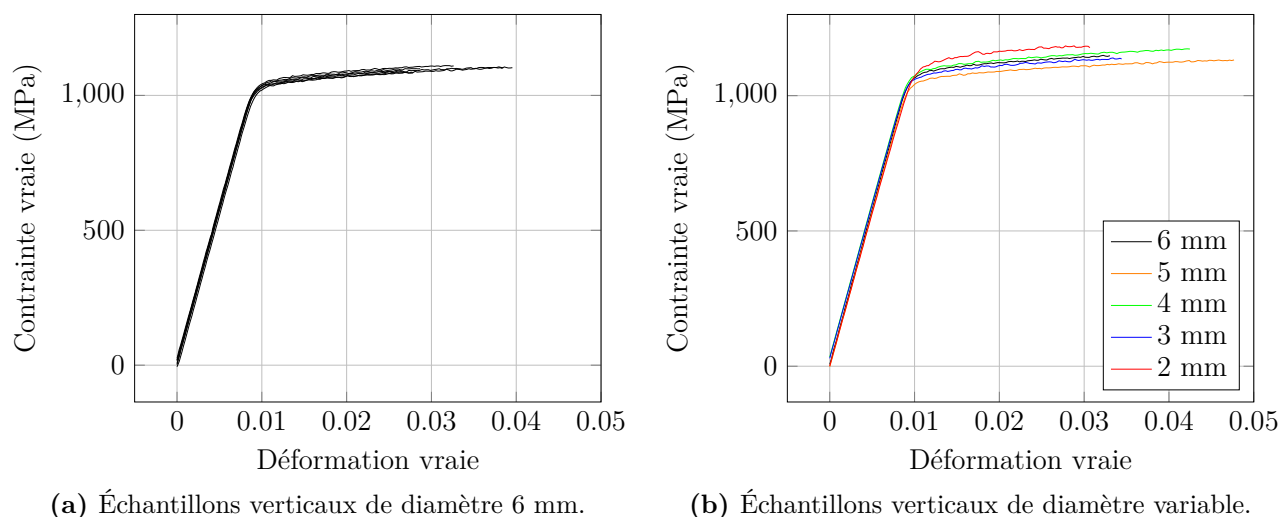


Figure 1.3 Courbes contrainte-déformation pour des éprouvette de 6 mm de diamètre et pour des éprouvettes de diamètre variable

Des éprouvettes brutes de différents diamètres (2 à 6 mm) ont été testées en traction. Les résultats (Figure 1.3b) montrent que la taille de l'éprouvette n'influe quasiment pas sur les propriétés mécaniques. Cela concorde avec les résultats concernant les microstructures présentés dans le paragraphe précédent.

En revanche, les valeurs d'allongement obtenues sont bien plus faibles que les valeurs annoncées par le fournisseur ARCAM (15 %). De plus, la limite d'élasticité et la contrainte maximale sont supérieures aux valeurs annoncées.

D'où proviennent ces changements ?

1.2.2 Vers la compréhension des différences de résistance à la traction et de ductilité

Afin de comprendre ces différences de propriétés mécaniques entre les valeurs attendues et celles obtenues, différents effets ont été analysés.

Le taux d'oxygène présent dans les poudres doit être inférieur à 0.2 % pour des poudres neuves. Du fait du procédé, les poudres non-fondues sont réutilisées à chaque fabrication.

Ainsi des poudres peuvent être réutilisées des dizaines de fois avant d'être fondues. Lors de ces étapes de chauffe-refroidissement, les poudres peuvent se charger en oxygène. Ainsi on peut atteindre des teneurs en oxygène de l'ordre de 0.5-0.6%. L'oxygène se place sur des sites interstitiels du réseau cristallin et restreint des plans de glissement [28, 29]. Il en résulte une augmentation de la résistance mécanique et une baisse de la ductilité (voir figure 1.4). Cependant, cela ne permet pas d'expliquer la si faible ductilité.

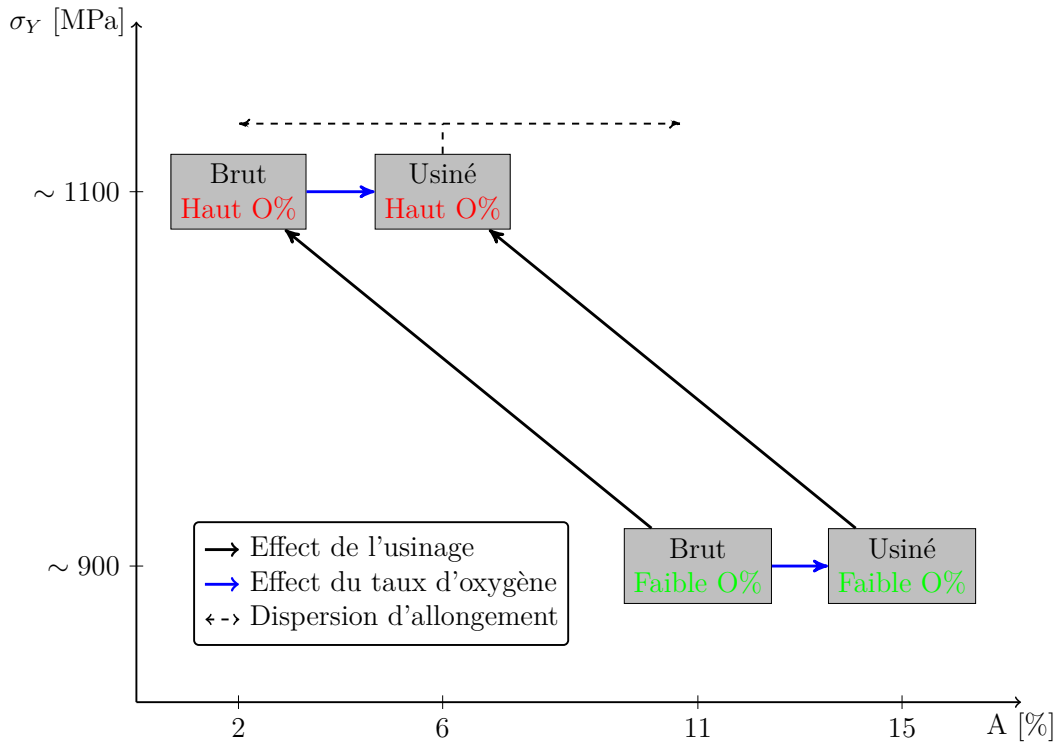


Figure 1.4 Représentation schématique des effets de chaque paramètre sur les propriétés mécaniques de pièces en Ti-6Al-4V fabriquées par EBM. Représentation dans l'espace "limite d'élasticité-allongement à rupture".

L'influence de l'usinage des échantillons sur la ductilité a ainsi été évaluée. Les échantillons usinés présentent des limites d'élasticité et contraintes maximales similaires aux échantillons bruts mais un allongement à rupture plus élevé. Ainsi pour retrouver les propriétés annoncées par le fournisseur, il faut des échantillons sans irrégularités de surface avec un taux d'oxygène inférieur à 0.2 %.

Les échantillons usinés présentent une dispersion d'élongation beaucoup plus grande que pour des échantillons bruts. Des observations par tomographie aux rayons X et fractographie post-mortem ont été réalisées afin de caractériser la porosité en 3D dans l'échantillon et pour déterminer les faciès de rupture. La dispersion d'allongement à rupture est liée à la localisation (ou non) des pores proches de la circonférence de l'échantillon. Le changement de mode de déformation des grains peut aussi jouer un rôle dans cette versatilité.

Chapitre 2

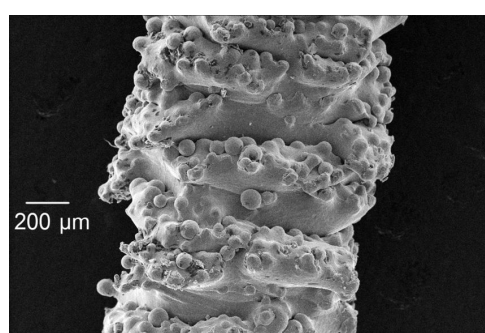
Méthode pour la prédiction de la rigidité de structures treillis produites par EBM

Afin de caractériser les structures treillis produites par EBM, il a fallu dans un premier temps s'intéresser à la géométrie à l'échelle des poutres.

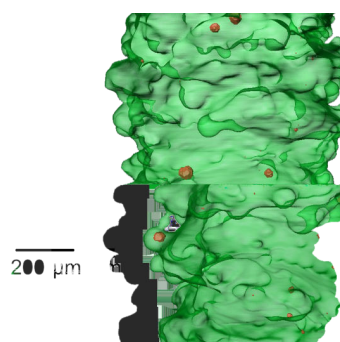
2.1 Caractérisation structurale et mécanique de poutres unitaires

2.1.1 Apparence générale et porosité

La forme générale d'une poutre d'un millimètre de diamètre fabriquée par EBM est représentée sur la figure 2.1. La micrographie MEB (figure 2.1a) montre bien les irrégularités de surface qui sont présentes sur les pièces fabriquées par EBM.



(a) Micrographie MEB.



(b) Volume reconstruit en 3D de la poutre (vert) et des pores (rouge).

Figure 2.1 Morphologie et répartition de la porosité pour une poutre verticale de diamètre 1 mm.

Cette rugosité est à deux échelles. Des poudres collées à la piscine de fusion créent une première rugosité. Une structure en "pile d'assiettes" est visible et crée une rugosité à

plus grande échelle. Cette irrégularité provient d'un mauvais contrôle de la position et de la taille de la piscine de fusion.

La porosité peut aussi être évaluée grâce aux résultats de tomographie aux rayons X. En utilisant des paramètres standards pour la fusion, les pores observés sont tous sphériques et la porosité totale est toujours inférieure à 0.1%. Les pores sont répartis de manière aléatoire dans le volume des poutres comme le montre la figure 2.1b. La faible porosité des poutres ne joue pas de rôle dans le comportement élastique de celles-ci.

La figure 2.2 montre les différences entre la géométrie conçue et celle fabriquée pour des poutres de diamètre 1 mm fabriquées avec le jeu de paramètres standard "Net" de Arcam. Les poutres produites sont systématiquement plus fines que celles conçues. A l'échelle de la structure treillis, les densités produites seront inférieures aux densités du design initial : $\bar{\rho}_{FAB} \leq \bar{\rho}_{CAD}$.

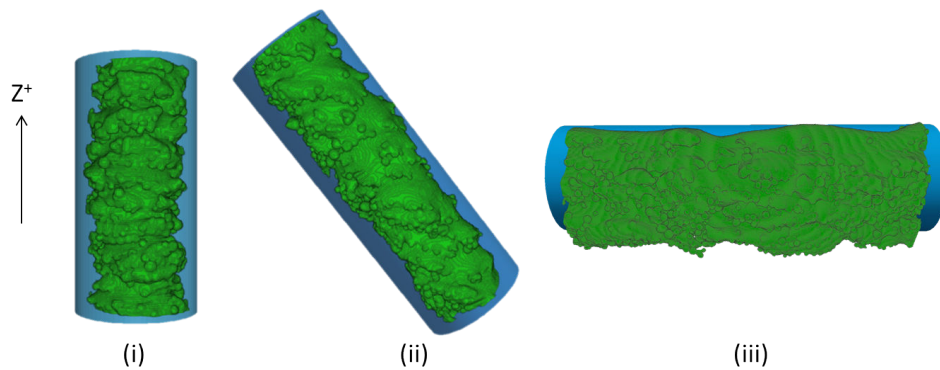


Figure 2.2 Variation de la géométrie des poutres (vert) d'un millimètre de diamètre en fonction de leur orientation. Comparaison avec le design initial (bleu) pour trois orientations : verticale (i), oblique (ii) et horizontale (iii). La direction de fabrication est indiquée par la flèche noire.

Des différences géométriques existent entre les poutres de différentes orientations. Ces différences sont dues à des histoires thermiques différentes en fonction de l'orientation. En effet, lors de l'élaboration de poutres horizontales, la zone qui repose sur de la poudre subit un excès de fusion. Ceci est dû à des problèmes d'évacuation thermique dans la poudre non fondue.

→ La **différence de tailles** entre les poutres conçues et fabriquées produit une différence de densité de la structure et donc une différence de rigidité entre la structure treillis initiale et celle fabriquée.

Comme montré dans la figure précédente (Figure 2.1a), une large irrégularité de surface est observée. Cette irrégularité de surface a été quantifiée et représente une rugosité arithmétique $Ra \sim 40\mu m$ et une hauteur maximum : $Rt \sim 200\mu m$. Ces valeurs fluctuent largement en fonction de l'orientation de la poutre analysée.

→ A cause de ces irrégularités de surfaces, une part importante de la matière de la poutre ne transmet pas les charges efficacement. Il faut donc discriminer la **matière mécaniquement "efficace" et "inefficace"**.

2.1.2 Concept pour relier les caractéristiques géométriques et la prédiction mécanique

Afin de prendre en compte ces deux effet (différence de taille et matière "efficace ou inefficace"), l'idée a été de remplacer la poutre fabriquée par un cylindre de diamètre équivalent ayant la même rigidité que la poutre fabriquée (rouge sur la figure 2.3). Ce cylindre est appelé "cylindre mécaniquement équivalent". Il est obtenu par une simulation numérique sur la géométrie de la poutre fabriquée (calcul FFT effectué directement sur l'image voxélisée d'une poutre).

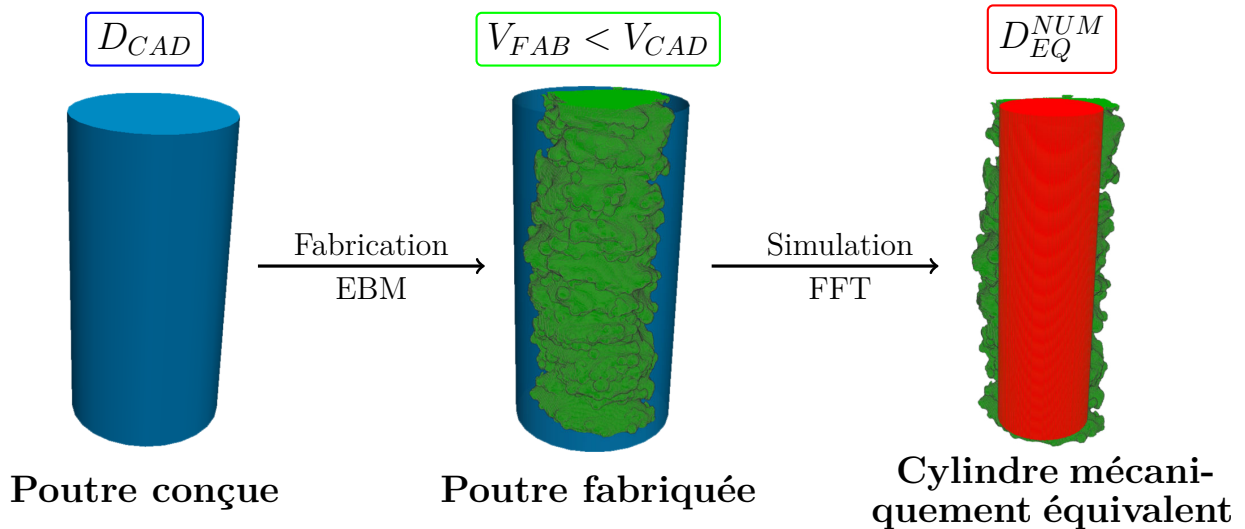


Figure 2.3 Schéma résumant la méthodologie pour extraire le diamètres mécaniquement équivalents.

Pour des poutres de diamètre initial de 1 mm (fabriquée avec le thème "Net" d'Arcam), le diamètre mécaniquement équivalent varie entre 0.58 et 0.70 mm selon l'orientation de la poutre. Il y a donc une différence de 40% sur les diamètres.

Ce concept de cylindre mécaniquement équivalent a besoin d'être validé par comparaison avec des données expérimentales.

2.2 Prédiction des propriétés élastiques de la structure Octet-truss

Afin de valider ce concept de diamètre équivalent, nous nous sommes focalisés sur une structure treillis particulière : l'Octet-truss (voir figure 2.4a). Selon le critère de Maxwell [8], cette structure est dominée par les efforts de traction-compression dans les poutres.

Une simulation par Éléments Finis des propriétés élastiques de cette structure a été réalisée. Une méthodologie d'homogénéisation est appliquée pour simuler les propriétés effectives d'un milieu infini composé de cellules unitaires d'Octet-truss. Des conditions aux limites périodiques sont appliquées sur la cellule unitaire.

Une première simulation est réalisée avec des diamètres initiaux D_{CAD} (en vert sur le graphe de la figure 2.5).

Ces résultats de simulation sont comparés à des résultats obtenus par compression uniaxiale sur des structures Octet-truss. La figure 2.4b montre le dispositif de compression

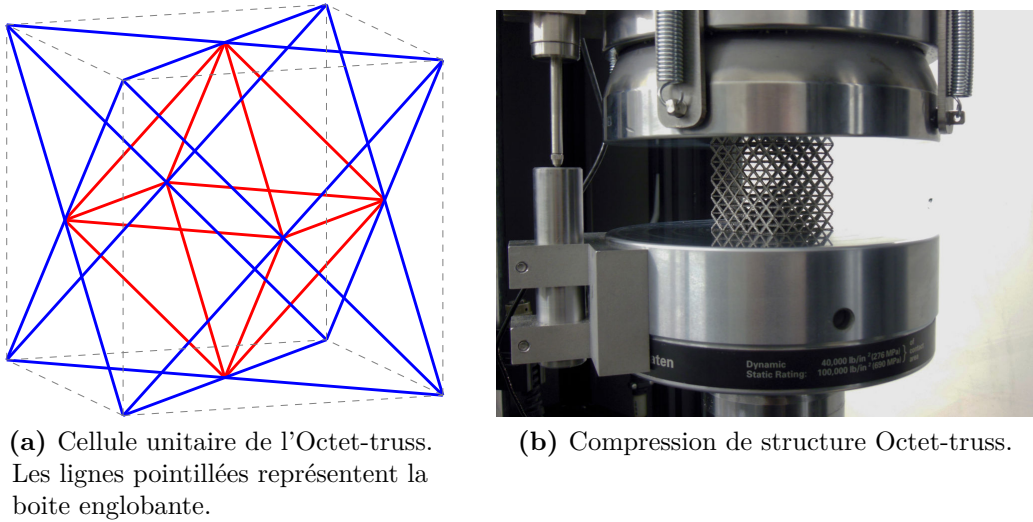


Figure 2.4 Cellule unitaire de l'Octet-truss et photo du dispositif de compression.

d'une structure Octet-truss. Des cycles de charges-décharges sont appliqués afin de déterminer le module d'Young effectif de la structure. Ces tests ont été effectués sur des structures de différentes densités. Les résultats sont reportés dans la figure 2.5 en noir.

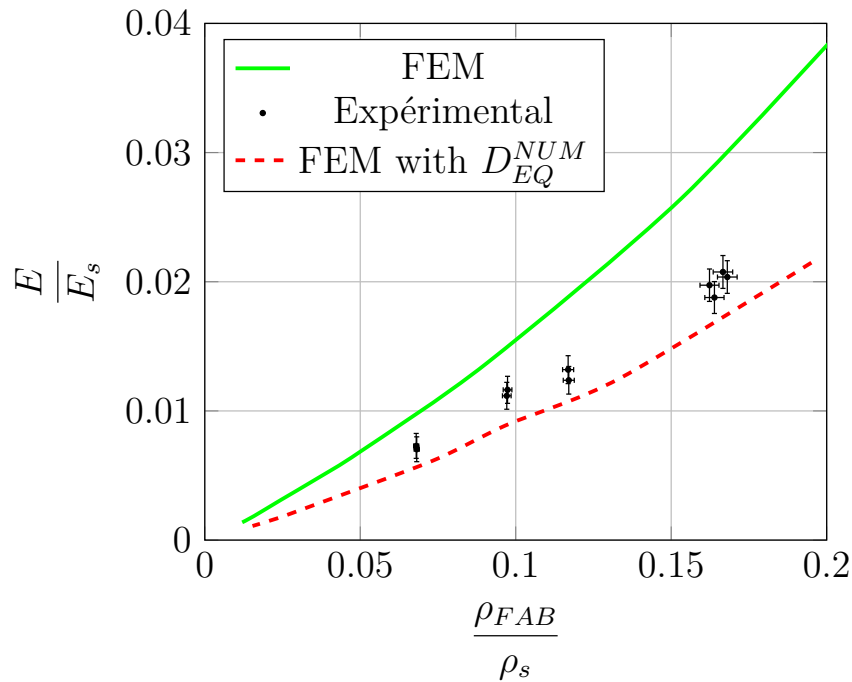


Figure 2.5 Module d'Young relatif en fonction de la densité relative pour une structure Octet-truss. La courbe noire correspond à la simulation avec la géométrie initiale. Les valeurs expérimentales sont indiquées en noir et comparées à la simulation incluant la correction de diamètre équivalent D_{EQ}^{NUM} (en rouge).

Une deuxième vague de simulation a été réalisée dans les mêmes conditions mais en remplaçant D_{CAD} par D_{EQ}^{NUM} . Les résultats de cette simulation sont représentés en rouge. Les résultats expérimentaux sont bien moins rigides qu'attendu. Ceci est dû aux deux effets listés précédemment (différence géométrique et matière "inefficace"). L'utilisation du

diamètre mécaniquement équivalent dans la simulation éléments finis permet de simuler des propriétés élastiques plus proches de celles réelles. Cependant, les propriétés simulées avec ce diamètre équivalent sont légèrement inférieures à celle des structures fabriquées. Cela est probablement dû au fait que le concept de diamètre équivalent est basé sur une équivalence de rigidité au niveau des poutres mais ne permet pas de prendre en compte l'état de contraintes au voisinage des noeuds.

2.3 Variation du diamètre mécaniquement équivalent avec le diamètre nominal et l'orientation des poutres

L'application du diamètre mécaniquement équivalent a été faite sur des poutres d'un millimètre de diamètre. Afin de pouvoir l'utiliser de manière plus globale, ce concept doit être généralisé à des poutres de différents diamètres nominaux (D_{CAD}) et différentes orientations (α). Dans ce but, des poutres de diamètres $D_{CAD}=1, 1.5, 3, 5$ mm et orientations $\alpha=0^\circ, 45^\circ$ et 90° ont été fabriquées avec le thème standard "Melt" (Figure 2.6).

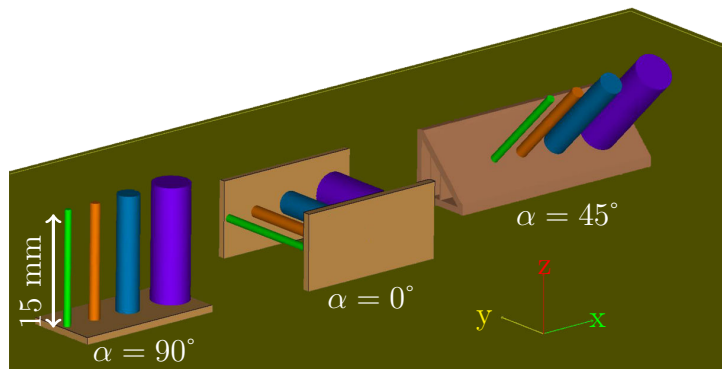


Figure 2.6 Dessin CAD des poutres avant fabrication par EBM. La direction de fabrication suit la direction z.

L'analyse par tomographie aux rayons X permet l'extraction du diamètre mécaniquement équivalent pour chaque orientation et diamètre. Une surface de réponse est appliquée sur ces valeurs afin de produire un résultat analytique de variation du diamètre équivalent en fonction de l'angle et du diamètre des poutres :

$$D_{EQ}^{NUM} = (K_1\alpha + K_2) D_{CAD} + C_1\alpha + C_2 \quad (2.1)$$

où $K_1 = 1.02 \cdot 10^{-3}$, $K_2 = 8.65 \cdot 10^{-1}$, $C_1 = -3.37 \cdot 10^{-3}$ et $C_2 = -1.16 \cdot 10^{-2}$.

Résumé

La figure 2.7 résume la méthodologie développée dans ce chapitre. La structure "idéale" présente une densité $\bar{\rho}_{CAD}$ et une rigidité \bar{E}_{CAD} . L'effet de la différence géométrique est visible (1). Elle décroît la densité et donc le module d'Young (\bar{E}_{C_1}). Si on discrimine la

2.3. Variation du diamètre mécaniquement équivalent avec le diamètre nominal et l'orientation des poutres

matière inefficace (2), le module d'Young final est encore diminué (\bar{E}_{C_2}). Le diamètre mécaniquement équivalent prend en compte ces deux effets (1+2).

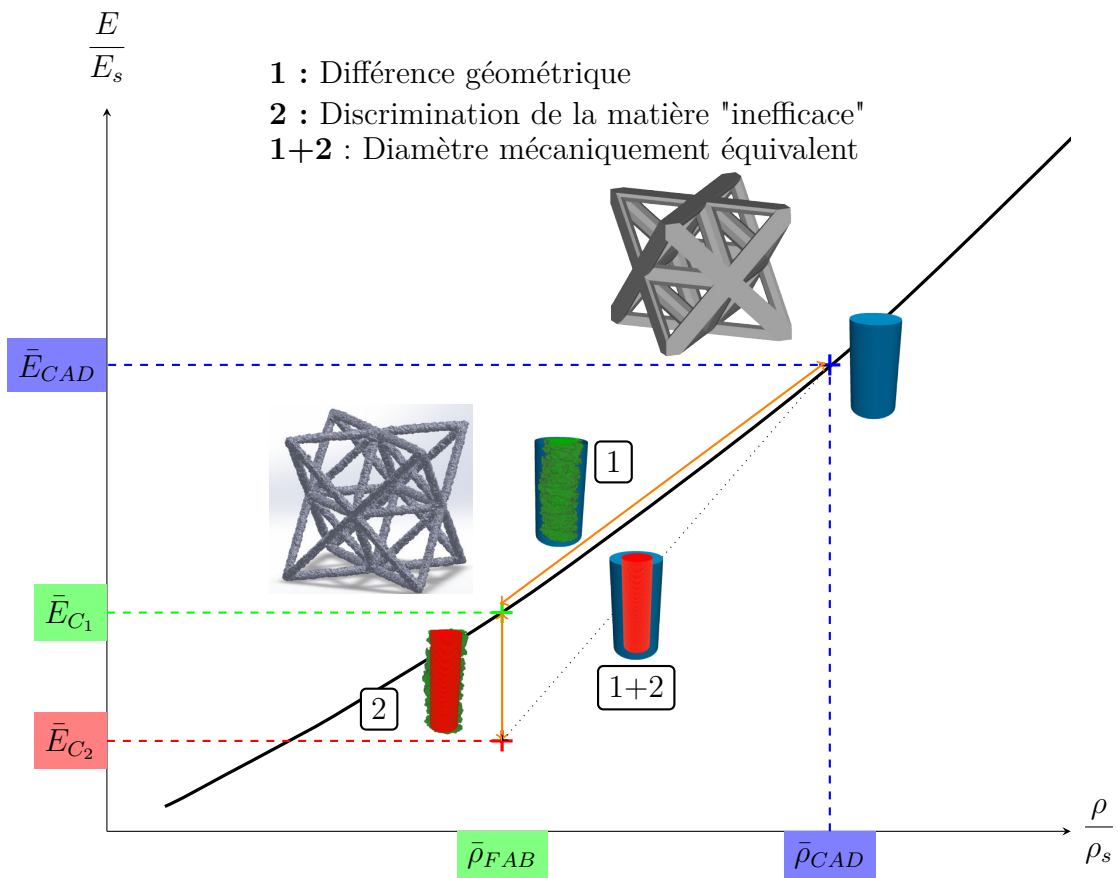


Figure 2.7 Graphique résumant la méthodologie présentée dans ce chapitre.

Chapitre 3

Optimisation des structures treillis

Ce chapitre a pour but d'utiliser le diamètre mécaniquement équivalent dans deux exemples : l'optimisation de l'orientation de fabrication d'une structure treillis et l'optimisation paramétrique de structures treillis.

3.1 Optimisation de l'orientation d'une structure treillis pour sa fabrication par EBM

3.1.1 Démarche

L'utilisation du diamètre mécaniquement équivalent permet de prédire, pour une structure treillis, sa position optimale (φ) dans l'enveloppe de fabrication. Cet optimum dépend de la propriété finale souhaitée (module d'Young, module de cisaillement, coefficient de Poisson...).

Notre étude se focalise sur la structure Octet-truss. Les simulations étant itératives, la simulation est basée sur des éléments poutre avec le formalisme de Timoshenko. La structure Octet-truss est représentée sur la figure 3.1.

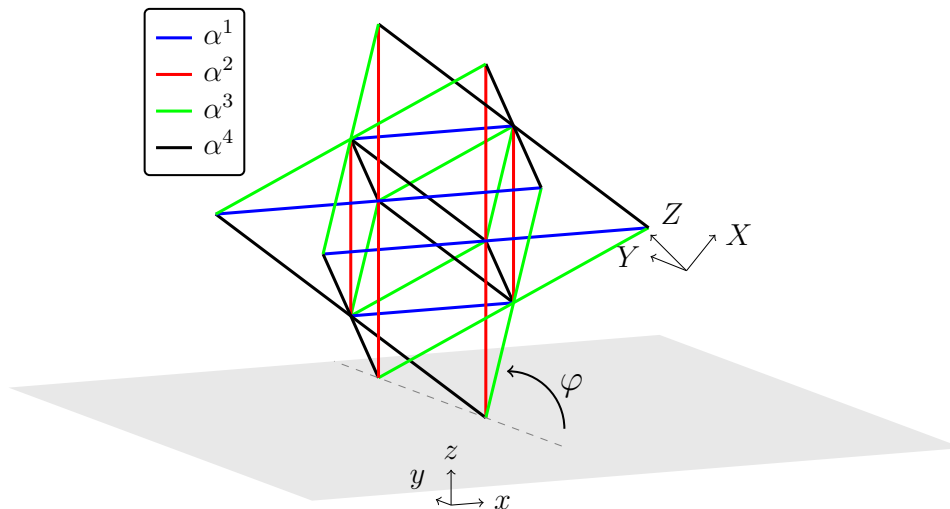


Figure 3.1 Orientation des poutres (α^i) en fonction de l'orientation globale de la structure treillis (φ). x, y, z représente le système de coordonnées global et X, Y, Z représente le système de coordonnées local du treillis.

La valeur analytique du diamètre équivalent développé dans le chapitre précédent dépend de l'orientation de la poutre. Afin de l'appliquer à chaque poutre indépendamment, il a fallu déterminer l'orientation de chaque poutre (α^i) en fonction de l'orientation de la structure (φ). Il existe pour cette structure quatre groupes de poutres ayant la même orientation (rouge, vert, bleu noir sur la figure 3.1). Les relations suivantes ont été déterminées :

- $\alpha^1 = |45 - \varphi|$
- $\alpha^2 = 90 - |45 - \varphi|$
- $\alpha^3 = \sin^{-1} \left(\frac{\sin(\varphi)}{\sqrt{2}} \right)$
- $\alpha^4 = \sin^{-1} \left(\frac{\cos(\varphi)}{\sqrt{2}} \right)$

3.1.2 Résultats

En utilisant ces relations, il est possible d'extraire les positions optimales pour certaines propriétés. On s'intéresse ici à une structure Octet-truss de densité 4.5 %. Quelques résultats ont été tracés en figure 3.2.

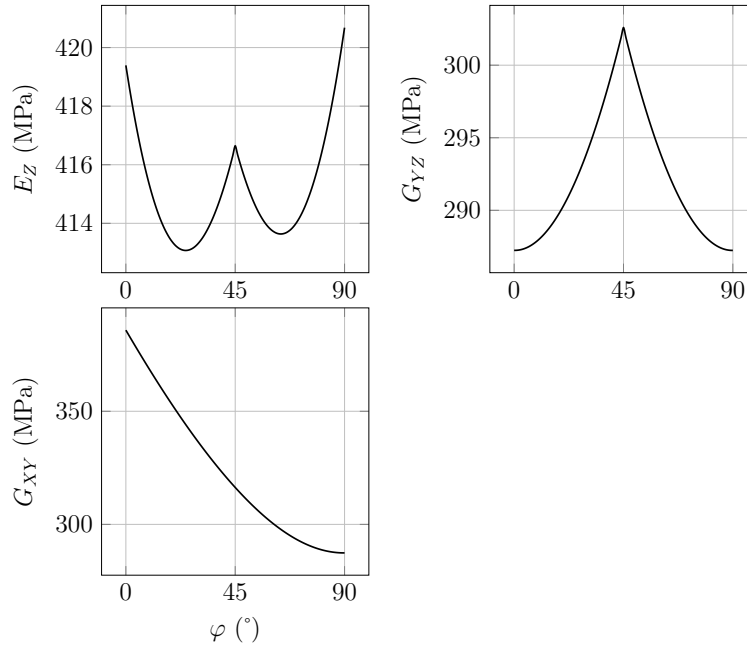


Figure 3.2 Variation de modules d'Young et de cisaillement en fonction de l'angle de fabrication de la structure treillis (φ).

La prise en compte des diamètres équivalents permet de prédire que pour l'optimisation du module de cisaillement G_{XY} , la position optimale sera proche de $\varphi = 0^\circ$. Cette prise en compte est essentielle car le module de cisaillement peut varier de 25 %. Pour ce qui est du module d'Young selon la direction Z, bien que les variations soient faibles, la prise en compte des diamètres équivalents permet de voir un optimum local pour $\varphi = 45^\circ$.

Sachant que les positions $\varphi = 0^\circ, 90^\circ$ sont des positions interdites (difficulté de sortir la pièce après réalisation), il faudra donc privilégier une fabrication à 45° pour optimiser cette propriété.

3.2 Optimisation paramétrique de structures treillis fabriquées par EBM

3.2.1 Démarche

L'utilisation des diamètres équivalents permet en outre la création de procédures d'optimisation paramétrique "réalistes" i.e. qui prennent en compte les défauts de fabrication.

L'optimisation paramétrique est basé sur un script de minimisation (de type quasi-Newton) pour la détermination des nouveaux paramètres à chaque itération. Pour chaque itération, le jeu de paramètres est testé pour voir s'il satisfait les contraintes d'optimisation. Ensuite les diamètres sont changés en diamètres équivalents pour être utilisés dans une simulation éléments finis. La fonction objectif est ensuite calculée à partir des propriétés effectives simulées (E , G , ν). La convergence est atteinte lorsque la fonction objectif tend à être constante.

Les paramètres de l'optimisation paramétrique (schématisés sur la figure 3.3) sont :

- D_{CAD} : Le diamètre nominal des poutres.
- l : La longueur des poutres.
- θ : L'angle d'ouverture de la structure. L'Octet-truss régulier présente un angle $\theta=90^\circ$.
- L'angle de fabrication de la structure treillis φ est soit fixé à 45° ou inclus dans le jeu de paramètres.

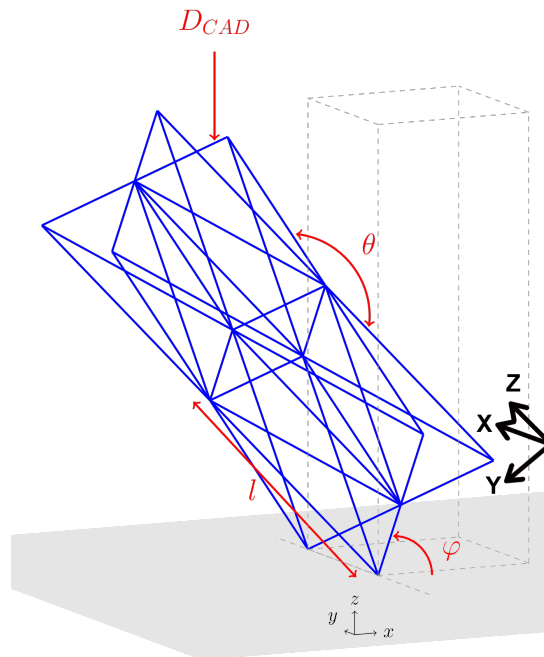


Figure 3.3 Schéma représentant les paramètres pour la procédure d'optimisation.

Des contraintes sont affectées à ces paramètres. On retiendra que la densité ne peut être supérieure à 5 %, le diamètre nominal doit être supérieur ou égale à 1 mm, les

longueurs de poutres sont limitées ($1\text{mm} \leq l \leq 3\text{cm}$), l'angle d'ouverture ne peut pas atteindre des positions extrêmes ($10^\circ \leq \theta \leq 170^\circ$) et l'angle de fabrication ne peut pas atteindre les positions interdites ($10^\circ \leq \varphi \leq 80^\circ$).

Dans cet exemple, l'objectif est de maximiser le module d'Young selon la direction Z (voir figure 3.3). Aucune sensibilité aux conditions initiales n'a été révélée.

3.2.2 Résultats

Deux procédures d'optimisation ont été réalisées. Dans la première, l'angle de fabrication de la structure n'est pas un paramètre, il est fixé ($\varphi = 45^\circ$). Dans la seconde, il fait partie des paramètres.

Les paramètres optimum sont similaires pour les procédures d'optimisation : $D_{CAD} = 1.04\text{mm}$, $l = 3\text{cm}$, $\theta = 156^\circ$. Cependant, dans le cas de l'optimisation avec l'angle de fabrication φ , l'optimum final est $\varphi = 80^\circ$. La géométrie finale est représentée pour ces deux cas dans la figure 3.4. On observe que les géométries finales sont similaires, seul l'angle de fabrication change.

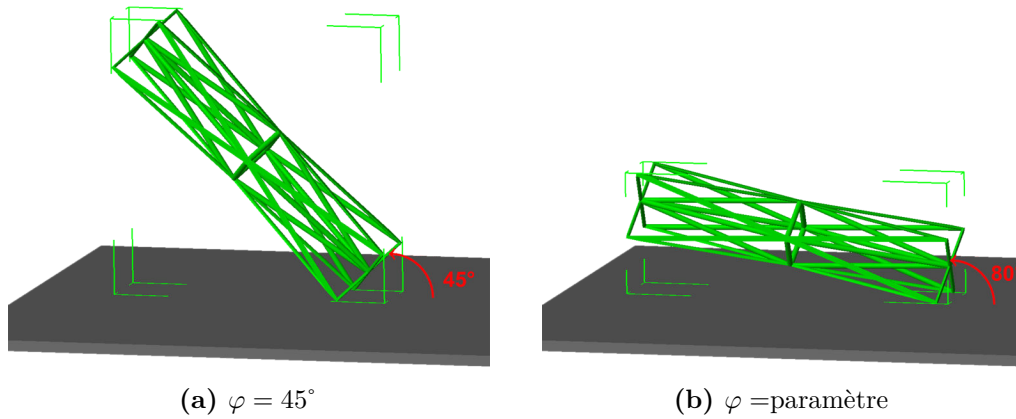


Figure 3.4 Géométrie résultant des deux procédures d'optimisation.

Les modules d'Young finaux sont 2.5 GPa pour la simulation où $\varphi = 45^\circ$ et 3.1 GPa quand φ est un paramètre. **La prise en compte de l'angle de fabrication de la structure (φ) permet donc une augmentation de 20 % de la rigidité finale.**

3.2.3 Développements futur

Dans cet exemple, nous avons choisi de nous focaliser sur l'optimisation du module d'Young de la structure Octet-truss dans une direction. Le code présenté ici permet de représenter les "vraies" propriétés des structures treillis fabriquées par EBM.

En ce sens, ses applications sont plus larges. On peut penser à une optimisation avec des fonctions objectif multi-critères (Combinaison module d'Young et module de cisaillement), multi-physiques (combinaison rigidité et conductivité thermique). Il est aussi envisageable de faire varier le diamètre de chaque poutre indépendamment dans l'optimisation.

Chapitre 4

Amélioration de la précision géométrique et de la rugosité des poutres

4.1 Amélioration de la qualité de surface par des post-traitements

Dans le manuscrit en anglais, deux post-traitements ont été étudiés : l'électro-polissage et l'attaque chimique. Nous nous focaliserons ici sur l'attaque chimique (qui apparaît plus appropriée pour ce genre de structures). Les résultats sur l'étude d'électro-polissage peuvent être trouvés dans la section 13.1 du manuscrit en anglais.

L'étude de l'attaque chimique résulte d'une collaboration avec l'Université libre de Bruxelles¹. Elle a pour but de retirer les particules qui ont collé aux poutres et de réduire l'effet pile d'assiettes expliqué dans le chapitre 2.

4.1.1 Démarche

La solution d'attaque utilisée est composée de 3% HF and 13% HNO_3 . Les échantillons sont trempés deux fois quatre heures. Les échantillons utilisés sont présentés dans la figure 4.1.

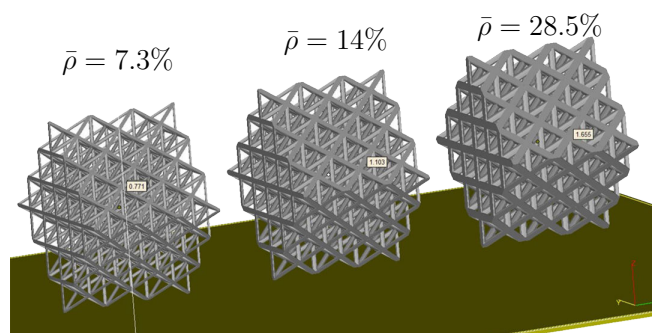


Figure 4.1 Structures Octet-truss utilisées pour l'attaque.

¹Collaboration avec Stéphane Godet et Charlotte de Formanoir. L'attaque chimique a été réalisée à Bruxelles, la production et la caractérisation des structures ont été menées à Grenoble

Leur densité varie entre 7.3 % et 28.5 %. Les longueurs de poutres ont été modifiées pour atteindre ces valeurs (0.8 mm, 1.1 mm et 1.7 mm).

4.1.2 Résultats

Après attaque, la structure présente une densité plus faible (28.5%→21%, 14%→7%, 7%→4%). Pour la caractérisation géométrique, nous nous sommes focalisés sur la structure la plus dense qui présente une densité finale de 21 %. A partir de cette structure deux poutres ont été extraites et comparées à une poutre initiale. Une poutre a été extraite du bord de la structure ("externe") et une autre du centre de la structure ("interne") afin de quantifier l'homogénéité de l'attaque.

Les géométries sont présentées en figure 4.2. L'attaque chimique permet l'amélioration de la surface des poutres. Qualitativement, l'attaque chimique paraît homogène. Elle permet l'enlèvement des particules collées à la surface et la diminution de l'effet "pile d'assiettes".

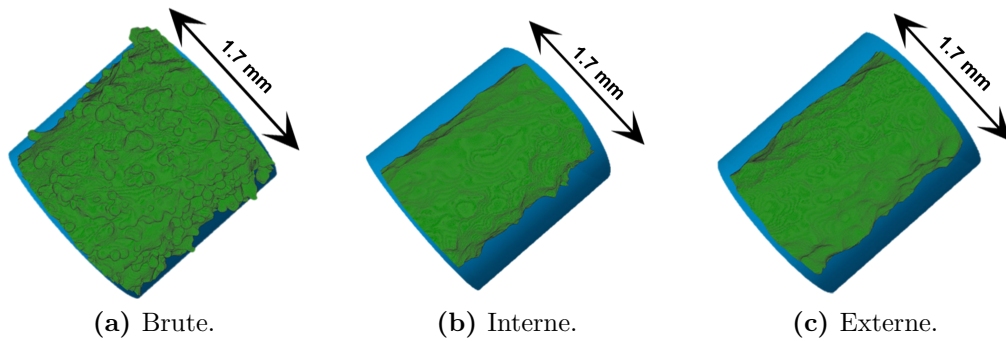


Figure 4.2 Image des poutres de 1.7 mm de diamètre brutes et à différents endroits de la structures attaquée ("Interne" et "Externe"). Le cylindre bleu représente le diamètre nominal $D_{CAD} = 1.7mm$.

L'analyse quantitative de la rugosité a été réalisée suivant la méthode développée dans le manuscrit en anglais (paragraphe 7.1.3). Les poutres attaquées présentent la même rugosité $Ra \simeq 25\mu m$, contre une rugosité initiale $Ra = 35\mu m$. L'attaque chimique permet donc une réduction notable de la rugosité.

Le module d'Young des structures avant et après attaque a été déterminé par compression uniaxiale. Les résultats sont tracés sur la figure 4.3. Le module d'Young de la structure "Brute" est inférieur à celui de référence (obtenu par simulation élément finis dans la figure 2.5). Le module d'Young de la structure après attaque (rouge) est plus proche de la valeur de référence (vert). **Cette amélioration vient de la réduction du volume de matière "inefficace" dans les poutres.**

Ainsi, l'attaque chimique permet un traitement homogène pour réduire la rugosité et augmenter la fraction de volume mécaniquement "efficace" dans les poutres fabriquées par Electron Beam Melting.

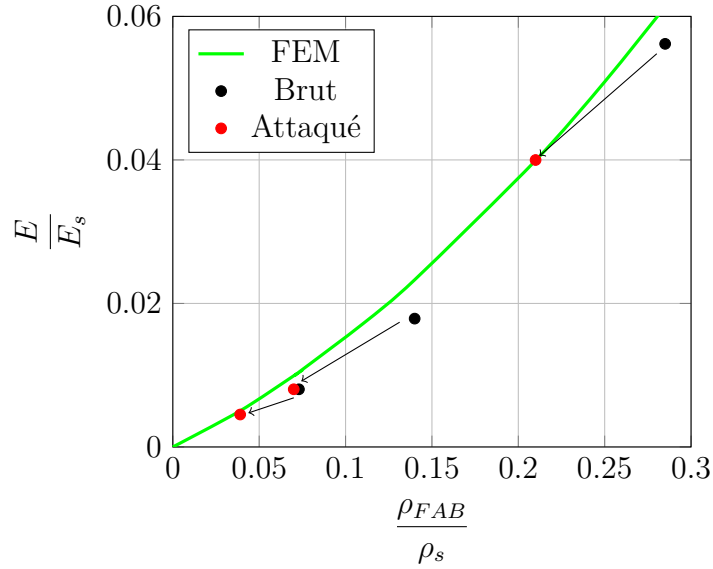


Figure 4.3 Module d'Young relatif en fonction de la densité relative pour des structures treillis brutes (noir) et après attaque chimique (rouge). La courbe verte représente la courbe de référence obtenue par simulation éléments finis.

4.2 Amélioration de la précision géométrique par changement des paramètres de fabrication

Le but de cette section est d'améliorer la taille des poutres en jouant sur les paramètres et stratégies du procédé. Nous nous concentrerons sur le changement de stratégies de fusion pour fondre des poutres de 1 mm avec un diamètre mécaniquement équivalent plus proche du nominal.

4.2.1 Démarche

Comme mentionné dans le chapitre 2, les poutres de 1 mm produites par EBM sont plus fines que celles conçues. L'idée a été de jouer sur les paramètres et stratégies de fusion pour réduire cette différence de taille. Pour faire cela, il a fallu jouer sur le décalage entre le premier contour et le contour du modèle CAD (figure 4.4). Le premier contour a été modifié de $CO_1 = 0.3mm$ à $CO_1^{OPT} = 0.128mm$.

La valeur du nouveau décalage de contour (CO_1^{OPT}) est le résultat d'une simulation thermique réalisée à Grenoble². Des simulations ont été lancées avec plusieurs valeurs de décalage CO_1 jusqu'à trouver la valeur permettant de fondre une poutre ayant des dimensions proches du diamètre nominal.

La valeur du second décalage CO_2 n'a pas été modifiée. Des contours internes ont été rajoutés pour permettre la fusion de l'ensemble de la poutre.

²Réalisée par Nicolas Béraud (actuellement doctorant au laboratoire G-Scop, Université Grenoble Alpes)

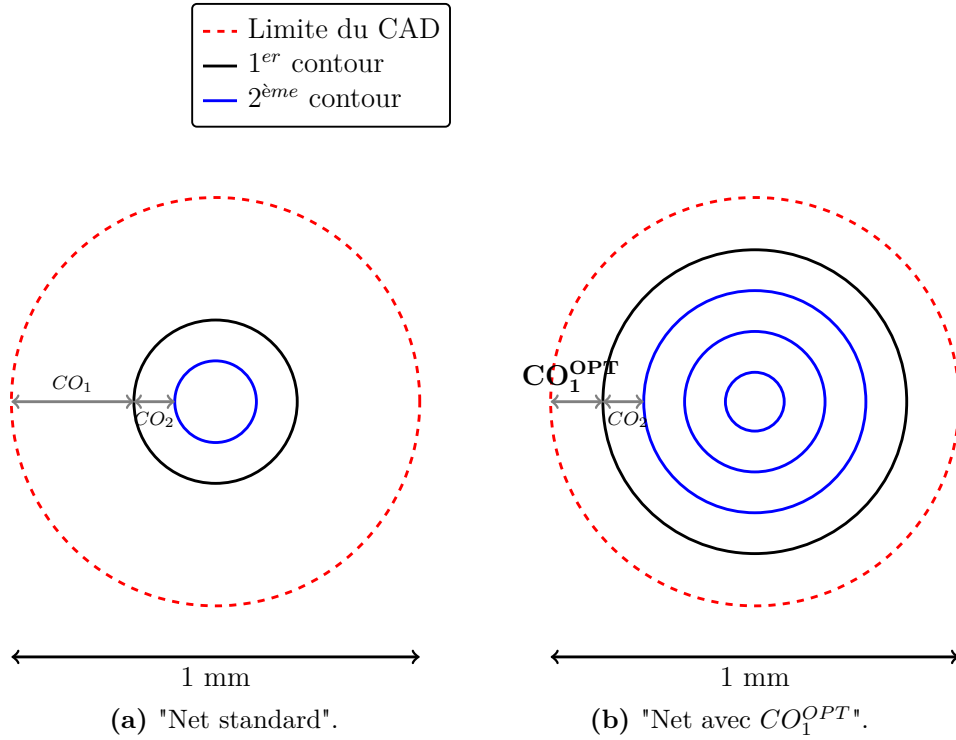


Figure 4.4 Schéma du chemin de fusion pour un cylindre vertical de diamètre 1 mm en utilisant différentes stratégies de fusion ("Net standard" et "Net avec CO_1^{OPT} ").

4.2.2 Résultats

Une poutre verticale de 1 mm de diamètre a été fabriquée avec cette nouvelle stratégie de fusion et analysée par tomographie aux rayons X. La géométrie finale est représentée dans la figure 4.5b et comparée à la stratégie standard "Net" (figure 4.5a).

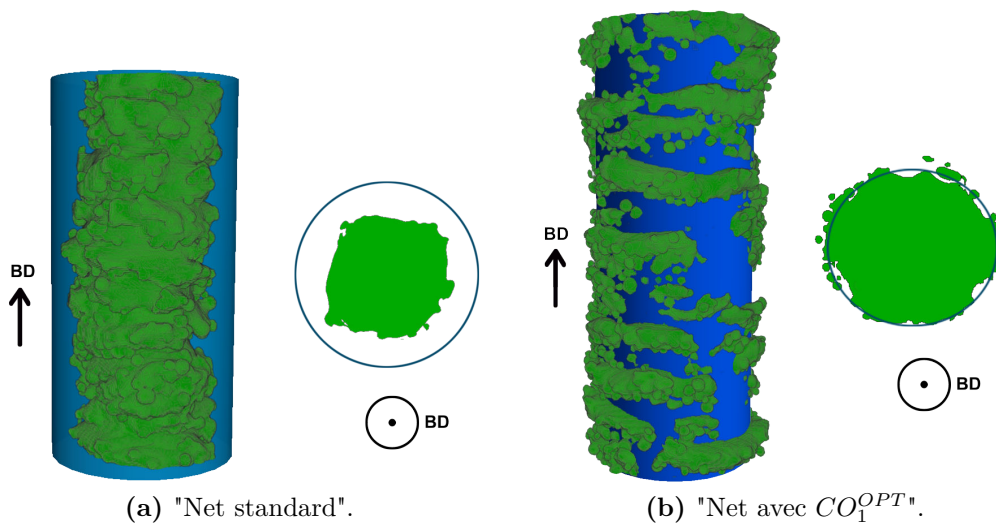


Figure 4.5 Vues verticales et de section pour des poutres verticales de diamètre 1 mm produites avec les deux stratégies. La direction de fabrication est indiquée par la flèche noire.

La poutre fabriquée avec la nouvelle stratégie est plus large et se rapproche plus du

cylindre nominal (bleu). La rugosité de surface semble du même ordre de grandeur pour les deux stratégies. L'analyse quantitative de la poutre produite avec la nouvelle stratégie montre que le diamètre mécaniquement équivalent est passé de 0.46 mm à 0.84 mm. La différence géométrique entre la dimension voulue et celle réalisée est donc drastiquement réduite.

Cependant, cette modification de stratégie n'a pas modifié la rugosité de surface. L'effet de la matière mécaniquement "inefficace" est toujours présent.

La variation du décalage du premier contour permet de réduire la différence de diamètre entre la géométrie souhaitée et celle réalisée. En revanche, elle ne permet pas une réduction du volume de matière "inefficace".

Conclusion et perspectives

Conclusion

Objectifs et méthodes

Le but de cette thèse était de caractériser et optimiser les structures treillis créées par Fabrication Additive en utilisant la technologie Electron Beam Melting. Il a fallu d'abord caractériser la microstructure et les propriétés mécaniques du Ti-6Al-4V fabriqué par EBM.

Suite à cela, nous avons caractérisé les structures treillis avec des poutres de 1 mm grâce à la tomographie aux rayons X notamment. La caractérisation géométrique couplée avec une simulation mécanique (de type FFT) a permis d'extraire la rigidité effective de chaque poutre, et par extension le concept de **diamètre mécaniquement équivalent**. Ce concept a été validé en l'appliquant sur une structure Octet-truss. Sa rigidité a été mesurée par compression uniaxiale et comparée aux simulation éléments finis prenant en compte le diamètre équivalent.

La nécessité d'utiliser ce concept de diamètre mécaniquement équivalent dans la simulation et l'optimisation mécanique a été montrée. Elle permet de prendre en compte les contraintes de fabrication du procédé EBM.

Enfin, la précision géométrique et de la qualité de surface des poutres fabriquées par EBM a été améliorée grâce à des post-traitement de surface (attaque chimique) ou en changeant des paramètres et stratégies de fusion.

Résultats principaux

Caractérisation du Ti-6Al-4V produit par EBM

La microstructure de pièces massives et de poutres fines a été étudiée. Dans les deux cas, la microstructures est composée de fines lamelles α à l'intérieur d'une matrice β . Les grains parents β sont orientés selon la direction de fabrication.

Les poutres fines présentent la même taille de lamelles mais des grains parents β plus fins. Cela peut être l'explication de leur plus haute dureté.

Les mêmes propriétés mécaniques (essais de traction) ont été déterminées pour des structures fines et massives. L'effet de la rugosité et du taux d'oxygène ont été mis en évidence.

Méthode de prédiction de la rigidité de structures treillis

- En utilisant les paramètres standard de fusion, le taux de porosité des pièces reste constamment inférieur à 0.1 %. Les pores sont sphériques et proviennent du procédé d'atomisation des poudres.
- Les poutres produites sont systématiquement plus fines que celles conçues. Les structures treillis fabriquées sont donc moins denses que celles désirées.
- Dû à une large irrégularité de surface, les poutres peuvent être séparées en matière mécaniquement "efficace" et "inefficace". La rigidité de la poutre est portée par la matière "efficace".
- En calculant la rigidité d'une poutre, il est possible de déterminer le cylindre équivalent ayant la même rigidité que la poutre fabriquée. Ce cylindre a un diamètre mécaniquement équivalent (D_{EQ}^{NUM}). Ce concept prend en compte les deux effets précédents : la différence de taille et la matière "efficace".
- Ce concept a été validé en comparant des simulations éléments finis et des données expérimentales sur une structure Octet-truss.
- Une relation analytique reliant ce diamètre équivalent avec l'orientation de la poutre (α) et le diamètre nominal (D_{CAD}) a été établie : $D_{EQ}^{NUM} = f(\alpha, D_{CAD})$.

Optimisation mécanique de structures treillis

- La relation analytique précédente a été utilisée pour optimiser le placement d'une structure Octet-truss dans l'enceinte de fabrication.
- La relation analytique a été implémentée dans une procédure d'optimisation paramétrique. Cette optimisation mécanique permet une amélioration de la distribution de matière en prenant en compte les contraintes de fabrication dues au procédé EBM.

Amélioration de la précision géométrique et de la morphologie de surface

- Le post-traitement de structures treillis par attaque chimique permet une diminution homogène de la rugosité de surface et donc une amélioration de la proportion de matière mécaniquement "efficace".
- Le changement de paramètres et stratégies de fusion permet de réduire le décalage géométrique entre la poutre conçue et celle fabriquée. L'optimisation de ces paramètres et stratégies doit passer par une simulation thermique du procédé.

Perspectives

Généralisation du concept de diamètre mécaniquement équivalent

Le diamètre mécaniquement équivalent défini dans ce travail de thèse permet de prendre en compte les différences géométriques et mécaniques entre le design initial et la pièce fabriquée. A travers deux exemples, nous avons montré l'importance de la considération des contraintes de fabrication dans la simulation mécanique.

Les règles définies dans ce travail ont des implications à plus large échelle. Il serait intéressant d'introduire dans des codes commerciaux un concept similaire lié à un procédé particulier (EBM, LBM ou DMD). Il faudrait aussi déterminer précisément les contraintes de chaque procédé : *e.g.* diamètre minimal de poutres, angles interdits pour la fabrication, taille minimum de cellules, contraintes de dépoufrage, nécessité de support. . .

Le concept de diamètre équivalent développé ici est valide pour des propriétés élastiques. Pour certaines applications (biomédical ou aéronautique), les **propriétés en fatigue** sont de grande importance. La rugosité de surface va jouer un rôle très important pour cette propriété. Une étude préliminaire a été menée pour réduire ces irrégularités de surface par attaque chimique. Cependant, il serait intéressant de voir l'impact de ces attaques chimiques sur les propriétés en fatigue de structures treillis.

L'approche développée dans ce travail de thèse peut être un point de départ pour l'étude des propriétés en fatigue de structures treillis.

Application des structures treillis

Les structures treillis sont intéressantes pour des application de légèreté. Elles peuvent être introduites directement dans le processus de conception ou émerger d'une optimisation topologique. Certaines méthodes (*e.g.* SIMP method [30, 31]) définissent une répartition optimale de la matière en niveaux de gris. Ces niveaux de gris correspondent à un niveau donné de propriétés mécaniques [32]. Ces géométries en niveaux de gris peuvent être remplacées par des zones "treillis" et des zones denses. Une **génération conforme** des structures treillis sur les interfaces avec les zones denses est donc nécessaire.

Dans ce sens, nous avons développé un logiciel de génération de structures treillis périodiques et aléatoires. Il permet la création de structures à gradient de densité qui peuvent être utilisées comme structures d'interface (comme le montre la figure 4.6).

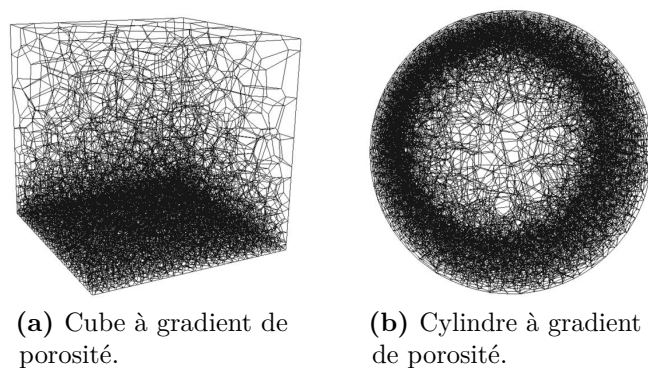


Figure 4.6 Exemple de structures à gradient de densité créées par le logiciel de génération de structures treillis.

Structures treillis comme architecture d'accueil

L'**ostéointégration** des prothèses est essentielle pour améliorer la performance des implants. L'utilisation de zones poreuses dans une prothèse permet de diminuer le module d'Young effectif de la prothèse et donc de réduire l'effet de "stress-shielding" qui provoque

une mauvaise distribution des concentrations autour de la prothèse et peut à terme endommager l'os à l'interface avec l'implant.

Les zones poreuses peuvent être aussi utilisées comme structures d'accueil pour les cellules osseuses. Afin d'optimiser l'ostéointégration, il faut contrôler la taille et distribution des poutres et des pores. Les résultats de ce travail de thèse peuvent donner des pistes en ce sens. Un exemple de cupule pour l'implant de hanche a été réalisé dans le cadre de la thèse. On peut voir le modèle et sa réalisation en figure 4.7.

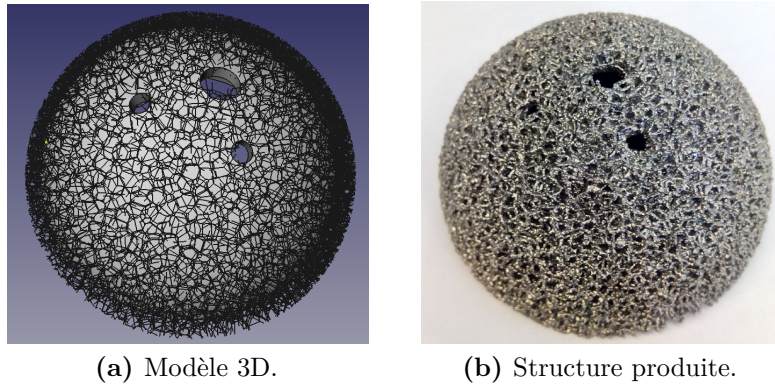


Figure 4.7 Modèle et cupule produite. L'architecture de surface a été obtenue en générant une structure aléatoire avec le code de génération de structures treillis.

Simulation thermique du procédé EBM

La nécessité d'avoir des outils prédictifs à propos de l'histoire thermique de la fabrication EBM a été soulignée durant ces travaux de thèse. Elle a permis un meilleur contrôle de la qualité dimensionnelle des pièces. Un tel outil peut être de différents niveaux de complexité [33, 34]. Nous avons pu comparés la géométrie d'une poutre fabriquée par EBM avec la prédiction d'un modèle thermique simple actuellement développé à Grenoble [35]. C'est une première étape qu'il faudrait continuer de développer pour améliorer le contrôle dimensionnel et microstructural des pièces fabriquées par EBM.

General Introduction

General Introduction

Throughout time, monolithic materials fulfilled the expectations of engineers and researchers. They managed to find ways of reaching the required properties by tuning the composition and the microstructure of the material.

Nowadays applications have brought multifunctional sets of requirements which only "architected materials" can reach. Lattice and cellular structures are part of these architected materials where matter and void are combined in a desired way to reach the requirements. Some examples are depicted in Fig. 8.

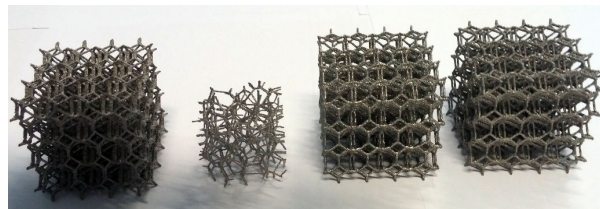


Figure 8 Examples of lattice structures manufactured by Electron Beam melting

The optimized lattice structures usually have very entangled and complicated shapes. Hence it is extremely difficult to manufacture them by conventional techniques such as casting, molding, forging or machining. Additive Manufacturing (AM) brings a new step in the production of such parts. Indeed, it is possible to manufacture very complex shapes with hardly any limitations.

If AM allows the freedom in shape for the production of parts, it also brings along new limitations that have to be characterized in order to reduce them and to take them into account in the steps of simulation and optimization.



Figure 9 The machine used in this study: Arcam A1

This thesis began with the arrival in Grenoble of an Electron Beam Melting[©] (EBM) machine (Fig.9). During this work the results presented are obtained using the EBM technology, more precisely with an A1 machine.

The aim of the PhD thesis is, first, the structural and mechanical characterization of lattice structures produced by such technology. From the comparison between the design and produced structures, a criterion is extracted. In a second step, "realistic" simulations and optimizations are carried out using such a criterion. Finally, the improvement of the strut's geometry is investigated using post-treatments or by tuning process parameters and strategies.

Thus, the manuscript is structured as follows:

□ **Part I: Generalities and overview:** This part aims at giving some basic knowledge on lattice structures and Additive Manufacturing processes. In the first chapter, the necessity of using "architected material" and more particularly lattice structures is explained. Properties and classical models for the elastic properties of lattice structures are exposed. The second chapter deals with AM technologies and particularly the Electron Beam Melting technology. In the last chapter, the starting point of this PhD and the strategy used are presented.

□ **Part II: Characterization of the material properties:** The second part is focused on characterizing the constitutive material of the lattice structures. Microstructural and mechanical aspects of dense Ti6Al4V fabricated by EBM are discussed and compared with conventional alloys. The microstructures of dense parts and thin struts are compared.

Mechanical properties of as-built and machined tensile test samples with different diameters are also compared to fully characterize the properties of the Ti6Al4V alloy fabricated by EBM. Once the mechanical properties of the alloy known, it is possible to investigate the properties of lattices structures.

□ **Part III: A methodology for the stiffness prediction of lattice structures produced by EBM:** In this part, the structural and mechanical behavior of 1 mm-diameter single struts are analyzed in a first chapter while a second chapter aims at applying the notion obtained at the strut's scale for the prediction of the elastic behavior of a lattice structure.

After a review on geometrical variability of struts produced by AM, the second chapter presents the developed tools and methods used for the structural characterization of single struts. The roughness and porosity of struts with different diameters and build orientation are presented. Some tools are extracted to predict the stiffness of the struts by discriminating the mechanically "efficient and inefficient" matter. The struts can be replaced by a cylinder with a *mechanical equivalent diameter*.

The third chapter focuses on the validation of the tools developed on the analysis of single struts for the stiffness prediction of global lattice structures. The periodic octet-truss structure is considered as a representative structure. Homogenization FEM methods are applied on this structure to simulate a global structure from a unit-cell. The use of the concept of mechanical equivalent diameter allows the simulation of the "true" properties of lattice structures manufactured by EBM.

The last chapter aims at generalizing the stiffness prediction of lattice structures by establishing an analytical equation of the mechanical equivalent diameter as a function of the nominal diameter and build orientation.

□ **Part IV: Simulation and mechanical optimization of lattice structures :**

The first chapter exposes the beam simulation that is used for the optimization of lattice structures. The range of validation of such a simulation is defined.

Using the beam simulation and the analytic value of the mechanical equivalent diameter, the optimal orientation of a lattice structure is assessed. Depending on the desired properties and lattice architecture, an optimal placement can improve its mechanical properties.

A parametric optimization has been developed. This optimization allows to take into account the process constraints by simulating the "true" properties of the lattice.

□ **Part V: Towards the improvement of strut's size and surface morphology:**

This part exposes some preliminary results on the improvement of the strut's size and surface morphology.

Post-treatments such as Electro-Chemical Polishing and Chemical Etching are applied on lattice structures made by EBM to assess the possibility of improvement of the surface imperfections of the as-built structures.

Process parameters and strategies are also tuned to optimize the geometrical accuracy of the produced struts.

□ **Conclusion and Future work**

The main conclusions of this work focus on the understanding of the discrepancies between designed and produced lattice structures for struts with a small diameter. From this PhD work several ideas are emerging for future works. They focus mainly on:

- The generalization of the concept of "mechanical equivalent diameter" into commercial optimization codes and for more complex loading such as fatigue.
- The application of lattice structures (in terms of conformal implementation within bulk parts).
- Using lattice as hosting architecture (osseointegration, lattice-polymer composite).
- The thermo-mechanical simulation of the AM process.



Part I

Generalities and Overview

This part aims first to present some basic knowledge on architected materials and especially lattice structures. A second chapter focuses on the different Additive Manufacturing (AM) processes and especially on the Electron Beam Melting (EBM) technology. The third chapter displays the global issues that this thesis attempts to answer.



Chapter 1

Lattice structures

This chapter proposes a review on architected materials. The benefit in terms of mechanical, thermal properties and sound absorption of such structures is exposed. A focus is made on lattice structures. Their manufacturing routes are described and the contribution of Additive Manufacturing (AM) is highlighted.

1.1 Introduction

When looking at the nature, it is impressive to see how architected it is. After centuries of evolution, it presents a structure well adapted to its own environment. Wood is a good example of such an adaptation. It is architected at different scales to balance the high stiffness of cellulose fibrils with some flexibility of the structure [36]. Researchers and engineers are now trying to understand the mechanisms that occur in nature to apply them in materials science and design.

The need for architecting the materials comes from industrial set of requirements. Such demands are more and more complex so that fully dense and monolithic material cannot fulfill them.

1.1.1 Architected materials

Architected materials: Definitions

Several definition of "architected" materials can be found in the literature:

According to Mike Ashby, "*Architected or 'hybrid' materials are combinations of two or more materials or of material and space, configured in such a way as to have attributes not offered by any of one material alone*" [1]. This definition focuses on the applications that architected material can offer.

Architected materials are created at a certain scale. Bréchet et al. [37] have proposed another definition of an architected material based on the length scale. The strategy of producing an architected material is to distribute "*matter at the level of the component*". It means that the creation of an architected material is to develop "either geometries or association of materials, or microstructure gradients, at scales which are comparable to the scale of the component".

"Architected material" gathers a lot of different structures. Figure 1.1 displays different classes of architected materials. Composites are composed of two or more

materials. Reinforcement inside a matrix can be unidirectional, multidirectional or isotropic depending on the application. Usually, the reinforcement material allows an increase of the stiffness or toughness of the structure. The reinforcement material can be in the form of particles or fiber (short or long) [38].

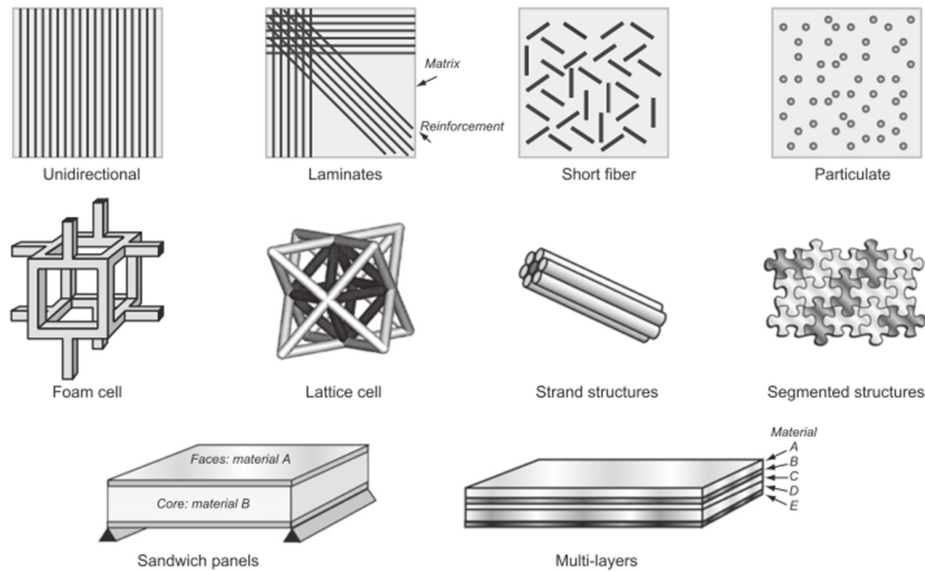


Figure 1.1 Examples of architected materials. Image from [1].

Strand materials are longitudinal composites allowing flexibility along with high tensile strength in one direction. Within the architected materials, sandwich structures are of great interest since they exhibit a high flexural strength to density ratio.

The last part is composed of cellular structures, foams and lattices. Their particularity is that they are not a combination of two materials but an association of one material and space. This category of architected material is the one studied in this work.

1.1.2 Properties of architected materials

Architected materials as a solution to fill space in material science - Example of lightweight structures

The need for architected materials comes from the fact that monolithic materials are not anymore sufficient for fulfilling the required properties. As an example, this section focuses on producing parts with high stiffness-to-density ratio.

Figure 1.2 shows a Young's modulus versus density map for bulk materials. Large categories of materials are represented with the transparent surfaces whereas the white ellipses depict each bulk material. What can be seen is that there are holes in the Young's modulus-density space. It means that for example a material with high elastic modulus and low density is impossible to find in bulk form.

Architecturing the matter throughout the properties space allows to reach those regions of properties where monolithic materials cannot.

In this work, we consider as **cellular material** every architected material which is composed of one material and space. It is composed of an assembly of cells (regular or stochastic). The matter can be distributed in the faces or in the edges. Cellular structure

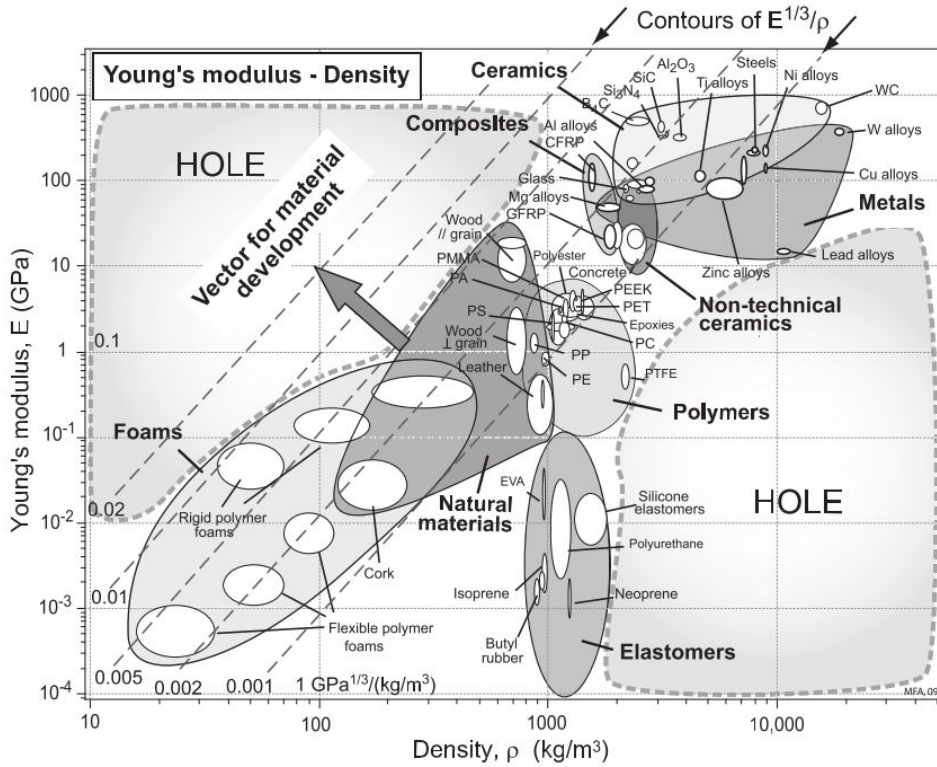


Figure 1.2 Young's modulus versus density space. From [1].

composed of matter within the faces are called "closed-cell" in opposite to "open-cell" structures for which the matter is only in the edges. The term **foams** originally designates cellular structures manufactured from the specific process of foaming. It has then been generalized to every cellular material. This study will not treat such structures.

Lattices structures are composed of a connected network of struts [39]. The PhD work is focused on such structures.

They can be classified according to its periodic or stochastic structure. Random or stochastic lattice structures are composed of an assembly of cells without any symmetry or periodicity. Periodic lattice structures are composed of a repetition of a unit-cell in every directions. Such structures will be investigated in this study.

Another classification of lattice structures can be carried out according to their deformation modes. They can either deform by bending or stretching of the cell wall. This classification will be treated in the next paragraph.

1.2 Metallic lattice structures

Metallic lattice structures having open cells are widely used as heat exchanger media to dissipate heat from a hot source [3, 4]. They are also used as heat transfer media for phase change material (PCM). The lattice structure embedded in PCM material permits a more homogeneous heat flux thus a more controlled phase change [5].

Acoustic properties of lattice structures have been less studied. A relatively new field of research on metamaterials focuses on finding new properties for architected materials. For example, Körner et al. designed antichiral lattices that exhibit phononic band gap [6]. Using an Additive Manufacturing technique, they were able to produce such structures

and optimize the unit cell to reach the needed eigenfrequencies.

In this section we focus on the elastic properties of lattice structures since it is the main interest of the PhD work.

1.2.1 Elastic properties of periodic lattice structures

Lattice solids can be gathered in categories according to their deformation mode. This section tends to explain the differences in terms of elastic properties according to this classification. We focus on periodic lattices.

Maxwell Criterion: stretching and bending-dominated structures

Deshpande et al. proposed a standard classification based on the nodal connectivity of the lattice structure [7]. Their classification is based on early research of Maxwell [8] which sets a topological rule for an assembly of pin-jointed struts to be rigid. They are classified as a "mechanism" if they don't satisfy this rule and as a "structure" if they do.

Considering a 3D structure composed of b struts and j nodes the criteria is:

$$M = b - 3j + 6 \quad (1.1)$$

If $M \geq 0$, the structure is rigid in the sense of Maxwell. Using this criteria on unit-cells made of non-rigid elements allows the discrimination of structures that are "bending-dominated" or "stretching-dominated".

Table 1.1 shows the geometry and deformation mode of some unit cells. Some represented unit cells are widely studied such as the hexahedron (cube) which is bending-dominated. The tetrakaidecahedron has been analyzed in details because it is representative of the structure of an open-cell structure obtained by foaming [40]. The simplest foam model from Gibson and Ashby [9] is depicted as a bending-dominated structure. It is treated in the next paragraph 1.2.1.

The represented stretching-dominated structures are the tetrahedron (composed of 6 struts and 4 nodes), the icosahedron ($b=30$, $j=12$), and the octet-truss. The octet-truss is the chosen structure for this study.

A more exotic set of lattices are the auxetic structures. They have undergone numerous studies in the past years. These structures exhibit a negative Poisson's ratio [43]. It means that these structures expand laterally when stretched. These lattices possess large shear moduli, high indentation resistance and high energy absorption [44]. An idea of different auxetic geometries can be found in various papers [45, 46]. Although these structures have a growing importance, they will not be discussed later on.

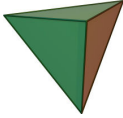
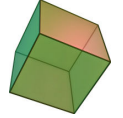
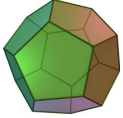
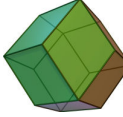
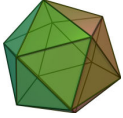
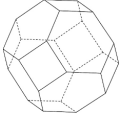
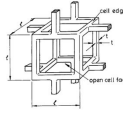
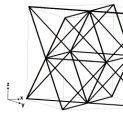
Elastic behavior of bending-dominated structures

Taking as an example the simplest foam model for "bending-dominated" structures, the elastic behavior of an open-cell foam has been analytically determined by Gibson and Ashby [9]. The bending-dominated lattice is modeled as a cubic array of struts.

Considering that the structure deforms by cell wall bending, the Euler-Bernoulli beam theory can be used. As a result, the scaling law of stiffness for such structures can be derived:

$$\frac{E}{E_S} \propto \left(\frac{\rho}{\rho_S} \right)^2 \quad (1.2)$$

Table 1.1 Examples of unit-cells with their corresponding failure mode.

Name of unit-cell	Deformation mode	Scheme
Tetrahedron	Stretching-dominated	
Hexahedron	Bending-dominated	
Dodecahedron	Bending-dominated	
Rhombic dodecahedron [41]	Bending-dominated	
Icosahedron	Stretching-dominated	
Tetrakaidecahedron [40]	Bending-dominated	
Simplest foam model [9]	Bending-dominated	
Octet-truss [42]	Stretching-dominated	

where E and ρ are the Young's modulus and the density of the structure respectively. E_S and ρ_S are the Young's modulus and density of the constitutive material.

\implies The relative Young's modulus of a bending-dominated structure scales with the square of the relative density.

It is also possible to determine the plateau stress σ_{pl} from figure 1.3 considering that the structure collapses by cell edges bending. The plastic plateau appears when the force exerted on them exceeds their fully plastic moment. The plateau strength σ_{pl} normalized by the yield strength of the solid material $\sigma_{y,s}$ can be expressed as:

$$\frac{\sigma_{pl}}{\sigma_{y,s}} \propto \left(\frac{\rho}{\rho_S} \right)^{3/2} \quad (1.3)$$

In figure 1.3, the typical stress-strain curve of a bending dominated structure is plotted. A first step of linear elastic regime is represented, followed by plastic plateau corresponding to the cell edge bending of the structure. After a certain strain, the densification occurs. It corresponds to the moment where the opposite edges of the cells are in contact.

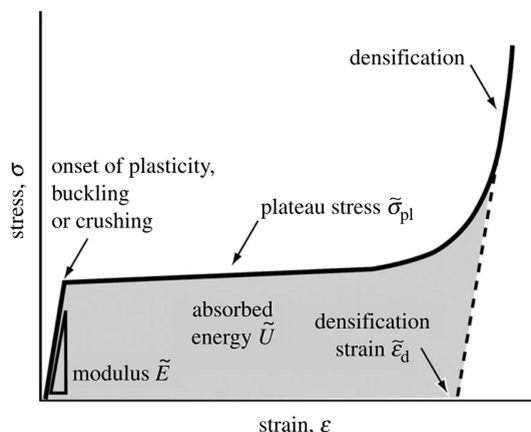


Figure 1.3 Stress-strain curve for a bending-dominated structure. Image from [39].

Elastic behaviour of stretching-dominated structures

Using the same approach as previous paragraph, and considering the tensile loading of the struts, it is possible to derive the elastic properties as a function of the relative density for a stretching-dominated structure. We consider here only the elastic stretching of the struts. The relative Young's modulus is then calculated as:

$$\frac{E}{E_S} \propto \left(\frac{\rho}{\rho_S} \right) \quad (1.4)$$

⇒ The relative Young's modulus of stretching-dominated structures scales linearly with the relative density.

The elastic limit is supposed to be related to the first struts that yield plastically. If so, the collapse stress is:

$$\frac{\sigma_{pl}}{\sigma_{y,s}} \propto \left(\frac{\rho}{\rho_S} \right) \quad (1.5)$$

If the struts have a high slenderness ratio, the collapse mechanism will be rather buckling of the struts than yielding. Then following Euler buckling criterion, the buckling strength is:

$$\frac{\sigma_{el}}{E_S} \propto \left(\frac{\rho}{\rho_S} \right)^2 \quad (1.6)$$

The slenderness ratio of the strut manages the collapse mechanism of the structure. The slenderness is related to the relative density. Low density lattices will then buckle before yielding whereas high density structure will mainly collapse by stretching of the struts.

Figure 1.4 shows a typical stress-strain curve of a stretching-dominated structure. The behavior is slightly different than for a bending-dominated structure (Figure 1.3). Indeed, such structures have higher Young's modulus and yield strength than for a bending-dominated one at a given relative density. Because of the mode of stretching of the struts (tension or compression), the initial yield is followed by plastic buckling or brittle collapse of the struts (depicted as "post-yield softening").

Summary

Figure 1.5 depicts the relative Young's modulus as a function of the relative density for different structures in log-log scale. Two lines are plotted representing the behavior of

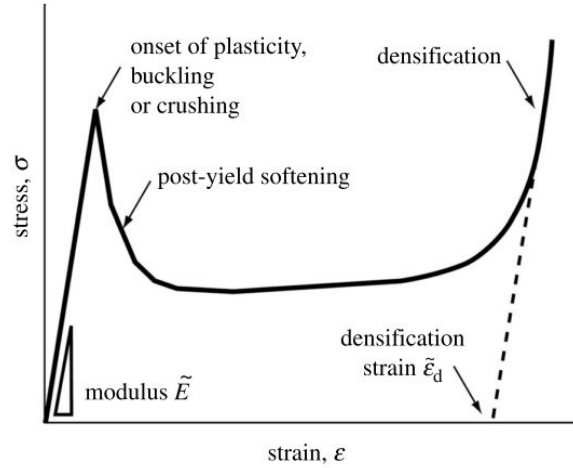


Figure 1.4 Stress-strain curve for a stretching-dominated structure. Image from [39].

stretching-dominated and bending-dominated structures. The slope of the curve is the power-law exponent of the Young’s modulus versus density law. Foams mainly deform by bending whereas honeycombs deform mainly by stretching when pulled along their longitudinal axis.

⇒ Generally, a stretching-dominated structure is stiffer than a bending-dominated one for the same density.

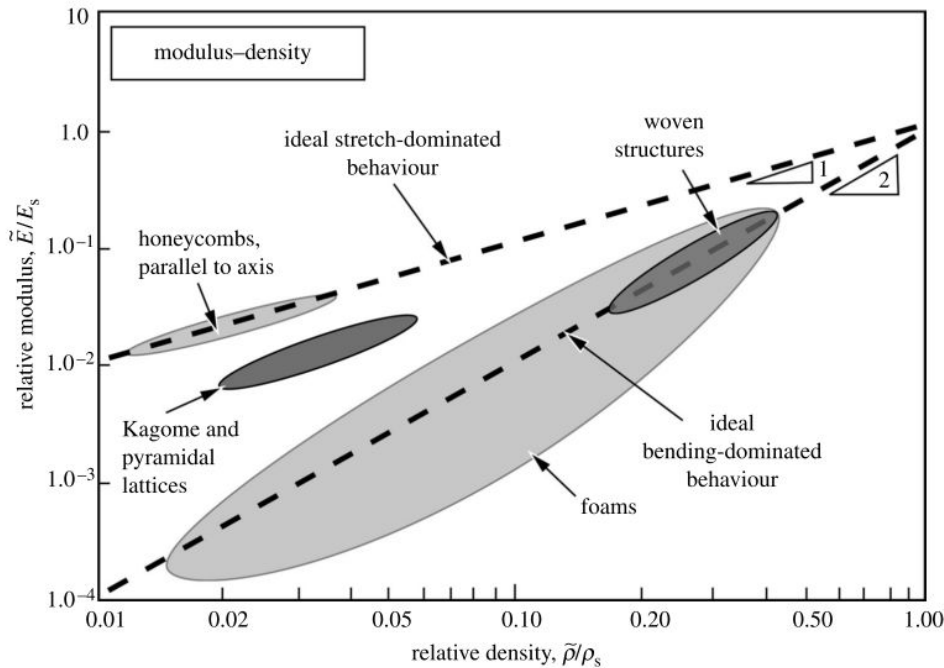


Figure 1.5 Young’s modulus versus density. Variations of scaling laws depending on the deformation mode. Image from [39].

Limitation of Scaling laws The previous scaling laws for bending-dominated and stretching-dominated structures are based on the Euler beam hypotheses. The consequence is that a model to be valid should deal with a minimum slenderness ratio ($1/t$). As a

consequence, the scaling laws have a limited range of validity of density.

1.2.2 Conventional manufacturing techniques

Conventional techniques have been mainly focused on the manufacturing of random foams [47]. From a liquid metal, an injection of gas forms bubbles into the liquid and thus a foam when cooled down.

Space holder techniques are based on the use of another material (which can be removable or not) to build a highly porous structure. Removable space holder have been widely used for metallic foams. In powder metallurgy, the space holder material is usually a polymer or carbon particles. For casting, salt can be used as space holder or a preform can be infiltrated by the liquid metal [48, 49]. Replication methods are also of great interest to produce metallic lattice structures. As an example, Schaedler et al. [50] coated a polymer lattice with a nickel alloy and then removed the polymer. This replication allows the formation of ultralight metallic microlattices.

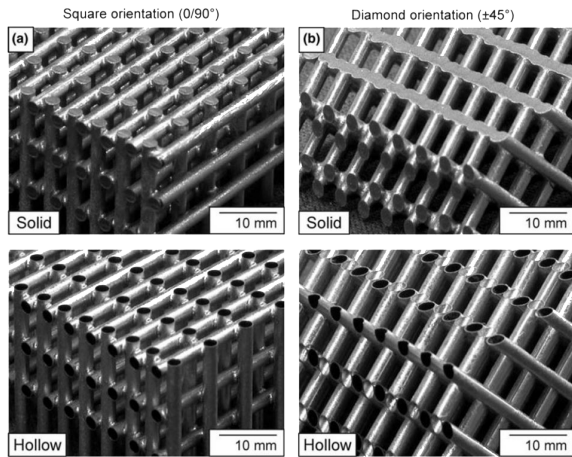
Producing lattice structures through conventional techniques has been a challenge over the years. Most of the published work are concentrated on sandwich structures with a lattice core [3, 10–12]. Three different techniques have emerged:

- Wadley presented a Kagome sandwich obtained by **investment casting** of a preform. The result is satisfying but this process cannot be applied to tortuous or large structures and only some metallic alloys with a high fluidity can be used.
- Another method is forming a lattice structure from a **metallic wire assembly**. Queheillalt [13] used solid and hollow stainless steel wires and assembled them using a tool to assemble the wire in colinear layers as shown in figure 1.6a. The assembly undergo a final heating step to link the wires by brazing.
- Producing lattice structures from an **expanded metal sheet** is the most widely used method. Kooistra et al. [11] explained in details how to form a tetrahedral core for a sandwich panel from an aluminium sheet. Figure 1.6b explain the different steps used in their study.

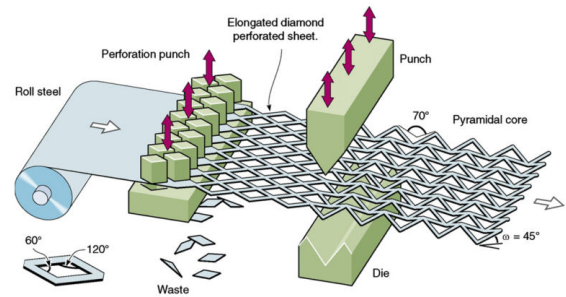
From the metal sheet, a first step of perforation allows the design of elongated diamond which will be folded later on. The final structure is a pyramidal core. This core can be used directly in a sandwich panel or stacked on top of each other to form a lattice. Following the second method, Wadley formed an octet-truss structure by stacking tetrahedral cores with interleaved planar hexagonal perforated layer [12].

These conventional manufacturing methods for lattice structures have many drawbacks. For investment casting, the liquid metal should be fluid enough to flow inside the preform depending on the size and tortuosity of the structure. Metallic wire assembly permits only the formation of a limited amount of designs. Lattice manufacturing from an expanded metal sheet allows the production of more various shape but produces a large amount of waste. Moreover, the alloy used has to be ductile enough to be perforated and punched. It limits the variety of alloy that can be processed.

Manufacturing lattice structure has always been a challenge for engineers. Additive Manufacturing permits in the contrary a high degree of freedom of manufacturable shapes.



(a) Examples of structures fabricated by metallic wire assembly. Image from [13].



(b) Sketch of the process of lattice manufacturing from an expanded metal sheet. Image from [11].

Figure 1.6 Conventional manufacturing techniques for the production of metallic lattices.

For the past ten years, it has become a viable answer for the manufacturing of lattice structures.

Chapter 2

Metallic Additive Manufacturing

Contents

1.1	Introduction	43
1.1.1	Architected materials	43
	Architected materials: Definitions	43
1.1.2	Properties of architected materials	44
	Architected materials as a solution to fill space in material science - Example of lightweight structures	44
1.2	Metallic lattice structures	45
1.2.1	Elastic properties of periodic lattice structures	46
	Maxwell Criterion: stretching and bending-dominated struc- tures	46
	Elastic behavior of bending-dominated structures	46
	Elastic behaviour of stretching-dominated structures	48
	Summary	48
1.2.2	Conventional manufacturing techniques	50

During this chapter, a short review on the current AM technologies is carried out. A focus is made on the Electron Beam Melting technology.

2.1 Current technologies and challenges

For the last 25 years, important innovations have emerged in the Additive Manufacturing processes. They can be divided into the powder bed techniques (Electron Beam Melting-EBM, Laser Beam Melting-LBM and Selective Laser Sintering-SLS) and the Direct Deposition methods (Electron Beam Fabrication Freeform-EBF³, Direct Metal Deposition-DMD, Wire Arc Additive Manufacturing-WAAM) [51–53].

The raw material of the AM techniques is either powder or metallic wire.

Within powder bed techniques, the EBM and LBM technologies melt powders layer by layer with a heat source. The SLS technique uses a laser beam to melt polymer-based binder containing metal powder. Then a step of sintering allows the removing of the binder and the consolidation of the metal.

The EBF³ uses an electron beam to melt a metallic wire onto a substrate whereas DMD processes use a laser beam to melt metal powders that are projected on a substrate. The WAAM process allows the production of large parts by melting a wire using a TIG welding torch on a substrate.

In the next section the focus is made on two processes representative of both categories: LBM and DMD.

2.1.1 Direct Metal Deposition

In the Direct Metal Deposition processes, the raw material is usually a metal powder but can be wire or pellets [54, 55]. A laser beam is focused on a substrate. At the end of the nozzle, the raw material carried by a carrier gas meets the laser beam and is projected onto the substrate. Figure 2.1 depicts the process components. In some technologies, the nozzle is moving while the substrate stays fixed. Other technologies prefer the nozzle to stay fixed and the substrate to move.

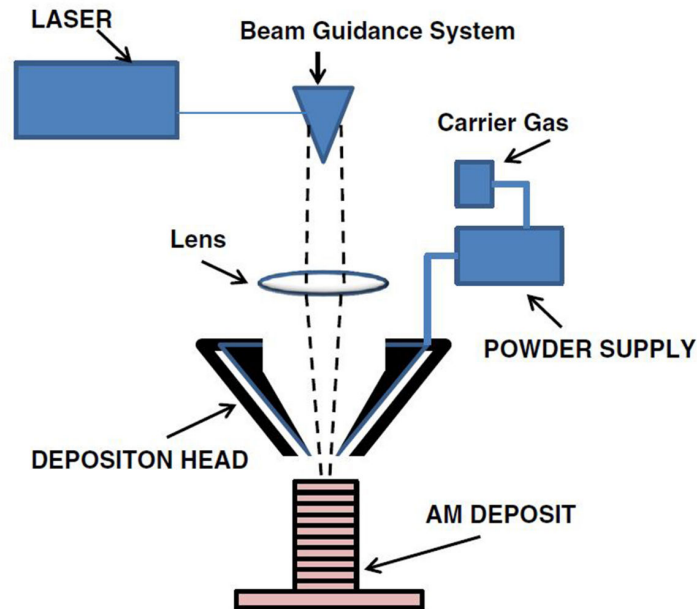


Figure 2.1 Scheme of DMD processes. Image from [53].

This technique allows the production of large parts and does not require a confined environment. The nozzle is usually fixed into a multi-axis robot to be able to deposit material in any directions. The carried gas act as a protecting environment to limit oxidation of the deposited material.

The benefit of such a device is that it can create large parts and be used as a re-manufacturing process. Indeed, this technology is more suitable for the reparation of damaged parts. Re-manufacturing is almost impossible for powder-bed techniques because the part needs to be embedded in a powder-bed and the broken surface needs to be flat enough to manufacture onto it. The raw material can be easily graded to produce functionally graded or multimaterials structures.

A large range of alloys have been processed by DMD processes such as Ti-alloys, Ni-based superalloys, Co alloys or stainless steels.

2.1.2 Laser Beam Melting

The Laser Beam Melting process is a good representation of the powder bed AM processes. It is also the most used nowadays. It relies on layer-by-layer addition of powder. As seen in figure 2.2, the LBM technology is based on a high energy laser (around 0.2kW [15]) that produces a beam in direction of a mirror which allows its deflection.

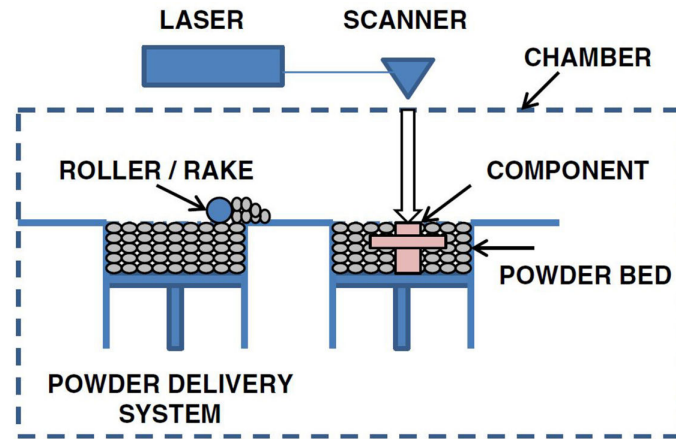


Figure 2.2 Scheme of LBM processes. Image from [53].

The whole process operates in a protective atmosphere (Argon or Helium mainly). Layers are of 20-100 μm high. The powder is kept in a reservoir that goes up at each layer while a rake dispatches the powder onto a start plate. The laser beam melts the selected surface of the layer and let the loose powder unmelted. Locally the temperature increases but the whole build is kept at room temperature.

The problematic of overhanging surfaces is critical. The loose powder does not allow a high dissipation of the heat and a mechanical support. Thus, melted supports are critically needed for the fabrication of overhanging surfaces.

Each melted point undergo a rapid cooling from above melting temperature to the room temperature thus resulting in a martensitic microstructure for titanium based alloys [15, 16]. The cooling behavior of a point melted by LBM is represented with the blue curve in figure 2.4. The cooling is rapid from the melting temperature (T_M) to the room temperature (T_R).

As a consequence of this high thermal gradient, the parts produced by LBM have important residual stresses and need to undergo a specific heat treatment after production.

2.2 Electron Beam Melting (EBM)

The EBM technology is another additive manufacturing process. The ARCAM company in Gothenburg (*Sweden*) is the only seller in the world for this technology. This section explains the process in terms of components and parameters. This section describes the basic parameters and process strategies since they affect the final properties.

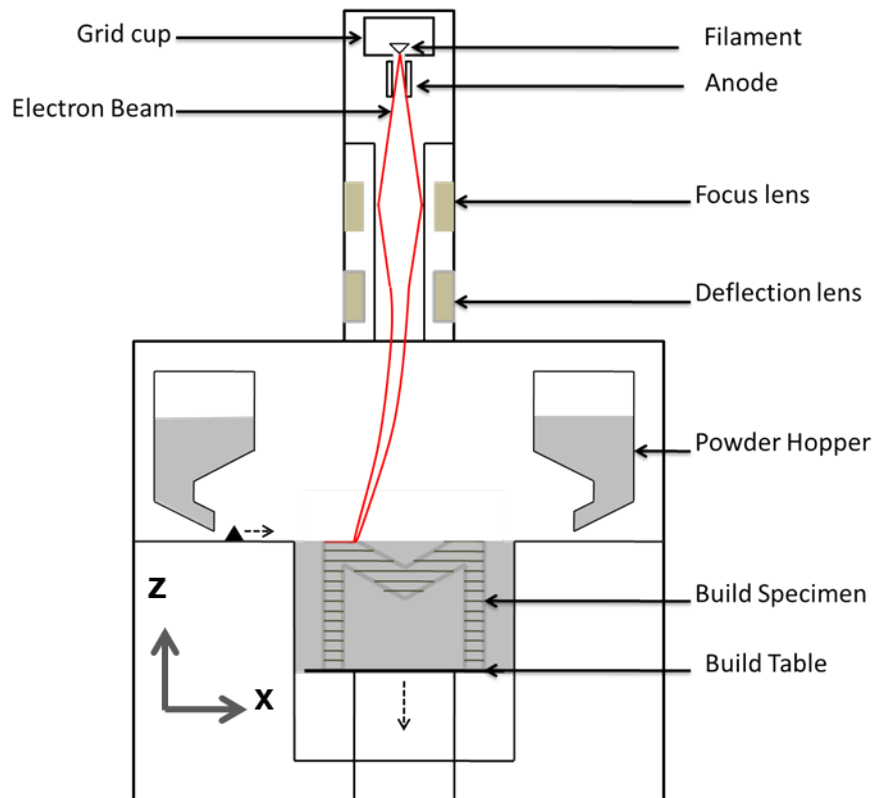
Table 2.1 Summary of the characteristics of the A1 EBM machine.

Power	50-3000W
Build Temperature	$\sim 700^{\circ}C$
Deflection rate	Up to 8000 m/s
Maximum build size	200x200x180 mm
Beam spot size	0.2 mm-1.0 mm
Chamber pressure	10^{-4} mbar

2.2.1 Description of the process

Global Description

The Electron Beam Melting technology is composed of an electron beam that selectively melts metal powder layer by layer following a CAD file (Fig.2.3). The first material is a metal powder that is held in two hoppers and spread onto the build plate layer by layer using a rake. The layer height is kept at $50 \mu m$ for this study. At the end of the fabrication, the melted powder creates the part and the unmelted one will be reused for new fabrications.

**Figure 2.3** Scheme of the EBM process using an A1 machine.

During the whole process, the chamber is held under vacuum ($\sim 10^{-4}$ mbar) to prevent the electrons to be stopped by air molecules. Using an electron beam as a heat source allows a high power and high build rate. The beam can indeed move on the surface with a speed up to 8000 m/s with a power varying from 50 to 3000 W. The global characteristics of the A1 Electron Beam Melting machine are summed up in table 2.1.

Preheating

A particularity of this process is that, at every layer, the beam scans the whole surface before melting the part. A highly defocused electron beam scans the surface in two steps. The first preheating scans the entire surface with a low energy whereas the second step of preheating is located around the produced parts with a higher energy.

Tushar Mahale [14] explained in details the "smoke" mechanism and its reduction by the preheating process. The smoke effect is a cloud of metal powder due to electrostatic interactions between the metal powders and the electron beam.

To prevent this phenomenon, the preheating steps allow an increase of the electrical and thermal conductivity of the powder stack by creating necks between particles. The increase of the thermal conductivity allows also an efficient evacuation of the thermal flux throughout the powder.

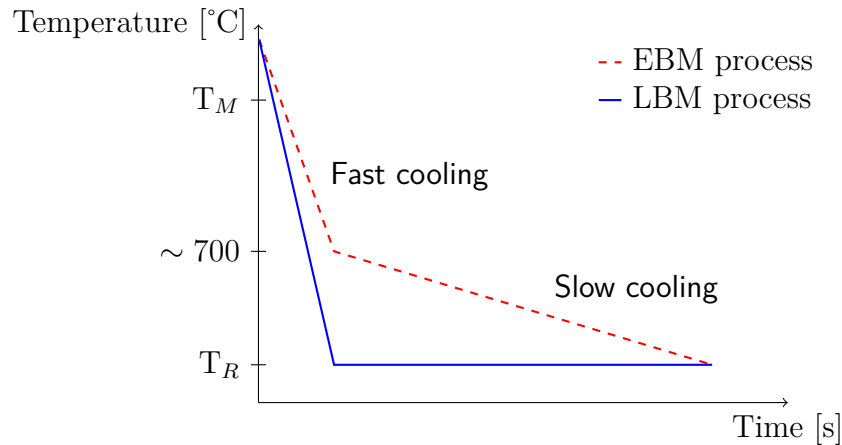


Figure 2.4 Scheme of the cooling speed for a melted point during the EBM and LBM manufacturing of Ti-6Al-4V.

The preheating steps allow a constant temperature of $\sim 700^{\circ}\text{C}$ for the current layer. Thus, each point that is melted undergo two cooling rates (c.f. red curve in figure 2.4): a first rapid cooling rate from the melting state to the maintained temperature and a second slow cooling from 700°C to the room temperature. As a result, a controlled microstructure is produced (c.f. section 4.2.2). Those differences in cooling speed between the EBM and LBM technologies result in differences of microstructure. Moreover, the slow cooling from 700°C to the room temperature reduces the final residual stresses.

2.2.2 Description of the components

The machine used in this work is an A1 machine with a maximum build chamber of 210x210x180 mm.

Electron gun

The upper side of the machine is composed of an electron gun (upper part) where a tungsten filament is heated up to 2600°C . A 60 kV accelerating electric field is applied between the filament and the anode. The accelerated electrons pass then through different electro-magnetic coils.

First they undergo a field that reshape the electron beam in order to avoid astigmatism artifacts (not included in Fig 2.3). Then, an electro-magnetic field is applied at the focus coil to sharpen the beam at the build surface. The producer of the machine developed a routine to modify the focusing according to the position of the beam spot to ensure a constant focalization at each point. The minimum spot size with this machine is around $200 \mu m$ of diameter. The last coil produces a field that deviates the beam to reach the CAD coordinates on the surface.

Build chamber

The build chamber is held under secondary vacuum (around 10^{-4} mbar) whereas the vacuum in the electron gun is stronger (10^{-7} mbar). The vacuum prevents the oxidation of the titanium with temperature and avoid the interaction of the air particles with the electron beam. A constant flux of helium (10^{-3} mbar) is introduced to avoid beam scattering to change the quality of the vacuum.

The start plate (or build plate) is a 316L stainless steel plate where the first layer of powder will be spread. It aims at supporting the build parts and acts as a heat sink. Squared plates with a size of 150mm, 170 mm 190 mm and 210 mm are available. The start plate undergo a heating step before each fabrication to reach $700^{\circ}C$. The temperature is controlled by a thermocouple under the plate. When it reaches this value, the build starts.

Powder Recovery System (PRS[©])

The PRS is a cabinet where the powder block - consisting of melted and sintered powder - is blasted under a pressure of 8 bars. The blasting material is the raw material of the fabrication.

It allows to break the necks between sintered particles resulting from the preheating and to take out the melted parts. The left particles are sieved and reused in the next builds. The sieving allows the recycling of particles from 20 to $140 \mu m$.

2.2.3 Description of the raw material

The raw material for this process is metal powder. In our case, the material is a Ti-6Al-4V alloy. It is an α/β titanium alloy commonly used in aeronautics and bio-medical industries. More information about this alloy can be found in section 4.1.

In order to be able to flow using the rake, the initial powder has to be spherical. To do so, the powder used has been created by gas atomization. Due to the production process, some internal pores are present in the initial powder. This initial porosity has been widely reported in the literature [18–21]. These pores are due to the argon gas used in the atomization. During the formation of the powder, this gas can be entrapped and form pores.

Figure 2.5 (a) shows a X-ray tomography image of the initial powder. The spherical shape is highlighted as well as the pores (in red). The size distribution (b) shows that the pores are present only in large particles and that the porous particles can represent up to 50 % of the particles (for large diameters).

Figure 2.6 shows the shape of particles after their multiple use in the machine. Their shape is purely spherical but some necks can be seen (white arrows). These necks have

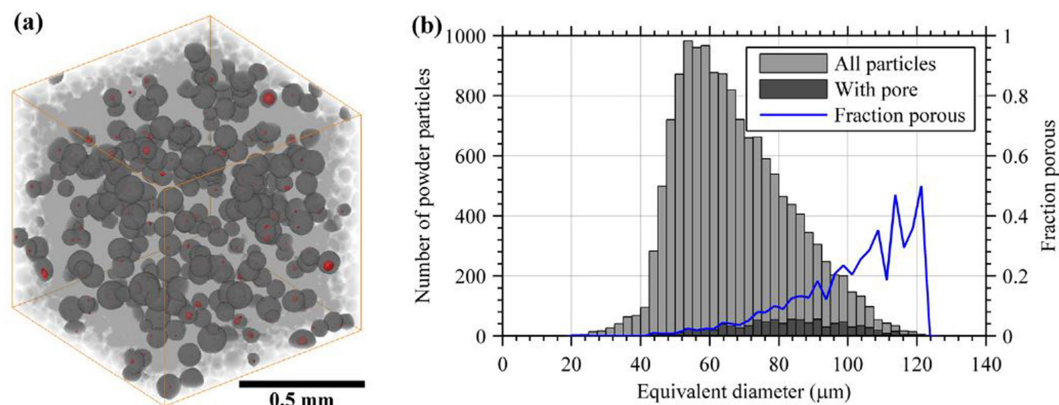


Figure 2.5 (a) X-ray tomography of initial powder used in the EBM machine. In red the initial pores entrapped in the powder. (b) Size distribution of the powders and powder containing pores. In blue, the fraction of porous powders is plotted. From [18].

been created during the preheating step during different builds and broken by the blasting with the PRS.

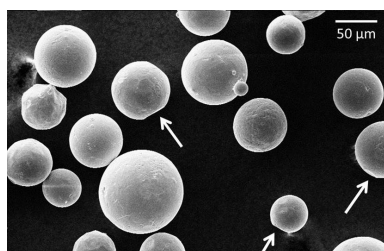


Figure 2.6 SEM micrograph of recycled Ti-6Al-4V powder. White arrows pointing at necks.

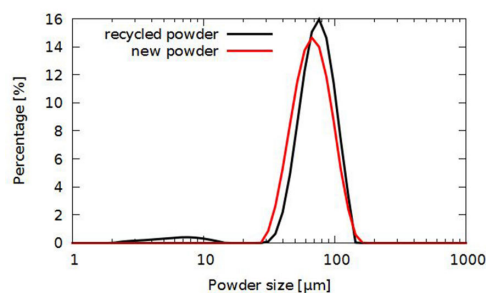


Figure 2.7 Size distribution of new and used Ti-6Al-4V powder.

The Particle Size Distribution (Figure 2.7) shows the influence of the recycling of the powders on their size. The median diameter for the recycled powder ($78 \mu m$) is larger than the one of the new powder ($62 \mu m$). The PSD gets narrower for reused powders. This is consistent with the work of Tang et al. [56] that showed a slight increase of the median diameter and a narrowing of the PSD with the number of reuse. The increase of the particle size with the recycling steps could be related to the loss of satellites and agglomeration of powders during recycling. It could also explain the narrowing of the PSD.

2.2.4 Process parameters and strategies

This section aims at presenting the standard parameters and strategies that will be tuned later on (chapter 14).

A "theme" is a set of process strategy and parameters. The standard themes from ARCAM are called "Melt", "Net", "Point-net" and "Wafer". The first one is the most used since it is applicable for melting any geometry. The "Net" theme is optimized for thin structures (less than 1 mm diameter struts) as it follows only contour paths. The "Point-net" theme gives process parameters for the fabrication of parts from wireframe

geometries. Finally, the "Wafer" theme is made to melt supports. The supports are created to support overhanging surfaces of dense parts. Their theme is customized for a partial melting of the support [57]. The partial melted supports act as heat sink and mechanical support but are relatively easy to remove.

In this section, the scan strategy and process parameters will be exposed and the values from the "melt" theme will be described.

Standard scan strategy

The standard scan strategy will be explained using the scheme of a slice from a CAD file (Figure 2.8).

The limits of the CAD file are represented by the dotted red line. The first path of the beam (called first contour) is shifted from the CAD limit by a certain value called the *first contour offset* (CO_1). The beam scans a second contour at a distance CO_2 (*second contour offset*) from the first one. The inner surface is then melted by hatching. The raster scan melts line by line following a snake strategy. The line distance between each scan line is called *line offset* (LO).

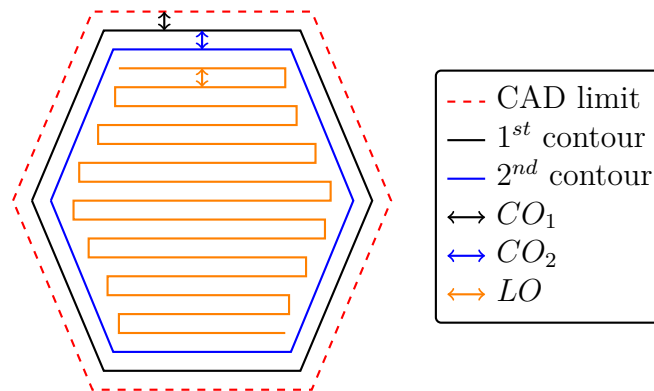


Figure 2.8 Scheme of a slice of a CAD file. The dotted red line represent the CAD limits. Black line: first contour, Blue line: 2^{nd} contour. Orange: Hatching.

Every parameter is linked to the predicted size of the beam spot and resulting melt pool. The parameters that can be changed in the scan strategy are:

- The first contour offset
- The second contour offset
- The number of contours having the same parameters as the second contour
- The line offset
- The hatching way (back and forth or always same way)
- The hatching direction (scan line change of 90° at every layer)

The values used in the "Melt" theme have been obtained by ARCAM after numerous studies to minimize the porosity and control the produced microstructure and dimensions.

Main process parameters

The process parameters are the parameters affected by the electron beam. They are different for the 1st contour, the 2nd contour and the hatching. This section aims at presenting the most relevant parameters:

- The beam current (I).
- The beam speed (V)
- The focusing of the beam : Focus Offset (FO)

Much more parameters are used in the standard themes. For hatching, an algorithm calculates at each position the speed and current of the electron beam depending on its distance to the end of a scan line and its distance to a overhanging surface. The algorithms that finally produce the instructions to the beam are based on thermal considerations. This algorithm is not tuned in this work. Changes will focus on the beam current, speed and focus offset.

Combining the process parameters and the melting strategies described here, global parameters can be defined.

Global calculated parameters

The beam power (P) is the accelerating voltage (60 kV) multiplied by the beam current (I). From this definition, an energy can be calculated as:

$$E = P.t = \frac{PL}{V} \quad (2.1)$$

where L is the length scanned by the electron beam and t is the time of melting.

The volume energy E_V is defined as follows:

$$E_V = \frac{E}{S_{CAD}h_{layer}} = \frac{PL}{VS_{CAD}h_{layer}} \quad (2.2)$$

where h_{layer} is the height of a layer (50 μm in our case) and S_{CAD} is the surface of the designed part at the current layer. The parameter takes into account the melted surface but do not include the time to melt. Another interesting parameter is the volume power:

$$P_V = \frac{P}{S_{CAD}h_{layer}} \quad (2.3)$$

These densities of energy and power will be used in chapter 14 to classify the changes in the process strategies and parameters.

2.2.5 Manufacturing lattice structures by Electron Beam Melting

Manufacturing lattice structures using AM has been of great interest recently. The first patent reporting lattice structures manufactured by additive manufacturing date from 2004 [58]. It shows the possibilities in terms of shapes of lattice structures that can be manufactured. The lattice structure fabrication is highly related to biomedical applications

and in-growth tissue.

In this section the manufacturing of lattice structures by EBM is investigated. However, the Laser Beam Melting technology allows also the manufacturing of such structures [59–62]. Lattice structures produced by LBM can have thinner struts than for EBM. However, the EBM technology allows more freedom for the manufacturing of lattice structure composed of horizontal struts.

Ti-6Al-4V alloy

Heinl et al. showed in 2007 the feasibility of the EBM technology to produce freeform open-cell structures [63]. They showed the possibility of varying locally the density of a lattice structure.

The properties of hexagonal lattice structures produced by EBM was investigated in 2008 by Cansizoglu et al. [64].

In 2010, Murr et al. showed the possibility of bio-mimicking of the trabecular bone using additive manufacturing [65]. They produced a knee implant with an inner dense material and an outer lattice structure to promote the cell propagation onto the prosthesis (see figure 2.9a)

Yang et al. [44] fabricated re-entrant lattice structure to investigate the properties of auxetic structure produced by EBM.

Horn et al. [66] produced open-cells rhombic dodecahedron with several densities for flexural properties analysis (see figure 2.9b. Li et al. analyzed the static mechanical properties of three structures (Cubic, G7, rhombic dodecahedron) in compression [67].

A group from Sheffield University studied the metallic foams manufactured by the Electron Beam Melting technology [68]. They reproduced structures from X-ray tomography images of randomly packed bed of glass beads.

To investigate the blast loading response of lattice structures made by additive manufacturing, McKown et al. [69] produced octahedral lattice structures with various cell topology.

A study on the fatigue of cellular structures manufactured by EBM has been carried out by Jamshidinia et al [70, 71] on three different cell shapes (cross-A, Honeycomb and Octahedral). In parallel, a study from [72] carried out on rhombic dodecahedra manufactured by EBM focused on the deformation mode of such structure.

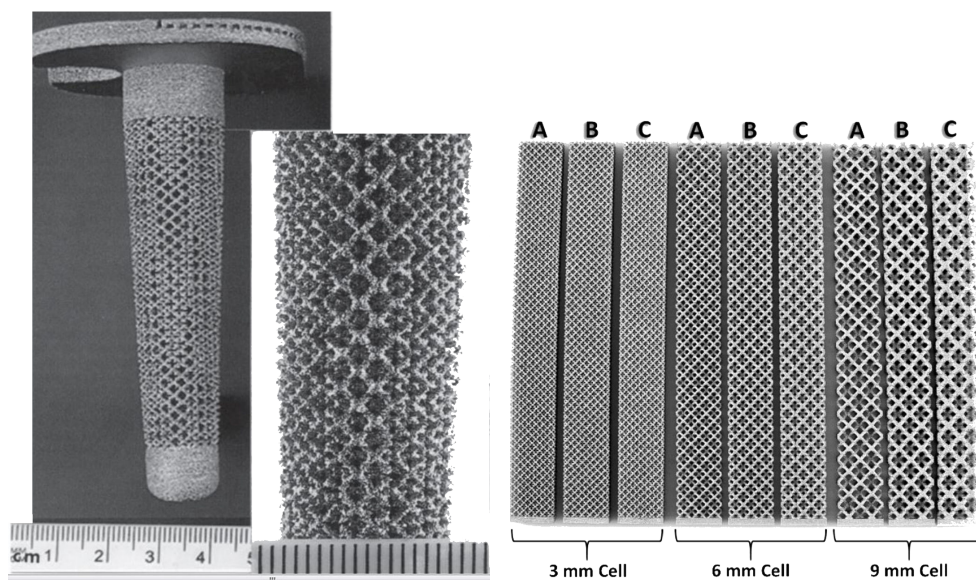
Other materials

Lattice structures have been manufactured by EBM with other materials than Ti-6Al-4V although it is nowadays the most common alloy.

Ramirez et al. [73] have elaborated copper lattice structures (random and periodic) (figure 2.9c). The final structures contained Cu_2O precipitates formed during the EBM manufacturing that participate to the hardening of the alloy. The production of such architected structures have a wide range of applications in the thermal management or the heat exchange.

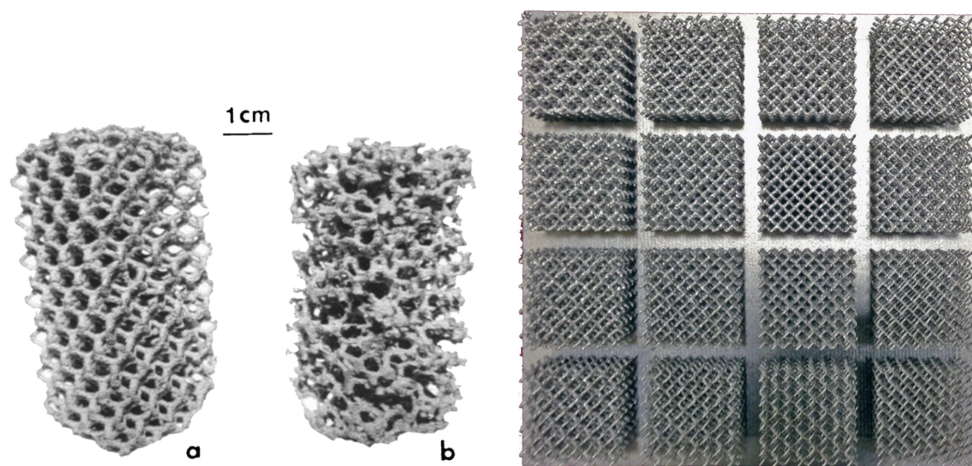
Lattice structures in Inconel 625 were manufactured and mechanically analyzed by List et al. [74]. Structures based on a diamond unit cell were manufactured with different process parameters (see figure 2.9d). The variation of those parameters showed a process window to fabricate more controlled geometries and stiff structures.

Murr et al. [75] fabricated lattice structures of Co-29Cr-6Mo and Ni-21Cr-9Mo-4Nb alloys by Electron Beam Melting. The basic unit cell is a Dodec-dodec unit cell from the software magics (Materialise).



(a) Knee implant in Ti-6Al-4V manufactured by EBM. Image from [65].

(b) Rhombic dodecahedron structures produced by EBM. Image from [66].



(c) Stochastic and regular copper-based lattices produced by EBM. Image from [73].

(d) Nickel-based diamond lattice structures produced by EBM. Image from [74].

Figure 2.9 Examples of lattice structures produced by EBM from the literature.

2.3 Limitations

The Electron Beam Melting technology and more generally the Additive Manufacturing processes allow a nearly complete freedom in the design of the produced parts. But they bring new limitations inherent to the process. Some limitations are listed here for the EBM technology.

Powder Removal At each layer, the whole surface of powder undergo a preheating which creates necks between particles (c.f. 2.2.1). For the unmelted powder these necks have to be broken in the PRS system. The 8 bar blasting is highly efficient to this purpose if the structure is not too tortuous. A previous PhD student took a look at this constraint [76]. For a 10 mm diameter cylinder hole, only 23 mm in height can be blasted. The rest of the sintered powder cannot be removed by blasting.

The powder removal from lattice structures has been investigated by Hasib et al. [77]. They tried a chemical etching process for removing the sintered powder. Their results are promising but for larger structures, the etching affects the integrity of the struts before removing all the sintered powder.

Spatial resolution The minimal beam spot is set by Arcam as 0.2 mm. Depending on the resulting melt pool, a minimal resolution emerges. This minimal resolution will be discussed in part III and considered as an important constraint to build very thin struts.

Wafer Eventhough it is less critical than for the LBM technology, thick overhanging parts cannot be produced by EBM without wafer supports. It results in curling/warping of the part due to differential thermal expansion/contraction in the part. The supports allow a mechanical reinforcement to avoid the buckling of the overhanging surface as well as an increase of the evacuation of the heat. In this PhD work, no wafer supports are employed for manufacturing lattice structures.

Accessible Materials A research group at El Paso developped several materials for the EBM technology: Inconel 625 [78], Co-Cr-Mo super alloy [75], Rene 142, Nb, Fe [79]. Körner group at Erlangen, Germany developed also some alloys for a fabrication with EBM. Inconel 718 [80], Ti-48Al-2Nb-2Cr [81]

At NCSU, a large development of new materials by EBM was carried out especially in the PhD thesis of Tushar Mahale [14] TiAl alloys, GRCop-84, Aluminium 2024,6061, 7075 ...

Chapter 3

Problematic raised and starting point of the work

3.1 Problematic of the PhD thesis

This work will focus on lattice structures made by the Electron Beam Melting technology. This AM technology allows the production of almost every shape. It has much less manufacturing constraints than conventional technologies. However new manufacturing constraints have to be taken into account.

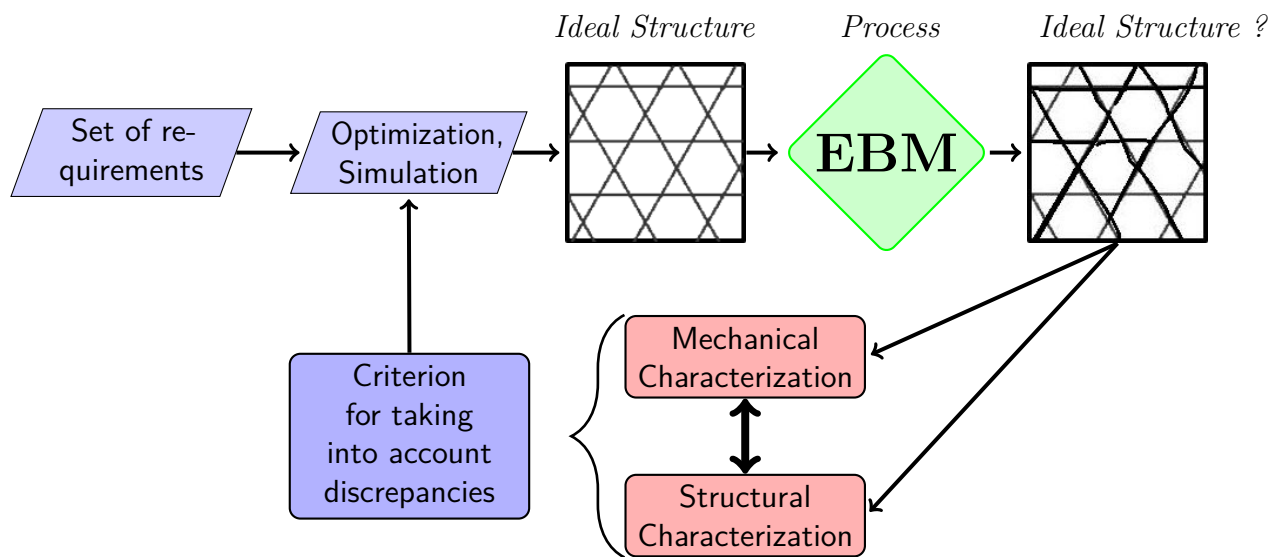


Figure 3.1 Problematic of the PhD thesis.

For the production of lattice structures (especially structures with thin struts), the manufactured structures will be different than the designed ones. Figure 3.1 shows the global thoughts which gave birth to this PhD thesis. From an engineer perspective, lattice structures can be a good answer to a complex set of requirements. After defining the global requirements, a step of simulation and mechanical optimization is carried out to create the ideal geometry that fulfills the required expectations.

The complex shape resulting from the optimization is manufactured with the electron beam melting technology. However; the obtained lattice structure does not have the exact designed geometry due to the process constraints. The main questions are:

- How far from the design is the fabricated geometry?
- How the geometrical discrepancies will affect the desired mechanical properties?
- How to include the process constraints into optimization/simulation procedures?

3.2 Strategy of the PhD

To answer this problematic, the following strategy has been followed:

Characterization of the produced parts

Characterization of the constitutive material made by EBM : Firstly, the properties of the constitutive material have been investigated. Microstructure analysis and tensile tests have been carried out. The influence of roughness and strut size on the mechanical properties has been assessed.

Characterization of lattices structures produced by EBM : When the properties of the bulk material fabricated by EBM were known, the lattices structures produced by EBM have been characterized.

A first structural characterization on single struts has been carried out using X-ray tomography. The shape and porosity of the struts were characterized and a global criterion related to the effective stiffness of the struts was extracted: the mechanically equivalent diameter.

The concept of mechanically equivalent diameter was applied to an Octet-truss lattice structure. The use of this concept for the prediction of the elastic properties of such a structure was validated by comparison with experimental data.

Optimization of the produced lattice structures

Parametric optimization: A code has been created for the parametric optimization of lattice structures. The particularity of this code is to take into account the process constraints by using the mechanically equivalent diameter into the simulation step. The code is based on a python minimization routine coupled with a Timoshenko beam simulation using CAST3M software.

Optimization of the strut's shape by tuning process parameters and strategies:

The process parameters were tuned to investigate their influence on the shape and porosity of the produced struts. The help of a thermal simulation developed by Nicolas Béraud [57] allowed a faster improvement of the process strategy.

Optimization by post-processing: In collaboration with the Ecole Technologique Supérieure de Montréal (Canada) and Université Libre de Bruxelles (Belgium), several attempts on post-processing of lattice structures have been tested. In Canada, electro-chemical polishing was carried out whereas chemical etching was experimented in Belgium.

Part II

Characterization of the material properties

Before looking at the mechanical properties of lattice structures, the microstructural and mechanical properties of bulk and thin parts have to be investigated.



Chapter 4

Microstructural characterization

Contents

3.1	Problematic of the PhD thesis	65
3.2	Strategy of the PhD	66

4.1 Conventional Titanium alloys

In this section, conventional microstructures and crystallography of titanium alloys and especially Ti-6Al-4V are discussed.

4.1.1 Metallurgy of Titanium alloys

Generalities on Titanium

Titanium was discovered more than 200 years ago but its commercial production started in the 1950's. Indeed, its extractive metallurgy is highly complex and requires a high temperature carbochlorination of the natural titanium oxide (TiO_2) [82]. The titanium tetrachloride produced is then reduced by liquid magnesium or sodium to obtain pure titanium.

Although the fabrication process is energy-consuming, titanium resource is virtually unlimited since it is the ninth most abundant element on earth. It is a lightweight material that can reach mechanical properties close to those of steel alloys even though it is two times lighter. However, its price is higher: 9 \$ per kg for titanium vs 1.9 \$ per kg of aluminum and 0.3 \$ per kg of steel (in 2007) [83].

Table 4.1 shows typical properties of Ti, Fe, Ni and Al based alloys (from a very schematic point of view). Titanium based alloys exhibit higher melting point and comparable yield strength to Iron and Nickel based alloys. They have a high corrosion resistance even if they are extremely reactive to oxygen content.

Titanium alloys are interesting for airframes and aeroengines because of their high specific strength and high temperature workability. The use of titanium alloys in offshore structures has become more and more common in recent years for their high corrosion resistance to seawater, high mechanical strength and high flexibility. Their high resistance to corrosion make this alloy suitable for petrochemical application.

	Ti	Fe	Ni	Al
Melting Temperature (°C)	1670	1538	1455	660
Allotropic Transformation (°C)	$\beta \xrightarrow{882} \alpha$	$\gamma \xrightarrow{912} \alpha$	-	-
Crystal Structure	bcc \rightarrow hex	fcc \rightarrow bcc	fcc	fcc
Room Temperature E (GPa)	115	215	200	72
Yield Stress Level (MPa)	1000	1000	1000	500
Density (g/cm ³)	4.5	7.9	8.9	2.7
Comparative Corrosion Resistance	Very High	Low	Medium	High
Comparative Reactivity with Oxygen	Very High	Low	Low	High
Comparative Price of Metal	Very High	Low	High	Medium

Figure 4.1 Typical properties of Titanium based alloys as compared to other structural alloys based on Iron, Nickel and Aluminum. Image from [83].

Titanium alloys (Commercially Pure and Ti-6Al-4V alloys) are also used in the bio-medical industry for their good bio-compatibility, in particular as implant material.

Crystallography and effect of alloying elements

Pure titanium exhibits two different crystallographic structures: the α phase with an hexagonal closed-packed crystal (hcp) structure at room temperature and the β phase, a body-centered cubic structure (bcc) at high temperature.

The allotropic transformation occurs at 882°C. Below this " β transus", the crystal structure is in α phase (hcp) and above this temperature it is in β phase (bcc).

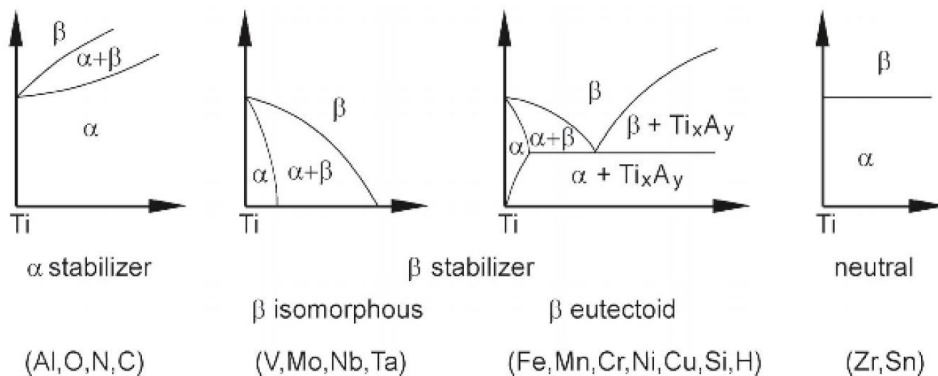


Figure 4.2 Effect on adding alphagene or betagene alloying element. Image from [83].

The addition of alloying elements changes the microstructure by substantially modifying the thermodynamic equilibrium (shown in figure 4.2). Alloying elements such as Al, O, N, C are considered as α -stabilizers since they promote the α domain by increasing the transus temperature. V, Mo, Nb, Ta are β -stabilizers elements. They are called isomorphous because they do not produce eutectoid but rather stabilize the β phase at room temperature as shown in figure 4.2. Some alloying elements called β eutectoid-stabilizers allow a creation of a two phase domain $\alpha+\beta$ above the eutectoid temperature. Some other elements are neutral, i.e. with no predominant effect on the microstructure. They are soluble in the α phase and do not modify the phase equilibrium.

Depending on the stabilizer content, the alloy is considered as a fully α alloy, a two phase $\alpha + \beta$ alloy or fully β alloy. α alloys have a high creep resistance and are easy to

weld whereas β alloys have a higher density and tensile strength.

The raw material for Electron Beam Melting is Ti-6Al-4V.

4.1.2 Ti-6Al-4V alloy

Generalities

Ti-6Al-4V alloy is the most common titanium alloy. The composition of the alloy is shown in table 4.1.

	Aluminum	Vanadium	Iron	Carbon	Oxygen	Titanium
Content [wt%]	5.5-6.75	3.5-4.5	<0.3	<0.1	<0.2	Balance

Table 4.1 Composition of the Ti-6Al-4V alloy according to the standard ASTM F1108 (for cast material).

The Ti-6Al-4V alloy is widely used for aerospace airframe and engine components as well as implant material for biomedical applications. This alloy is considered for any application requiring a combination of high strength at relatively low temperature, light weight, high corrosion resistance and great biocompatibility [83]. The main applications for the aerospace industry are aircraft structural parts (such as landing gear beams, ...), aerospace attach devices (fasteners and fittings) or rotating parts in aero-engines (Fan and compressor blades).

Classification of the Ti-6Al-4V alloy

Because of the addition of aluminum and vanadium, the resulting alloy is considered as $\alpha + \beta$.

Figure 4.3 shows a scheme of its pseudo-binary phase diagram as a function of the addition of the β -stabilizer V. The red dashed line represents the composition of the Ti-6Al-4V alloy. It presents a high temperature β phase from the melting temperature (1660°C) to the β transus ($\sim 980^\circ\text{C}$). At this temperature, a phase transformation occurs either by diffusion controlled nucleation or diffusionless depending on the amount of β stabilizers and the cooling rate. The resulting microstructure is $\alpha + \beta$ or $\alpha + \alpha'$.

If the cooling rate is high enough ($>400^\circ\text{C/s}$), martensite α' phase can be formed between the martensite start temperature (M_S) and the martensite finish temperature (M_F). The martensite start is around 575°C [84].

The room temperature microstructure of such alloys will change depending on their thermo-mechanical history. The temperature maintained during a build in the EBM machine is shown in blue in the scheme (preheat temperature).

Microstructures of Ti-6Al-4V

Typical thermo-mechanical treatments for this alloy require a deformation and a recrystallization step below or above the β transus [83]. Depending on the temperature of these steps and depending on the cooling rate after the recrystallization step, three different types of microstructures are observed in Ti-6Al-4V alloys: fully lamellar, fully equiaxed or duplex microstructures (Figure 4.4).

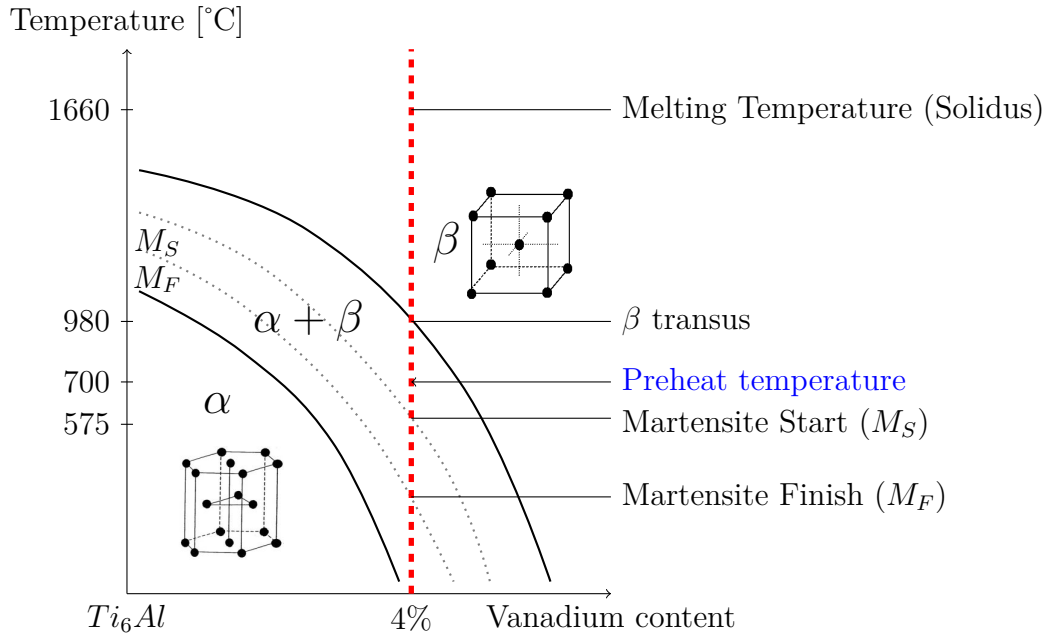


Figure 4.3 Schematic pseudo-binary phase diagram of the Ti-6Al-4V alloy.

The lamellar microstructure (see figure 4.4a) is obtained classically by a thermal treatment in the β domain (II), 30-50°C above the β transus. The cooling rate is then tuned to control several features of the α phase.

The processing route is similar for duplex (see 4.4b) and equiaxed (see 4.4c) microstructures. Deformation (II) and recrystallization (III) occur at temperatures below the β transus. The cooling rate of the step III dictates the microstructural features of the α phase leading to a duplex microstructure for high cooling rates and an equiaxed one for slow cooling rates [83].

Morphologies of the α phase at room temperature The α phase nucleates preferentially at the prior β grain boundaries to form a layer of α_{GB} . Figure 4.5 represents schematically the different morphologies of the α phase within a prior β grain. During the cooling, α plates nucleate at the interface of the α_{GB} and grow within the β grain as parallel plates. The formed α phase is called α_P . It grows following a special crystallographic relationship with the β phase in which it nucleates. This relation is called the Burger relationship [83]. The α_P plates are called colonies and belong to the same variant of the Burger relationship.

For high cooling rates (typically $>10^\circ/\text{s}$), the size of the α colonies and the thickness of the single plates become smaller. The formed colonies cannot fill the prior β grain and new colonies start nucleating at the interface of the α plates. This new α colonies in combination with the previous ones form the so called "basket weave" or Widmanstätten structure (α_W) [83].

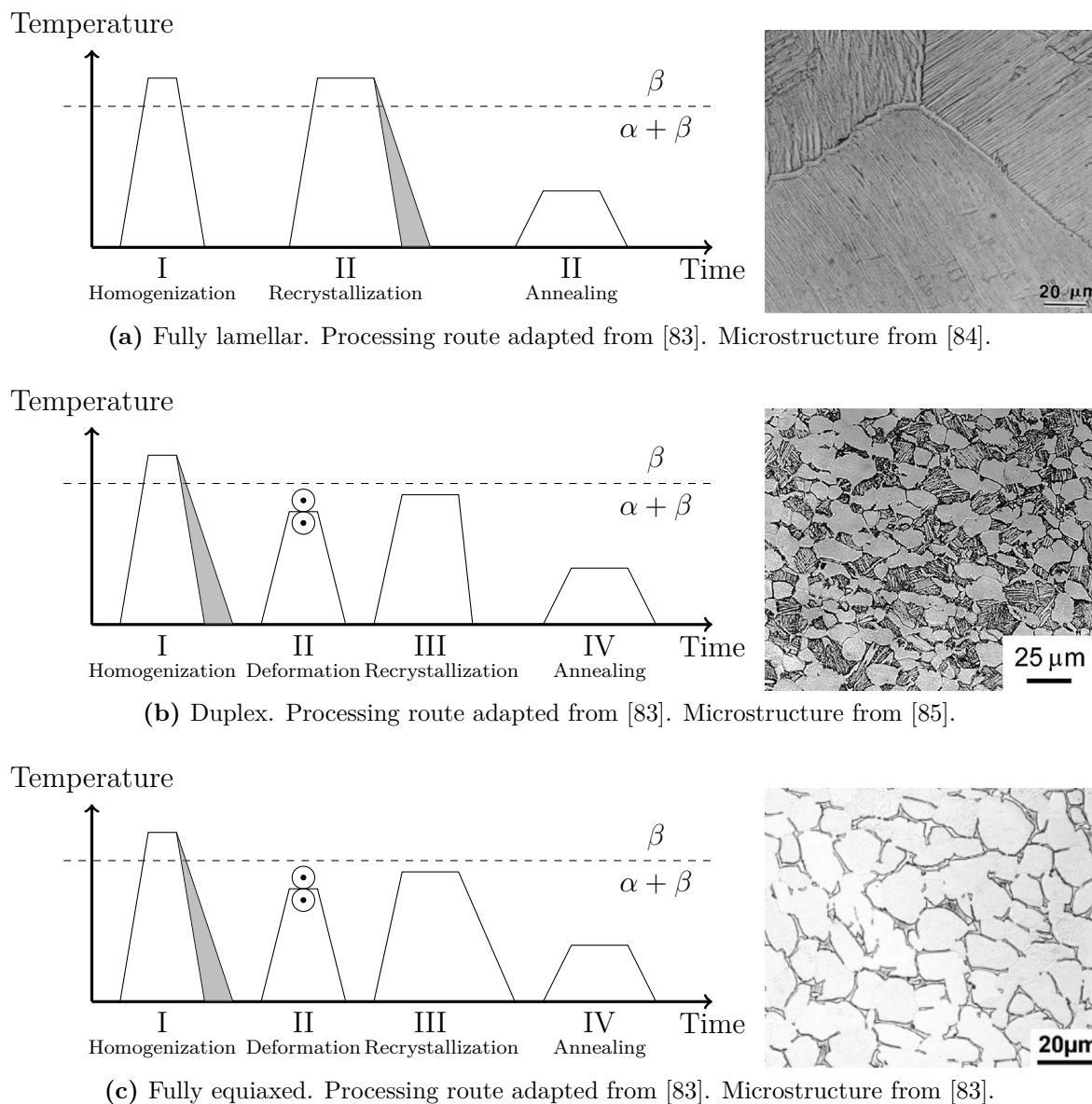


Figure 4.4 Examples of the three types of microstructures observed in Ti-6Al-4V alloys. The α phase is represented in white and the β phase in black.

The cooling rate from the β phase domain dictates several microstructural features. The width of the α lamellae, the size of the α colonies and the thickness of the α_{GB} layers at prior β grain boundaries all decrease when increasing cooling rates. Thus, when increasing the cooling rate, the number of variants within a prior β grain increases.

4.2 Ti-6Al-4V produced by EBM

The microstructural features of Ti-6Al-4V produced by EBM are reviewed. Microstructures of bulk parts and struts are compared ¹.

¹The data presented in the subsequent paragraphs are coming from personal results on one hand and from literature on the other hand. The results coming from the literature are referenced in the caption.

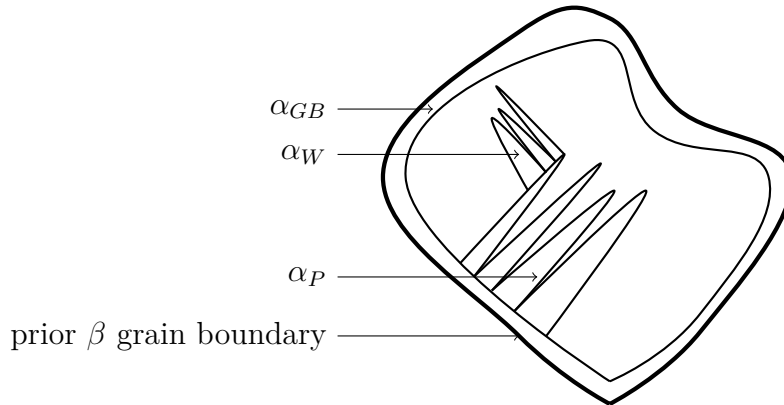


Figure 4.5 Scheme of the microstructure of acicular Ti-6Al-4V alloys.

4.2.1 Materials and methods

This section deals with microstructural observation of Ti-6Al-4V samples fabricated by EBM. Prior to the observation, the samples have been prepared with the following protocol:

Polishing: The specificity of the polishing of titanium parts is that there is an ultimate step of mechanical-chemical polishing using a solution consisting of 80 *vol%* silica suspension (OPS) and 20 *vol%* hydrogen peroxide (H_2O_2). A large polishing time (~ 30 min) is required to obtain good surface quality.

Etching: The Kroll's etching reagent has been used for revealing the microstructure. It is composed of 100 ml H_2O , 2 ml HF , 4 ml HNO_3 . Samples were etched for 10 s and immediately rinsed with ethanol.

Optical Microscope (OM): An olympus upright microscope with an inner camera has been used for imaging the etched samples.

Scanning Electron Microscope : SEM imaging and chemical analysis have been carried out with a Zeiss Leo S440 SEM mounted with an EDX detector.

Electron BackScatter Diffraction: For EBSD mapping, a Field Emission Gun SEM was used. The EBSD mapping allowed the identification of the crystallographic orientations of α and β phases. A software developed by C. Cayron at CEA Grenoble has been used to reconstruct the parent β phase [86]. The software uses the Burger relationship between the bcc and hcp phases to reconstruct the most probable orientations of the parent β phases.

4.2.2 Microstructures

Bulk parts

Figure 4.6 is a 3D reconstruction from OM images coming from three perpendicular planes. The build direction is represented by the black arrow.

A strong anisotropy of the microstructure is observed between the face parallel and perpendicular to the build direction. The microstructure is composed of prior β grains delineated by α_{GB} (represented in red). The prior β grains are aligned with the build

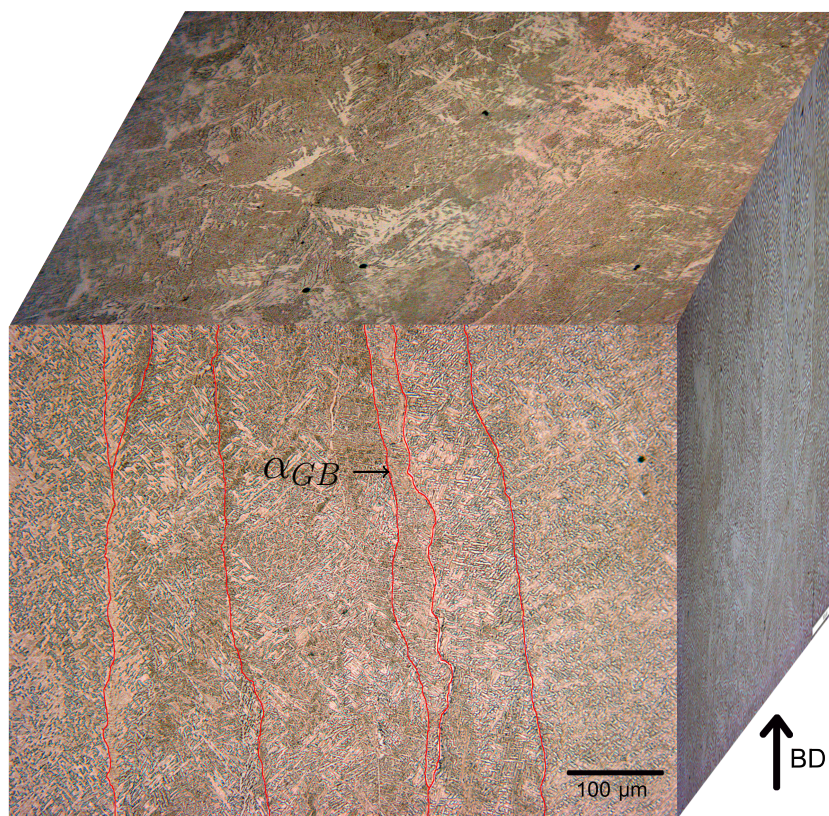


Figure 4.6 3D Optical micrographs of a bulk sample fabricated with the standard "Melt" theme.

direction. The width of each prior β grain is about 150-200 μm . This microstructure can be seen on faces that are colinear to the build direction. Within the prior β grains, an $\alpha + \beta$ phase has grown during cooling. The α phase exhibits a lamellar structure with a fine microstructure.

In contrast, the micrograph perpendicular to the build direction depicts no anisotropy. The lamellar α phase is embedded in β grains that appear equiaxed in this plane. This difference between vertical and horizontal planes has been reported in various studies on EBM produced parts, e.g. [22–25].

The orientation of the prior β grains along the build direction has been explained by Antonysamy et al. and Al-Bermani et al. [87, 88]. During the fabrication, the columnar grains grow upwards due to the re-melting of the previous layers. It provides the conditions for an epitaxial growth of the β phase following the thermal gradient. Thus, in bulk parts, the prior β grains can cross the whole sample [88].

The lamellar structure of the α phase seems to be consistent with a Widmanstätten morphology. Figure 4.7 shows the microstructure of a plane perpendicular to the build direction at higher magnification.

Three types of α lamellae are depicted: The α layer at β grain boundaries (α_{GB}), the α laths grown from the grain boundary (α_P) and the α laths nucleated at the α_P interface (α_W). The width of the α laths is roughly 1 μm and the size of the colonies is approximately 10 μm .

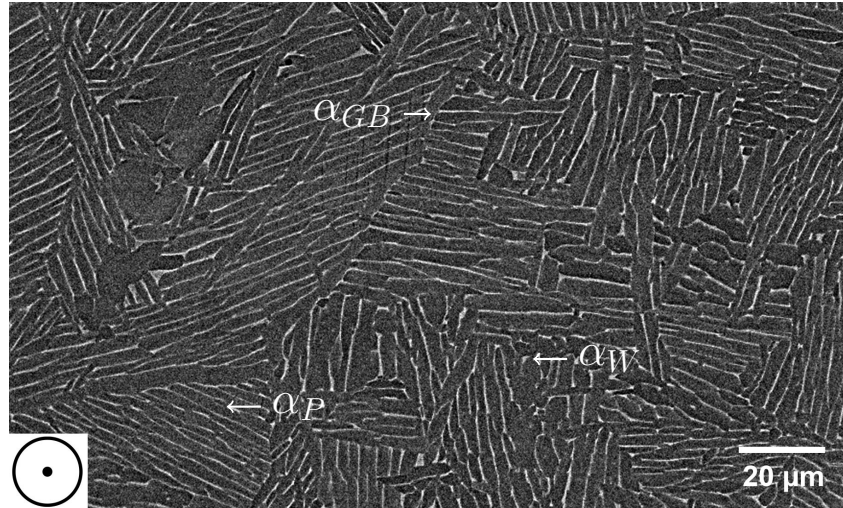


Figure 4.7 SEM micrograph of a plane perpendicular to the build direction for a bulk part.

Gil et al. [89] showed that a cooling rate of $3.5\text{ }^{\circ}\text{C/s}$ results in α plates with a width of 5 to $7\text{ }\mu\text{m}$. Since the α lath are thinner in our case, the cooling rate during the EBM process is much higher. As explained in paragraph 2.2.1, the cooling of a melted point with the EBM process is in two steps. The first step is a rapid cooling from high temperature to about 700°C which provide the fine α plates microstructure. On the other hand, the second cooling from 700°C takes place much more slowly during the process. It is assumed to have limited influence on the growth of the α laths since the diffusion coefficient is low at this temperature.

EBSD analysis allows the analysis of the crystallographic orientation of such bulk parts. Al-Bermami et al. [87] worked specifically on that topic. They produced EBSD maps of α and β phase at room temperature and investigated the parent β phase orientation at high temperature using the Burgers relationship of the bcc-to-hcp transformation.

Figure 4.8 shows the EBSD results on a vertical plane of a bulk part manufactured by EBM. The black arrow shows the build direction.

Figure 4.8a depicts the crystallographic orientation of the α phase. Colonies with the same crystallographic orientation are observed.

Figure 4.8b shows the reconstructed parent β phases. As depicted in figure 4.6, the parent β grains are oriented along the build direction and so along the thermal gradient. The width of a parent β grain is about $150\text{-}200\text{ }\mu\text{m}$. It is consistent with the β grain size observed with the optical micrograph (Figure 4.6).

Figure 4.8c highlights the crystallographic orientation of the parent β grains along the $\langle 001 \rangle$ direction. The beta grains have a strong fiber texture along the build direction. Indeed, this preferential orientation results from the most favorable path for heat flow and the epitaxial growth direction.

When melting a part by EBM, the first layers undergo the influence of the start plate. That may significantly affect the microstructure. Figure 4.9a shows the SEM image of the bottom of a part. The arrow indicates the build direction. A gradient of microstructure appears from the bottom of the part.

To investigate the change in microstructure, three Energy-Dispersive X-ray analysis have been carried out at the locations represented by black crosses. The resulting EDX

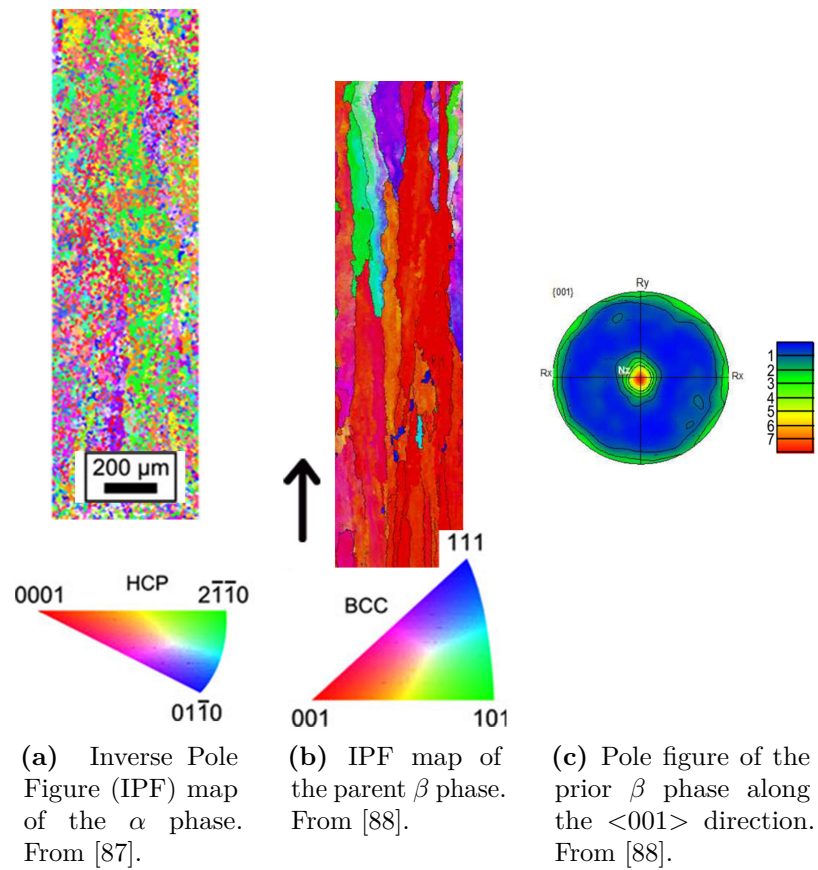


Figure 4.8 EBSD maps showing the microstructure of the α phase at room temperature and the reconstructed parent β phase at high temperature. Images from [87,88].

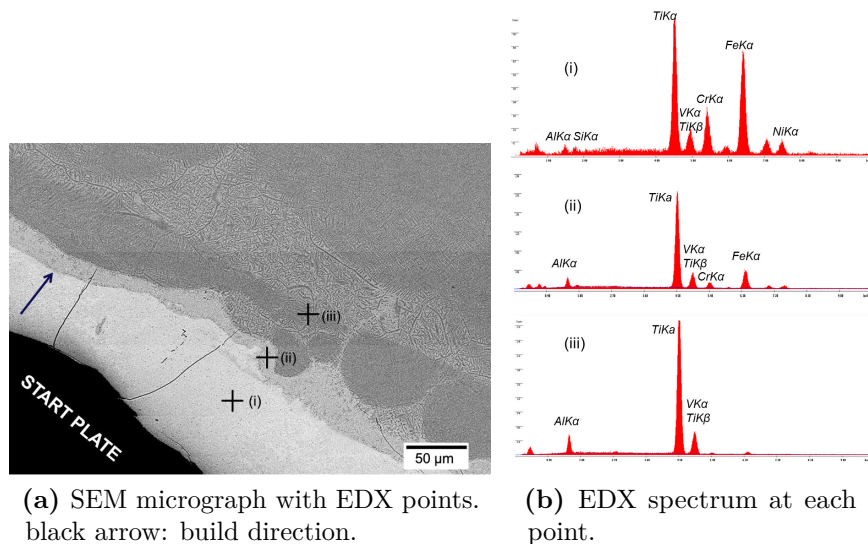


Figure 4.9 BSE SEM micrograph with corresponding EDX analysis at three different points.

spectra are displayed in figure 4.9b. The point close to the start plate presents a high concentration of Iron, Chromium, Nickel in addition to the alloying elements of the Ti-6Al-4V alloy. Those elements are coming from the Stainless Steel start plate. They diffused from the start plate through the fabricated part. Al-Bermani studied this phenomenon [87] and explained that the alloying elements of the start plate act as β -stabilizers.

The second EDX spectrum shows less concentration of β stabilizers and the third one is a typical EDX spectrum of a Ti-6Al-4V alloy. This means that the height of the affected zone is less than $150 \mu\text{m}$.

This affected zone has to be taken into account as it should affect the mechanical properties. To get rid of this effect, parts should be fabricated $200 \mu\text{m}$ over the start plate.

Thin struts

The main purpose of the PhD is to study lattice structures fabricated by EBM. Those structures are composed of thin struts. The microstructure of those struts is now considered and compared to the one of bulk samples.

Figure 4.10 shows SEM micrographs of struts with two different diameters (1 mm and 3 mm) for two different planes (perpendicular and parallel to the build direction). The observations reveal that the microstructure is similar between 1 mm and 3 mm struts whatever the cross-section is (perpendicular or parallel to the build direction). The microstructure of thin struts is still lamellar. The α lath width seems in the same range for both strut diameters and bulk part (figure 4.7).

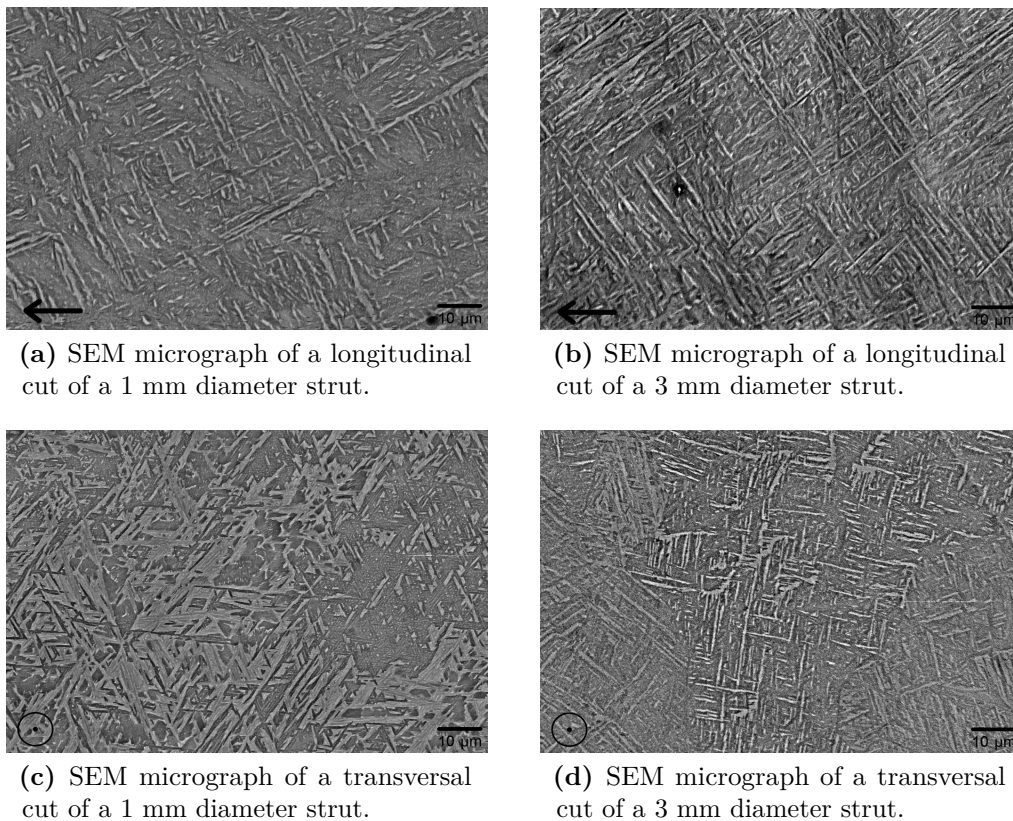


Figure 4.10 SEM micrographs of different sides of a 1mm and 3mm vertical struts. The build direction is represented by the black arrows.

From these SEM micrographs, the microstructure seems similar between bulk parts and thin struts.

Micro-hardness test have been carried out on struts and bulk parts. Figure 4.11 tends to show a difference of hardness between bulk parts and struts. Indeed, the micro-hardness decreases as the strut size increases.

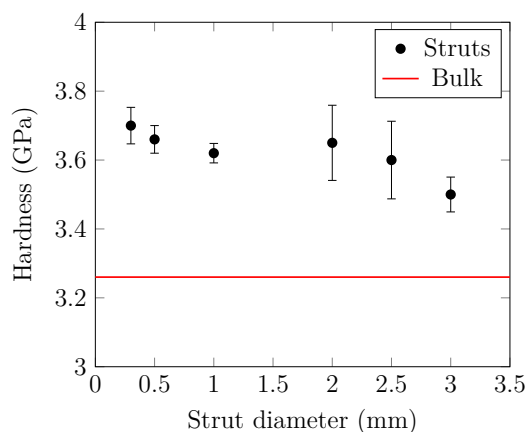


Figure 4.11 Vickers microhardness of bulk part and struts with different diameters.

The results show that the struts have a slightly higher hardness (3.5-3.7 GPa) than bulk material (3.25 GPa). One explanation of this difference could be a change of the prior β grain size and crystallographic orientation. The size and crystallographic orientation of the prior β grains have been obtained by EBSD. Figure 4.12 depicts the EBSD maps of a 1 mm strut.

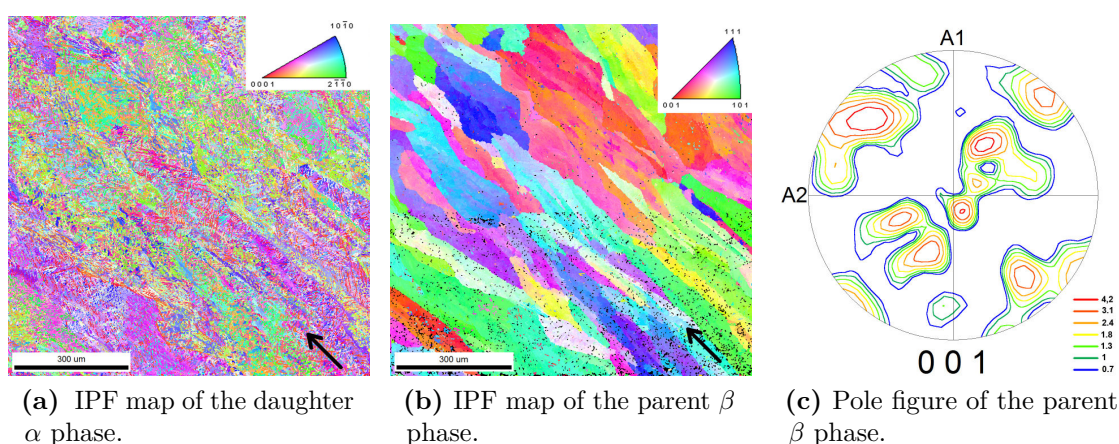


Figure 4.12 EBSD maps showing the orientation of the α phase at room temperature and the reconstructed parent β phase at high temperature for thin strut manufactured at 45°. Image obtained by C. De Formanoir at ULB [90] on struts manufactured at Grenoble university.

The first image shows the α phase orientation map. A global orientation of the α colonies along the build direction can be seen. Large α colonies are present in the strut

with a preferred orientation along the $\{0001\}$ direction (pink color). Figure 4.12b shows the prior β grain elongated in the build direction with a mean width of roughly 70-100 μm . The prior β grains are indeed thinner for thin struts than for bulk parts (150-200 μm). This could be due to a faster cooling rate and the influence of radial thermal flux.

The last image shows the pole figure of the $\{001\}$ direction of the parent β grain. It is less textured than in bulk parts. This has also been demonstrated by Antonysamy et al. [88]. They showed that, in thin struts, the parent β phase is no more oriented only along the build direction but also in direction of the side of the part. This change of crystallographic orientation is due to the thermal flux that is also oriented towards the edges of the struts.

These changes in prior β grain size can explain the increase of hardness for small struts.

The microstructure of thin struts produced by EBM has been much less studied than the one of bulk parts. The first to refer to the microstructure of such struts was Murr et al [65] in 2010. They highlighted the production of acicular martensite (α') for small struts. However, for their study, they used a preheating step at 640°C which is closer to the Martensite Start temperature.

From our preliminary observations made on struts, no evidence of martensite transformation has been found. This could be due to a higher temperature of preheating (about 700°C) compared to 640 °C.

4.2.3 Porosity

The quantity and morphology of pores may strongly affect the mechanical performances of the built parts. The EBM process tends to produce defects when melting layer by layer if the process parameters are not optimized. For EBM produced parts, two types of porosity have been revealed as shown in figure 4.13: spherical and non-spherical porosity.

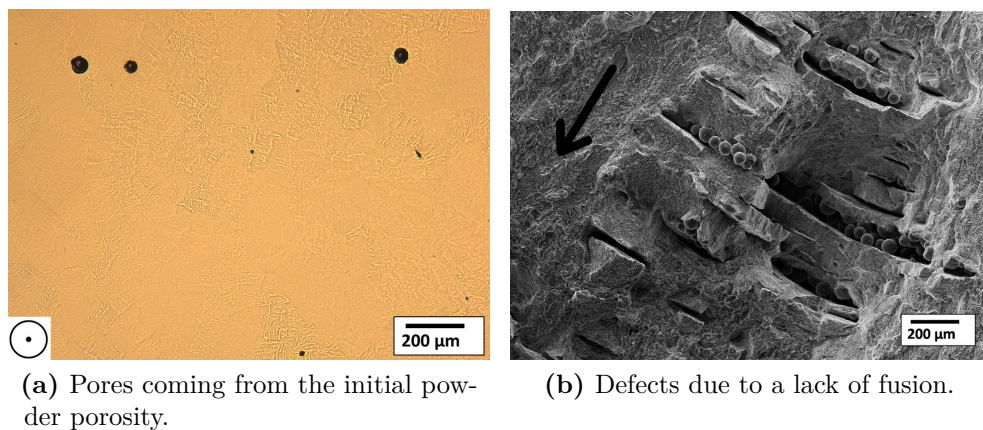


Figure 4.13 SEM micrographs of the two types of pores that can appear in EBM parts. The build direction is represented by the black arrow and the circle.

As mentioned in the previous part (section 2.2.3) and shown by Tammam-Williams et al [18], the initial powder presents an internal porosity due to Argon gas entrapped

during solidification of the particle. This phenomenon has been widely reported in the literature [18, 20, 26, 27]. The internal pores within the initial powders do not totally close when melting.

As shown in figure 2.5 (from the study of Tammam-Williams et al.), the larger the particle, the higher is the probability to observe entrapped porosity. Their study showed that pores can range from 5 μm to 120 μm with a median diameter of 12 μm . Figure 4.13a shows a typical SEM view of a polished surface. It exhibits some spherical pores with a cross-section lower than 100 μm . They are shown in black. The build direction is perpendicular to the plane.

The other category of porosity is the non spherical one. These pores result from a lack of melting due to non-appropriate process parameters or melting strategy. They are more damaging as they generate higher stress concentrations. The figure 4.13b is a SEM micrograph of a surface fracture of an horizontal tensile specimen. The large pores result in this case from a lack of fusion and especially a bad overlap of the melting from one layer to another. It is usually the consequence of a overhanging surface produced with no supports or bad process parameters.

In summary, in parts built with standard sets of process parameters, almost every pore exhibits a spherical shape. When deteriorating the process parameters, large non-spherical pores may appear.

Chapter 5

Mechanical properties

Contents

4.1	Conventional Titanium alloys	71
4.1.1	Metallurgy of Titanium alloys	71
	Generalities on Titanium	71
	Crystallography and effect of alloying elements	72
4.1.2	Ti-6Al-4V alloy	73
	Generalities	73
	Classification of the Ti-6Al-4V alloy	73
	Microstructures of Ti-6Al-4V	73
4.2	Ti-6Al-4V produced by EBM	75
4.2.1	Materials and methods	76
4.2.2	Microstructures	76
	Bulk parts	76
	Thin struts	80
4.2.3	Porosity	82

This chapter aims at characterizing the mechanical properties of the Ti-6Al-4V alloy produced by Electron Beam Melting. The comparison between the obtained results and the mechanical results claimed by the supplier Arcam is highlighted.

5.1 Mechanical properties of conventional Ti-6Al-4V alloy

The typical values of mechanical properties of Ti-6Al-4V alloys depending on their microstructure are depicted in table 5.1 as they appear in ASTM standards. The values reported here are minimal values for satisfying the standards.

Duplex microstructures exhibit larger strength and ductility than fully lamellar microstructures. The duplex microstructures in wrought alloy have undergone a recrystallization step. They are supposed to have better mechanical properties than the alloy

	Ti-6Al-4V cast <i>widmanstätten</i> (ASTM F 1108)	Ti-6Al-4V wrought <i>duplex</i> (ASTM F 1472)
Yield strength (0.2 %) [MPa]	758	860
Ultimate Tensile Strength [MPa]	860	930
Elongation [%]	>8	>10
Young's modulus [GPa]	114	114

Table 5.1 Mechanical properties of Ti-6Al-4V alloys with lamellar and duplex microstructures.

resulting from casting since the low cooling rate in casting provides coarser microstructures.

The microstructure features of Ti-6Al-4V alloys defined in the previous chapter (chap 4) influence drastically their mechanical properties. For lamellar microstructures, the cooling rate from the β phase region dictates the α colony size and influences the related strength and ductility.

5.2 Samples and experiments

To investigate the mechanical properties of EBM-produced parts, tensile tests are carried out. The static properties have been studied without considering fatigue or dynamic mechanical properties.

5.2.1 Tensile test

The tensile test experiments have been carried out on a MTS 810 tensile test machine with a 100 kN load sensor.

For the tensile test, a constant strain rate of $2.5 \cdot 10^{-4} s^{-1}$ has been used. An axial extensometer with a gauge length of 25 mm has been attached to the sample to measure the true strain of the sample and avoid the possible errors due to the elastic deformation of the load frame and cross head.

5.2.2 Tensile samples

Geometries

The tensile samples have been designed to have a cross-section small enough to be able to reach the failure with the 100 kN tensile machine. The produced sample is obtained as-built from the EBM fabrication.

The designed tensile sample is shown in figure 5.1. The geometry satisfies the standard ASTM E-08 [91].

Fabrication strategy

In this study, the influence of the build direction on the mechanical properties is not treated even though literature showed that it may have a slight influence [92, 93]. Hence,

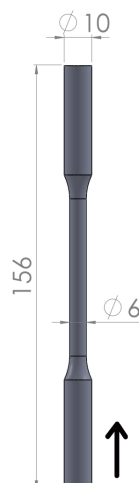


Figure 5.1 CAD models of the as-built tensile sample. The build direction is represented by the black arrow. (dimensions are in mm)

due to the crystallographic anisotropy of the microstructure, the ductility is larger in vertical samples than for samples built horizontally but the tensile strength is lower.

The tensile samples produced in this study were fabricated vertically.

All the tensile samples were built using the standard "Melt" set of parameters.

5.3 Mechanical properties of EBM-built Ti-6Al-4V alloy

5.3.1 Main Results

As-built tensile test samples with a 6 mm diameter have been produced vertically by EBM and tested to investigate their mechanical behavior. Comparison is made with values announced by the supplier. A 6 mm-diameter tensile sample is considered as a bulk part.

Six samples were tested to investigate the **reproducibility** of the Electron Beam Melting process. All the samples had the design of figure 5.1. They were manufactured in the same build with the same parameters. They were mechanically tested without machining.

The stress-strain curves of the tensile tests are shown in figure 5.2.

The samples exhibit almost the same mechanical behavior. They show an elastic regime until a Yield strength (at 0.2 % in strain) of roughly 1050 MPa. No work-hardening is observed. The inset is a zoom in the plastic regime. The mechanical behavior is the same for the six samples. **This shows that the EBM process allows a good reproducibility.**

The mean values of mechanical properties corresponding to the curves of figure 5.2 are reported in table 5.2.

The 6 mm as-built samples exhibit a higher strength (Yield strength and Ultimate Tensile Strength) than the ones certified by Arcam. Moreover, the as-built samples reveal a drastically lower ductility.

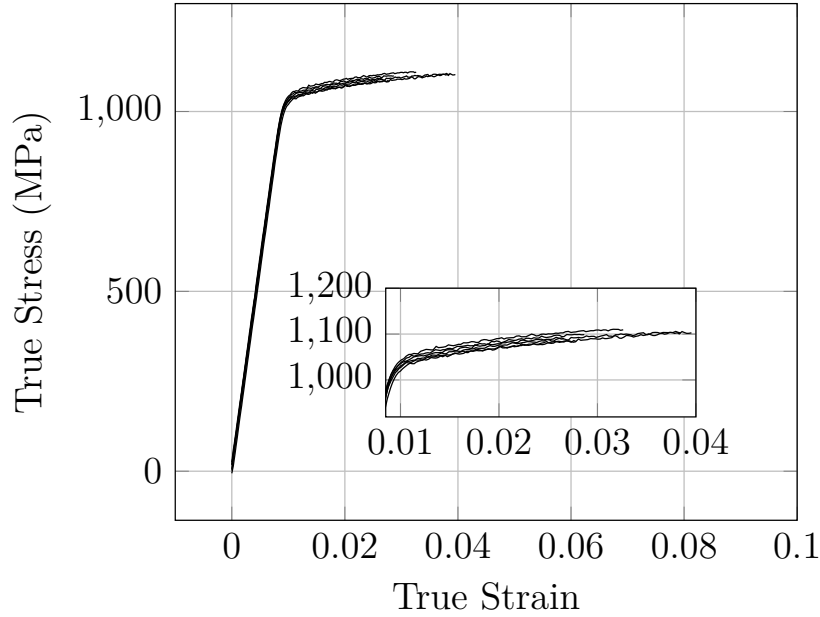


Figure 5.2 Stress-Strain curves for as-built 6mm vertical samples.

	As-built 6mm diameter <i>Mean value \pm STD</i>	Arcam data <i>Claimed by supplier</i>
Yield strength (0.2 %) [MPa]	1045 ± 9	950
UTS [MPa]	1100 ± 10	1020
Elongation [%]	2.3 ± 0.5	14
Young's Modulus [GPa]	114 ± 1	120

Table 5.2 Mechanical properties of as-built 6mm samples produced by EBM compared with the supplier data.

Size effect

To investigate the influence of a microstructural variation between thin struts and bulk parts, tensile test have been carried out on as-built samples with diameters ranging from two to six millimeters. Their geometry is depicted in figure 5.3.

For each diameter, two samples have been fabricated and tested. As shown earlier on the 6 mm diameter samples, there is a good reproducibility for each diameter. Thus, for an easier visualization, only one stress-strain curve per diameter has been plotted in figure 5.4.

The samples show globally the same trend. When zooming in the plastic regime, some discrepancies can be highlighted between the samples.

Samples with a 2 mm diameter exhibit a higher YS and UTS than other samples whereas samples with a 5 mm diameter presents the lowest value.

The data have been reported in table 5.3.

A change of specimen size has a very limited effect on strength and ductility. It confirms the fact that the microstructure is not very sensitive to the strut diameter (as explained section 4.2.2).

As a summary:

- No clear change of mechanical properties was observed when varying the diameter of the tensile specimen.

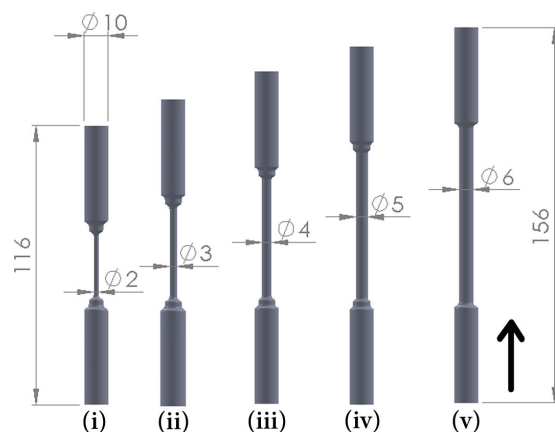


Figure 5.3 CAD models of the as-built tensile samples with different diameters. The build direction is represented by the black arrow.

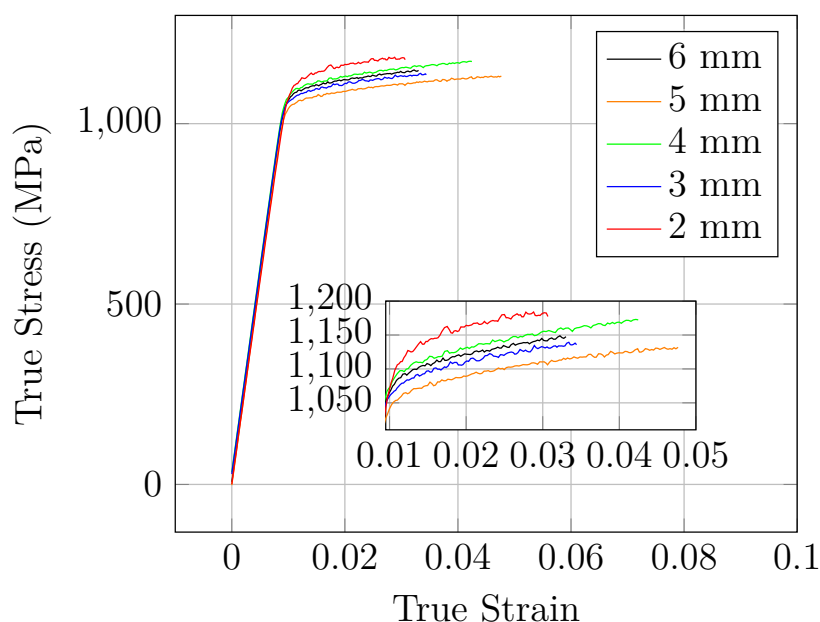


Figure 5.4 Stress-Strain curves for as-built vertical samples with samples varying from 2 to 6 mm. Correction with equivalent diameters.

Diameter of as-built sample	2 mm	3 mm	4mm	5mm	6mm	δ_{max} (%)
	<i>Mean value</i>					
Yield strength (0.2 %) [MPa]	1114	1076	1089	1075	1093	3.5
UTS [MPa]	1173	1139	1160	1140	1149	2.9
Elongation [%]	1.67	2.44	2.68	2.8	2.2	40.4
Young's Modulus [GPa]	113	114	114	114	114	114

Table 5.3 Mechanical properties of as-built samples produced by EBM with a diameter ranging from 2 to 6 mm.

- The Young's modulus value is in the expected range (~ 114 GPa).
- The strength (YS and UTS) is largely higher than the values claimed by the supplier.

- The elongation to fracture is very low (<3%).

The origin of the high strength and low ductility is now investigated.

5.3.2 Origin of the high strength

As seen in the previous paragraph, there is no size effect on the strength of the produced samples. The slight fluctuations observed between samples with different diameter cannot explain the large difference of strength (YS and UTS) compared to the values claimed by the supplier.

When the EBM machine has been received, a preliminary study was carried out for the validation of the mechanical properties of produced parts. In the following, the results coming from this work will be called "*Preliminary study*". On the contrary, the results coming from a second mechanical study will be called "*Final study*".

The stress-strain curve resulting from this preliminary study is shown in red in figure 5.5. It is compared with one tensile test result from the final study (in black). The samples are both as-built with a 6 mm diameter following the geometry of figure 5.1.

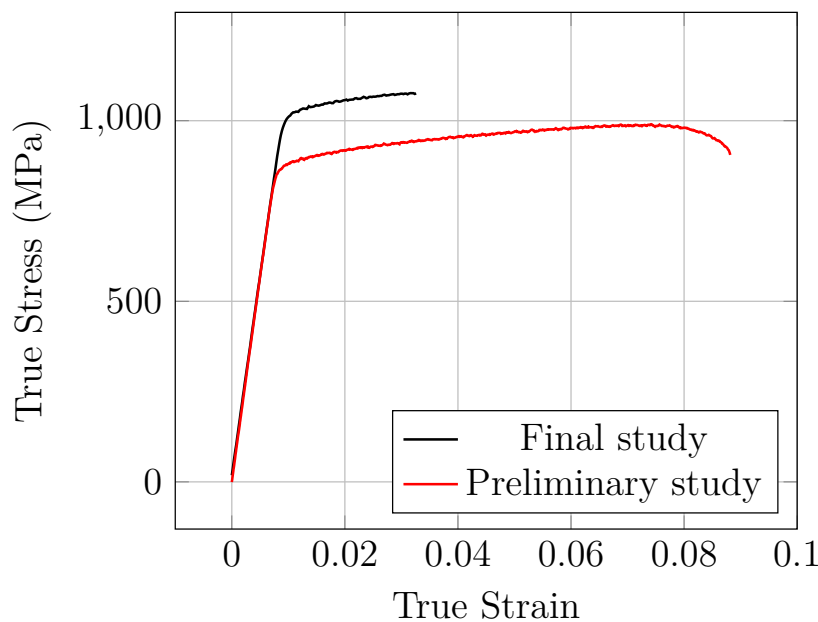


Figure 5.5 Stress-Strain curves for as-built 6 mm vertical samples in the preliminary and final study.

The results show a large difference in strength and ductility between both samples. The values of mechanical properties are reported in table 5.4.

The tensile test samples of the preliminary study exhibit much lower strength and larger ductility. The values of strength for the preliminary study are in the range of the values claimed by the supplier (Table 5.2). A large decrease of ductility occurs between the preliminary study and the final one (from 8% to 2 %).

The increase of the strength and decrease of the ductility is typical for a titanium alloy when getting enriched by oxygen. A small literature review tends to explain the effects of such interstitial element on the mechanical performance of the alloy.

	Preliminary study	Final study
Yield strength (0.2 %) [MPa]	878	1045
UTS [MPa]	990	1100
Elongation [%]	8.0	2.3
Young's Modulus [GPa]	114	114

Table 5.4 Mechanical properties of as-built 6mm samples from the preliminary and final study.

Literature Review

Interstitial elements can impact drastically the mechanical properties of titanium alloys. Among these elements, oxygen is the most influential one. Oxygen is an α -stabilizer that acts as solid solution strengthener. Jaffee et al. [29] showed that increasing oxygen concentration induces an increase of strength and hardness as well as a decrease of ductility of the alloy.

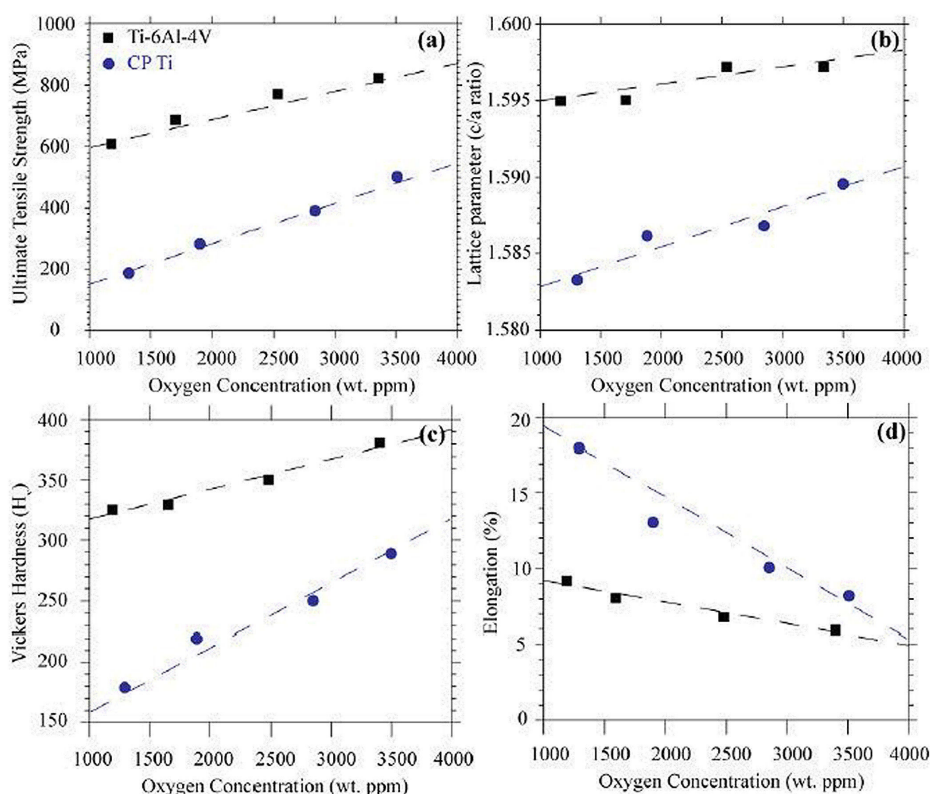


Figure 5.6 Influence of the oxygen content on the mechanical properties of Ti-6Al-4V and CP Ti alloys. From [28].

The influence of a variation of oxygen concentration on the mechanical properties of Ti-6Al-4V was also reported by Oh et al [28] (Figure 5.6). The same trend is visible for both alloys showing an increase of strength and decrease of ductility when increasing the amount of oxygen. If a Ti-6Al-4V alloy contains 0.4 wt% of oxygen, the final UTS will reach 900 MPa whereas its elongation will decrease to 6-7% instead of the standard value of about 15 %.

The oxygen atoms modify the dislocation path within the hcp crystal. Oxygen atoms

occupy the octahedral sites of the HCP crystal structure [28]. As a result, the critical resolve shear stress increases. Thus, it increases the hardness and strength of the alloy.

Interstitial level investigation

The interstitial concentration of samples coming from the preliminary study and the final study has been assessed. The chemical analysis has been carried out by the "Institut des Sciences Analytiques" (ISA) from the CNRS lab at University of Lyon. High temperature combustion and analysis of produced gas has been used for the elementary analysis of the interstitials.

Table 5.5 shows the values obtained for the preliminary and final study as compared with the specifications from the supplier. As mentioned earlier, the tensile samples of the preliminary study has been produced just after the initiation of the machine at Grenoble university (with new powders). On the contrary, the tensile samples of the final study have been fabricated with powders that underwent numerous reuses.

	Arcam Ti-6Al-4V	Preliminary study	Final study
Al [%]	6	5.73	6.37
V [%]	4	3.90	4.52
O [%]	0.15	0.27	0.53
N [%]	0.01	0.018	0.037
Fe [%]	0.1	0.18	0.22
C [%]	0.03	<0.01	0.01

Table 5.5 Table of interstitials concentrations from the supplier specification, the preliminary study and the final one.

The tensile sample for the preliminary study exhibits interstitial concentrations close to the one announced by the supplier except for the oxygen content which is much higher (0.27% instead of 0.15%). The chemical analysis on samples of the final study shows a large increase of the Oxygen (0.53%) and Nitrogen content.

Thus, the reuse of the Ti-6Al-4V powder throughout the builds can lead to an increase of the interstitials content (especially oxygen). It can modify largely the mechanical properties of the produced part (according to figure 5.5).

A study from Tang et al. [56] was focused on the effect of the reused times on the size, shape, chemical and flowability of Ti-6Al-4V powder processed by EBM. They used initial powder with an Extra Low Interstitial content (ELI). Their results showed an increase from 0.08 % to 0.19% of oxygen content after 21 uses. The Al and V content stayed generally identical. Their results have the same trend as ours but the range of oxygen content is relatively different. Indeed, in their range, the increase in oxygen content produces a increase of yield strength and ultimate tensile strength but no change in terms of elongations. In our range of oxygen concentration, the ductility decreases largely.

⇒ In summary, oxygen pick-up occurs during the reuse of the powder and can lead to a drastically reduction of the ductility and increase of the strength of the produced Ti-6Al-4V.

Recommendations for controlling oxygen pick-up of produced parts

Controlling the amount of oxygen of the Ti-6Al-4V produced part is of great importance. This oxygen pick-up during recycling of the powder has been largely investigate internally

by Arcam. Their study points out the steps when oxygen pick-up occurs within the different steps of manufacturing by EBM.

The main pick-up of oxygen occurs during the melting within the EBM machine. Even if the build chamber is pumped under secondary vacuum, some moisture can be trapped in aluminum residues inside the machine and release oxygen during the manufacturing. The titanium being very sensitive to oxygen at high temperature, this results in a significant increase of oxygen in the melted and also in the sintered powder surrounding it. This powder will be then reused multiple times before being melted. During those reuses, the powder can accumulate oxygen.

Some recommendations can be listed:

- Use of Extra-low interstitial Ti-6Al-4V powder (ELI powder). It exhibits an initial oxygen concentration $\leq 0.1\%$
- For each build, mixing new powder with reused one to keep a constant oxygen content
- Clean carefully the inner surface of the EBM machine to avoid moisture to be entrapped in aluminum residues.

5.3.3 Origin of the low elongation to failure

As studied in the previous paragraphs, the oxygen pick-up plays a role in the decrease of the ductility of the produced parts. However, even when producing parts with a low oxygen content, the ductility is lower than the value claimed by the supplier (8 % vs 15 %).

Other sources can be imagined. The reduction of the elongation to failure can be linked to the surface irregularities (that can act as a crack initiator) or to internal porosities. The aim of the next paragraphs is to estimate the degrees of importance of each effect.

Effect of surface irregularities

The global standard for testing specimen fabricated by AM consist in producing oversized parts and then machine them to fit the designed geometry (ASTM F2971-13) to be further mechanically tested. However, the AM techniques are attractive to produced as-built parts.

To be able to see the influence of the roughness on the mechanical properties and to compare with literature values obtained on machined samples, samples with a 6 mm diameter (geometry of figure 5.1) have been produced by EBM and machined to different diameters (5, 4, 3, 2 mm). The comparison between as-built and machined samples with the same diameter have been carried out. The machined sample with a final diameter of 5 mm is shown in figure 5.7.

The mechanical properties of the machined sample are compared with an as-built sample with a 5 mm diameter. However the same trend has been observed for machined samples with any final diameter.

Figure 5.8 shows the stress-strain curve for as-built (dotted line) and machined (full line) samples with a 5 mm diameter. The points in blue correspond to the elongation of machined samples with a low ductility and the points in red delimit the large elongations. The triangles correspond to the final elongation of 5 mm diameter samples as-built.



Figure 5.7 5 mm diameter sample machined from an as-built sample with a 6 mm diameter.

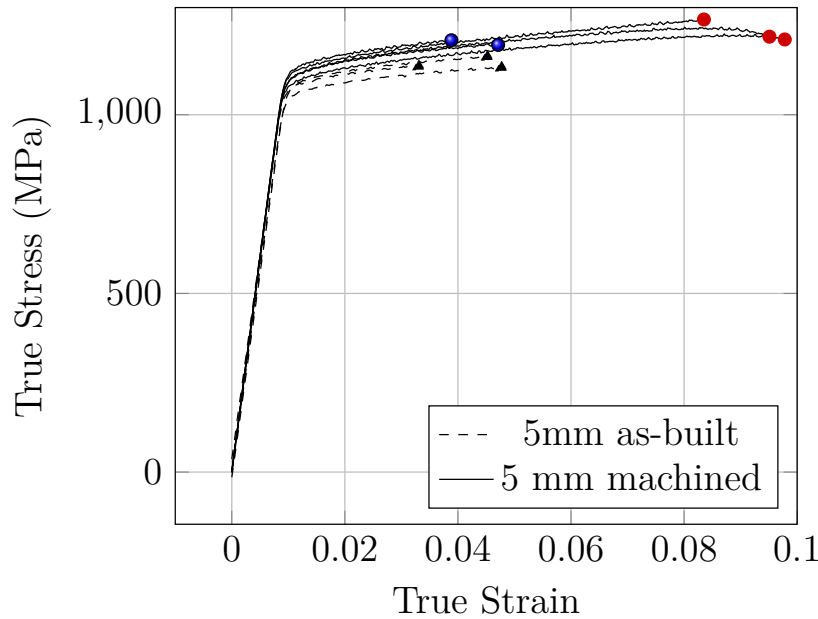


Figure 5.8 Stress-Strain curves of 5mm as-built and machined samples.

This figure highlights two effects:

- In terms of strength, as-built samples and machined samples have roughly the same values.
- In terms of ductility, as-built samples exhibit always a low elongation (around 3%) whereas machined samples have a much more complicated behavior. Some samples fail at low elongation (blue points) and other fail at higher values (red points) although they have been manufactured within the same build, with the same set of process parameters and the same orientation. Machined samples with a large elongation exhibit necking.

The results are summarized in table 5.6.

The roughness can be considered as a site of stress accumulation and the fracture can thus initiate in early stage of the tensile test. The standard deviation of the elongation to failure increases drastically from 0.8 % for as-built samples to 2.8 % for machined samples. The variability of elongation of 50 % is therefore observed.

Such differences in terms of elongation for EBM parts have been already reported by Karlsson et al. [21]. They carried out tensile tests on machined samples with Digital

	5 mm as-built <i>Mean values \pm STD</i>	5 mm machined <i>Mean values</i>
Yield strength (0.2 %) [MPa]	1075 \pm 17	1110 \pm 15
UTS [MPa]	1140 \pm 17	1230 \pm 27
Elongation [%]	2.8 \pm 0.8	6.2 \pm 2.8
Young's Modulus [GPa]	114 \pm 1	112 \pm 1.4

Table 5.6 Mechanical properties of 5 mm-diameter samples as-built and machined.

Image Correlation (DIC). Their results showed large discrepancies in terms of ductility (elongations between 4 and 7 %). Using the DIC, they showed that samples with larger elongation have a more homogeneous strain field than samples with a short elongation. From the fractography analysis, they attributed the difference of elongation to the location of pores within the sample. For the samples that break early, the porosity was located both at the surface and in the bulk whereas for samples with larger ductility, the pores were located mainly in the bulk.

Towards the understanding of the elongation dispersion

From the previous considerations, machined samples with a 2 mm diameter have been analyzed by tomography prior to tensile test and post-mortem to investigate the amount and position of pores within the sample and correlate it with the failure zone. A sample with a diameter of 2 mm has been chosen to simplify the X-ray tomography conditions. It is reliable since the machined tensile test samples exhibit the same elongation dispersion whatever their diameter is. The tomograph used was an EasyTom XL 150 from RX Solutions [®]. To map the entire volume, a stacked tomography mode has been used. The voxel size for the analysis was 2.5 μm .

The fracture surface has been analyzed to investigate if microstructural features can influence the mechanical properties.

The tensile sample exhibits a Yield strength of 1120 MPa, an ultimate Tensile Strength of 1217 MPa and an elongation to failure of 4.1 %.

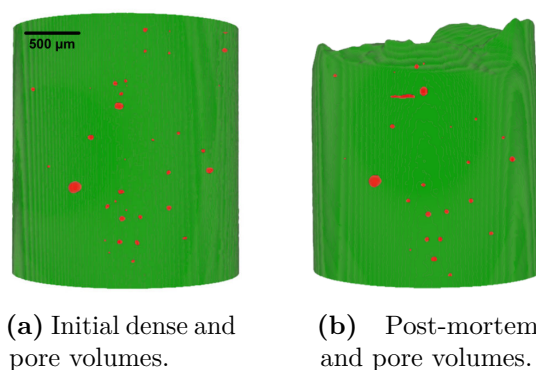


Figure 5.9 3D views of the dense and pore volumes for initial and post-mortem samples.

The reconstructed volumes from X-ray tomography are shown in figure 5.9. The dense volume is represented in green and the pores in red. The shape of the pores has changed close to the zone of failure.

The pores have globally a spherical shape in the initial volume. As mentioned previously (4.2.3), the pores are coming from the atomization process to form the titanium powder. No irregular pores are observed which means that the melting during the manufacturing process occurred efficiently.

Pore Analysis The aim was to be able to predict the zone of failure on the sample prior to tensile test (figure 5.9a). The initial volume has been cut into circumferential volumes to see the influence of pore close to the surface. The circumferential volume kept ranged from 0.1mm to 0.4 mm in radius.

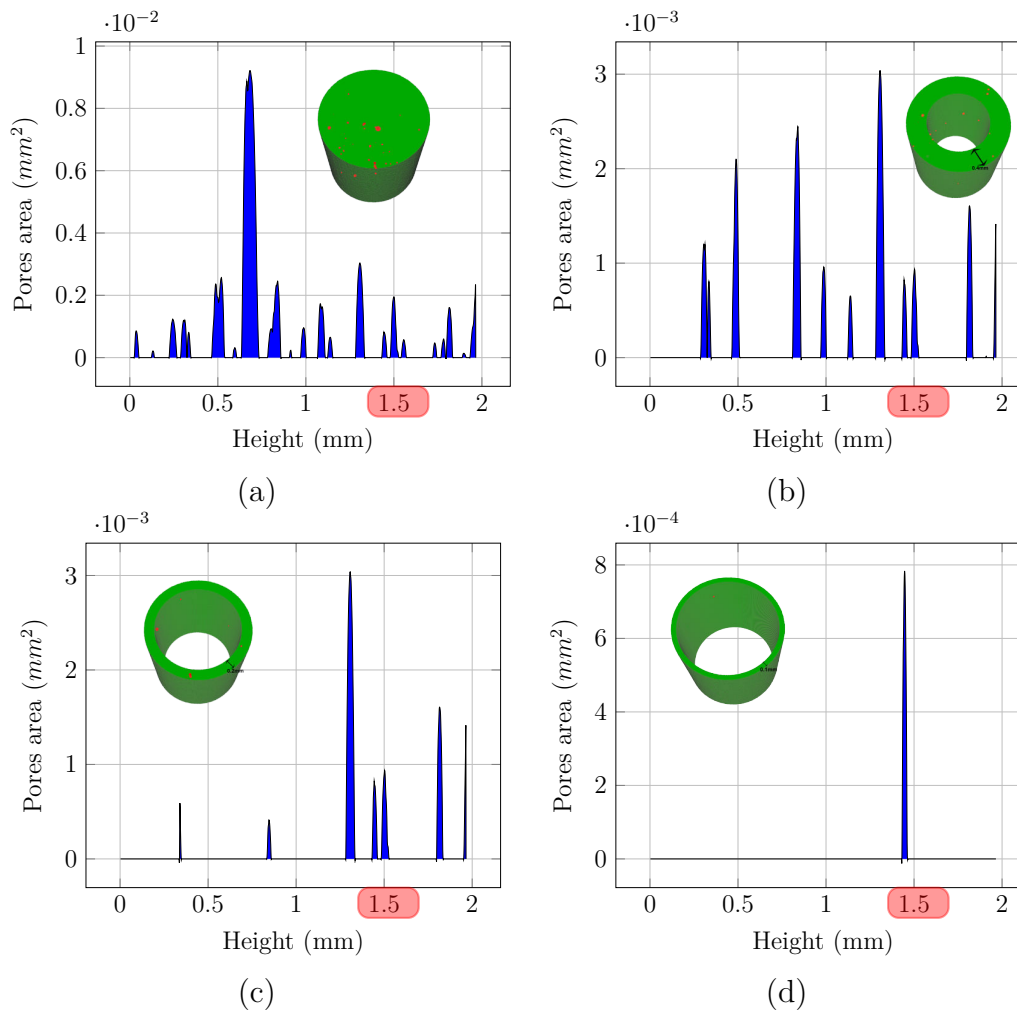


Figure 5.10 Analysis of pores area along the volume height for the entire volume (a), a circumferential volume with a thickness of 0.4 mm (b), 0.2 mm (c) and 0.1 mm (d). The failure zone is represented by the red rectangle.

For each 3D image, the area of pore at each stack is extracted. It allows to extract the stack presenting the highest surface of pores. This analysis is carried out on the three circumferential volume and on the global volume. The pores area is plotted as a function of the height in figure 5.10. The zone of failure is located around 1.5 mm and is represented by a red rectangle in the x-axis. It has been identified by comparing the 3D volume prior and after the tensile test. The correlation of the pores location allowed the matching of the volumes.

The figure 5.10 (a) shows the pores surface at each height of the global sample. The height of maximum porosity does not correspond to the height of failure. However, when keeping a small circumferencial volume of 0.2 mm (c), the height of maximum surface area of pores corresponds to the height of failure. For the circumferencial volume with a thickness of 0.1 mm, the porosity is located only within the failure height (see figure 5.9).

These results highlight the correlation between porosity location and failure zone. The pores at the periphery of the struts are responsible to the breaking of the sample. It can explain the elongation variability.

The broken part has been observed by SEM to investigate the fracture surface.

Fractography analysis The fracture surface has been observed by SEM. The images are exposed in figure 5.11. The first image (at low magnification) shows the global shape of the fracture surface. At this magnification, one can distinguish, the plane zone (in the middle and delimited by the blue curve), the zones going up and down (in the circumference).

A part of the plane zone reaches the surface at the bottom right corner. This is the part where the fracture started.

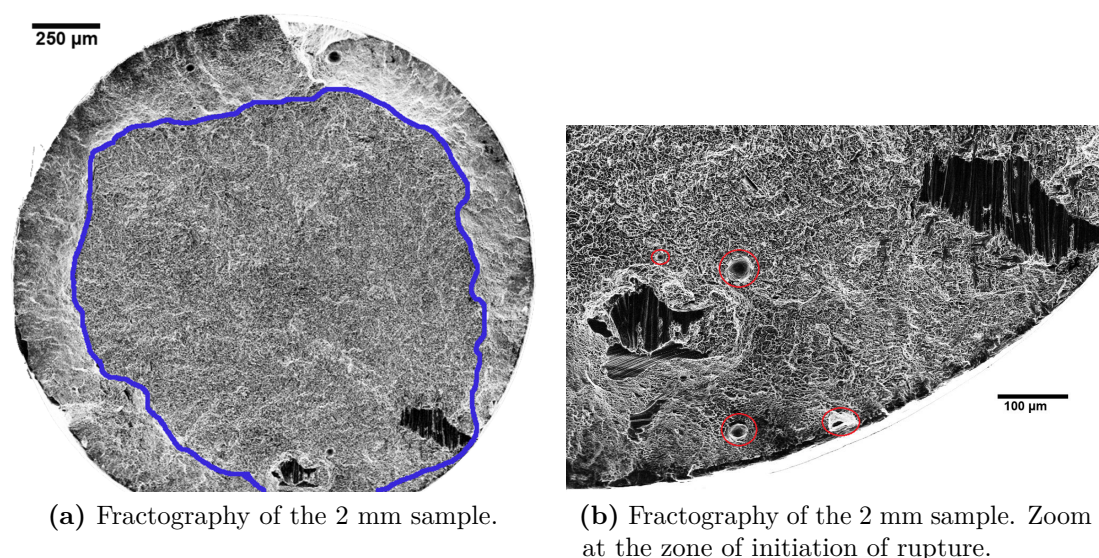


Figure 5.11 Fracture surface observation by SEM. Global images at low magnification (a) and zoom at the initiation of rupture (b).

The figure 5.11b shows a zoom on this zone. Pores are pointed out by a red circle. As seen in the tomography analysis, some pores are located close to the surface. They have been identified as critical pores.

The fracture surface is globally composed of dimples representative of a ductile failure. However, some black area are observed especially in the zone where the failure started. These areas are plane and do not exhibit a dimple shape. Chemical analysis of such area has been carried out using Energy Dispersive X-ray Spectroscopy. Their composition is the same as the composition of the dimples. Thus, they do not result from pollution during the manufacturing.

Lütjering found the same observation on conventional Ti-6Al-4V alloy [83]. It corresponds to a zone of intergranular type of fracture. At a given cooling rate, the fracture

mode changes from transgranular to intergranular. It could be an explanation because the size of the black area corresponds to the size of a prior β grain (100-200 μm).

The mode of fracture is indeed hybrid composed mainly of dimples resulting from a transgranular fracture. However some grains exhibited a more brittle mode of fracture since intergranular fracture occurred.

The location and amount of such brittle mode of fracture can influence largely the ductility of the produced samples and play a significant role in the elongation dispersion.

Summary

Microstructural characterization:

- Some microstructural features of Ti-6Al-4V produced by EBM are similar for small struts and bulk parts:
 - A strong anisotropy exists between the build direction and other directions. Due to epitaxial growth during the directional cooling, the prior β grains are oriented along the build direction.
 - Both small struts and bulk parts present a lamellar microstructure with an α lath width of roughly $1 \mu m$.
- However, the β grain size is slightly smaller ($70-100 \mu m$) for thin struts than for bulk samples ($150-200 \mu m$).
- Two types of porosity can be observed: spherical and non-spherical ones. The first one comes from the powder production process and the second one results only from bad melting.

Mechanical characterization:

As-built samples manufactured by EBM presented a much larger strength and drastically lower ductility than the values announced by the supplier ARCAM. To understand this difference of mechanical properties, several effects have been analyzed separately. The influence of each effect has been summarized in figure 5.12.

- The increase of oxygen content during the multiple reuse of the Ti-6Al-4V powders lead to a higher strength and a lower elongation to failure (black arrows in the figure).
- Tensile samples with different diameter have been tested. No size effect has been observed in terms of mechanical properties. It is consistent with the previous microstructural observations.
- Machined samples exhibit the same strength as as-built ones but can have larger elongation to failure (blue arrows in figure 5.12). A large versatility of ductility has been found for machined samples (dashed arrow in the figure 5.12).
- X-ray tomography and fracture surface analysis helped to understand this versatility in elongation. The dispersion of elongation to failure is mainly due to the presence and amount of pores on the periphery of the strut. It can be also influenced by a change in the deformation mode. This versatility has been only investigated on machined samples with a high oxygen content but we suppose that it occurs also for machined samples with a low oxygen content.

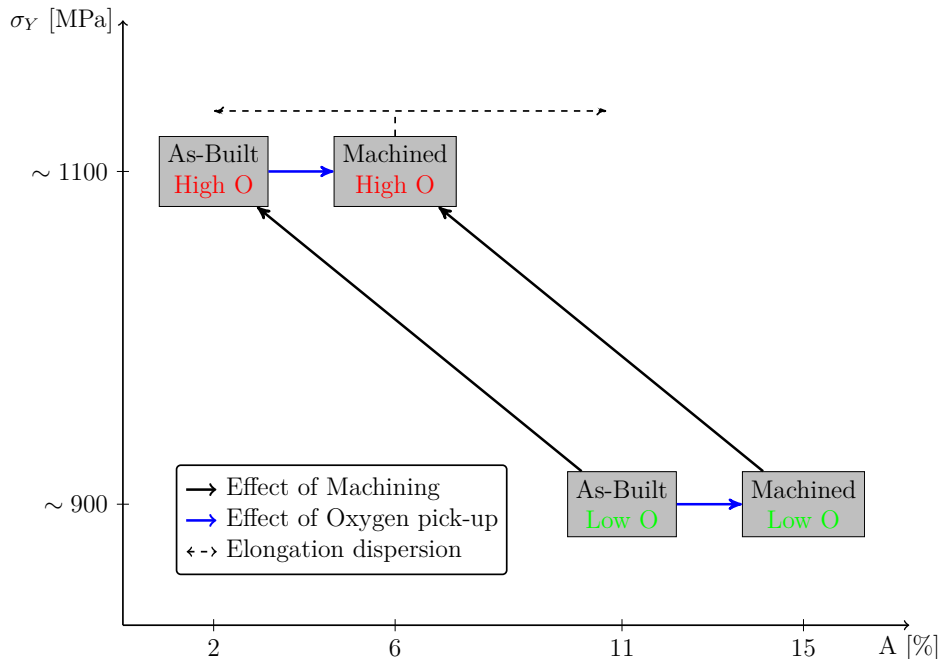


Figure 5.12 schematic representation of the effects of each parameters on the mechanical properties of Ti-6Al-4V parts built by EBM. Representation in the Yield strength-Elongation to failure space.

Part III

A methodology for the stiffness
prediction of lattice structures
produced by EBM

In this part, a precise methodology for determining effective geometry and mechanical properties of lattice structures produced by EBM is presented. A well-know triangulated structure is used as a reference structure. The methodology presented here aims at being general and could be applied to any geometry and AM process.



Chapter 6

Review on geometrical and mechanical variability in AM of lattice structures

Contents

5.1	Mechanical properties of conventional Ti-6Al-4V alloy	85
5.2	Samples and experiments	86
5.2.1	Tensile test	86
5.2.2	Tensile samples	86
	Geometries	86
	Fabrication strategy	86
5.3	Mechanical properties of EBM-built Ti-6Al-4V alloy	87
5.3.1	Main Results	87
	Size effect	88
5.3.2	Origin of the high strength	90
	Literature Review	91
	Interstitial level investigation	92
	Recommendations for controlling oxygen pick-up of produced parts	92
5.3.3	Origin of the low elongation to failure	93
	Effect of surface irregularities	93
	Towards the understanding of the elongation dispersion	95

This section aims at setting a point of reference of the literature that shows a variability in terms of shape and/or mechanical response for lattice structures produced by Additive Manufacturing technologies. Few studies focused on the geometrical and mechanical characterization of the produced struts and their comparison to the designed geometry.

6.1 Electron Beam Melting

One of the first attempt to characterize the geometrical variability of struts has been made in 2008 by Cansizoglu et al. [64]. They reported the properties of periodic lattices (consisting of hexagonal unit-cells) under compression and three-points bending. They showed that geometrical discrepancies can appear between the designed structure and the fabricated one depending on the strut angle. Their explanation is based on geometrical considerations (see figure 6.1). Depending on the strut angle, layer thickness and melt pool depth, the overlapping zone can be reduced for struts with a low orientation angle (so-called *staircase* effect). They forbid the strut to have an angle lower than 20° to prevent the phenomenon.

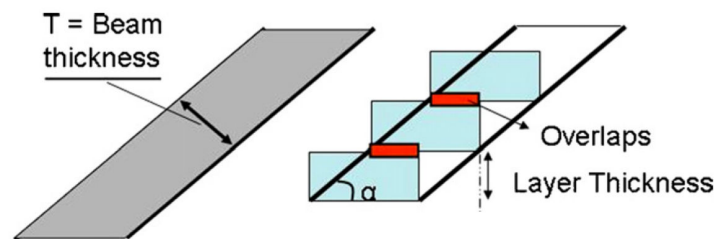


Figure 6.1 Scheme showing the problems of bad overlapping between each layer for low strut angles. Image from [64].

However, their study was based on struts produced by EBM with a layer height of $100\ \mu\text{m}$. As explained in chapter 2, the layer thickness in our study is $50\ \mu\text{m}$. From image 6.1, when decreasing the layer thickness, the overlapping becomes larger. Thus, this phenomenon will not be predominant anymore. Moreover, their study focused on the theoretical analysis of the overlapping zone but did not take into account that at each layer re-melting occurs leading to a better structural integrity of the struts.

Yang et al. focused on a re-entrant structure produced by EBM [94]. They reported a high variability in strut size and roughness. As an outlook, they suggested an effective strut size from a 2D scheme of a strut (Figure 6.2).

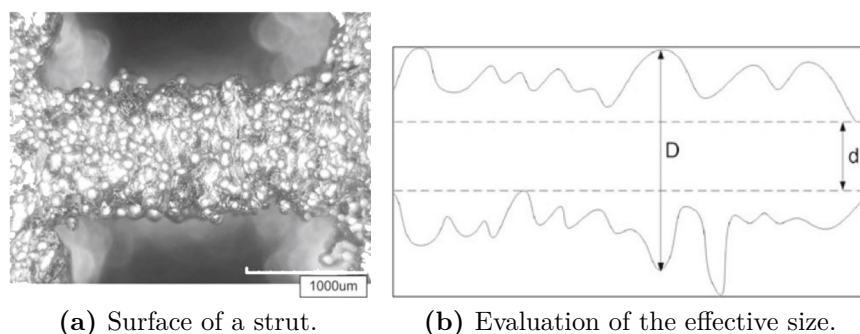


Figure 6.2 Strut size of an EBM part. Image from [94].

From the 2D observation of a strut (figure 6.2a), they proposed to take into account only the internal section (d in figure 6.2b) that falls entirely within the strut. However, no link between this effective size and the effective mechanical properties was carried out. They highlighted that "to accurately determine the actual strut sizes is therefore a

challenge".

More recently, a group from Sheffield University studied metallic foams manufactured by Electron Beam Melting [68]. They used a tomographic image from a replicated foam as the basis of their CAD model. Their aim was to reproduce isostructural foams and compare it to a recent model.

In their work, they also focused on the produced struts. They carried out X-ray tomography on struts ranging from 0.58 to 1.8 mm of diameter with a voxel size of approximately $20 \mu m^3$ (see figure 6.3). The internal porosity fraction was quantified as less than 0.1 % for any strut diameter and no clear evolution of the porosity content with the strut diameter was observed.

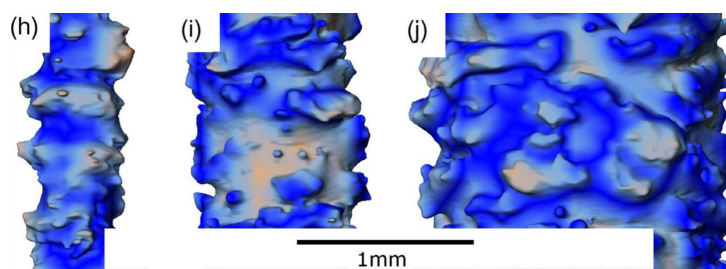


Figure 6.3 3D view of the produced strut from tomographic images. Image from [68].

From figure 6.3, they qualitatively explained that the scale of the surface roughness seems constant whatever the diameter of the strut. Thus the effect of the surface roughness become predominant for small struts. In their study, they suggested to keep a strut diameter larger than 1 mm to control the mechanical properties of the produced lattice.

6.2 Other AM processes

6.2.1 Laser Beam Melting

X-ray tomography is a largely used tool in the characterization of Laser Beam Melting struts.

A study from Van Bael et al. [61] focused on the characterization and improvement of the geometrical and mechanical controllability of porous structures manufactured by LBM. Their methodology involves an optimization loop.

The first loop is the "experimental" run where lattice structures are produced, characterized by X-ray tomography and mechanically tested. From the tomography analysis several features are extracted: strut thickness, lattice density, surface area and structure volume. The initial design is then adjusted according to these results and manufactured in a second step.

Focusing on a particular geometry, they succeeded in reducing the geometrical and mechanical mismatch between the designed and fabricated structures. One major observation is that they could not melt struts with a diameter lower than $200 \mu m$.

This methodology is interesting since it relies on a fully 3D geometrical investigation and allows to reduce the geometrical and mechanical mismatch between designed and produced porous structures. However, their protocol requires a first step of "experimental"

run before the "production" run for each produced design. There is a need for a more general tool that can be applied to any geometry for an AM process.

Other studies deal with the structural characterization of lattice structures produced by LBM. Hasan et al. [95] produced lattice structures made of BCC unit-cells. They characterized the struts using SEM and EDX showing that the struts with a diameter of around $380 \mu\text{m}$ present micro-voids and a dendritic microstructure due to contamination.

Yan et al. [96] evaluated the manufacturability of lattice structures by LBM. The lattice structures are composed of gyroid unit-cells. X-ray tomography characterization revealed that the lattice structures were manufacture without defects.

6.2.2 Direct Metal Deposition

Recently, Park et al. [97,98] worked on the way of taking into account the versatility of the deposition of the DMD process into the mechanical properties of lattice structures manufactured by such technology.

From the DMD process, they assumed a random distribution of the deposited radius (r in figure 6.4) centered on the desired value. They used a normal distribution based on already known fluctuations. A strut is then constructed by piling melted layers. An effective radius is extracted from the strut (r'). For a designed strut diameter of 1.5 mm, the effective strut diameter is calculated between 1.36 mm and 1.42 mm depending on the normal distribution parameters and the angle of fabrication.

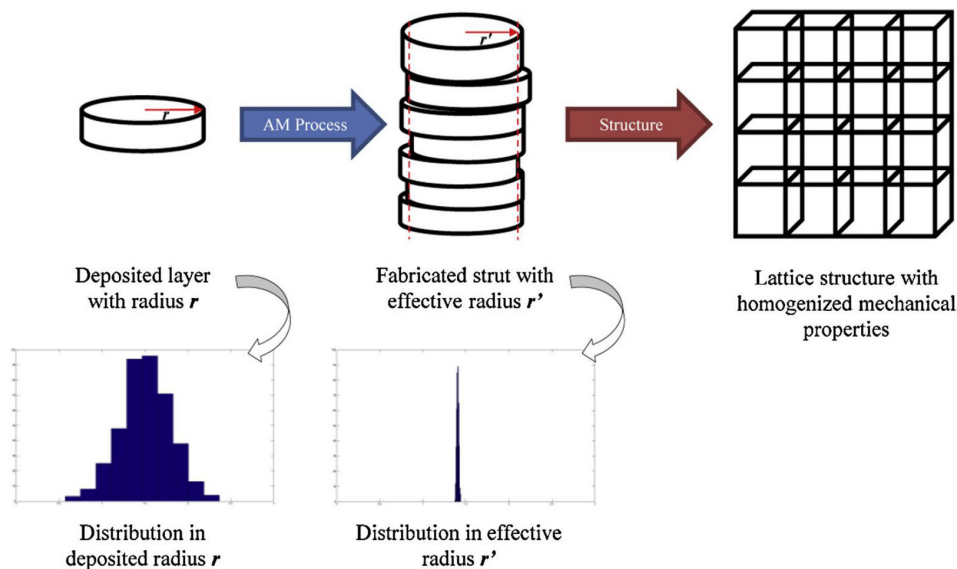


Figure 6.4 Overall methodology of effective radius from a distribution of deposited radius . Image from [98].

Then this effective radius is implemented into numerical simulation and compared with experimental values. The statistical parameters of the distribution are then tuned to obtain good agreement with the experimental data.

Their study is interesting since it allows the prediction of the mechanical properties of the produced structures. Their methodology was however based on a deposition variability but do not rely on 3D characterizations on produced struts.

Conclusion

Little amount of studies on the geometrical and mechanical characterization of produced struts are available in the literature. For the EBM process, some studies reached the conclusion that it would be challenging to fully characterize the internal and external geometry of struts. This is the aim of the following chapters.

Chapter 7

Structural and mechanical characterization of single struts

Contents

6.1	Electron Beam Melting	106
6.2	Other AM processes	107
6.2.1	Laser Beam Melting	107
6.2.2	Direct Metal Deposition	108

The structural and mechanical characterization of single struts is the main attention of this PhD thesis. As previously mentioned, the difference between the expected and produced struts is larger when producing struts in the range of the spatial resolution of the process. For the Electron Beam Melting process, we choose to expose the methodology that follows on 1 mm diameter struts. In a following chapter, the same methodology will be generalized on struts with different diameters.

In a first section, the methodology and tools used will be exposed. Then, struts with a 1 mm diameter and different orientations will be characterized. The last section aims at defining geometrical tools that link the geometrical features and the mechanical properties of such struts.

7.1 Materials and methods

7.1.1 Fabrication of 1 mm struts

Single struts with a circular cross-section having a 1 mm diameter and a height of 15 mm were manufactured by the Electron Beam Melting process. The figure 7.1 shows the manufactured struts.

In order to investigate the variation of the geometry with the build direction, struts with different orientations (α) have been elaborated. Horizontal struts have a build orientation $\alpha = 0^\circ$ whereas vertical struts exhibit $\alpha = 90^\circ$. This study focuses on three orientations: vertical ($\alpha = 90^\circ$), oblique ($\alpha = 45^\circ$) and horizontal ($\alpha = 0^\circ$) struts. No support were used to create the struts for any orientation.

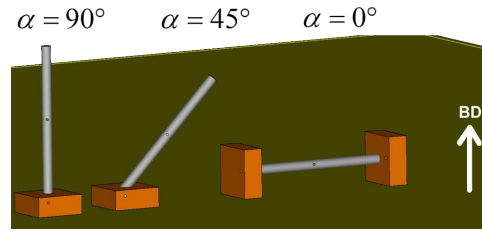


Figure 7.1 Scheme of the designed struts before manufacturing by EBM. The build direction is represented by the white arrow.

As mentioned earlier, the process parameters and strategies are gathered into "themes". Basic themes are given by the supplier (Arcam ®). The standard theme for bulk part is the "Melt" theme. However, for very thin struts they recommend using the "Net" theme. In this part, 1 mm struts are manufactured using the "Net" set of process parameters and strategies.

The strategy for manufacturing vertical struts with a 1 mm diameter can be explained using the scheme of figure 7.2. It represents the melting path of the electron beam at a

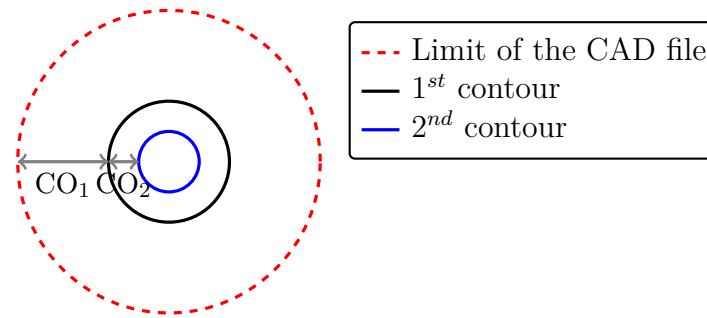


Figure 7.2 Scheme of the melting path at a given height for a 1 mm circular vertical strut when using the "Net" theme.

given height for a vertical strut with a 1 mm diameter.

The limit of the CAD file is represented by the dashed red line. The electron beam scans a first path (1st contour in black) with special process parameters and a second one (2nd contour in blue) with other process parameters. The first contour offset (CO₁) is the distance between the CAD limit and the first contour. It is set to 0.3 mm. The second contour offset (CO₂) is set to 0.1 mm.

The values of the beam speed and current are reported in table 7.1.

	1 st contour	2 nd contour
Offset [mm]	0.3	0.1
Speed [mm/s]	470	470
Current [mA]	2.4	2
	Global	
Volume Energy [J/m^3] (14.1)	$2.1 \cdot 10^{10}$	

Table 7.1 Values of the process parameters for the "Net" theme when melting vertical struts with a 1 mm diameter.

Both contours have the same speed but their current is slightly different. The outer

contour exhibits a larger current to be able to melt until the limit of the CAD file. The volume energy is calculated using the equation (14.1).

For horizontal and oblique struts with a 1 mm diameter, the same parameters were used.

7.1.2 X-Ray Tomography

The struts were characterized by X-ray tomography to investigate their inner volume and their outer surface.

The working principle of the X-ray tomography is shown in figure 7.3. A sample (here a grey cylinder) is placed on a rotating platen. A diverging beam of X-ray goes through the sample until it reaches the CCD camera. A radiograph is taken at each rotation of the sample. The radiograph is a grayscale image that represents the absorption of the sample.

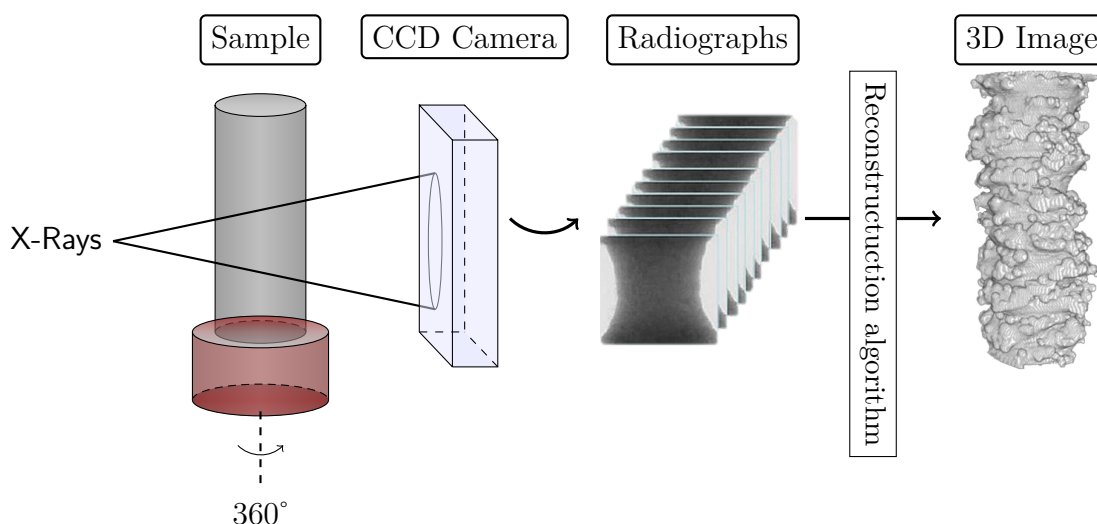


Figure 7.3 Scheme of the principle of the X-ray tomography.

From the greyscale radiographs at each rotation (several hundreds commonly), a 3D image is computed using a reconstruction algorithm. This 3D image is the image used for image analysis.¹

In this study, the voxel size is $(2.5 \mu m)^3$. The tomography conditions are as follows: a voltage of 80 kV and 600 projections. To reduce the noise, at each rotation, the radiographic image was taken as an average of three images. The height of visualization with such a resolution is about 2 mm.

Strut visualization

The visualization of the 3D image was carried out using the open-source software Paraview.

In the following, the produced struts will systematically be depicted in green whereas the designed ones in blue. The internal pores will be shown in red.

¹X-ray tomography has been mainly carried out at INSA-Lyon, in the laboratory MATEIS, under the responsibility of Jérôme Adrien. The machine used for tomography is a v|tome|x from GE Sensing & Inspection Technologies Phoenix X|ray. The X-ray tube allows a voltage up to 160 kV. The detector is a Varian Paxscan with a matrix of 1920 x 1536 pixels.

7.1.3 Image Analysis

The 3D images coming from the tomography have plenty of information that needs to be extracted by image analysis. The image analysis was carried out using the software ImageJ. In-house plugins and macros were used to compute several features on the image.

Porosity measurement

To investigate the porosity, the volume of solid and pores has to be quantified. To do so, a plugin developed by P. Lhuissier, L. Salvo and V. Boulos [99] was used. It allows a labeling of objects connected in 3D. From this labeled image, it can calculate several 3D parameters such as the coordinates of the center of gravity, the volume of the objects, their surface, their sphericity, their moment of inertia ...

Using this methodology, the volume of the dense part (V_{dense}) and the volume of the pores (V_{pores}) can be extracted. The porosity level is defined as:

$$Po = \frac{V_{pores}}{V_{dense} + V_{pores}} \quad (7.1)$$

Moreover, information on each pore is available. From this information, one can discriminate the amount of spherical and non-spherical pores, the size distribution...

Roughness measurement

The surface roughness has been quantified using 3D images of the struts. The contour of the strut has been extracted following the methodology of figure 7.4. The 3D image is rotated every 10° along its longitudinal axis. For each rotation, the plane corresponding to the center of the strut is extracted. From this 2D cut, the coordinates of the upper contour are extracted.

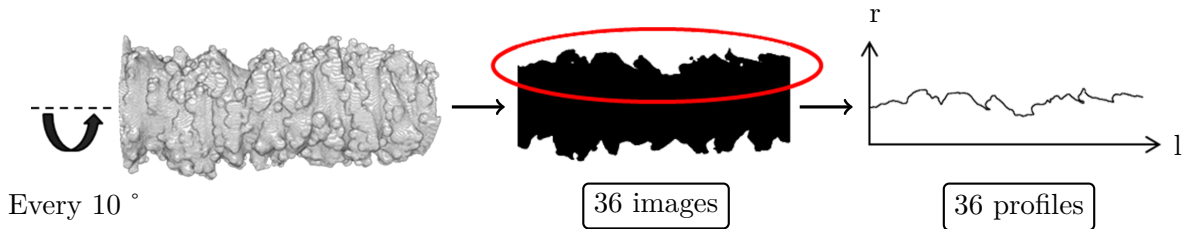


Figure 7.4 Principle of working of the ImageJ macro for extracting the contours of a strut.

A first step allows to shift the profiles in r so that their mean value is zero. The arithmetic roughness (R_a) and the maximum roughness height (R_t) are calculated using the equations that follows:

$$R_a = \frac{1}{L} \int_0^L |r(l)| dl \quad (7.2)$$

$$R_t = r_{max} - r_{min} \quad (7.3)$$

The values of roughness are calculated for each profile. It allows to distinguish a difference in roughness between different sides of the strut. No high-pass and low-pass filters are applied to the profile in order to cut off the short and long order wave profile

part. Moreover, the length of analysis for our study is about 3 mm. However, the EN ISO 4288:1998 standard require a minimal length of 8 mm.

That's why the arithmetic roughness calculated with this method does not corresponds to the arithmetic roughness commonly defined.

Such differences cannot allow the comparison of roughness values with other measurement methods but permits the comparison of struts analyzed with this particular method.

7.2 Structural characterization of struts

3D geometrical characterization at the scale of a strut provides interesting insights to understand the mechanical behavior of lattice structures produced by EBM.

7.2.1 General Appearance

The general shape of a vertical 1 mm diameter strut produced by EBM is shown in figure 7.5. A large surface irregularity is observed in the SEM micrograph of figure 7.5a.

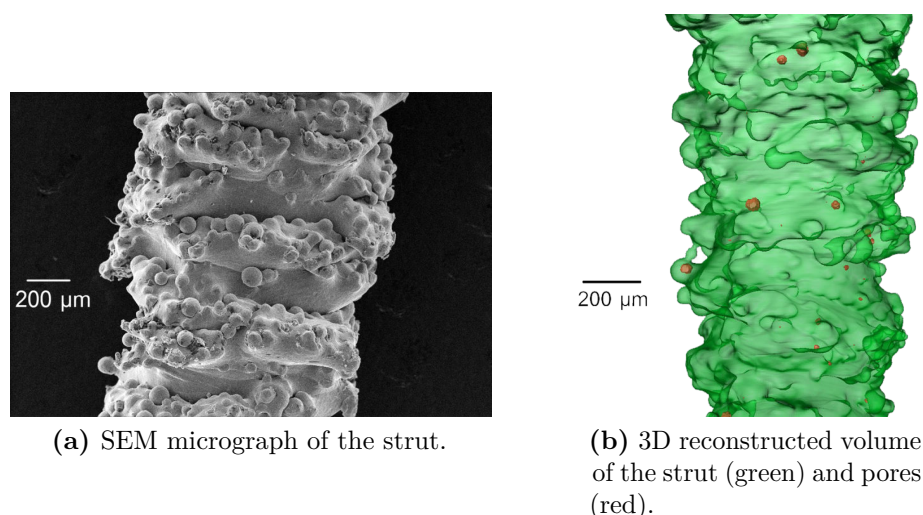


Figure 7.5 Morphology and porosity of vertical 1 mm strut.

Non-melted initial powders are stuck on the surface of the strut. A "plate-pile" like stacking structure is also observed on the surface of the strut.

7.2.2 Porosity

Figure 7.5b shows a reconstructed volume of a 1mm-diameter vertical strut (green) containing few pores (red). The size and morphology of the pores throughout the struts are quantified.

The porosity level within the struts remains really low ($<0.1\%$) for any strut orientation as mentioned in table 7.2. It fluctuates between 0.02 and 0.05 %.

From the volume (V) and the surface (S) of each pore, a sphericity parameter has been determined. It gives information on the shape of the pore. It is calculated using this

formula:

$$Sphericity = 6V\sqrt{\frac{\pi}{S}} \quad (7.4)$$

The sphericity parameter is equal to one for a sphere and less for any other shape. The mean values of sphericity are reported in table 7.2. Pores have generally a spherical shape. It is consistent with the observation of figure 7.6.

	Vertical	Oblique	Horizontal
Porosity [%]	0.035	0.039	0.048
Mean pore diameter [μm]	16.4	25.4	24.7
Mean sphericity	0.80	0.81	0.84

Table 7.2 Porosity level, mean pore diameter and mean sphericity of the pores for three orientations of struts with a 1 mm diameter.

Figure 7.6 highlights the distribution of pores within the strut for three strut orientations. No real trend has been observed in the repartition of pores. Indeed, as mentioned in section 4.2.3, the spherical porosity is present in the initial powder and comes from its forming process. Thus, the porosity is distributed randomly within the part.

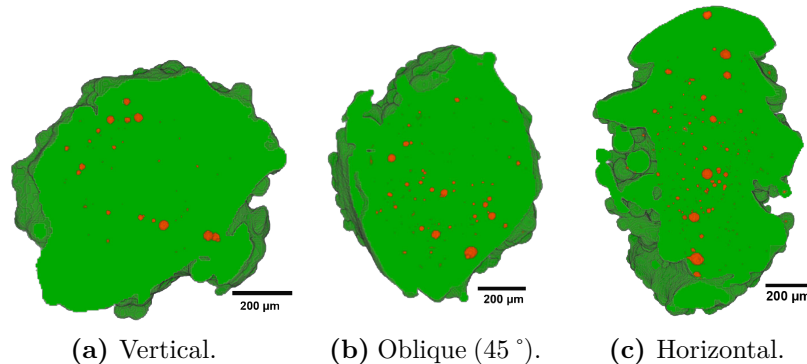


Figure 7.6 Projected visualization of the pore for 1 mm struts with different orientations.

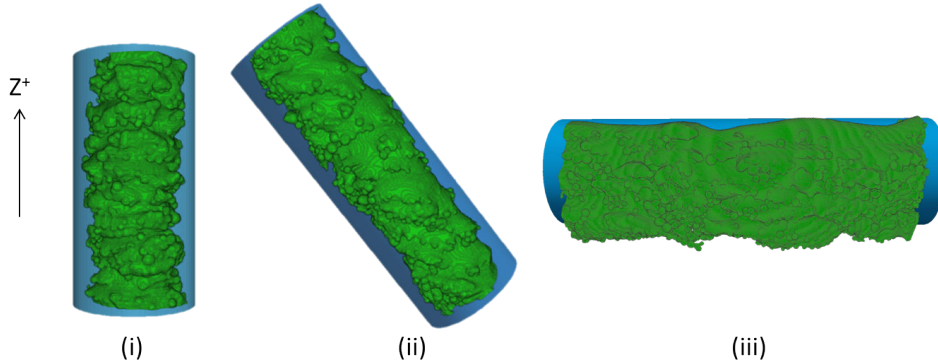
The mean size of the pores is exposed in table 7.2. Because the spherical shape doesn't come from the EBM process, the orientation of the strut has not much influence on the mean pore diameter (around $20 \mu m$). The range of pore diameter is consistent with the values found by Tammis-Williams et al. [18].

The porosity content is lower than 0.1% for struts manufactured by EBM. Therefore the elastic properties of the struts won't be affected by this porosity level. In the following, the struts will be considered as a constitutive material with a Young's modulus of 114 GPa (value determined in chapter 5). On the contrary, such a porosity content could be of crucial importance if fatigue properties are considered.

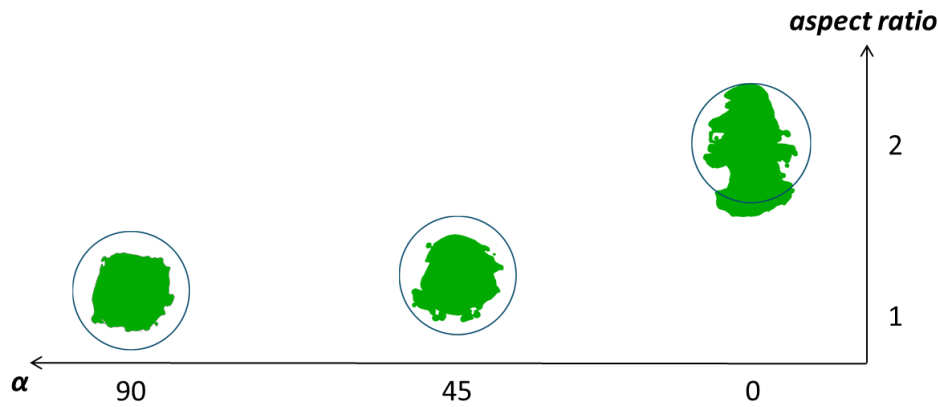
7.2.3 Shape and size

Figure 7.7a highlights the geometrical discrepancies between the designed geometry (blue) and the manufactured one (green). The produced struts are systematically thinner than

the CAD geometry, in particular for vertical and oblique struts. As a consequence, the fabricated volume (V_{FAB}) is smaller than the designed one (V_{CAD}). Thus, for a lattice structure, the manufactured density ($\bar{\rho}_{FAB}$) is lower than the designed one ($\bar{\rho}_{CAD}$).



(a) Difference between designed and produced strut.



(b) Aspect ratio of the cross-section of strut.

Figure 7.7 Geometry variation with orientation for struts with a 1 mm diameter (green). Comparison with the designed strut (blue) for three orientations: vertical (i), oblique (ii) and horizontal (iii). The build direction is indicated by the black arrow.

Figure 7.7b shows the variation of the cross-section shape of the struts as a function of their orientation. The shape varies widely with respect to the strut angle. For vertical and oblique struts, the cross-section is rather equiaxed whereas for horizontally built struts, the cross-section is clearly elongated along the build direction.

These shape differences with respect to the build orientation can be discussed using thermal considerations. Figure 7.8 shows a schematic view of the EBM fabrication of three struts with specific orientations: $\alpha = 90^\circ$, 45° and 0° . The electron beam is represented in red, the resulting melt pool is shown in a yellow-to-red color and the red arrows illustrate the thermal flux. Struts are surrounded by sintered powder.

The thermal conductivity of the sintered powder is lower than the thermal conductivity of the bulk. As a result, the heat flux is more likely to go through the melted part. The start plate (bottom plate) is considered as a heat sink.

For vertical and oblique struts, as the thermal flux is well dissipated through the strut, the equiaxial shape of the cross-section is rather well respected (Figure 7.7b). For horizontal struts, the thermal flux is accumulated on the down-facing side. As a

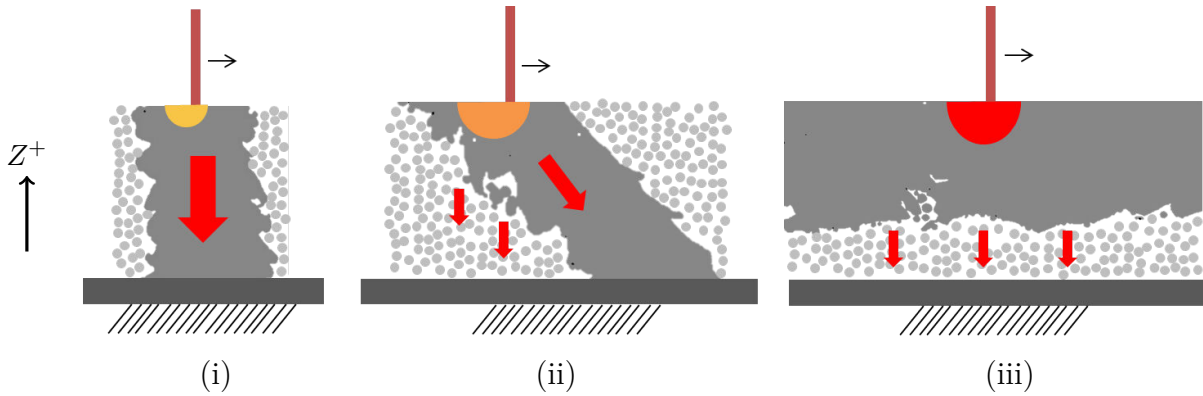


Figure 7.8 Schematic view of the thermal behavior during EBM process for different orientations: (i) vertical, (ii) oblique and (iii) horizontal. Red arrows indicate the thermal flux density and direction.

result, over-melting takes place and the section becomes distorted along the build direction.

- The difference in size between the designed and manufactured strut produces a difference of density between the designed lattice structure and the designed one. **This results in a difference of stiffness between the designed structure and the produced one.**
- Horizontal struts have a different bending response compared to the vertical ones since their cross-section is elongated. In this study, because of the lattice structure considered (octet-truss), only uniaxial loadings are treated. As a result, the shape of the cross-section is not considered as a relevant parameter. The cross-section area remains the most important parameter for tensile loading of the struts which is considered for the present study.

7.2.4 Surface irregularities

The thermal history during the EBM process not only influences the strut's shape but also its surface irregularity. The over-melting zones of the struts exhibit a high roughness whereas the top-facing zone of the struts exhibits a rather low roughness.

The surface irregularities are qualitatively analyzed from the 3D images. As explained in figure 7.8, the roughness depends on the build orientation. For a vertical strut, (Figure 7.7a), the roughness is similar all around the circumference of the strut. However, for oblique and horizontal struts (green in (b) and (c)), a significant difference in terms of roughness was observed between the top-facing side and the down-facing one.

The roughness can be observed at two scales. Firstly, the "plate-pile" like stacking irregularity is caused by the versatility of the beam to melt the required surface at each layer. At a finer scale, figure 7.5a shows spherical powder particles that increase the roughness. These powder particles are stuck to the melt pool but are not fully melted.

The roughness was quantitatively analyzed for a 1 mm diameter strut with various build orientations (figure 7.9). Graphs display the arithmetic roughness (R_a) and the maximum height (R_t) for 36 profiles taken from the circumference of the strut, as explained in 7.1.3.

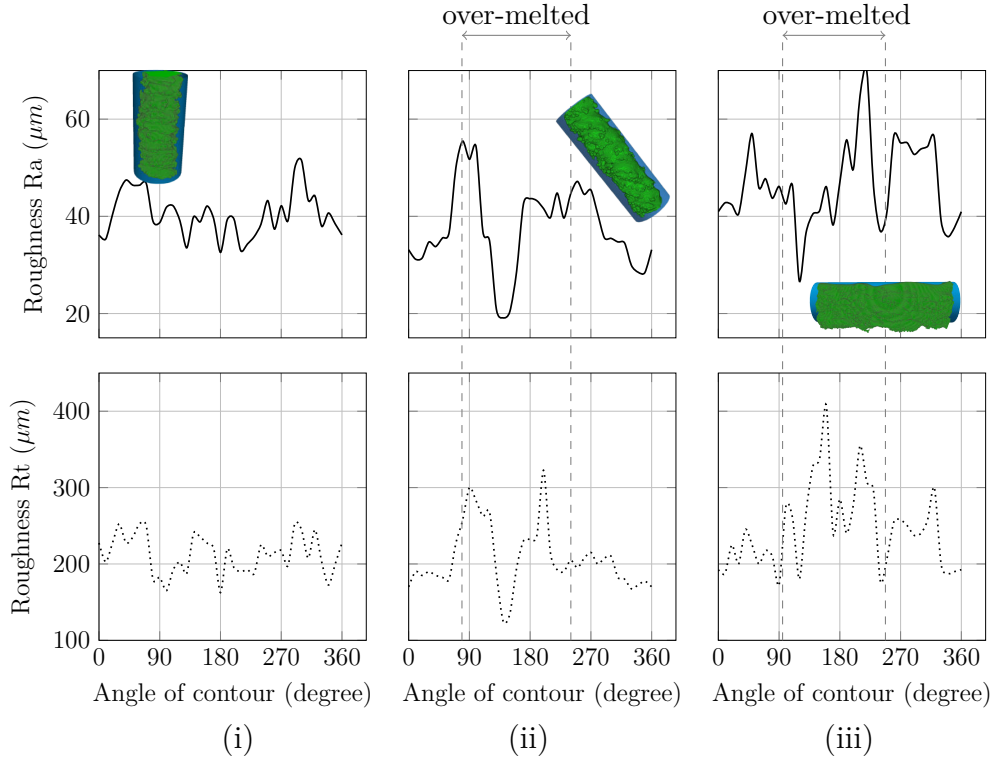


Figure 7.9 Arithmetic and maximum roughness calculated from the 3D images of single struts with a 1 mm diameter. Three orientations: vertical (i), oblique (ii) and horizontal (iii).

The data presented in figure 7.9 allow to compare the surface irregularities of struts depending on their orientation. As explained in section 7.1.3, the length of roughness measurement is shorter than the one recommended by the standard. Thus, the given values are indicative but allow to discriminate the different configurations.

For a vertical sample (figure 7.9 (i)), the roughness (Ra or Rt) does not fluctuate significantly along the circumference of the strut. On the contrary, for oblique and horizontal struts, the roughness fluctuates significantly for angles around 90° to 250° . This corresponds to the over-melted zone where more particles are stuck to the melting pool.

The arithmetic roughness (Ra) for the vertical sample exhibits an average value of about $40 \mu\text{m}$ with a standard deviation of $5 \mu\text{m}$. The arithmetic roughness of the horizontal strut presents a similar average value of $46 \mu\text{m}$ with a standard deviation of $10 \mu\text{m}$.

The mean value of the maximum height of the profile for a vertical strut (Rt) is $212 \mu\text{m}$ with a standard deviation of $26 \mu\text{m}$. For a horizontal sample (figure 7.9 (iii)), the mean value is $247 \mu\text{m}$ with a standard deviation of $55 \mu\text{m}$.

Thus, there is an increase of the surface irregularities when producing struts with a low angle ($<90^\circ$).

Summary:

→ The difference between the nominal volume (V_{CAD}) and the fabricated one (V_{FAB}) has been highlighted in figure 7.7a. This geometry discrepancy is important regarding the design of cellular structures. It will widely impact the desired mechanical properties of the lattice structure, especially the elastic ones.

→ Moreover, due to the highlighted irregularities, a significant part of the strut does not transmit loads efficiently. A concept is needed to discriminate the "mechanically efficient matter" and the "mechanically inefficient matter".

Two approaches are suggested in the next section to define a parameter that will help to take into account the "true" elastic response of single strut.

7.3 Concepts to link geometrical features and mechanical prediction

In this section two approaches are proposed to predict the effective stiffness of struts produced by EBM. Both concepts aimed at replacing the produced strut by a circular cylinder having the same stiffness. The first approach is based only on geometrical considerations and the second one results from a numerical simulation at the scale of the strut.

Thus, the shape of the cross-section is not considered even if it fluctuates largely. It is supposed to be valid for stretching-dominated structures. However, for the prediction of bending-dominated structures, the concepts should be refined to take into account the moment of inertia of the cross-section.

7.3.1 Geometrical equivalent diameter D_{EQ}^{GEOM}

The first approach is purely geometrical and is based on the inscribed cylinder of a produced strut.

Inscribed cylinder assessment

Figure 7.10 summarizes the different steps to evaluate the diameter of the inscribed cylinder (D_{EQ}^{GEOM}).

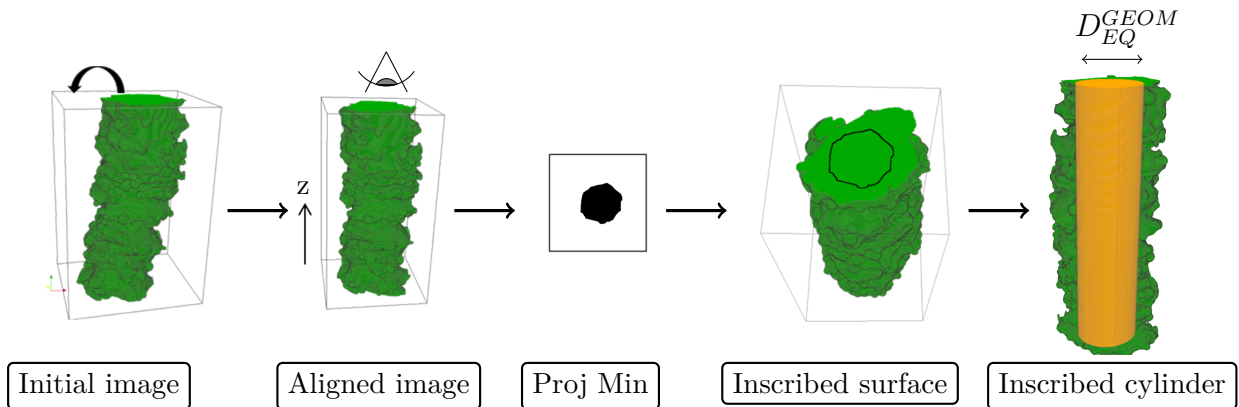


Figure 7.10 Summary of the steps to find the inscribed and circumscribed diameters.

The methodology to assess the inscribed cylinder is as follows:

Alignment of the strut with the z-axis of the image During tomography, the strut can be misaligned with the z-direction of the image. A procedure has been developed to tilt the image and find the optimal position.

Projection of the minimum surface The tilted image has now its neutral fiber aligned with the z-axis of the image.

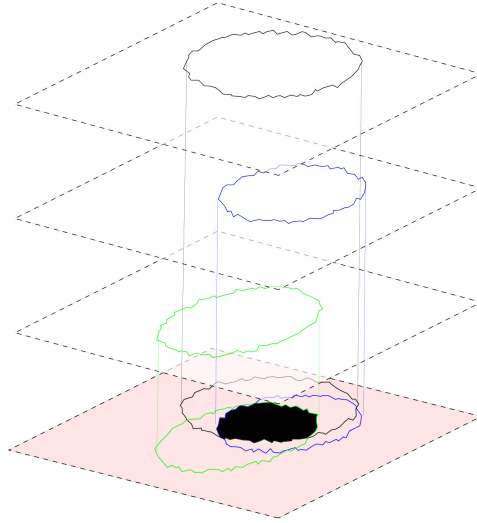


Figure 7.11 Stacks projections for the inscribed surface evaluation.

Figure 7.11 depicts the method to evaluate the inscribed surface. Every stack is projected onto a perpendicular plane (red in figure 7.11). The inscribed surface (S_{ins}) is defined as the area common to all the projected surfaces (in black).

Inscribed cylinder diameter The inscribed cylinder is defined as the circular cylinder having a section equal to the inscribed surface. Its diameter is then given by:

$$D_{EQ}^{GEOM} = \sqrt{\frac{4S_{ins}}{\pi}} \quad (7.5)$$

The inscribed cylinder is represented in orange in figure 7.10.

The inscribed cylinder will be denoted geometrical equivalent cylinder and its diameter is the geometrical equivalent diameter.

Figure 7.12 illustrates the nominal geometry of a 1 mm diameter strut (in blue) and compares it with the manufactured one (in green). The inscribed cylinder (or geometrical equivalent cylinder) is highlighted in orange. The mechanical elastic response of the strut is assumed to be carried by the inscribed cylinder. This hypothesis can be justified in particular when axial stresses are predominant as in stretching-dominated structures, like the octet-truss one.

7.3.2 Numerical equivalent diameter D_{EQ}^{NUM}

In a refined approach, the mechanical behavior of the struts can be estimated from a numerical calculation performed directly on the voxelized image resulting from X-ray tomography.

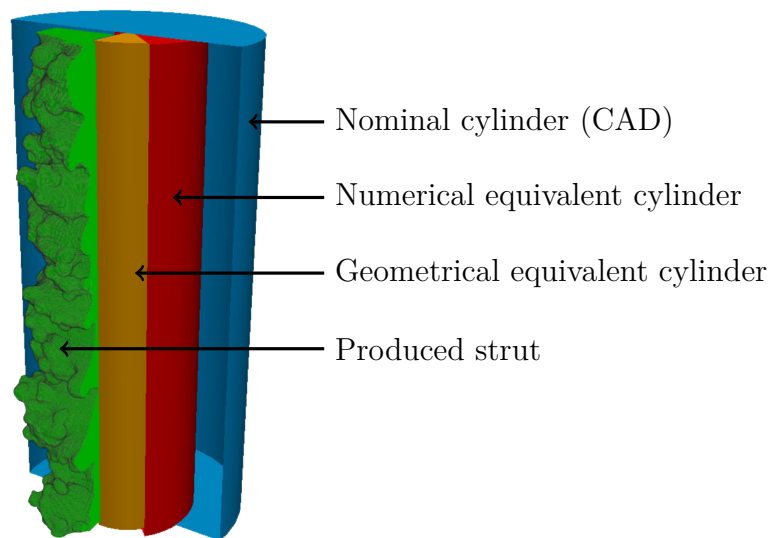


Figure 7.12 Pie chart representation of the developed tools for a 1 mm strut built vertically. Nominal diameter (blue), produced strut (green), numerical equivalent cylinder (red) and geometrical equivalent cylinder (orange).

Fast Fourier Transform (FFT)

The elastic behavior of a strut is determined through a numerical approach relying on a Fast Fourier Transform (FFT) calculation using the software CraFT [100]².

The interest of such a technique comes from the fact that it does not require a meshing step before analysis as for Finite Element calculations. The FFT analysis can be computed directly on voxelized volumes. Meshing such irregular geometries would have been indeed a real challenge.

How does it work? The software is an iterative numerical method based on FFT to investigate the effective properties of heterogeneous materials composed of two phases. The FFT analysis allows a simulation of the homogenized elastic response of such a composite. A more precise explanation of the theoretical and computational method is presented in appendix A.

The input of the software are :

- The 3D image (voxels) of the microstructure.
- A description of each phase of the microstructure. The two phases are dense Ti-6Al-4V and void. The constitutive laws can be chosen between isotropic linear elasticity, elastic perfectly plastic behavior or anisotropic linear elasticity.
- The loading conditions.
- The accuracy for the convergence conditions (see appendix A).

The outputs of the software are the global stress and strain tensors.

²CraFT has been developed in the french laboratory "Laboratoire de Mécanique et d'Acoustique" (LMA) in Marseille.

Methodology We present here the methodology used to prepare the image for the FFT simulation and to extract the numerical equivalent diameter (c.f. figure 7.13).

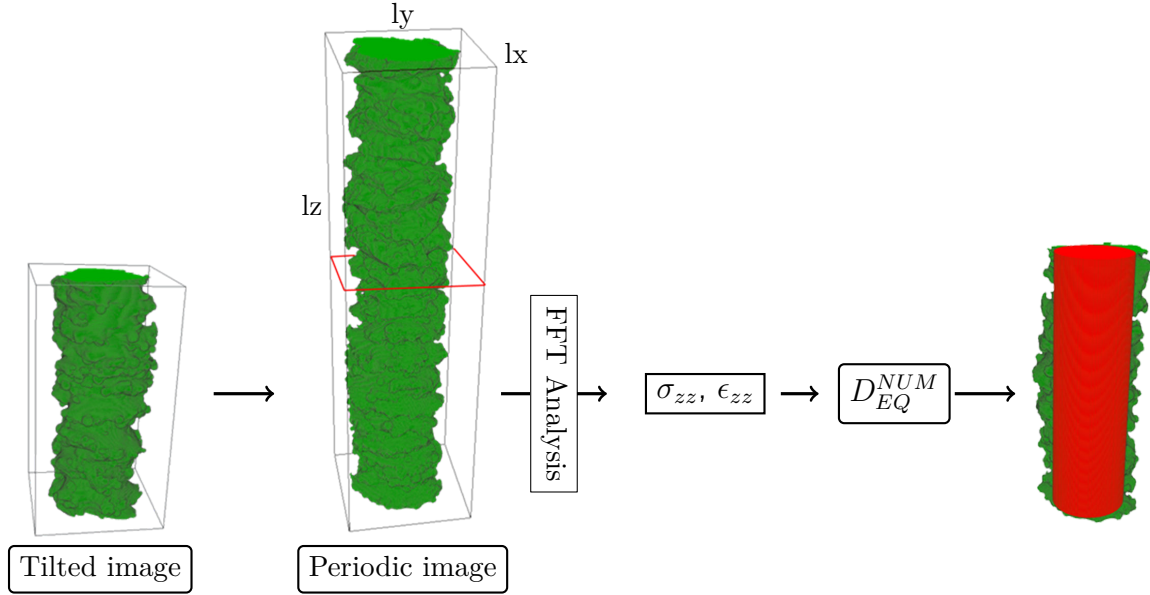


Figure 7.13 Summary of the steps to obtain the numerical equivalent diameter.

Since the FFT software relies on Periodic Boundary Conditions, the tilted image of figure 7.10 is duplicated. The copy is flipped along the z direction and concatenated to the initial image.

The loading conditions are a prescribed load along the z direction. The Ti-6Al-4V is isotropic with a Young's Modulus of 114 GPa and a Poisson ratio of 0.345. The value of the Young's modulus comes from the study of chapter 5 and the value of the Poisson ratio comes from an ASM handbook [101]. The void is represented with a zero Young's modulus and Poisson ratio.

As said earlier, the output of the FFT software are the stress and strain tensors. From the stress and strain along the z direction, the "Young's Modulus of the image" along this direction can be extracted using the Hooke's law :

$$E_z^{image} = \frac{\sigma_{zz}}{\epsilon_{zz}} \quad (7.6)$$

Extraction of the geometrical equivalent diameter: The expression "Young's modulus of the image" is an abusive terminology. It represents the global stiffness of the heterogeneous material composed of Ti-6Al-4V and void contained in the box $[lx \ ly \ lz]$. If the box is full Ti-6Al-4V is will be $E_z^{image} = E^{TA6V} = 114GPa$. We define the numerical equivalent diameter as the diameter of a Ti-6Al-4V cylinder leading to the same value as E_z^{image} (see figure 7.14). So that :

$$\begin{aligned} E^{TA6V} \frac{\pi (D_{EQ}^{NUM})^2}{4} &= E_z^{image} . lx . ly \\ \implies D_{EQ}^{NUM} &= 2 \sqrt{\frac{E_z^{image} . lx . ly}{\pi E^{TA6V}}} \end{aligned} \quad (7.7)$$

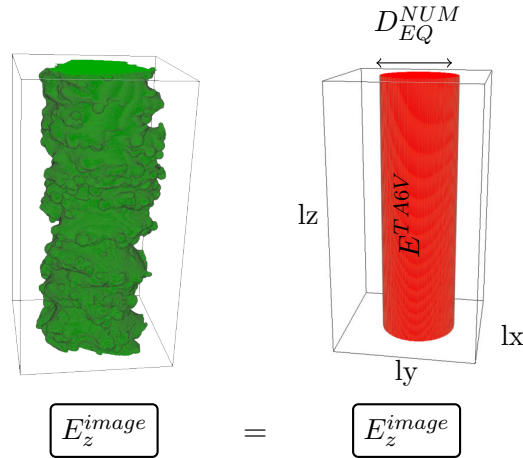


Figure 7.14 Identification of the numerical equivalent diameter D_{EQ}^{NUM} .

The numerical equivalent cylinder is represented in red in figure 7.12.

7.3.3 Representative Volume Element

The height of the image to be analyzed is a major parameter. In order to find the RVE of analysis for the numerical and geometrical equivalent diameters, the variation of these parameters with the height of the image has been plotted in figure 7.15.

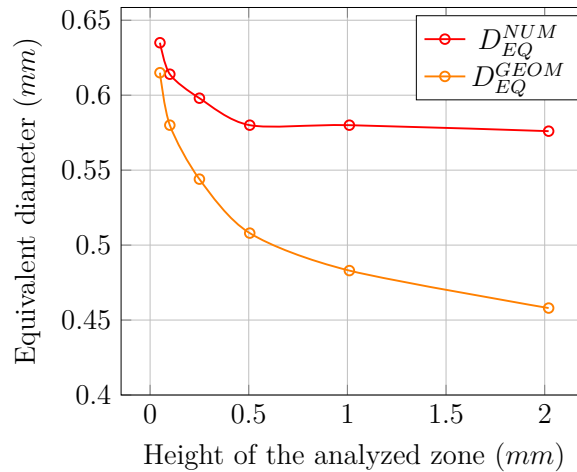


Figure 7.15 Influence of the height of the analyzed image on the final value obtained for the equivalent diameters.

For the FFT simulation, the numerical equivalent diameter is constant when computing the FFT simulation on images from 0.5 to 2 mm of height. The RVE is thus 0.5 mm in height. Since a layer in the EBM process is $50 \mu\text{m}$, a simulation of an image with a height of 0.5 mm means looking at 10 layers. It is statistically enough for the FFT simulation.

However, no plateau was found for the geometrical equivalent diameter. An analysis on a higher image is impossible to keep a resolution of $2.5 \mu\text{m}$ in the x-ray tomography. Thus, the geometrical equivalent diameter will be assessed on struts with a height of 2 mm.

7.3.4 Comparison

The values of geometrical and numerical equivalent diameters are reported in table 7.3 as a function of the strut's orientation. They are compared with the nominal diameter. Both equivalent diameters are significantly thinner than the nominal one.

Moreover, the geometrical equivalent diameter ($D_{EQ}^{GEO M}$) is thinner than the numerical one (D_{EQ}^{NUM}). It is consistent with the underlying hypothesis for the geometrical equivalent diameter (only axial stresses considered).

The numerical equivalent diameter (D_{EQ}^{NUM}) is similar for vertical and oblique struts but larger for horizontal one. As mentioned in section 7.2.3, for a horizontal strut, the cross-section is elongated along the build direction and the surface is larger due to an over-melting of the overhanging side. This results in a larger "mechanically efficient" volume and thus a larger numerical equivalent diameter.

α	90°	45°	0°
$D_{CAD}(mm)$	1	1	1
D_{EQ}^{NUM} (mm)	0.58	0.58	0.70
$D_{EQ}^{GEO M}$ (mm)	0.46	0.42	0.52

Table 7.3 Values of geometrical and numerical equivalent diameters for different strut's orientations.

The variation of the inscribed diameter ($D_{EQ}^{GEO M}$) with the strut's orientation is a bit surprising. As mentioned earlier, this diameter results from an intersection of projections throughout the strut. By doing so, the volume located within the surface irregularities are not taken into account. As shown in figure 7.9 a strut oriented at 45° presents a larger variation of roughness than a vertical one. However, as depicted in figure 7.7b, their cross-section is similar. It is the reason why the geometrical equivalent diameter is smaller for an oblique strut than for a vertical one. For the same reasons as for the numerical equivalent diameter, a horizontal strut exhibits a larger geometrical equivalent diameter than for other orientations.

7.3.5 Summary

Figure 7.16 sums up the methodology developed in this chapter.

A designed strut (blue) with a diameter D_{CAD} is produced by the EBM process. The produced strut (green) is smaller and presents roughness. Its mechanical response is approximated using geometrical or numerical tools. The geometrical equivalent diameter is represented in orange with its diameter $D_{EQ}^{GEO M}$. It is the larger cylinder inscribed in the strut. The FFT analysis on the strut provides a numerical equivalent diameter (in red) with a diameter D_{EQ}^{NUM} .

The next chapter aims at taking these equivalent diameters in the simulation of the stiffness of lattice structures produced by EBM

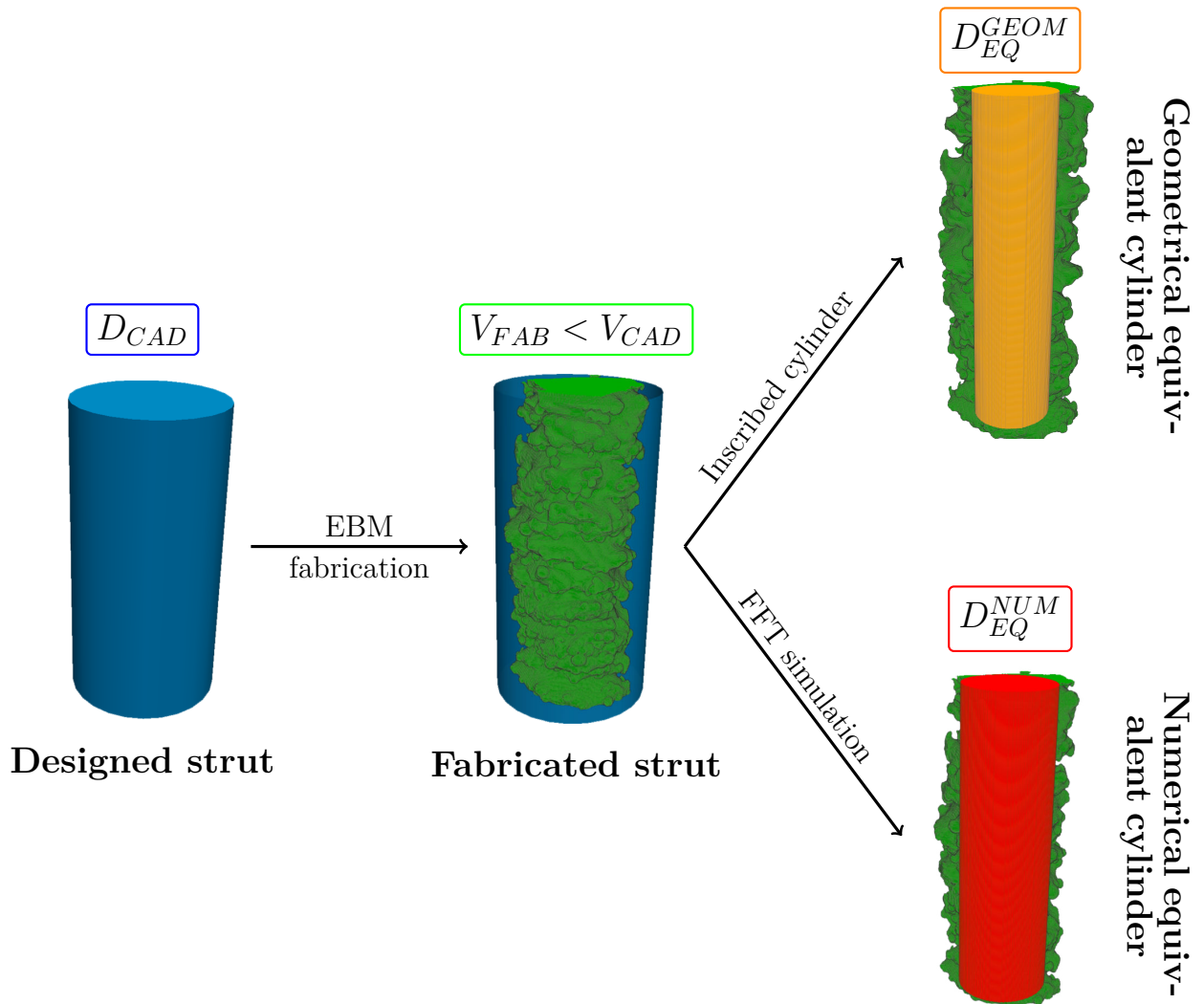


Figure 7.16 Summary scheme of the methodology of to extract the geometrical and numerical equivalent diameter.

Chapter 8

Prediction of the elastic properties of the Octet-truss structure manufactured by EBM

Contents

7.1	Materials and methods	111
7.1.1	Fabrication of 1 mm struts	111
7.1.2	X-Ray Tomography	113
	Strut visualization	113
7.1.3	Image Analysis	114
	Porosity measurement	114
	Roughness measurement	114
7.2	Structural characterization of struts	115
7.2.1	General Appearance	115
7.2.2	Porosity	115
7.2.3	Shape and size	116
7.2.4	Surface irregularities	118
7.3	Concepts to link geometrical features and mechanical prediction . . .	120
7.3.1	Geometrical equivalent diameter D_{EQ}^{GEOM}	120
	Inscribed cylinder assessment	120
7.3.2	Numerical equivalent diameter D_{EQ}^{NUM}	121
	Fast Fourier Transform (FFT)	122
7.3.3	Representative Volume Element	124
7.3.4	Comparison	125
7.3.5	Summary	125

8.1 The Octet-truss lattice

8.1.1 Generalities

The structure of interest is the octet-truss lattice [42, 102]. It consists of 36 struts forming 8 tetrahedral cells (in blue) around a central octahedral one (red) as shown in figure 8.1.

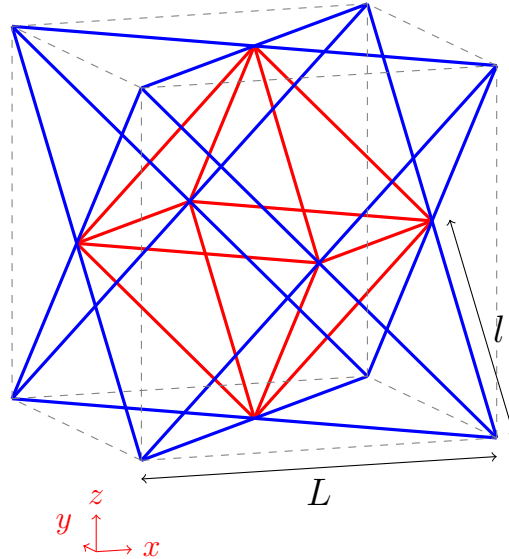


Figure 8.1 Octet-truss unit cell composed of 36 struts. The dashed lines represent the bounding box.

Following Maxwell's criterion, it has been shown that its mechanical behavior is governed by stretching of the struts [7]. Such a stretching-dominated structure is expected to be stiffer than a bending dominated one, for a same relative density since their variation of Young's modulus is linear with their relative density (see section 1.2.1). The octet-truss lattice is commonly used as an example of a stiff and light structure.

Considering only the central octahedral cell with struts having high aspect ratios and deformed by stretching, Desphande et al. [42] suggested a prediction of its stiffness. However, their model is only valid for large strut aspect ratio.

In the following, a Finite Element approach is carried out to predict the effective stiffness of such a structure.

8.1.2 Manufacturing by the EBM technology

Figure 8.2 shows the designed octet-truss structures that were manufactured and tested under uniaxial compression.

All the four samples are composed of struts with a 1mm diameter. They have been manufactured using the same set of parameters as for the single struts analysis 7.1.1 ("Net" theme). The length of the struts (l) is adjusted to reach four different densities (between 11 and 25 %).

The global structure is composed of five unit-cells per side. The problem of representativity of such an assembly arises. Due to the spatial limitations of the build envelope (210x210x180 mm) within the EBM machine, a structure with more unit-cells could not be

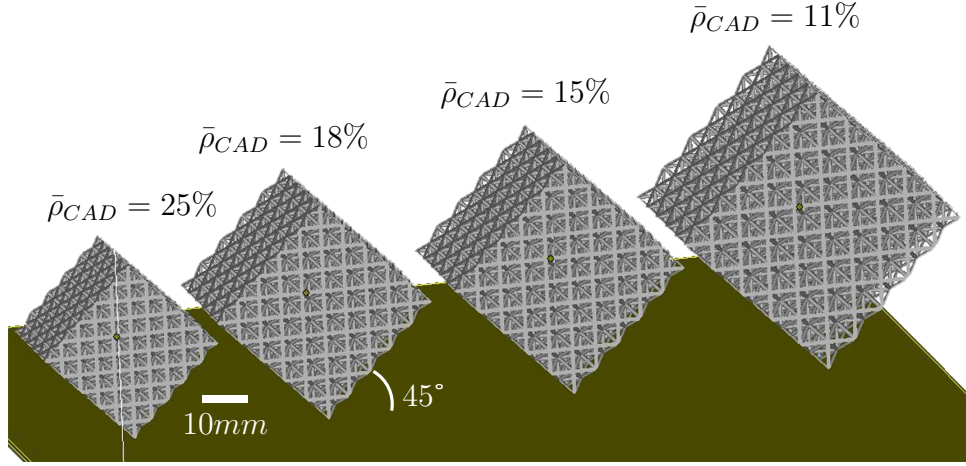


Figure 8.2 Designed octet truss with 4 different densities.

manufactured for this range of densities. An analysis of the minimal number of unit-cells is presented in a following paragraph (8.1.3).

The EBM process brings limitations in terms of reachable density. As said in the previous paragraph, the struts diameters are set to 1 mm and the length of the struts are modified to change the density. This limits the minimal density that can be reached for a structure with five unit cells per side. On the other side, high density octet-truss cannot be produced by EBM since they prevent sintered powder to be removed from the structures. That's why we focused on the range [10% 25%], sufficiently interesting in terms of weight saving.

In figure 8.2, the nominal density was denoted ($\bar{\rho}_{CAD}$). It is the density calculated on the designed structure. The length of the struts vary from 4.5 mm to 7.1 mm (see table 8.1).

$\bar{\rho}_{CAD}$ [%]	25	18	15	11
l [mm]	4.5	5.5	5.9	7.1

Table 8.1 Geometry of the designed octet-truss structures.

For each density, two samples were fabricated to investigate the reproducibility of the process and consistency of the measurement methods except for the octet-truss structure with a density of 25% for which four samples were manufactured. Samples were manufactured at 45° with respect to the horizontal start plate. This is done to simplify its removal from the start plate. For this configuration, the struts of the structure have three different strut angles ($\alpha=0^\circ$, 45° and 90°). In this case, the unit-cell of the structure is composed of six vertical and six horizontal struts along with 24 struts oriented at 45° (oblique).

The relative density was assessed after the manufacturing of the octet-truss structures by measuring the size and mass of the lattice. The fabricated density ($\bar{\rho}_{FAB}$) was compared to the designed one ($\bar{\rho}_{CAD}$). As mentioned in 7.2.3, there is a large difference in size between the produced struts and the designed ones (Figure 7.7a). This difference in size results in a difference in density which was calculated as:

$$\bar{\rho}_{FAB} = 0.63 \bar{\rho}_{CAD} \quad (8.1)$$

In this chapter when comparing simulation with experimental data, the relative density used will be the fabricated one: $\bar{\rho}_{FAB}$.

8.1.3 RVE analysis

The number of unit-cells in a lattice structure is of major importance. A lattice structure with low amount of unit-cell will be subjected to boundary effects and the measured mechanical properties will be affected.

A simulation of the uniaxial compression of such octet-truss using Mixed Boundary Conditions (MBC) has been carried out. A uniaxial displacement is imposed on the horizontal faces whereas vertical faces are imposed free of load. These boundary conditions are representative of the experimental conditions for uniaxial compression of lattice structures. The results are shown in figure 8.3.

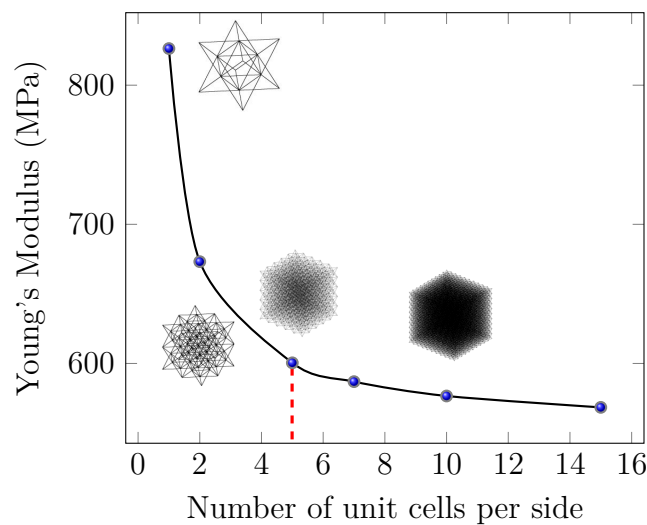


Figure 8.3 RVE analysis for determining the minimal number of unit-cells having the same Young's modulus of an infinite repetition of octet-truss.

The Young's modulus is overestimated for structures composed of a low number of unit-cells per side. It stabilizes when increasing the number of unit cells.

The value of five unit cells per side chosen for the produced octet-truss structures can be validated using these results since it limits the size effect.

8.2 Compression Test

8.2.1 Testing configuration

The compression testing has been carried out on the same machine as the tensile testing of previous part. It is a MTS 810 testing machine with a 100 kN load sensor. However some modifications have been developed to adapt this machine for compression testing of lattice structures.

The compression of lattice structures has to be carried out carefully. Indeed, some challenges are inherent with such measurement:

- Avoiding indentation of compression platens by the higher density titanium lattice structures

- Measurement of the true strain of the structure

To overcome these challenges, the following modifications have been developed:

Compression Platens Case-hardened steel alloy compression platens were bought to avoid indentation of the platens by the structure. The platens have a 150 mm diameter. The bottom one is fixed whereas the one from the top is spherical seated to ensure even pressure across the entire surface of the specimen. The compression platens are shown in the figure 8.4.

Extensometer An extensometer was bought to obtain the true strain of the lattice structure and to avoid the errors due to the deformation of the load frame and cross head. The extensometer has a displacement range of 25 mm and a linearity precision lower than 0.1 %.

In order to measure the true displacement, the extensometer has to be fixed to the compression platens. A special support has been developed to allow this fixation. It can be seen in figure 8.4.

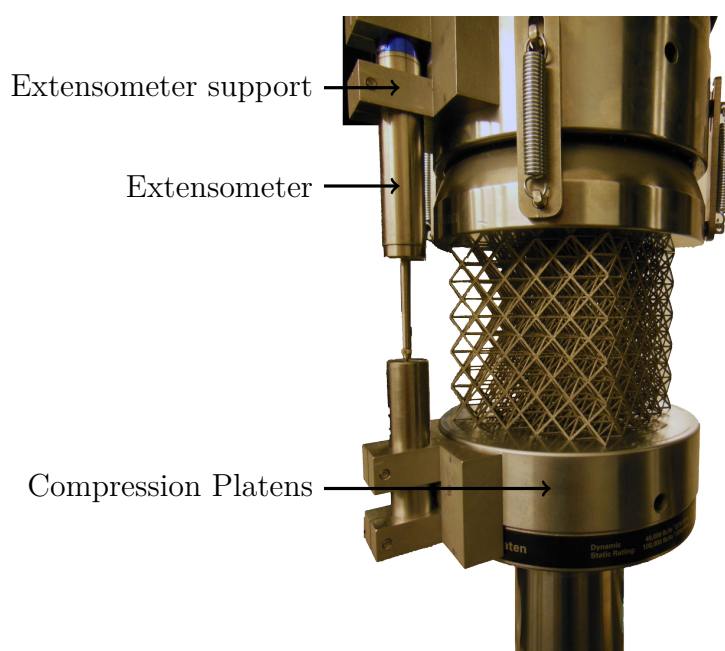


Figure 8.4 Compression device showing the modifications brought to the testing machine. The hardened steel compression platens on which special part have been created and fixed to support the extensometer.

8.2.2 Young's Modulus determination

To be able to calculate the Young's modulus of the structure, a special cycle composed of loadings-unloadings is applied on each lattice structure. It is represented as an example in figure 8.5 (left graph). It consists of loadings and unloadings at the speed of 1 mm/min. At each 0.2% of strain, an unloading occurs until 60 % of the maximal load.

The Young's modulus is calculated at each unloading as the slope of the curve at the early stage of the unloading. The Young's modulus as a function of the strain is plotted

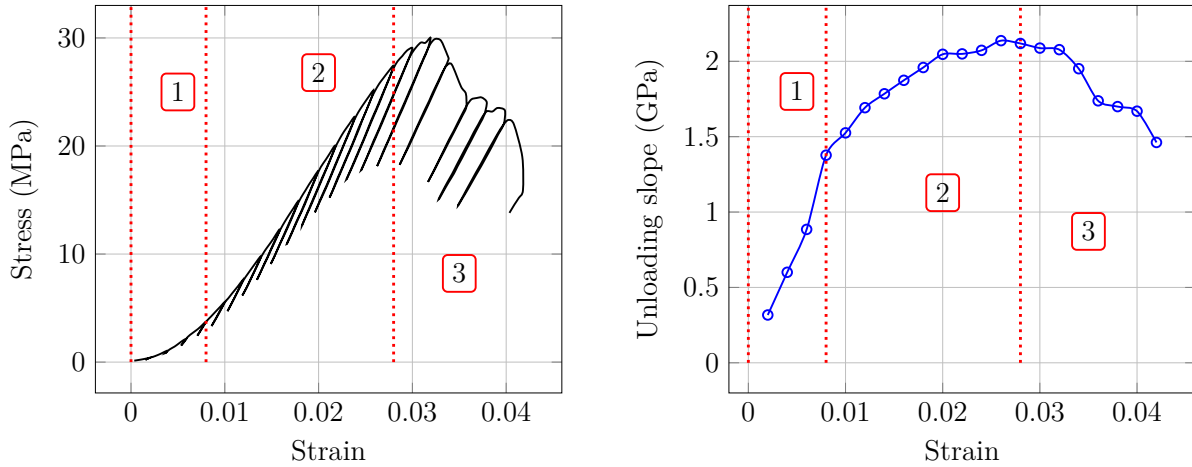


Figure 8.5 Typical stress-strain cycle applied to a lattice structure for determining its Young’s modulus (left). Unloading slopes as a function of the strain (right). Example for an octet truss with a 25% density.

in right graph of figure 8.5. Using both graphs, the compression of such structures can be divided into three stages:

Region 1 The first region corresponds to the positioning of the sample between the platens. If the opposite sides of the sample are not fully parallel and because roughness is present on the top and bottom surfaces, the first measurement of the force is not fully related to the elastic regime of the structure. The measured force is lower than the expected one. There is a rapid increase of the slope at unloading.

Region 2 After the first stage, the structure deforms in an elastic manner until the first strut becomes plastically loaded. The slope at unloading still increases in this region until it reaches a plateau. It means that at the early stages of elasticity, some struts are not fully loaded and do not act in the stiffness of the structure. In the plateau, the structure acts fully elastically.

Region 3 After a given strain, the first local damage occurs. It decreases the calculated unloading slope. The global structure reacts plastically.

We chose the Young’s modulus of the structure as the maximum of the calculated unloading slopes. It corresponds to the value of the fully elastic plateau. In some structures, the elastic plateau doesn’t exist. Indeed, the structure is not fully elastically loaded when the first local plastic deformation occurs. Thus, the Young’s modulus is taken as the maximum value. The results of stiffness on lattice structures are investigated in section 8.3.3.

8.3 Numerical Simulation

8.3.1 Homogenization and boundary conditions

When simulating the effective mechanical properties of an infinite media composed of a periodic repetition of a unit cell, the simulation can be reduced to the unit cell.

Such a unit-cell is represented in figure 8.6. The length of the unit cell is L , and its volume $V = L^3$. It is represented in volume instead of wireframe because it will be the base of a FEM simulation using volume elements.

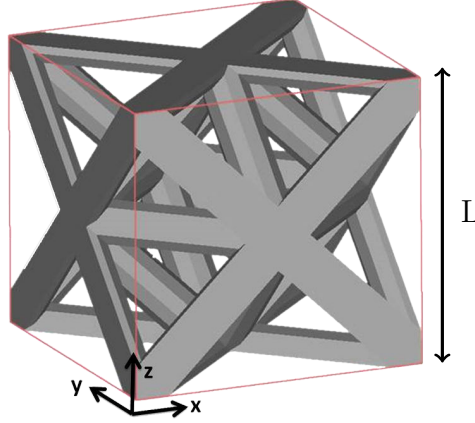


Figure 8.6 Unit cell for the numerical simulation of Octet-truss structure using FEM simulation.

The unit cell is composed of cylinders with a half circular cross-section at its contour.

The aim of the homogenization is to calculate the microscopic fields ($\underline{\underline{\varepsilon}}$ and $\underline{\underline{\sigma}}$) induced by macroscopic loadings $\underline{\underline{E}}$ or $\underline{\underline{\Sigma}}$. The global strain and stress are the mean values of microscopic fields in the RVE.

$$\begin{aligned}\underline{\underline{E}} &= \langle \underline{\underline{\varepsilon}} \rangle_V \\ \underline{\underline{\Sigma}} &= \langle \underline{\underline{\sigma}} \rangle_V\end{aligned}\quad (8.2)$$

In order to simulate the effective properties of such a structure, Periodic Boundary Conditions (PBC) were applied to the unit cell.

Periodic Boundary Conditions (PBC)

Let E_{ij}^0 be a macroscopic strain, j^+ is the face of the unit cell perpendicular to the j direction (x , y or z) and oriented towards the increasing values of j . For any point $M_j^+ \in j^+$ and its opposite point $M_j^- \in j^-$, the PBC consist in applying a relative displacement along every direction of nodes of opposite faces [103, 104]:

$$u_i(M_j^+) - u_i(M_j^-) = L \langle \underline{\underline{\varepsilon}} \rangle$$

Using the strain averaging relation (8.2), the PBC can be written as

$$u_i(M_j^+) - u_i(M_j^-) = L E_{ij}^0 \quad (8.3)$$

These PBC conditions will be applied on the RVE (Fig. 8.6) to investigate the effective elastic properties of such a structure.

8.3.2 Finite Element Modeling

The numerical simulation presented here is based on a FEM simulation using volume element. This simulation is more precise than a beam simulation since it does not rely on beam assumptions.

Loading conditions and engineering constant extraction

The Finite Element Analysis was carried out using the software COMSOL and volume elements. Due to the symmetry of the octet-truss, the stiffness matrix is cubic [42] and the Hooke's law becomes :

$$\begin{bmatrix} \sigma_{11} \\ \sigma_{22} \\ \sigma_{33} \\ \sigma_{23} \\ \sigma_{13} \\ \sigma_{12} \end{bmatrix} = \begin{bmatrix} C_{11} & C_{12} & C_{12} & 0 & 0 & 0 \\ C_{12} & C_{11} & C_{12} & 0 & 0 & 0 \\ C_{12} & C_{12} & C_{11} & 0 & 0 & 0 \\ 0 & 0 & 0 & C_{44} & 0 & 0 \\ 0 & 0 & 0 & 0 & C_{44} & 0 \\ 0 & 0 & 0 & 0 & 0 & C_{44} \end{bmatrix} \begin{bmatrix} \epsilon_{11} \\ \epsilon_{22} \\ \epsilon_{33} \\ 2\epsilon_{23} \\ 2\epsilon_{13} \\ 2\epsilon_{12} \end{bmatrix} \quad (8.4)$$

This is true for an octet-truss for which all the struts have the same diameter. However, the aim of this chapter is to use in the numerical simulation the equivalent diameters developed in the previous chapter (section 7.3). Therefore, the struts will have different diameters according to their orientation during the EBM process. In this case, the behavior is no more cubic but orthotropic:

$$\begin{bmatrix} \sigma_{11} \\ \sigma_{22} \\ \sigma_{33} \\ \sigma_{23} \\ \sigma_{13} \\ \sigma_{12} \end{bmatrix} = \begin{bmatrix} C_{11} & C_{12} & C_{13} & 0 & 0 & 0 \\ C_{12} & C_{22} & C_{23} & 0 & 0 & 0 \\ C_{13} & C_{23} & C_{33} & 0 & 0 & 0 \\ 0 & 0 & 0 & C_{44} & 0 & 0 \\ 0 & 0 & 0 & 0 & C_{55} & 0 \\ 0 & 0 & 0 & 0 & 0 & C_{66} \end{bmatrix} \begin{bmatrix} \epsilon_{11} \\ \epsilon_{22} \\ \epsilon_{33} \\ 2\epsilon_{23} \\ 2\epsilon_{13} \\ 2\epsilon_{12} \end{bmatrix} \quad (8.5)$$

The stiffness matrix is thus composed of 9 independent coefficients: C_{11} , C_{22} , C_{33} , C_{12} , C_{13} , C_{23} , C_{44} , C_{55} , C_{66} .

The stiffness coefficients are calculated using the strain energy (U). It is defined as:

$$U = \frac{1}{2} \int_V \underline{\underline{\sigma}} : \underline{\underline{\epsilon}} = \frac{1}{2} C_{ijkl} E_{kl}^0 E_{ij}^0 V \Rightarrow C_{ijkl} = \frac{2U}{E_{kl}^0 E_{ij}^0 V} \quad (8.6)$$

The conversion from 4-indices coefficients to 2-indices coefficients is related to the Voigt's notation. For example $C_{11} = C_{1111}$, $C_{12} = C_{1122}$ and $C_{44} = C_{2323}$.

To obtain the 9 coefficient of the stiffness matrix, 9 different types of loading are applied:

- **Uniaxial loading**

Example along x direction:

$$\underline{\underline{E}}^0 = \begin{bmatrix} E_{xx}^0 & 0 & 0 \\ 0 & 0 & 0 \\ 0 & 0 & 0 \end{bmatrix}$$

The stiffness coefficient is then calculated as: $C_{11} = \frac{2U}{(E_{xx}^0)^2}$. The coefficient C_{22} and C_{33} are obtained similarly:

$$C_{22} = \frac{2U}{(E_{yy}^0)^2}$$

¹The strength and strain matrices are represented in their vector form using Voigt's Notation

$$C_{33} = \frac{2U}{(E_{zz}^0)^2}.$$

- **Shear strain**

Example between x and y directions:

$$\underline{\underline{E}}^0 = \begin{bmatrix} 0 & \frac{E_{xy}^0}{2} & 0 \\ \frac{E_{xy}^0}{2} & 0 & 0 \\ 0 & 0 & 0 \end{bmatrix}$$

The stiffness coefficient is then calculated as: $C_{66} = \frac{2U}{(E_{xy}^0)^2}$. The coefficients C_{44} and C_{55} are obtained similarly:

$$C_{55} = \frac{2U}{(E_{xz}^0)^2}$$

$$C_{44} = \frac{2U}{(E_{yz}^0)^2}$$

- **Biaxial loading**

Example with biaxial loading in the x and y directions:

$$\underline{\underline{E}}^0 = \begin{bmatrix} E_{xx}^0 & 0 & 0 \\ 0 & E_{yy}^0 & 0 \\ 0 & 0 & 0 \end{bmatrix}$$

The stiffness coefficient is then calculated as: $C_{12} = \frac{1}{2} \left(\frac{U}{(E_{xx}^0)^2} + \frac{U}{(E_{yy}^0)^2} - C_{11} - C_{22} \right)$.

The coefficients C_{13} and C_{23} are obtained similarly:

$$C_{13} = \frac{1}{2} \left(\frac{U}{(E_{xx}^0)^2} + \frac{U}{(E_{zz}^0)^2} - C_{11} - C_{33} \right)$$

$$C_{23} = \frac{1}{2} \left(\frac{U}{(E_{yy}^0)^2} + \frac{U}{(E_{zz}^0)^2} - C_{22} - C_{33} \right)$$

When the stiffness matrix is fully known, the compliance matrix is then calculated by inverting the stiffness one:

$$\underline{\underline{S}} = \text{inv}(\underline{\underline{C}}) = \begin{bmatrix} S_{11} & S_{12} & S_{13} & 0 & 0 & 0 \\ S_{21} & S_{22} & S_{23} & 0 & 0 & 0 \\ S_{31} & S_{32} & S_{33} & 0 & 0 & 0 \\ 0 & 0 & 0 & S_{44} & 0 & 0 \\ 0 & 0 & 0 & 0 & S_{55} & 0 \\ 0 & 0 & 0 & 0 & 0 & S_{66} \end{bmatrix} = \begin{bmatrix} \frac{1}{E_1} & -\frac{\nu_{21}}{E_2} & -\frac{\nu_{31}}{E_3} & 0 & 0 & 0 \\ -\frac{\nu_{12}}{E_1} & \frac{1}{E_2} & -\frac{\nu_{32}}{E_3} & 0 & 0 & 0 \\ -\frac{\nu_{13}}{E_1} & -\frac{\nu_{23}}{E_2} & \frac{1}{E_3} & 0 & 0 & 0 \\ 0 & 0 & 0 & \frac{1}{G_{23}} & 0 & 0 \\ 0 & 0 & 0 & 0 & \frac{1}{G_{31}} & 0 \\ 0 & 0 & 0 & 0 & 0 & \frac{1}{G_{12}} \end{bmatrix} \quad (8.7)$$

The twelve engineering coefficients are extracted from the compliance as shown in equation 8.7.

8.3.3 Comparison between experiments and simulations

The octet-trusses produced by EBM have been mechanically tested using the protocol explained earlier (section 8.2). Figure 8.7 represents the relative Young's modulus (Effective Young's modulus of the structure divided by the Young's modulus of the dense Ti-6Al-4V) as a function of the relative density. The green curve represents the results of the FEM simulation using volume elements.

The errors due to the measurement of the density and of the Young's modulus have been quantified. The error in terms of density is mainly due to the accuracy of measurement of the length of the structure. On the other hand, the error of Young's modulus comes mainly from the accuracy of the linear regression during unloading.

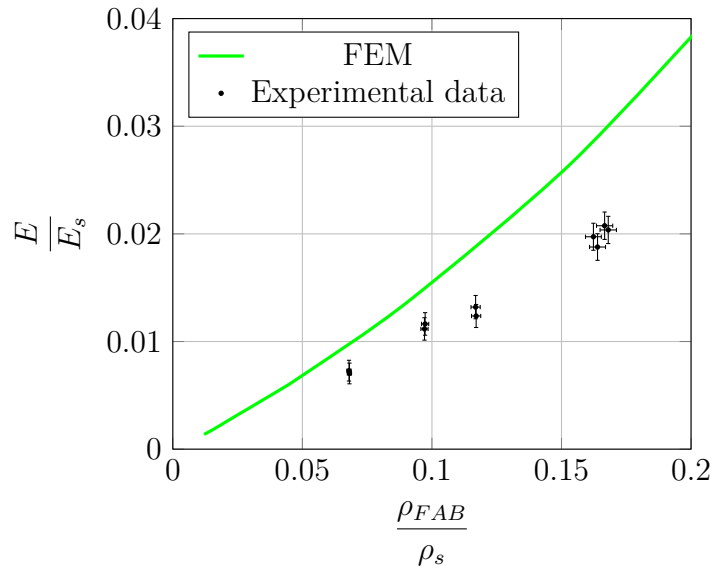


Figure 8.7 Relative Young's modulus variation as a function of the relative density using the FEM simulation. Comparison with the experimental data.

The experimental values are much lower than the simulated ones. It validates the concept of "inefficient" matter seen in the previous chapter.

8.4 Validation of the equivalent diameter

8.4.1 FEM with equivalent diameters

As mentioned earlier the octet-truss structures were manufactured at 45° to allow an easier removal from the start plate. As a conclusion, the structure is then composed of 6 horizontal, 6 vertical and 24 oblique struts as shown in figure 8.8.

For the FEM simulation, each strut is assigned a different equivalent diameter depending on its orientation. The protocol for the determination of the elastic constants is based on section 8.3.2.

8.4.2 Comparison with the experimental data

The results of these simulations are compared to the experimental values in figure 8.9. As seen before, the green curve represents the FEM simulation of the octet-truss structure

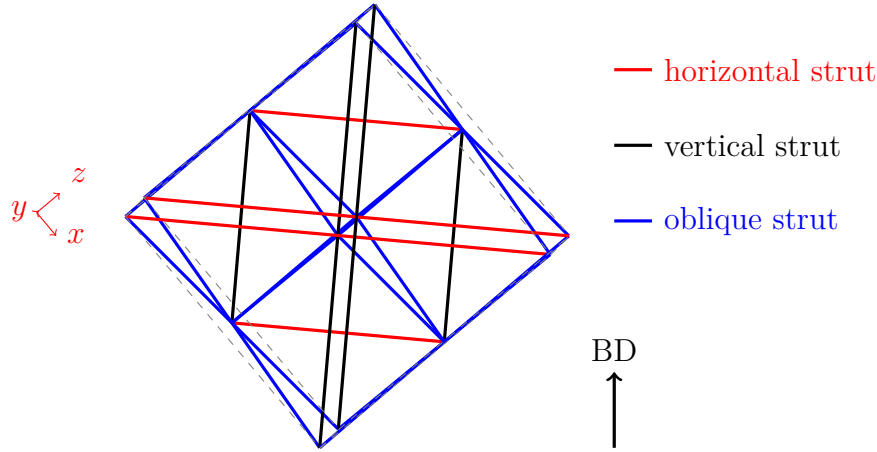


Figure 8.8 Octet-truss unit cell as fabricated at 45° . Representation of the vertical, horizontal and oblique struts.

with (D_{CAD}) . The black points sketch the experimental values of Young's modulus.

The red curve (dashed) depicts the results of the simulation using the numerical equivalent diameters (D_{EQ}^{NUM}), whereas the orange one (dotted) is obtained using simulation with the geometrical ones (D_{EQ}^{GEOM}).

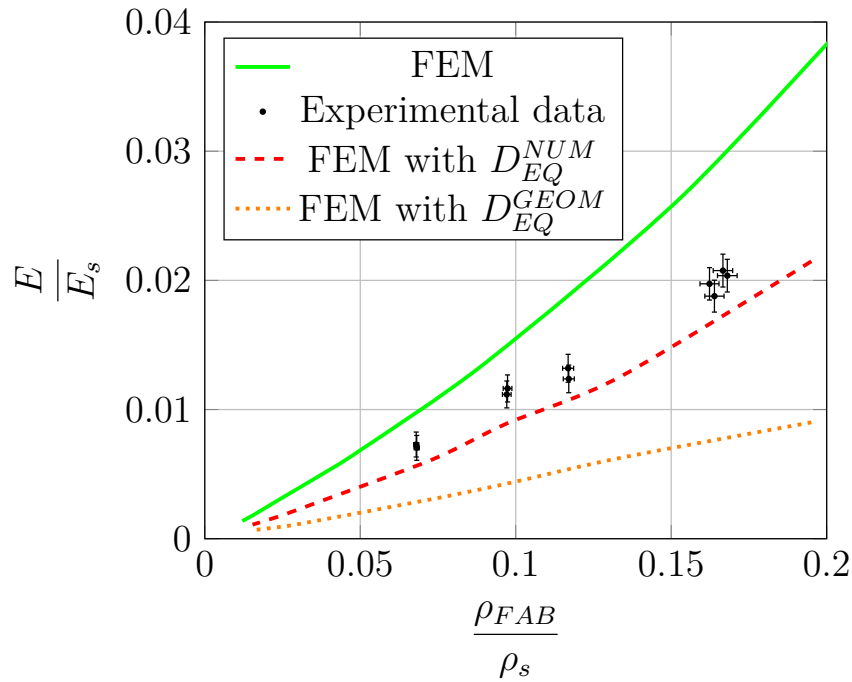


Figure 8.9 Relative Young's modulus as a function of relative density for the designed geometry (in green), including the correction of D_{EQ}^{NUM} using FFT calculation (in red) and a correction of D_{EQ}^{GEOM} using the inscribed cylinder (in orange). Experimental values are depicted in black.

From figure 8.9, it appears that the use of the geometrical equivalent diameter underestimates the mechanical properties. The numerical equivalent diameter derived from FFT simulation gives results closer to the experimental ones. Indeed, the geometrical equivalent diameter defined in section 7.3.1 is based on a minimal common projected surface. It leads thus to a lower bound for the stiffness prediction.

The equivalent diameter deduced from a numerical estimation of the strut's stiffness provides a better prediction of the stiffness because it takes into account the stress field in the strut. Young's modulus values obtained by FEM simulation with D_{EQ}^{NUM} are close to the experimental ones though slightly lower.

This underestimation is probably due to the fact that the equivalent diameters are based on 3D measurements made on struts only. The complexity of the stress state in the vicinity of the strut intersections (nodes of the lattice) is probably not fully captured. Moreover, the experimental use of an octet-truss with only five unit cells per side can lead to a slight error in the comparison with simulations results based on a periodic calculation.

As a result, the numerical equivalent diameter simulation enables to take into account the manufacturing constraints with an implicit safety coefficient since the stiffness is slightly underestimated.

This numerical equivalent diameter will be considered as a **mechanical equivalent diameter** in the following chapters.

Chapter 9

Variation of the mechanical equivalent diameter with strut size and orientation angle

Contents

8.1	The Octet-truss lattice	128
8.1.1	Generalities	128
8.1.2	Manufacturing by the EBM technology	128
8.1.3	RVE analysis	130
8.2	Compression Test	130
8.2.1	Testing configuration	130
8.2.2	Young's Modulus determination	131
8.3	Numerical Simulation	132
8.3.1	Homogenization and boundary conditions	132
	Periodic Boundary Conditions (PBC)	133
8.3.2	Finite Element Modeling	133
	Loading conditions and engineering constant extraction	134
8.3.3	Comparison between experiments and simulations	136
8.4	Validation of the equivalent diameter	136
8.4.1	FEM with equivalent diameters	136
8.4.2	Comparison with the experimental data	136

This chapter aims at obtaining an analytical value of the variation of the mechanical equivalent diameter for struts with different nominal diameters and build orientations. This analytical value can then be used in any "realistic" simulation and mechanical optimization.

9.1 Fabricated struts

In order to obtain an analytical value of the mechanical equivalent diameter, struts with different diameters and orientations were designed according to figure 9.1.

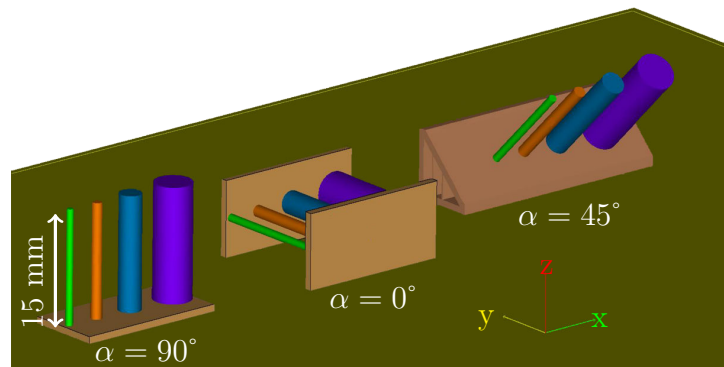


Figure 9.1 Designed struts prior to manufacturing by EBM. The build direction is along the z direction. Struts with different diameter (1, 1.5, 3, 5 mm) and build orientation ($\alpha=0^\circ$, 45° and 90°) have been manufactured.

The struts have four different diameters (1, 1.5, 3, 5 mm) and three different orientations (0° , 45° and 90°). The twelve struts are manufactured using the "Melt" set of process parameters (ARCAM theme) and are analyzed by X-Ray tomography to investigate the porosity content, roughness and to find the mechanical equivalent diameter of each strut (same methodology as the previous chapter 7.1).

In the previous study on single struts (chapter 7), the "Net" theme was used to build 1 mm struts. It is the theme recommended for very thin parts. However, struts larger than 1 mm produced with the "Net" theme exhibit a larger porosity. Figure 9.2 represents a longitudinal cut of a 1.5 mm diameter strut manufactured with the "Net" theme. Large pores are observed in the core of the struts. These pores result from a lack of melting in the center of the strut. Thus the hatching of the "Net" theme is not optimized and leads to porosity. It can only be used to produce very thin struts ($D_{CAD} \leq 1mm$).



Figure 9.2 longitudinal cut of a vertical 1.5 mm diameter strut manufactured with the "Net" theme. Large porosity is observed in the center of the strut.

That's the reason why, in this part the "Melt" theme is used to melt struts ranging from 1 to 5 mm. Moreover, it allows us to compare the two themes for 1 mm struts.

The strategy of the "Melt" theme is depicted in figure 9.3 for melting a 1.5 and a 5

mm diameter strut. The melting strategy is always the same. The electron beam starts to melt a first contour followed if possible by a second one. If the CAD is large enough, the beam scans the surface line by line in the hatching step.

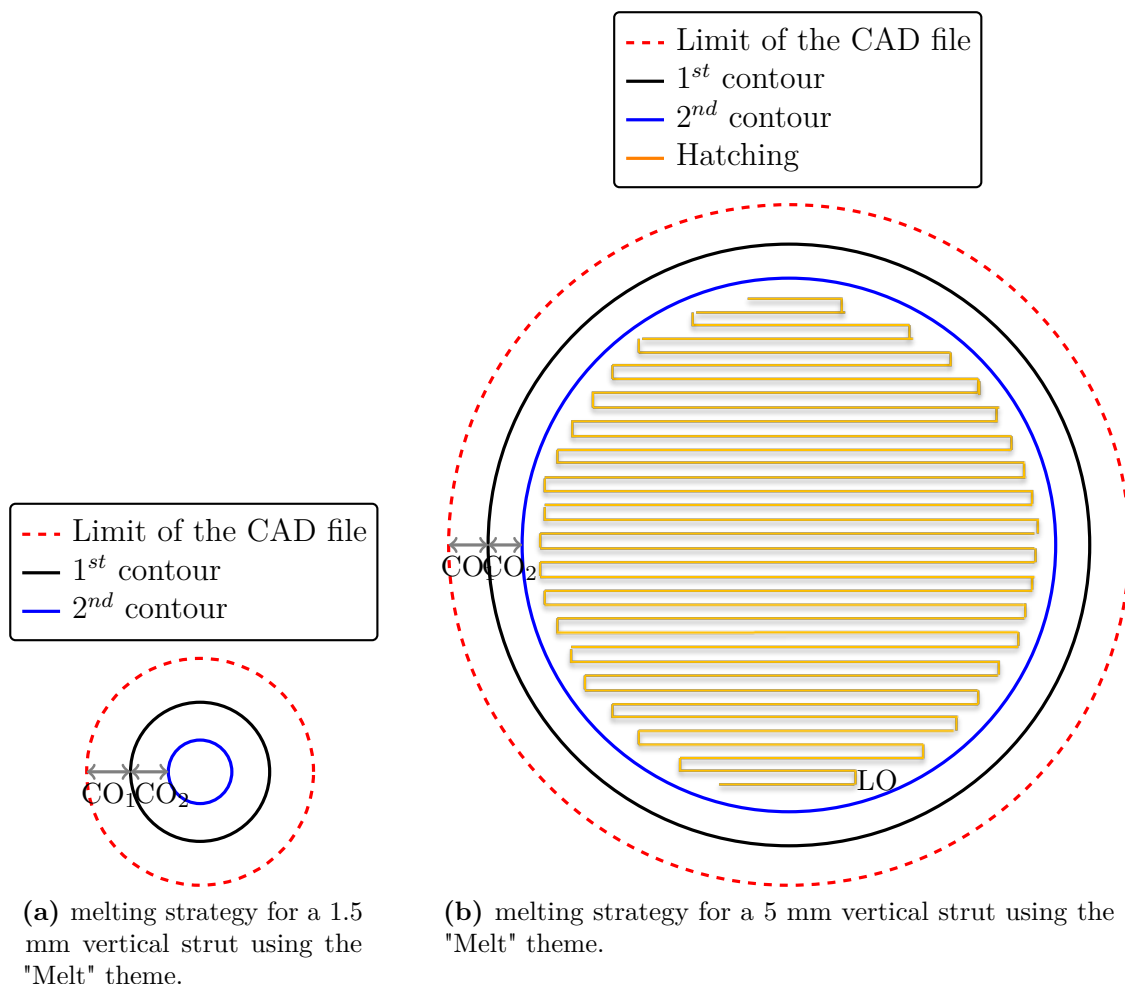


Figure 9.3 Scheme of the melting path at a random layer for a 1.5 mm and a 5 mm circular vertical strut when using the "Melt" set of parameters.

The values of beam current, speed and offsets are summarized in table 9.1.

MELT	1 st contour	2 nd contour	Hatching
Offset [mm]	CO ₁ =0.29	CO ₂ =0.25	LO=0.1
Speed [mm/s]	340	800	-
Current [mA]	4	10	-

Table 9.1 Values of the process parameters for the "Melt" theme for vertical struts with different nominal diameters (1 mm, 1.5 mm, 3 mm, 5 mm).

The parameters are constant for the 1st and 2nd contour whatever the geometry of the strut. The speed and current of the beam during hatching fluctuates depending on the geometry and the thermal history of the previous layers. These fluctuations are based on thermal balance consideration. They result from years of improvement by Arcam.

9.2 Structural analysis of the struts

A special attention is paid to the case of 1 mm diameter struts for which both themes ("Net" and "Melt") can be used.

9.2.1 Comparison between "Net" and "Melt" themes for 1 mm diameter struts

Figure 9.4 shows the difference in terms of beam strategy between a "Melt" theme and a "Net" theme for a 1 mm diameter strut built vertically. For a 1 mm diameter vertical strut built with the "Melt" theme, the beam scans only the 1st contour whereas for "Net" theme the beam scans two contours.

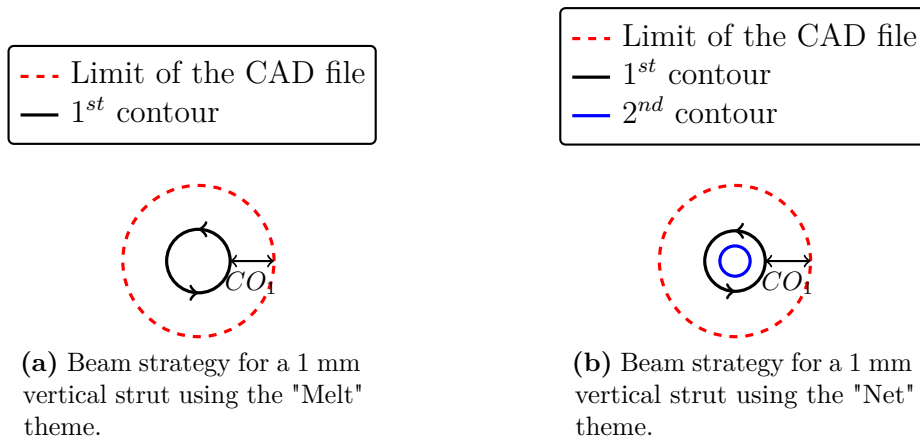


Figure 9.4 Scheme of the melting path at a random layer for a 1 mm using the "Melt" or "Net" set of parameters.

As mentioned in table 9.2, the first contour offset (CO_1) is similar for "Net" and "Melt" theme. For the "Net" theme, a second beam path is carried out with an offset of 0.1 mm from the 1st contour.

However, for both contours of the "Net" theme, the beam speed is two times higher and the beam current is much lower than the "Melt" theme. As a consequence, the volume energy is lower in the case of the "Net" theme ($2.1 \cdot 10^{10} \text{ J/m}^3$) even if there are two beam paths. The volume energy of the "Melt" theme has been calculated as $3.27 \cdot 10^{10} \text{ J/m}^3$.

	"Net" theme		"Melt" theme
	1 st contour	2 nd contour	1 st contour
Offset [mm]	0.3	0.1	0.29
Speed [mm/s]	470	470	340
Current [mA]	2.4	2	4
Volume energy (14.1) [J/m^3]	2.1 $\cdot 10^{10}$		3.27 $\cdot 10^{10}$

Table 9.2 Values of the process parameters for a 1 mm diameter vertical strut. Difference between the "Net" theme and the "Melt" theme.

As a consequence the melted volume is different and the mechanical equivalent diameter too. Indeed, figure 9.5, shows the produced struts (in green) and the designed ones (in

blue) for struts produced by the "Net" theme (a) or by the "Melt" theme (b). Different orientations were produced.

Generally, the produced struts using the "Net" theme are smaller than the ones produced using the "Melt" theme. The 1 mm struts produced with the "Melt" theme have a size closer to the nominal diameter.

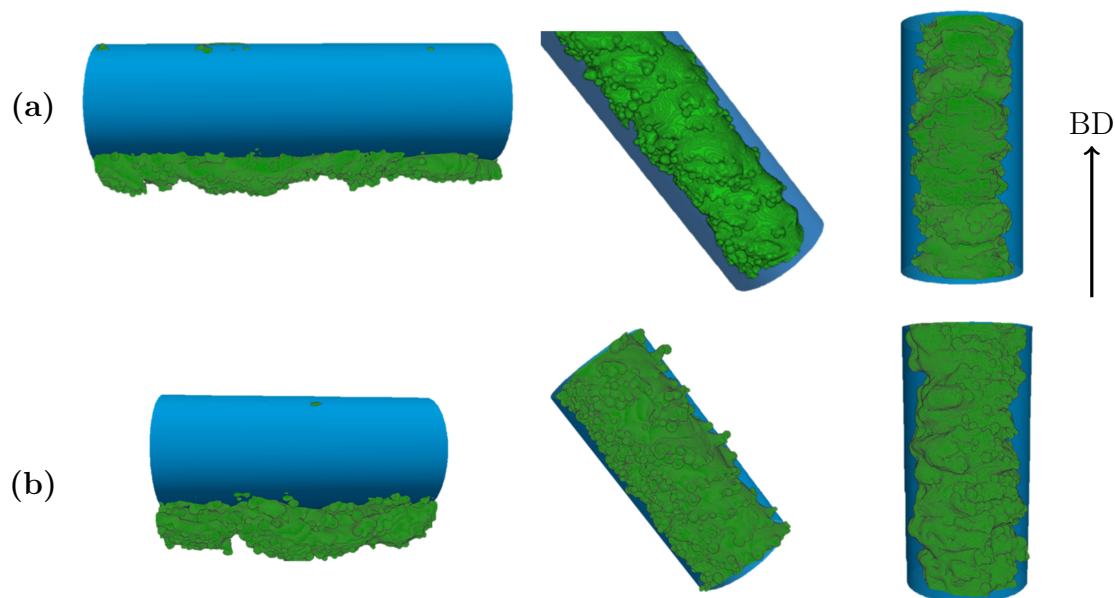


Figure 9.5 1 mm struts produced using the "Net" (a) and "Melt" (b) themes. Vertical, oblique and horizontal struts are compared. The build direction (BD) is represented with a black arrow.

However, because of the large energy input for the "Melt" theme, the horizontal struts exhibit a larger anisotropy of the cross-section. It is due to over-melting taking place for the first layers of melting of the horizontal strut. Indeed, for the first layers, the beam melts directly on sintered powder with a low thermal conductivity. The high energy beam over-melts multiple layers due to heat accumulation. This over-melting is larger in the case of the "Melt" theme than for the "Net" one.

The porosity content was also investigated using the same methodology as 7.1.3. The porosity content was found to be very similar for struts manufactured with the "Melt" theme and with the "Net" theme for any strut orientation. The porosity content was always lower than 0.1 %.

The roughness was calculated on struts produced with the "Net" and "Melt" themes using the methodology developed in 7.1.3. For any strut orientation and any type of roughness (R_a and R_t), the roughness is in the same range for struts produced with the "Melt" and "Net" themes with an arithmetic roughness around $40 \mu m$.

Since they exhibit the same roughness and a diameter closer to the nominal one, struts produced by the "Melt" theme have a mechanical equivalent diameter closer to D_{CAD} . Table 9.3 depicts the values of D_{EQ}^{NUM} for 1 mm struts with different orientations and themes.

α ($^\circ$)	90	45	0
"Melt" theme	0.68	0.78	0.92
"Net" theme	0.58	0.58	0.71
Ratio (M-N)/M [%]	16	25	25

Table 9.3 Values of D_{EQ}^{NUM} (in mm) for 1 mm struts produced with different orientation and different themes.

The mechanical equivalent diameters are larger for struts produced with the "Melt" theme. The produced struts have a larger stiffness than struts produced using the "Net" theme.

The "Melt" theme is therefore more efficient to produce controlled geometries whereas the "Net" theme allows the production of thin struts without a complete control of the produced geometry.

9.2.2 Analytical equation of D_{EQ}^{NUM}

For the rests of the chapter, struts fabricated with the "Melt" theme are analyzed.

This section aims at finding an analytical value of the mechanical equivalent diameter as a function of the nominal diameter and the orientation angle: $D_{EQ}^{NUM} = f(D_{CAD}, \alpha)$. This knowledge will be further used into a "realistic" simulation of lattice structures.

The struts with different build orientations and nominal diameters were manufactured with the "Melt" theme as shown in the section 9.1. Using the methodology developed in the last part 7.3.2, the mechanical equivalent diameter (D_{EQ}^{NUM}) of each strut was calculated.

The values of the normalized equivalent diameter (D_{EQ}^{NUM}/D_{CAD}) have been plotted as a function of the nominal diameter D_{CAD} in figure 9.6 for the three different orientations. The green line represents the values $D_{EQ}^{NUM}=D_{CAD}$. It confirms that for any strut size and orientation, the mechanical equivalent diameter is lower than the nominal diameter.

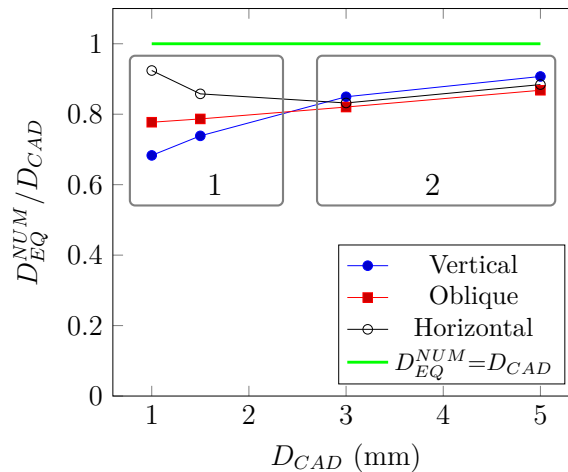


Figure 9.6 Normalized equivalent diameter (D_{EQ}^{NUM}/D_{CAD}) as a function of the nominal diameter (D_{CAD}) for struts with different orientations ($\alpha=0^\circ, 45^\circ, 90^\circ$) and nominal diameters ($D_{CAD}=1, 1.5, 3, 5$ mm). In green: the line representing the values $D_{EQ}^{NUM}=D_{CAD}$.

From this figure, two regimes can be identified:

Small size regime (1 in figure 9.6): For the small struts size, the horizontal struts present larger mechanical equivalent diameter than the oblique ones which are also stiffer than the vertical one. This has been explained in the previous part (7.3).

For a horizontal strut, over-melting takes place when melting the first layers of the strut. This over-melting leads to a large and elongated cross-section for the manufactured strut.

When melting an oblique strut, the down-facing side is undergoing a slight over-melting (especially when melting with the "Melt" theme which brings more energy). As a consequence the melted surface is slightly larger than for a vertical strut and so is the mechanical equivalent diameter.

large size regime (2 in figure 9.6): When melting larger struts (*e.g.* 2 mm diameter), the mechanical equivalent diameter is almost constant for any strut orientation. The phenomenon of over-melting still takes place but is less critical since the dimensions of the struts are larger.

As a result, the mechanical equivalent diameter is similar for any orientation.

From figure 9.6, the variation of mechanical equivalent diameter is assumed to be linear with the nominal diameter. Thus the following equation can be used:

$$D_{EQ}^{NUM} = K(\alpha)D_{CAD} + C(\alpha) \tag{9.1}$$

The variation of $K(\alpha)$ and $C(\alpha)$ is fitted by a linear regression as represented (in red) in figure 9.7. The coefficients of the polynomial are listed in table 9.4.

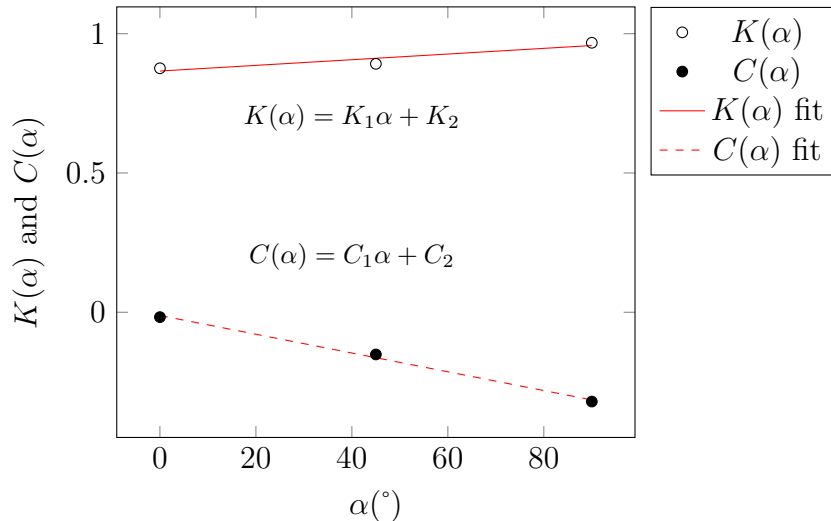


Figure 9.7 Variation of the coefficient K and C as a function of the orientation angle α .

	1	2
K	1.0210^{-3}	8.6510^{-1}
C	-3.3710^{-3}	-1.1610^{-2}

Table 9.4 Table with the values of coefficients of $K(\alpha)$ and $C(\alpha)$.

The analytical value can be thus written as (using the coefficient of table 9.4):

$$D_{EQ}^{NUM} = (K_1\alpha + K_2) D_{CAD} + C_1\alpha + C_2 \quad (9.2)$$

This analytical response surface has been plotted in figure 9.8. The response surface fits well with the values obtained by FFT simulation.

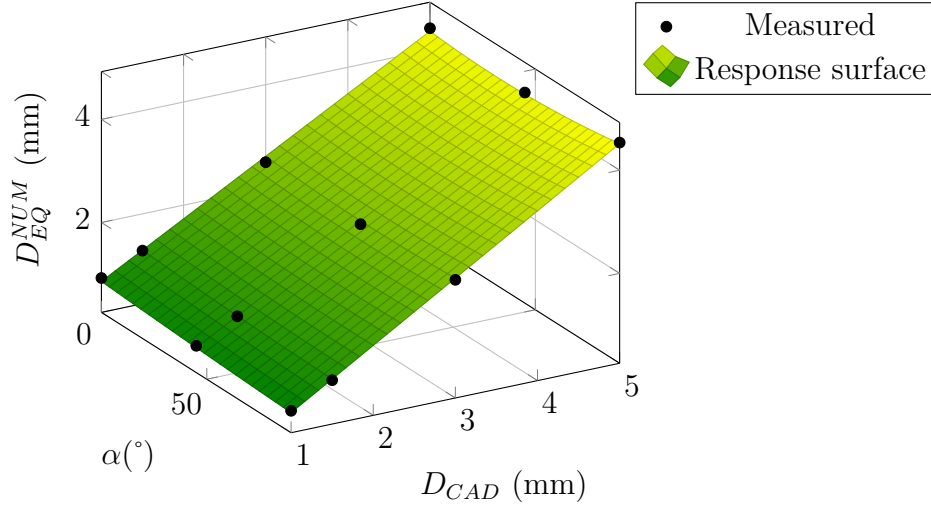


Figure 9.8 Response surface of the analytical values of the variation of D_{EQ}^{NUM} with D_{CAD} and α . Comparison with the simulated values (in black).

The maximal error between the measured values and the response surface has been quantified as 5 %. This is an acceptable range of error.

Thus, the analytical values obtained in equation 9.2 will be used to take into account the "effective" stiffness of the produced struts within the simulation of lattice structures (see next part IV).

Summary

This part aimed at presenting a methodology to predict the elastic properties of lattice structures produced by EBM from the structural characterization at the scale of the strut.

The results presented here are valid for this particular configuration but the methodology can be applied on any AM process to evaluate the "true" properties of lattice structures composed of struts with any diameter and process parameters.

Figure 9.9 sums up the procedure presented here.

The designed octet-truss has a relative density $\bar{\rho}_{CAD}$ and is composed of struts with a diameter D_{CAD} (in blue) ①.

The produced octet-truss exhibits a lower relative density ($\bar{\rho}_{FAB}$). The difference of density is due to a difference of size between the designed strut (blue) and the produced one (green).

This difference in density decreases the relative Young's modulus from \bar{E}_{CAD} to \bar{E}_{C_1} ①. However, the effective properties of the produced octet-truss is lower than this value ②. This is due to the high surface irregularities that represents a significant part of the volume. Some volume of the strut is not "mechanically efficient". A mechanical equivalent cylinder has been extracted from numerical simulations on the strut. This mechanical equivalent diameter having a diameter D_{EQ}^{NUM} has been validated by comparing the experimental data and FEM simulations using this D_{EQ}^{NUM} .

The results show that FEM simulation with the mechanical equivalent diameter allows a refinement of the prediction of the mechanical properties of lattice structures produced by EBM.

A generalization of the mechanical equivalent diameter D_{EQ}^{NUM} has been studied. The D_{EQ}^{NUM} was investigated for diameters ranging from 1 mm to 5 mm and with different build orientations ($\alpha=0^\circ$, 45° and 90°). An analytical value of $D_{EQ}^{NUM} = f(\alpha, D_{CAD})$ has been extracted. This analytical value will be further used in numerical simulation and optimization of lattice structures produced by EBM (part IV).

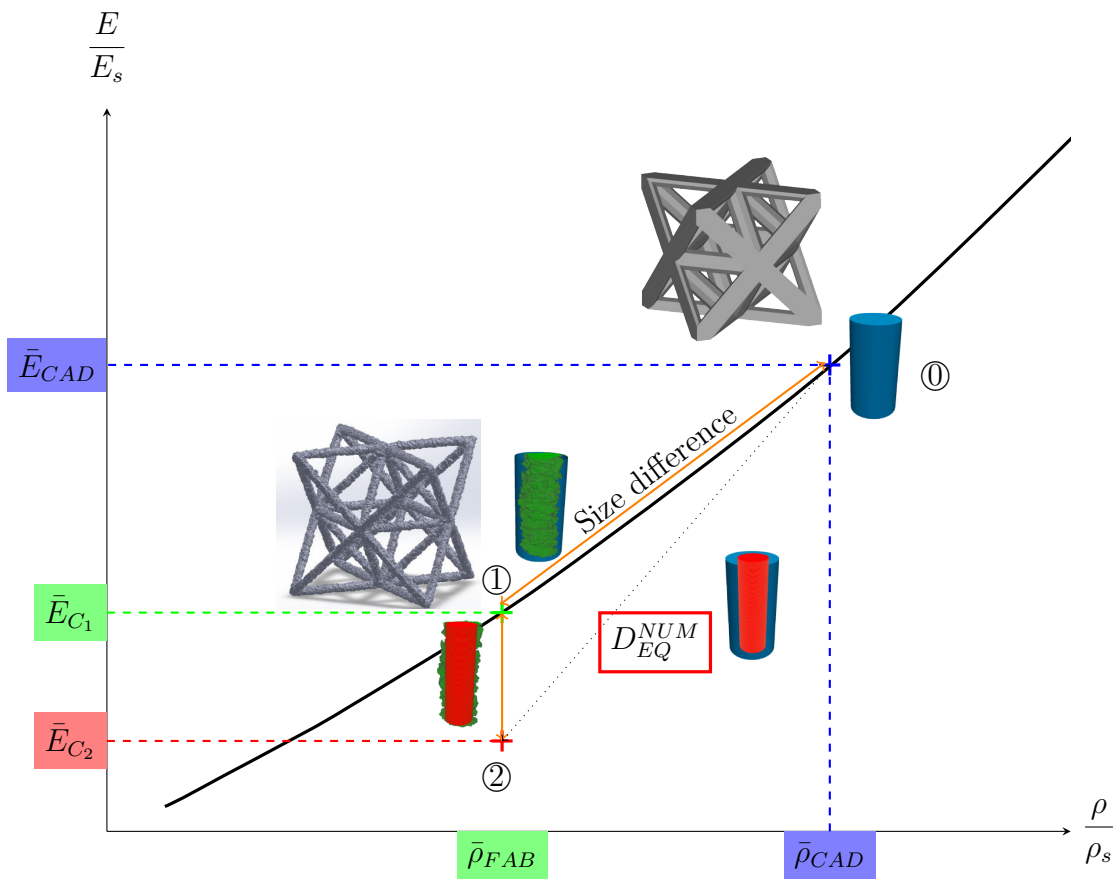


Figure 9.9 Summary graph of the part. It highlights the influence of the geometrical difference between the designed struts and the manufactured one (shape and roughness) on the mechanical properties of a lattice structure.

Part IV

Optimization of lattice structures

The aim of this part is to use the previous methodology to simulate and optimize the stiffness of lattice structures produced by EBM.

The FEM simulation using volume elements has been carried out on an octet-truss unit cell in a previous chapter (section 8.3). However for simulating larger structures or when using a repetitive amount of simulations, the use of beam elements is required. It allows a fast simulation but has a limited range of application. To determine this range of application, volume FEM and beam simulation are performed on the octet-truss unit-cell.

A direct application of the analytical equation of the mechanical equivalent diameter is investigated. The optimal orientation of a lattice structure is found depending on the properties that one wants to maximize.

A parametric optimization using the mechanical equivalent diameter is also explained. It allows the optimization of lattice structures by taking into account the manufacturing constraints.



Chapter 10

Beam Simulation for the octet-truss structure

Contents

9.1	Fabricated struts	139
9.2	Structural analysis of the struts	142
9.2.1	Comparison between "Net" and "Melt" themes for 1 mm diameter struts	142
9.2.2	Analytical equation of D_{EQ}^{NUM}	144

As mentioned earlier, the FEM simulation using volume elements is not suitable when simulating large structures or when a large number of simulations is needed (for example, an iterative procedure of optimization). A FEM simulation using beam elements is then suggested.

The software used for the FEM simulation using Timoshenko beams is CAST3M¹.

10.1 Methodology

10.1.1 Materials properties and cross-section parameters

The structure of interest for the beam simulation is the octet-truss structure (see figure 10.1). The aim is to simulate a periodic media composed of a repetition of octet-truss structures. For that purpose, a periodic simulation on an octet-truss unit-cell is performed.

The structure is composed of purely circular cylinders except for the struts in the contour of the unit cell which have to be represented by cylinders with a half circular cross-section to respect the periodicity of the cell (see figure 10.1).

To define the properties of the structure for the simulation, several parameters are used:

- Material properties : Young's Modulus of the constitutive material (E_s) and its Poisson ratio (ν_s).
- Geometrical properties: the cross-section area (A) and the moments of Inertia (I_y and I_z) and moment of torsion (I_g).

¹Developed by the French Alternative Energies and Atomic Energy Commission (CEA).

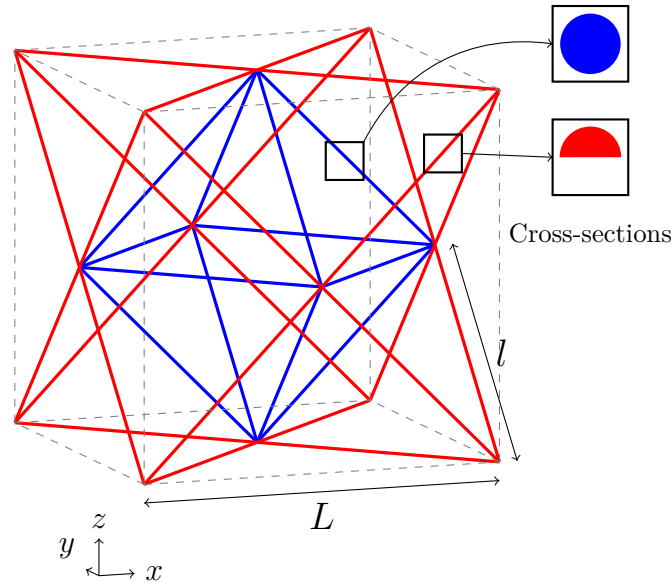


Figure 10.1 Octet-truss unit cell composed of 36 struts. The dashed lines represent the bounding box. The red struts represent the strut having a cross section of a half-circle.

The Periodic Boundary Conditions (PBC) are applied to the unit cell as explained in the previous part (section 8.3). A detailed example of the PBC implementation for a uniaxial compression is shown in appendix B.

The elastic strain energy is calculated to determine the nine independent coefficients of the stiffness matrix (see section 8.3). The engineering constants are then extracted using the compliance matrix. This whole methodology was explained in details for the FEM simulation using volume element but is similar in the case of beam elements simulation.

10.2 Range of application

The values of relative Young's modulus obtained on a regular octet-truss using beam elements are compared to the values obtained using volume elements in figure 10.2.

The values obtained using beam elements are lower than the one obtained with volume elements, especially for large density where the assumptions of the beam theory are not fulfilled anymore (stress states within the struts cannot be captured by the beam theory).

*The beam simulation is valid for relative density lower than about 5%. Further beam simulations will be limited to this range of relative density.*²

²In this range of density (<5%), the first order density can be used since it is close to the true relative density (more details are available in appendix C)

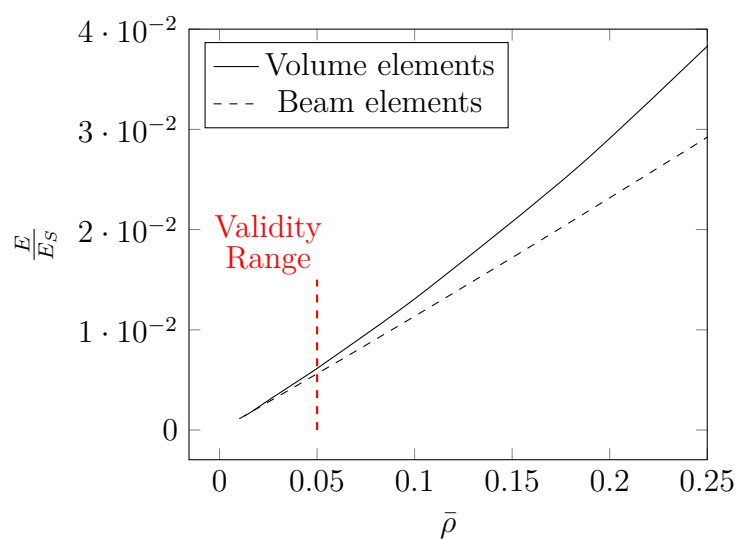


Figure 10.2 Relative Young's modulus of a regular octet-truss as a function of its relative density. Values from the FEM simulations with beams are compared to volume elements.

Chapter 11

Optimal orientation of lattice structures within the EBM build

Contents

10.1 Methodology	153
10.1.1 Materials properties and cross-section parameters	153
10.2 Range of application	154

This chapter aims at giving an example of the use of the concept of equivalent diameters within an elastic simulation of lattice structure. It is focused on a regular octet-truss lattice. The lattice can be built with different orientations during the build. The aim here is to find the optimum fabrication angle of the lattice that maximizes some properties ($E_X, E_Y, E_Z, G_{XY}, G_{XZ}, G_{YZ} \dots$). The beam simulation is used to compute the objective functions.

11.1 From lattice orientation to struts orientation

The position of the octet-truss during the EBM fabrication can be of great importance regarding its final stiffness. In this chapter, a regular octet-truss composed of struts with a 1 mm nominal diameter (D_{CAD}) and with a strut length (l) of 11 mm is studied.

The unit-cell orientation can change by a rotation along the y axis (see figure 11.1). The fabrication angle of the global structure is denoted φ whereas the orientation of the struts is denoted α . The structure is composed of 36 struts. Those struts can be divided into four groups depending on their angle α .

Geometrical relations give the struts angle α^i as a function of the fabrication angle of the lattice φ :

- $\alpha^1 = |45 - \varphi|$
- $\alpha^2 = 90 - |45 - \varphi|$
- $\alpha^3 = \sin^{-1} \left(\frac{\sin(\varphi)}{\sqrt{2}} \right)$
- $\alpha^4 = \sin^{-1} \left(\frac{\cos(\varphi)}{\sqrt{2}} \right)$

The determination of the different struts angles allows the assignment of equivalent diameter of each strut depending on its orientation following the analytical value extracted previously (see $D_{EQ}^{NUM} = f(D_{CAD}, \alpha)$ in section 9.2.2).

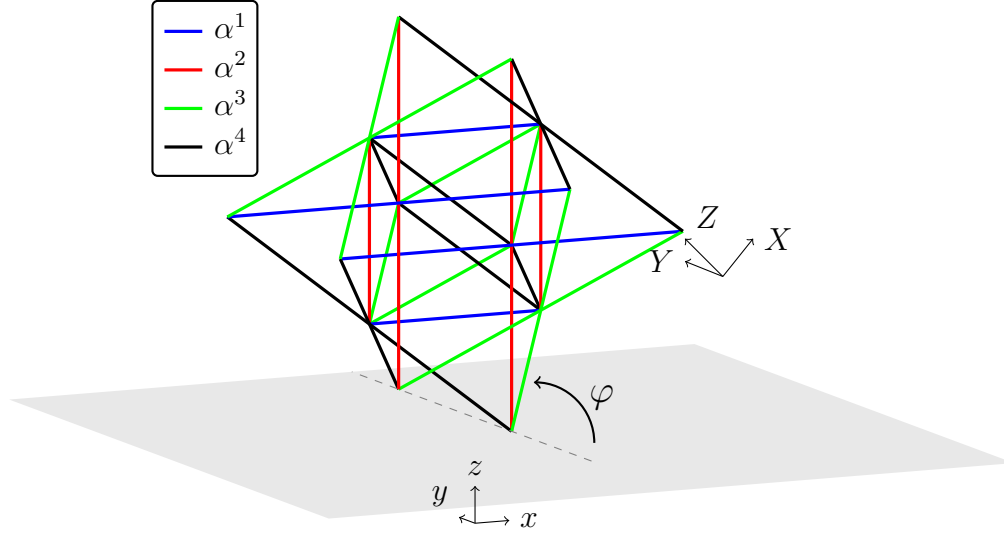


Figure 11.1 Orientation of the struts as a function of the orientation of the structure within the build. x, y, z represents the global coordinate system. X, Y, Z represents the local coordinate system of the lattice.

Within the simulation, each beam with a strut's orientation α^i has a mechanical equivalent diameter D_{EQ}^i .

The figure 11.2 shows the variation of the strut's orientation (α^i) as a function of the fabrication angle of the structure φ . The angle φ ranges between 0° and 90° . When $\varphi = 0^\circ$, the blue, red and black struts have an orientation angle of 45° whereas the green struts are horizontal.

When $\varphi = 90^\circ$, blue, red and green struts have a 45° orientation and the black struts have a 0° orientation.

The resulting mechanical equivalent diameters have been taken into account. They fluctuate between 0.65 mm and 0.85 mm depending on the struts orientation. As mentioned earlier (paragraph 9.2.2), the maximum equivalent diameter corresponds to horizontal struts ($\alpha = 0^\circ$) whereas the minimum corresponds to struts fabricated vertically.

11.2 Results of the simulation

For every degree of fabrication angle (φ), a beam simulation has been carried out to extract the engineering constants. The simulation is based on the method explained in the previous chapter (chap. 10) but takes into account the orientation angle of each struts and replace its diameter by the equivalent diameter.

Now that each strut is represented by a different diameter, the octet-truss structure is no more isotropic. The Young's moduli along the three local direction X, Y, Z (shown in figure 11.1) have been calculated for each fabrication angle of the lattice. It is plotted in figure 11.3.

The Young's moduli along the three orientations show the same trend: when varying the fabrication angle, they exhibit a maximum either in 0° or in 90° . They also exhibit a

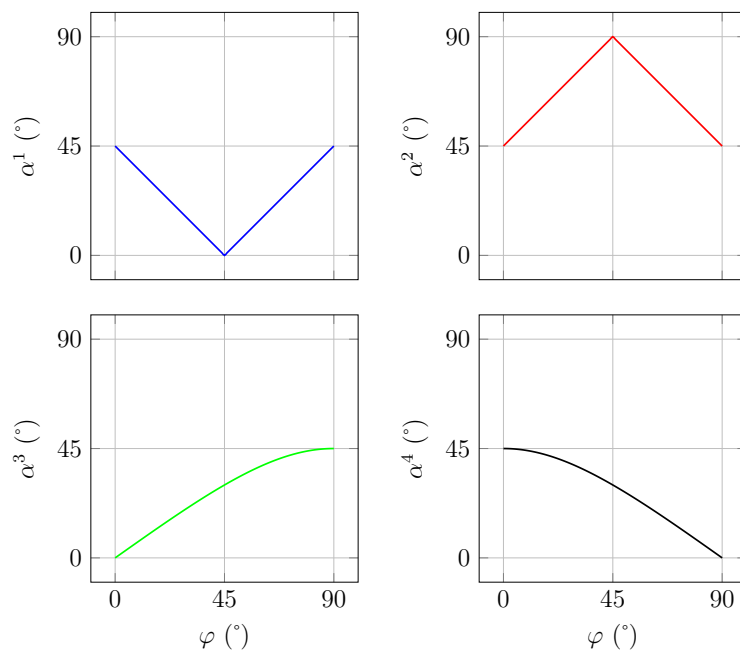


Figure 11.2 Variation of the orientation angle of the struts (α^i) as a function of the fabrication angle of the lattice (φ).

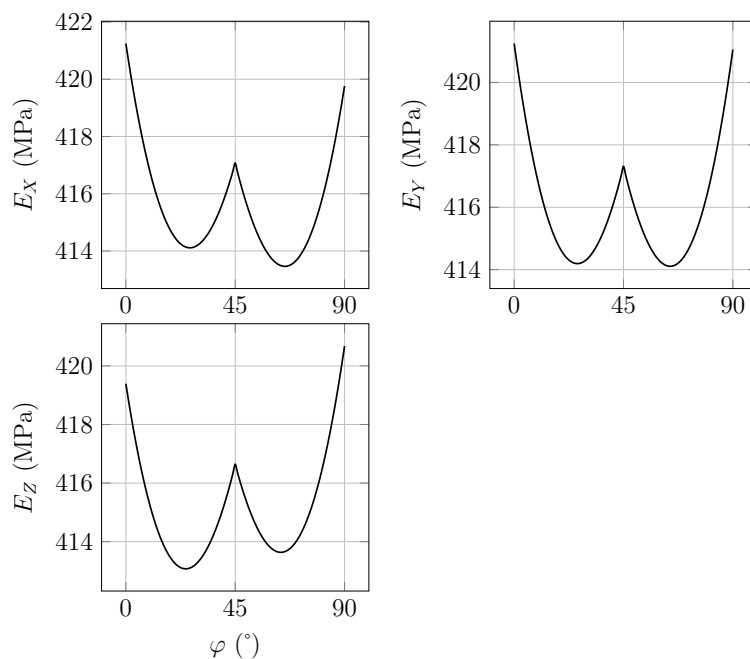


Figure 11.3 Variation of the Young's moduli as a function of the fabrication angle of the lattice (φ).

local maximum for $\varphi = 45^\circ$.

The maximum at $\varphi=0^\circ$ or 90° corresponds to a maximum number of horizontal struts aligned with the loading direction (see figure 11.1). It corresponds to either the green or the black struts. At $\varphi = 45^\circ$, the blue struts are built horizontally. Thus, the Young's modulus increase slightly and exhibits a local maxima.

However, when structures are built with an angle of $\varphi=0$ or 90° , their removal from the start plate is highly complicated and can lead to the damage of the lattice. As a

consequence, when maximizing the Young's modulus of such structure one will prefer a fabrication of the lattice with an angle of 10° or 80° rather than 0° or 90° .

Although the variation of Young's modulus is small in the case of a regular octet-truss ($\sim 2\%$), this methodology can be applied on structures for which the fabrication orientations can largely influence the resulting stiffness.

For the regular octet-truss, the shear modulus G is more impacted by a modification of the fabrication angle φ . Figure 11.4 depicts the variation of the shear moduli as a function of the fabrication angle.

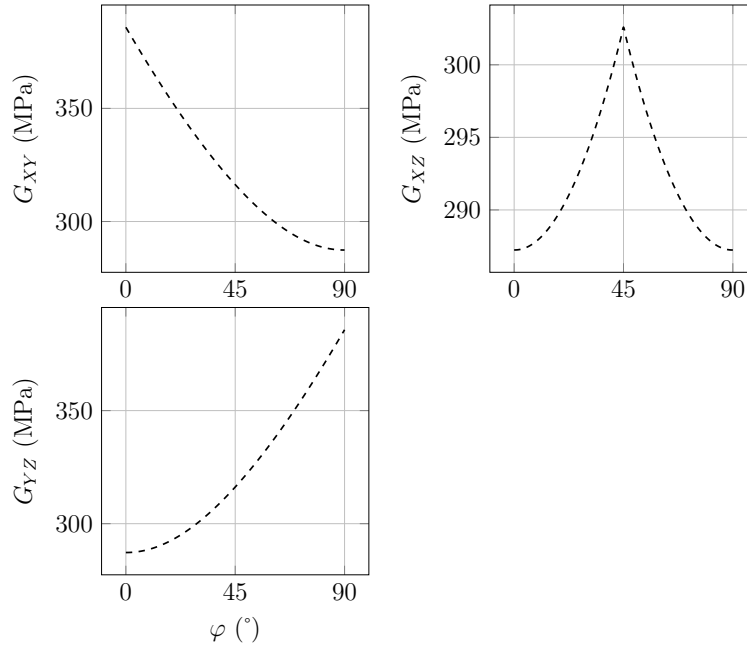


Figure 11.4 Variation of the shear moduli as a function of the fabrication angle of the lattice (φ).

The shear modulus along the xy plane decreases as the fabrication angle increases since the load is mainly carried by the green struts that are horizontal for $\varphi = 0^\circ$ and vertical for $\varphi = 90^\circ$. Similarly, the shear modulus G_{YZ} increases with the fabrication angle since the black diameter increases. The shear modulus G_{XZ} exhibits a maximum at $\varphi = 45^\circ$. It corresponds to the position where the diameter of the blue struts is maximal (horizontal struts).

In the case of the regular octet-truss lattice, the variation of shear modulus can be up to 25% in particular for G_{XY} and G_{YZ} . It is then important to tune the lattice orientation depending on its loading conditions.

Summary: The use of the equivalent diameter allows the prediction of the stiffness of a lattice structure depending on its orientation within the build. Depending on the lattice geometry, the variation of stiffness with the build orientation can be of critical importance.

Chapter 12

Parametric optimization of lattice structures made by EBM

Contents

11.1 From lattice orientation to struts orientation	157
11.2 Results of the simulation	158

In the previous chapter, a first application of the concept of the mechanical equivalent diameter has been performed. A single-parameter (fabrication angle of the lattice) optimization was performed.

Here, a multi-parameters optimization is performed. The general topology of the lattice is constant but the dimensions of some parameters can vary. The topology optimization is not used since it allows a shape variation of the matter. It is therefore impossible to directly use the equivalent diameters developed earlier.

12.1 Methodology and validation of the code

12.1.1 Scheme of the code

The aim of the parametric optimization is to define a set of parameters to adjust (strut diameter, length, angle between struts...) in order to maximize an objective function ($E_X, E_Y, E_Z, G_{XY}, G_{XZ}, G_{YZ} \dots$). The optimization is ruled by optimization constraints (maximum density, forbidden values for parameters...).

The specificity of this "realistic" optimization is that the objective function is calculated by taking into account the mechanical equivalent diameter ($D_{EQ}^{NUM} = f(D_{CAD}, \alpha)$).

An in-house procedure has been developed using a minimization code coupled with a FEM simulation using beam elements (CAST3M). The minimization script has been written in Python using the scipy library and the minimization algorithm called "Sequential Least Squared Programming" (SLSQP). It is an optimizer that allows a constraint minimization relying on the Han-Powell BFGS quasi-Newton method [105, 106].

The global architecture of the code is represented in figure 12.1:

The steps written in Python are shown in pink whereas the step of FEM simulation with CAST3M is shown in blue.

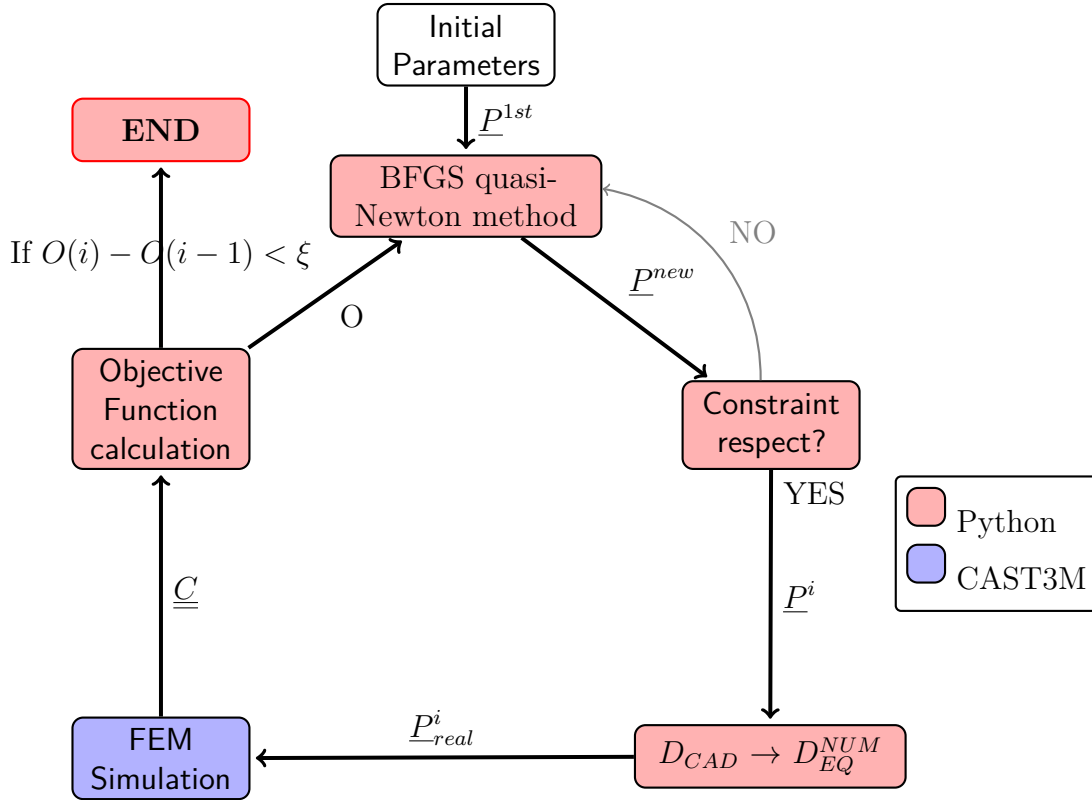


Figure 12.1 Schematic representation of the parametric optimization code architecture.

A set of initial parameters (\underline{P}^{1st}) is given to the SLSQP code to estimate the gradient and Hessian along each parameters. According to the direction of descent, a new set of parameters is proposed (\underline{P}^{new}). If they satisfy the minimization constraints, they will be further used, if not, a new set of parameters has to be given.

Within the parameters \underline{P}^i , the nominal diameter is modified into different mechanical equivalent diameters D_{EQ}^i for each strut depending on the orientation. The modified set of parameters is called \underline{P}_{real}^i .

A FEM simulation with beam elements is then computed using the equivalent diameters.

The output is the stiffness matrix (\underline{C}) from which the objective function (O) is calculated. If the difference in objective function is less than the convergence criterion (ξ), the algorithm stops. If not, the value of the objective function is given to the quasi-Newton method code for a new iteration. The objective function is composed of engineering constants coming from the stiffness matrix (E_Z for example). For example:

$$O = O(i) = \frac{E_Z(init)}{E_Z(i)}.$$

12.1.2 Validation of the code using the cantilever shape

To validate the code, an optimization of a cantilever composed of octet-truss unit-cells is carried out. The cantilever is composed of 18 octet-truss unit cells (six in x, one in y, three in z). It is rigidly fixed at its left end and loaded by a point force of 1kN at the center of the right surface (see figure 12.2).

For the purpose of validation of the code, no consideration of the manufacturing constraints are taken into account in the optimization. It could have been possible but

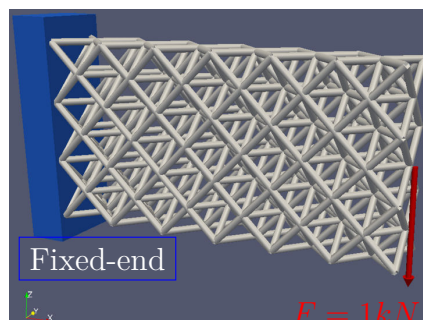


Figure 12.2 Cantilever composed of 18 octet-truss unit-cells. Loading conditions: Fixed-end at the left side and a point load of 1kN at the right end.

would require 72 parameters. In the optimization, the same diameter is affected for each unit-cell leading to 18 parameters (D_i).

The objective is to minimize the deflection at the point where the load is applied. The manufacturing constraints are set as follows:

- The relative density of the cantilever cannot be higher than 5%.
- The strut diameters cannot be lower than $400 \mu\text{m}$ (minimal resolution of the EBM process) and larger than 4 mm. $0.4 \text{ mm} < D_i < 4 \text{ mm}$

The initial diameters are set to 0.6 mm.

The algorithm takes 46 iterations to reach the convergence. The final geometry is shown in figure 12.3a. The colors corresponds to the size of the struts: a red strut exhibit a larger diameter than a blue one.

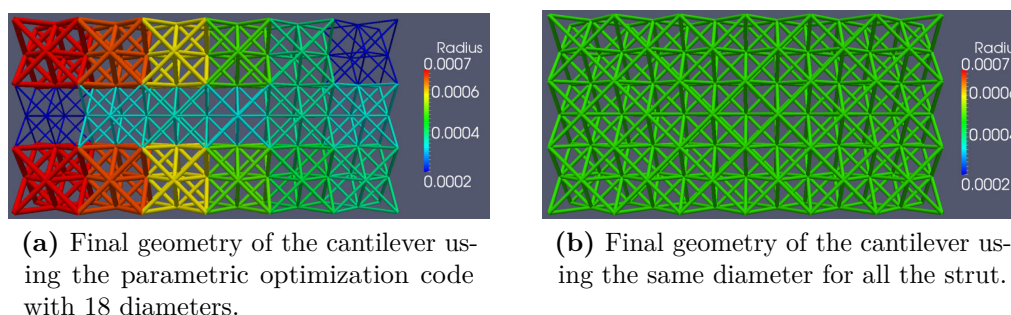


Figure 12.3 Final geometry of the cantilever made of octet-truss unit cells when using one diameter or 18 parameters.

The geometry resulting from this optimization is compared to the 5 % density cantilever having the same diameter for every struts (figure 12.3b). Both results have the same final density of 5 %. When the struts have the same diameter, the final deflection is of 2.18 mm whereas the parametric optimization results in a deflection of 1.55 mm (improvement of 30 %).

The final geometry in the case of the parametric optimization (12.3a) showed a specific distribution of the diameters. Unit-cells of larger density are distributed up and down

on the left side. It is really close to the optimal result of a topology optimization of a cantilever using the SIMP method developed by Sigmund [31] as shown in figure 12.4.

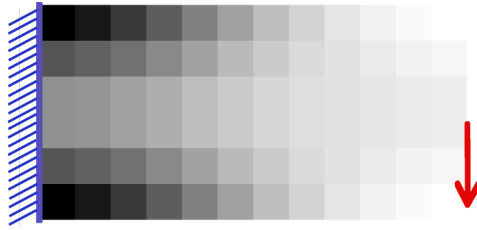


Figure 12.4 Final geometry of a cantilever using the SIMP method of topology optimization [31].

The comparison of shapes between the results with the parametric optimization and the topology optimization using the SIMP method allows the validation of the minimization code explained earlier 12.1.1.

12.2 "Realistic" Parametric Optimization of an octet-truss unit-cell

In this section, a parametric optimization that takes into account the mechanical equivalent diameters is developed. The optimization is based on the minimization detailed earlier (section 12.1.1). At each iteration, the objective function is calculated on an octet-truss unit-cell. The methodology developed in chapter 10 is used for the beam simulation of the structure with Periodic Boundary Conditions.

12.2.1 Parameters

The parameters for this parametric optimization are described in figure 12.5:

- D_{CAD} : The nominal strut diameter of the structure.
- l : The length of the struts.
- θ : The angle of opening of the structure. The regular octet-truss structure exhibits an angle $\theta=90^\circ$. For $\theta>90^\circ$, the octet-truss structure is elongated. On the contrary, octet-truss structures with an angle $\theta<90^\circ$ are flattened.
- The fabrication angle of the lattice φ is either set to 45° or include in the set of parameters.

12.2.2 Constraints

The optimization constraints are:

- $\bar{\rho} < 5\%$. The maximum density of the structure is set to 5 % to respect the limitations of the beam simulation.
- $D_{CAD} \geq 1mm$. The minimum nominal diameter is set to 1 mm.

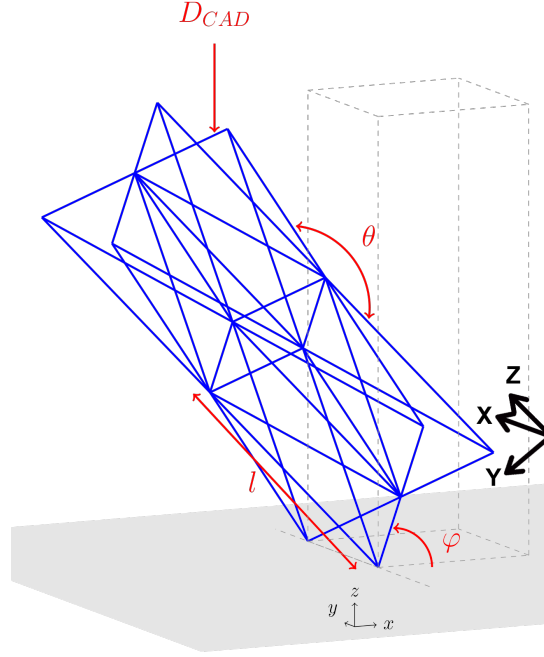


Figure 12.5 Scheme of the parameters for the parametric optimization procedures.

- $1mm \leq l \leq 3cm$. The produced lattice structures are composed of several unit-cells per sides. In order to be able to fit the dimensions of the build chamber of the EBM machine, the maximum strut length is set to 3 cm.
- $10^\circ \leq \theta \leq 170^\circ$. The opening angle can fluctuate largely but extreme positions are forbidden to avoid too flat structures.
- $10^\circ \leq \varphi \leq 80^\circ$. The constraints on this parameter have been highlighted in the previous chapter (chap 11). The forbidden position are for φ close to 0° and close to 90° where the removal of the structure from the start plate is difficult.

12.2.3 Objective function and initial parameters

The aim of this optimization is to maximize the Young's modulus along the Z direction (in the local coordinate system of the lattice): E_Z . Since the optimization is a minimization, the objective function is defined as:

$$O(i) = \frac{E_Z(init)}{E_Z(i)} \quad (12.1)$$

where $E_Z(0)$ is the initial value of Young's modulus

The initial parameters are set as : $D_{CAD} = 1.6mm$, $l = 2cm$, $\theta = 50^\circ$, $\varphi = 60^\circ$. For helping the numerical convergence of the algorithm, the parameters were normalized between 0 and 1.

→ The sensitivity of the initial conditions was assessed. The initial parameters were modified within their possible range leading to the same optimal parameters and final objective function value. Changing the initial parameters only led to a change in the number of iterations.

12.2.4 Results of optimization

Parametric optimization with parameters D_{CAD}, l, θ

For this optimization, the fabrication angle of the structure is set to $\varphi = 45^\circ$.

After 14 iterations, the convergence was achieved. Figure 12.6 shows the variation of the Young's modulus and parameters for each iteration. The Young's modulus converges to **2.5 GPa**.

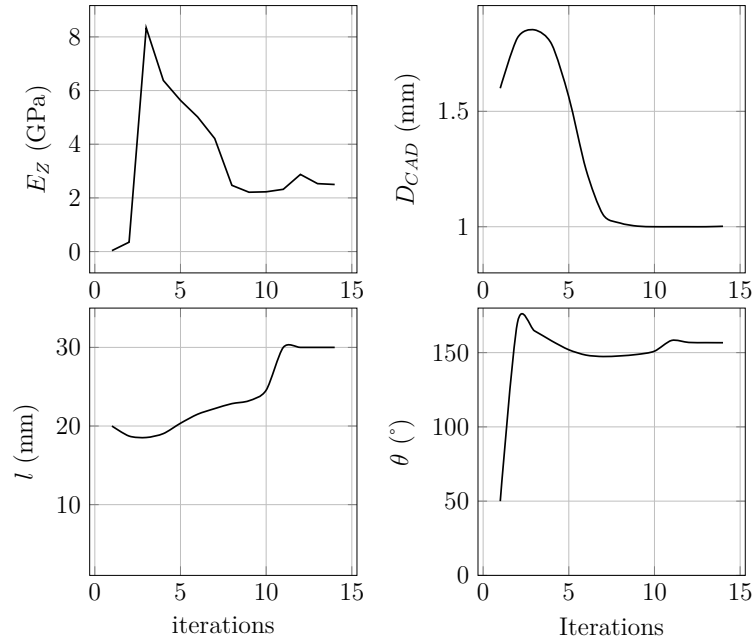


Figure 12.6 Variation of the parameters and objective function during the iterations of the optimization procedure.

The optimal parameters are: $D_{CAD} = 1.04\text{mm}$, $l = 3\text{cm}$, $\theta = 156^\circ$. The geometry is depicted in figure 12.7a.

Parametric optimization with parameters $D_{CAD}, l, \theta, \varphi$

For this optimization, the fabrication angle of the structure (φ) is a parameter.

After 17 iterations, the algorithm converges to the optimal geometry depicted in figure 12.7b. The optimal parameters are: $D_{CAD} = 1\text{mm}$, $l = 3\text{cm}$, $\theta = 157^\circ$, $\varphi = 80^\circ$.

The optimal Young's modulus is of **3.1 GPa** compared to 2.5 GPa for the previous optimization. **Hence, taking into account the lattice orientation angle (φ) within the optimization allows an improvement of 20 % in the final stiffness.**

12.2.5 Further development

We choose to focus here on the optimization of the Young's modulus along the Z direction by tuning a certain set of parameters.

The optimization code presented has the particularity of simulating the "true" properties of lattice structures fabricated by EBM. It can also easily be applied to other objective functions and parameters.

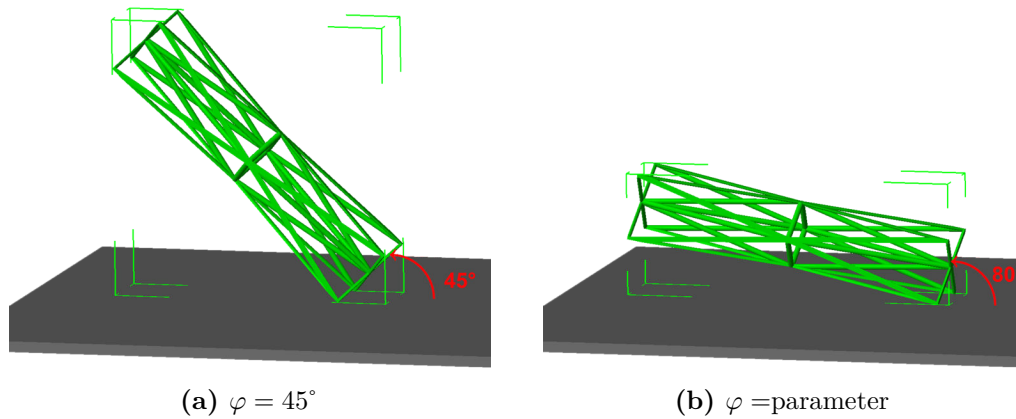


Figure 12.7 Geometry of the unit-cells that results from both parametric optimization procedures.

Some examples of other parametric optimizations are listed below:

Multi-diameters optimization The parametric optimization can take into account as parameters each strut diameter of the unit-cell. Depending on the objective function ($E, G, \nu \dots$), some struts will be enlarged whereas other will disappear. However, depending on the size of the simulated lattice, the numerical convergence can be difficult to achieve since there could be a large number of parameters.

Multi-criteria optimization The objective function is a combination of different engineering constants. For example one can minimize the weighted product of the Young's modulus along the Z direction and the shear modulus in the XY plane:

$$J = E_Z^\kappa G_{XY}^{1-\kappa} \quad (12.2)$$

Multi-physics optimization The objective function is a combination of stiffness and thermal conductivity. For examples one could need to minimize the weighted product J:

$$J = E_Z^\kappa \lambda_Z^{1-\kappa} \quad (12.3)$$

where λ_Z is the thermal conductivity along the Z direction. The thermal conductivity is also affected by the "efficient matter" within the struts.

Summary

Realistic mechanical optimization of lattice structures:

In this part, a methodology using an analytical equation of the equivalent diameters in a beam simulation has been presented. It was then applied to the optimization of orientation of an octet-truss lattice structure within the EBM chamber. This methodology was also used coupled to a parametric optimization based on a unit-cell simulation.

Beam simulation A FEM simulation using beam elements has been developed to allow a fast simulation of large structures or when a large repetitions of simulations are needed.

- The simulation was carried out on Timoshenko beams.
- The range of validity of this simulation was set to density less than five percent by comparing the Young's modulus results of simulation using volume element and beams.

Optimal orientation of lattice structures To validate the use of the equivalent diameters to simulate the "true" properties of lattice structures produced by EBM, the variation of the octet-truss orientation within the build has been investigated.

- Using the equivalent diameters, an optimal fabrication angle was extracted to maximize either a Young's modulus or a shear modulus.
- Depending on the architecture and on the mechanical properties to maximize, the optimal placement can improve the properties up to 30%.

Parametric optimization The analytical equation of $D_{EQ}^{NUM} = f(\alpha, D_{CAD})$ was used within a parametric optimization. At each step of the optimization the "true" properties are calculated.

- The parametric optimization relies on a quasi-Newton minimizer coupled with a beam simulation on the Octet-truss unit-cell.
- The contribution of the mechanical equivalent diameter is highlighted by comparing two parametric optimizations. When using the lattice orientation angle as a parameter of the optimization, it is possible to improve the resulting Young's modulus by 20 % using the concept of mechanical equivalent diameter.

Part V

Towards the improvement of strut's size and surface geometry

The previous parts focused on the mechanical characterization of lattice structures produced by EBM using standard process strategy. Struts size accuracy and surface irregularity were taken into account through the concept of mechanical equivalent diameter. The present part aims at improving this strut size accuracy and these surface irregularities. For that purpose, two methodologies were used:

- Using post-treatment. Electro-Chemical Polishing (ECP) and Chemical Etching (CE) treatments were used on lattice structures produced by EBM. The aim of these post-treatments is to decrease the surface irregularities, thus decrease the proportion of "inefficient" matter.
- Tuning the process strategy. The beam parameters and scan strategies were tuned to produce struts with a size closer to the nominal diameter.

Both studies should be considered as preliminary but give interesting insights to be further investigated.



Chapter 13

Improvement of the surface roughness through post-treatments

Contents

12.1	Methodology and validation of the code	161
12.1.1	Scheme of the code	161
12.1.2	Validation of the code using the cantilever shape	162
12.2	"Realistic" Parametric Optimization of an octet-truss unit-cell	164
12.2.1	Parameters	164
12.2.2	Constraints	164
12.2.3	Objective function and initial parameters	165
12.2.4	Results of optimization	166
	Parametric optimization with parameters D_{CAD}, l, θ	166
	Parametric optimization with parameters $D_{CAD}, l, \theta, \varphi$	166
12.2.5	Further development	166

When considering the fatigue properties of lattice structures produced by EBM, the surface roughness becomes critical since it acts as crack initiator. Reducing this roughness by a post-treatment becomes a necessary step. Furthermore, reducing the roughness can lead to improve the efficient matter within the strut (as seen in chapter 7).

In this chapter, two types of post-treatments are investigated. The experiences of Electro-Chemical Polishing (ECP) have been conducted during a one month visit at the LAMSI laboratory of "École de Technologie Supérieure", Montreal, Canada ¹. The study of the Chemical Etching (CE) was conducted within the frame of a collaboration with the laboratory 4MAT at "Université Libre de Bruxelles", Belgium.

Some studies have been carried out in the literature on the reduction of the surface roughness of lattice structures made by AM. Most of the studies have been released by Pika et al. [107–109] on lattice structures produced by LBM. They developed several image analysis tools to be able to extract the strut diameter, total pore size, closed pores size and surface roughness of struts.

¹ Under the supervision of V. Brailowski

They used Chemical Etching (CE) and Electro-Chemical Polishing (ECP) to improve the surface roughness of struts produced by LBM. CE and ECP on as-built struts allowed a decrease of the arithmetic roughness from $12\ \mu\text{m}$ to $6\ \mu\text{m}$. They used an aqueous solution composed of 1 %_{vol} of hydrofluoric acid (HF) for the CE and an electrolyte composed of acetic acid, HF and sulfuric acid for the ECP. The ECP was carried out with a current density of $120\ \text{mA}/\text{cm}^2$.

13.1 Electro-Chemical Polishing

13.1.1 Parameters and methodology

The structures used for this study are octet-truss lattices with different densities and nominal strut diameters. We focus here on the results obtained on an octet-truss lattice with a relative density of 6% and struts with a nominal diameter of 1 mm since it is representative of the possibilities and limitations of the ECP. Lattice structures with different densities exhibited the same trends when undergoing ECP.

The electrolyte used for the ECP was composed of 10%_{vol} of perchloric acid and 90%_{vol} of acetic acid. From the results of previous studies on the ECP of bulk parts², the passivation current density (value to form a passivation oxide layer) was found to be in the range of $10\ \text{mA}/\text{cm}^2$ for this electrolyte. The current density was set to this value for the whole study.

A scheme of the set-up is represented in figure 13.1a. The lattice structures were manufactured with a supplementary part at the top to fix the electrode on it (see top of lattice in figure 13.1b). They were immersed into the acid electrolyte for 20 min for half the volume of the lattice. A picture of a polished structure is represented in figure 13.1b.

The cathode was composed of five 316L stainless steel plates equidistant from the lattice. Since the reaction of ECP is exothermic, the electrolyte was cooled down using water at the border.

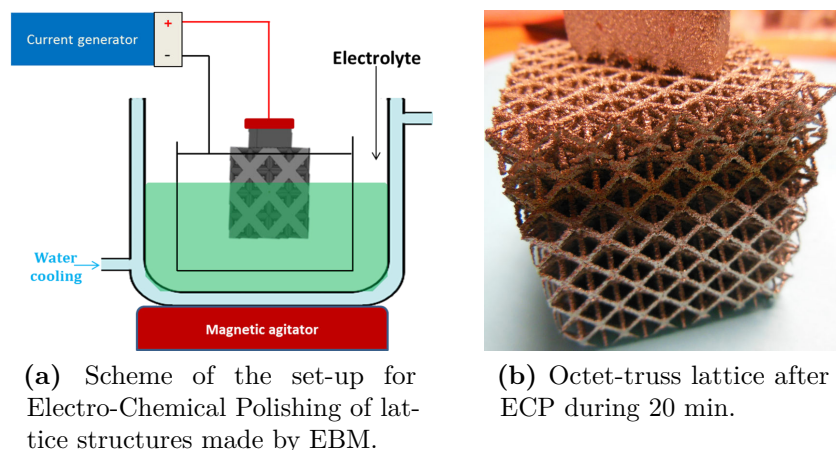


Figure 13.1 Scheme of the set-up and polished structure.

From figure 13.1b, a large difference of surface roughness is observed between the ECP

²Internship of Anthony Desenfant at LAMSI

zone (bottom) and the raw zone (top). The effect of this process on the roughness is investigated in the next section.

13.1.2 Results

SEM characterization

SEM analysis of the external struts of the lattice allowed a qualitative investigation of the effect of the ECP on the surface roughness of the struts. Figure 13.2 shows the micrographs of three struts of the same lattice after ECP.

Figure 13.2a depicts a strut in the non-immersed zone where no ECP occurred. It represents the raw surface of a 1 mm strut produced by EBM. The roughness characterized in 7.2.4 is observed. The black spots correspond to some pollution of the sample that could not be removed.

Figure 13.2b shows the surface of a strut in the center of a face of the lattice structure. The strut was directly in front of a plane of the electrode. Its surface seems smoother than for a raw strut. The powders stuck to the strut have been removed.

Figure 13.2c represents a strut at the bottom corner of the lattice. This strut faced three planes of the electrode. The polishing was therefore more efficient in this zone. The powders that stuck to the strut were removed by the ECP and only some wavy irregularities remain.

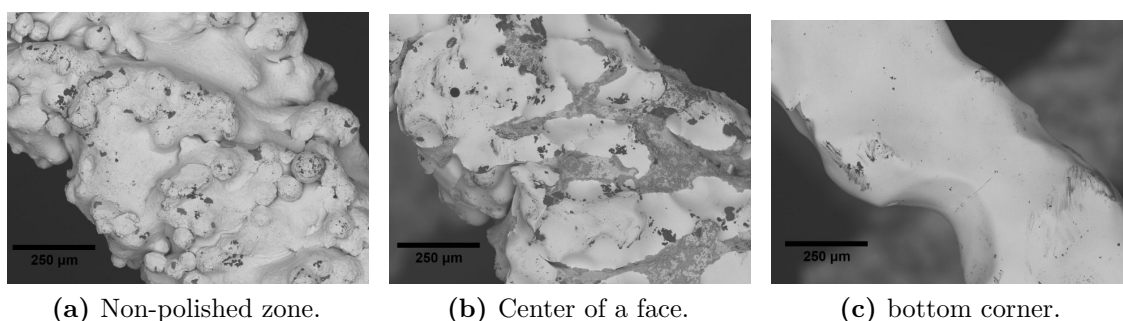


Figure 13.2 SEM micrographs of the external struts of the octet-truss lattice with a density of 6% after 20 min of ECP.

A grey surface seems to appear on the ECP struts. This phenomenon is not observed in raw struts. When zooming at this zone, it seems to be a layer of small platelets (Figure 13.3a). This zone has been analyzed using Energy-Dispersive X-Ray Spectroscopy (EDX).

The results of the EDX analysis on the yellow line in figure 13.3a are represented in figure 13.3b. They showed a decrease of the titanium concentration and an increase of the oxygen one, suggesting a presence of a Ti oxide layer.

Some studies have shown that ion-immersion on titanium surface can lead to a titanium oxide layer [110–113]. For example, Gong et al. [112] used the anodic oxidation to form an oxide layer in pure titanium sheets. They immersed the pure titanium sheet into an aqueous solution containing hydrofluoric acid. The morphology of the oxide layer that they obtained is very similar to the one of figure 13.3a. The titanium oxide layer is formed by applying the passivation current. It is employed often to an oxide layer with a controlled thickness and morphology. It can then be used in a corrosive environment.

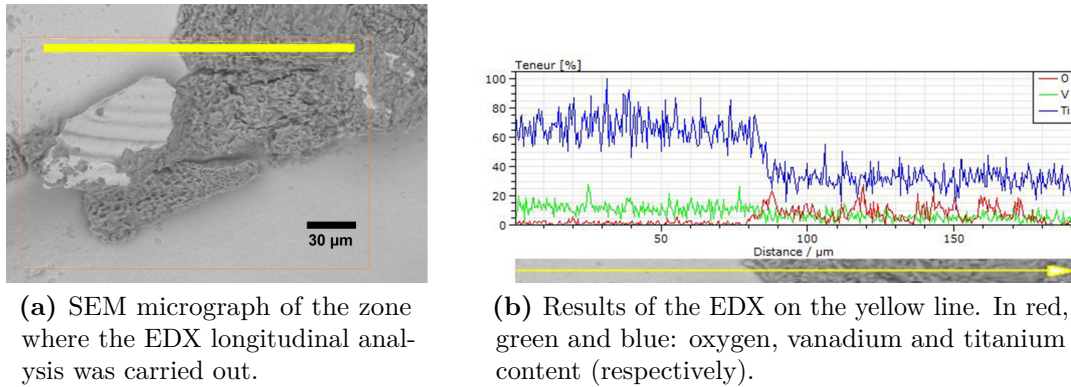


Figure 13.3 EDX analysis of the ECP octet-truss lattice structure.

X-Ray tomography characterization

X-Ray tomography was carried out on the ECP struts at different zones using the same methodology as paragraph 7.1.2. Struts built with the same orientation ($\alpha = 45^\circ$) are analyzed. Figure 13.4 shows the position of the struts that were structurally characterized by X-ray tomography.

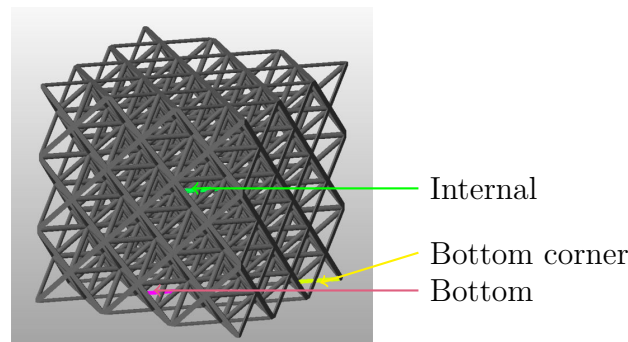


Figure 13.4 Position of the analyzed struts within the lattice. The lattice was fabricated with an angle $\varphi = 45^\circ$.

Four different struts with a 1-mm nominal diameter are compared. Struts that did not undergo ECP are denoted "Raw". From figure 13.4, struts that underwent ECP are denoted "Internal", "Bottom" and "Bottom Corner" depending on their position within the structure.

The geometry of the struts is shown in figure 13.5. The ECP effects are largely inhomogeneous. It confirms the observations made by SEM. The strut inside the lattice ("Internal") exhibits almost the same surface as the raw strut.

On the contrary, struts on the edges of the lattice underwent a larger ECP. The strut at the bottom corner of the lattice is largely polished and do not exhibit the two-scales roughness typical from the EBM process. However, when decreasing the roughness, the volume of the strut decreased drastically.

Using the methodology developed earlier (paragraph 7.1.3), the roughness was computed along the circumference of the four struts of figure 13.5. The results are plotted in figure 13.6.

The raw strut and the internal one exhibit the same trend of arithmetic roughness.

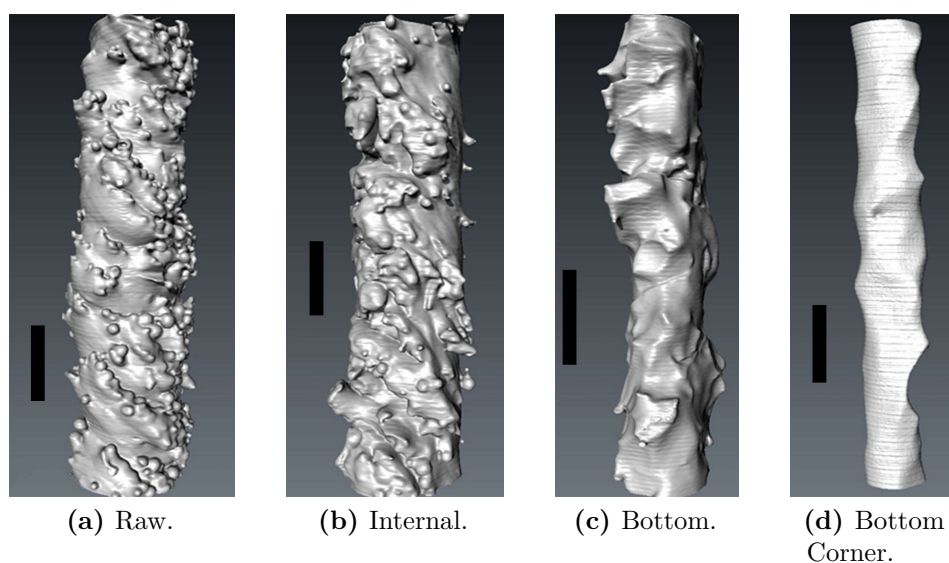


Figure 13.5 3D image of 1 mm struts as-built ("Raw") and at different locations within the lattice after ECP ("Internal", "Bottom" and "Bottom Corner"). The struts were fabricated with the same build angle of 45°. The scale bar represents 500 μm .

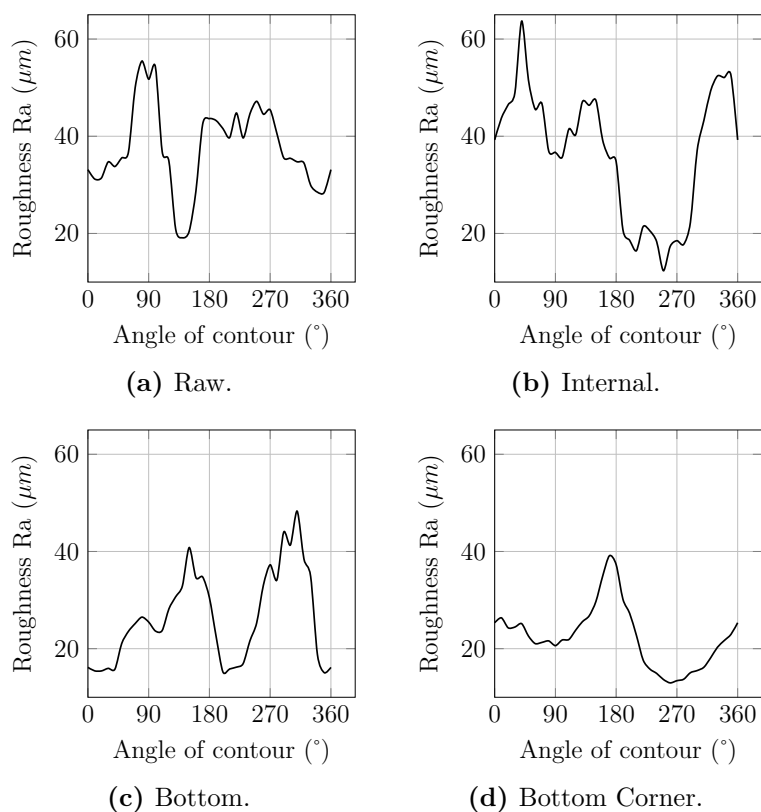


Figure 13.6 Variation of the arithmetic roughness for raw struts and struts undergoing ECP at different locations of the lattice structure.

The mean arithmetic roughness is the same for both struts ($\text{Ra}=44\mu\text{m}$). Thus, the internal

strut did not undergo any polishing.

On the contrary, a reduction of roughness is observed for the "Bottom" and "Bottom Corner" struts. The mean roughness for the bottom strut has been calculated as $27 \mu\text{m}$ and $22 \mu\text{m}$ for the "Bottom Corner" one.

The Electro-Chemical Polishing is thus very inhomogeneous for lattice structures. The polishing occurs preferentially in the struts that directly face the cathode plates. Struts inside the lattice structure undergo almost no polishing. Such a treatment does not seem adequate for lattice structures. Another post-processing process is presented in the next section: the Chemical Etching.

13.2 Chemical Etching

Chemical Etching on lattice structures produced by Laser Beam Melting has been studied by Pyka et al. [108]. They immersed a titanium structure in an aqueous solution composed of HF with a concentration ranging from 0.5wt% to 1.1wt%. Their aim was to remove the particles that stuck to the struts. They find an optimum when immersing structures for 12 min in a solution containing 0.6 wt% HF. In our case the aim is not only to remove the particles that stuck to the melt pool but also to decrease the "plate-pile" stacking effect. Different acid concentration and time of etching are used.

13.2.1 Parameters and methodology

As mentioned in the introduction, the results presented in this section are coming from a collaboration with the Université Libre de Bruxelles (ULB) ³.

The etching solution was composed of 3% HF and 13% HNO₃. The samples were etched two times for two hours. The samples used for the Chemical Etching are presented in figure 13.7.

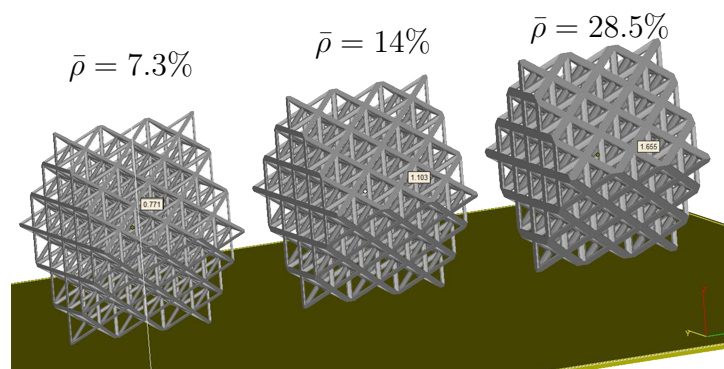


Figure 13.7 Octet-truss lattices used for CE.

They are composed of three unit-cells per side. The width and height of the structures are kept constant. The variation of density is carried out by a variation of struts diameters, set to 0.8 mm, 1.1 mm, 1.7 mm for a density of 7.3%, 14% and 28.5% respectively.

³Collaboration with Stéphane Godet and Charlotte de Formanoir. The chemical etching has been carried out at their laboratory and the production and structural characterization was conducted at Grenoble.

13.2.2 Results

Structural characterization

After CE, the lattice structures exhibit a smaller density (28.5%→21%, 14%→7%, 7%→4%). For the structural characterization, a focus has been made on the higher density structure which exhibits a final density of 21% (as-built 28.5%). From this structure, two struts were extracted and compared with an "as-built" one. One strut was extracted from the border of the lattice and is denoted "external" and another one came from the inside of the lattice and is denoted "internal".

The same X-ray tomography method has been used as for the ECP. The shape of the struts before and after CE are represented in figure 13.8. The Chemical Etching allows an improvement of the surface geometry of the struts. From a qualitative point of view, the etching seems homogeneous since the external and internal struts exhibit a similar surface.

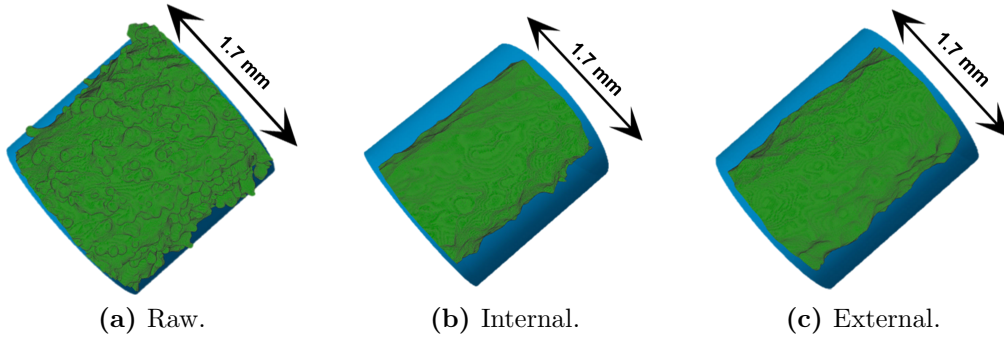


Figure 13.8 3D image of 1.7 mm struts as-built ("Raw") and at different locations within the lattice after CE ("Internal" and "External"). The blue cylinder represents the designed cylinder having a diameter $D_{CAD} = 1.7mm$.

The CE treatment allows the removal of the particles that stuck in the strut as well as a reduction of the plate-pile like stacking structure of the surface irregularities.

The arithmetic roughness of the struts is extracted using the same methodology as paragraph 7.1.3. The variation of the arithmetic roughness as a function of the angle of the extracted contour is plotted in figure 13.9 for the raw strut and for the internal and external struts after EC treatment. The mean roughness of the "as-built" strut is calculated as $35 \mu m$ whereas the mean roughness for the internal strut after EC is calculated as $26 \mu m$ and $24 \mu m$ for the external one.

Mechanical characterization

The mechanical equivalent cylinder was computed for each struts (following the methodology of paragraph 7.3.2). The percentage of inefficient matter can be computed using this formula:

$$\Delta_{EQ}^{NUM} = \frac{V_{Cyl}^{EQ} - V_{strut}}{V_{strut}} \quad (13.1)$$

where V_{strut} is the volume of the strut and V_{Cyl}^{EQ} is the volume of the mechanical equivalent cylinder. For the "as-built" strut, there is 7% of inefficient matter which is reduced to 3% after CE treatment.

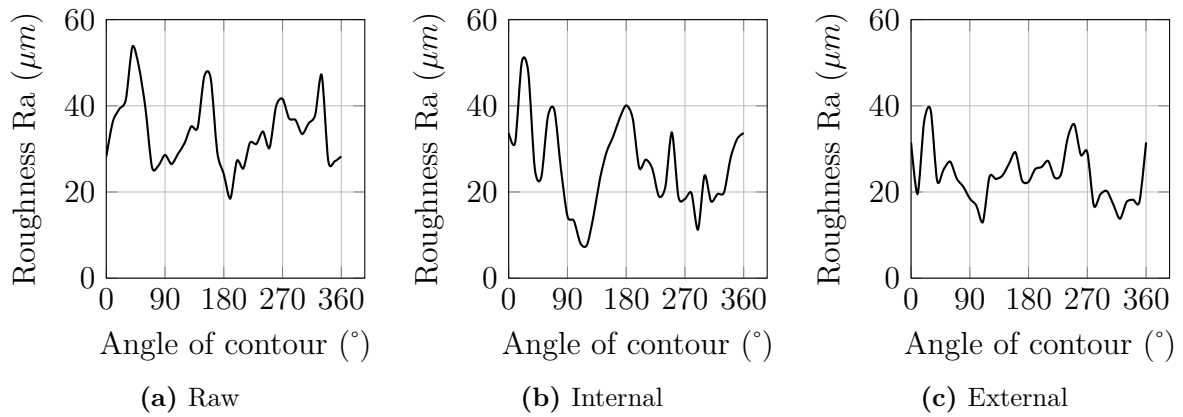


Figure 13.9 Variation of the arithmetic roughness for raw struts and struts undergoing CE at different locations of the lattice structure.

The Young's modulus of the structure before and after CE treatment was assessed by uniaxial compression following the same methodology as section 8.2. The results are plotted in figure 13.10.

The Young's modulus of the "raw" structure is lower than the reference one (obtained by FEM simulation in figure 8.9). The Young's modulus of the structures after CE is closer to the reference value of the simulation (green). **This improvement comes from the decreasing of the inefficient matter within the struts.**

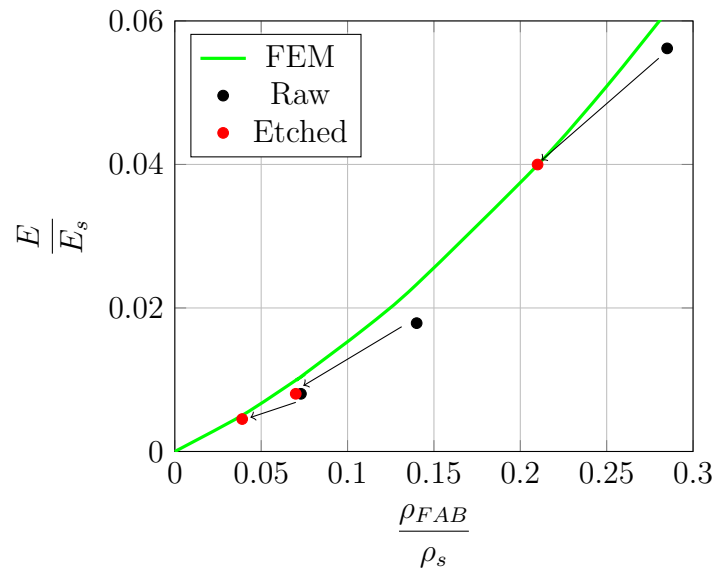


Figure 13.10 Relative Young's modulus as a function of the relative density for "as-built" lattice (black) and treated lattices (red) compared to the FEM simulation (green).

Thus, the Chemical Etching (CE) allows an homogeneous treatment to decrease drastically the roughness and increase the percentage of efficient volume within lattice structures manufactured by Electron Beam Melting.

Chapter 14

Improvement of the strut's size through the EBM process

Contents

13.1	Electro-Chemical Polishing	176
13.1.1	Parameters and methodology	176
13.1.2	Results	177
	SEM characterization	177
	X-Ray tomography characterization	178
13.2	Chemical Etching	180
13.2.1	Parameters and methodology	180
13.2.2	Results	181
	Structural characterization	181
	Mechanical characterization	181

The aim of this chapter is to improve the strut size and shape by tuning the process parameters and strategies. Two main approaches are studied.

The first one is to change the process strategies to produce struts that exhibit a mechanical equivalent diameter having the same size as the nominal diameter.

The second one is to allow concentric circle beam path for melting vertical struts with larger diameters (e.g. 5 mm) instead of a hatching strategy.

14.1 Improvement of the size accuracy for a 1 mm vertical strut

14.1.1 Methodology

As mentioned earlier (paragraph 7.2.3), when producing 1 mm struts with the "Net" theme, the produced struts are thinner than the designed ones. In order to be closer to the CAD diameter, the process parameters have to be changed. In this study we focus on vertical struts. The standard "Net" strategy for melting a vertical 1 mm-diameter strut is shown in figure 14.1a. The idea for producing larger struts is to decrease the first contour offset

(CO_1) but using the same process parameters (see paragraph 7.1.1). The internal contours have been added to fully melt the strut.

To do that, we have used a thermal Finite Element simulation ¹. This FEM simulation takes as input a Gaussian heat source that follows a path on a surface having the density and thermal conductivity of the sintered powder. Although the simulation of few layers is time-consuming, it allows a prediction of the optimal first contour offset to fully melt a cylinder with a 1 mm diameter.

The result of this simulation shows that the optimal first contour offset is 0.128 mm instead of 0.3 mm for the standard one. This optimal first contour offset is denoted CO_1^{OPT} (as shown in figure 14.1b).

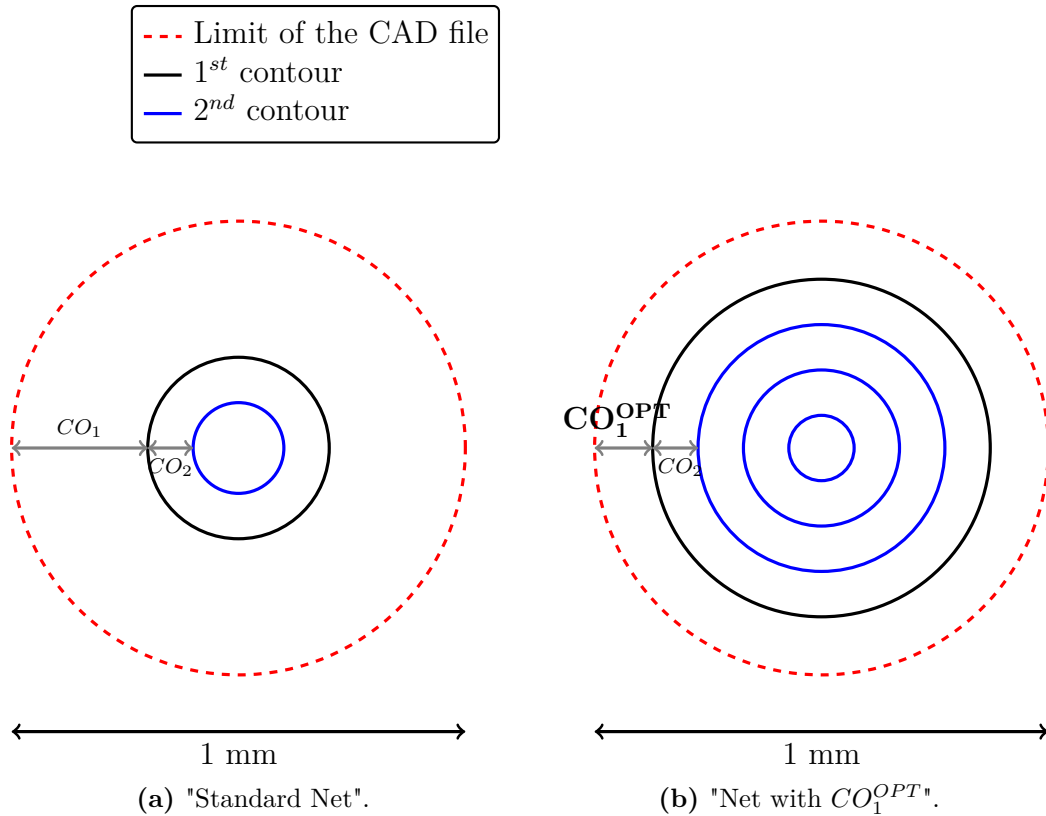


Figure 14.1 Scheme of the melting path at a random layer for a 1 mm circular vertical strut when using different set of parameters (standard "Net" theme and modified "Net" theme with the optimal first contour offset).

Figure 14.1 shows the difference of the process strategies between the standard "Net" theme (14.1a) and the process strategy using the optimal first contour offset(14.1b). The optimized theme exhibits 3 inner contours with the same process parameters to fully melt the area of the strut.

The volume energy has been calculated for both process parameters and strategies using the formula explained in the first part:

$$E_V = \frac{E}{S_{CAD}h_{layer}} \quad (14.1)$$

where E is the beam energy, S_{CAD} is the surface of the CAD file and h_{layer} is the height of the layer of the process.

¹Performed by Nicolas Béraud (Currently PhD student at G-Scop laboratory in Grenoble)

The "Net" theme has a volume energy of $2.1 \cdot 10^{10} \text{ J/m}^3$. For the modified "Net" theme with a first contour offset of 0.128 mm, the volume energy was calculated as $3.8 \cdot 10^{10} \text{ J/m}^3$. The new process theme ("Net with CO_1^{OPT} ") is then supposed to melt larger volume.

1 mm-diameter struts were produced vertically with the process parameter of the theme "Net with CO_1^{OPT} " and further analyzed by X-ray tomography.

14.1.2 Results

The structural analysis of vertical struts produced either with the "Net" theme or with the "Net with CO_1^{OPT} " theme is represented in figure 14.2. One can observe that the modified theme produces larger strut than with the standard "Net" theme. The roughness seems to be in the same order of magnitude.

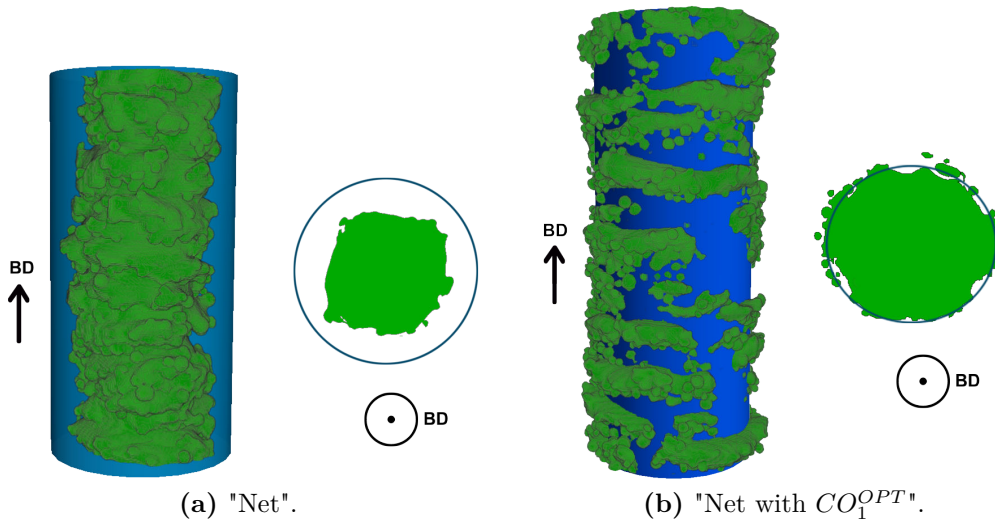


Figure 14.2 Vertical and cross-section views of the 1 mm-diameter vertical struts produced with both themes. The build direction is represented with the black arrows.

A quantitative analysis of the produced struts is carried out following the same methodology as in section 7.1. From this analysis, the porosity content, the mechanical equivalent diameter and the mean surface roughness are extracted. The values are reported in table 14.1.

Results show that the change of process parameters allowed a large increase of the mechanical equivalent diameter. Although it does not reach the nominal diameter (1 mm), the mechanical equivalent diameter is almost twice larger when optimizing the process parameters. Thus, the effect of size difference on the stiffness of the struts is reduced.

	D_{EQ}^{NUM} [mm]	Porosity [%]	R_a [μm]	R_t [μm]
"Net"	0.46	0.035	40.7	213.3
"Net with CO_1^{OPT} "	0.84	0.025	47.9	265

Table 14.1 Results of mechanical equivalent diameter, porosity level, and roughness of 1 mm-diameter vertical struts manufactured with two different process parameters.

However, the roughness does not decrease when using the "Net with CO_1^{OPT} " theme. On the contrary it increases slightly. This increase can be attributed to the larger volume energy for melting that can lead to remelting of the contour of the strut. This change of roughness increases the "inefficient" matter within the strut.

The porosity level remains really low ($<0.1\%$) for both themes.

The variation of first contour offset allowed to create struts with a diameter closer to the nominal one, but did not allow a reduction of the "inefficient" volume within the strut.

14.2 Variation of the scan strategy for 5 mm-diameter struts

This section presents a preliminary study which aims at changing the beam path strategy for large struts. The results presented here are focused on vertical 5 mm-diameter struts. The changes presented in this section are not based on a thermal FEM simulation but rely on a trial-and-error procedure.

14.2.1 Methodology

The standard methodology to manufacture large struts is to use the standard "Melt" theme. Figure 14.3a presents the strategy to melt a vertical 5 mm-diameter strut with this strategy. To melt a layer, the beam scans two circular contours and then follows a hatching path following a snake approach. Since the designed strut exhibits a circular cross-section, a change of the beam path strategy from a rectangular beam path to a circular one was investigated. Instead of having a rectangular hatching, the beam scans concentric contours from the outside to inside (14.3b).

The beam parameters for the "Melt" theme are sum up in the following table (14.2). The values in red are reference values that can fluctuate during the hatching step. Two different themes have been developed following the path of figure 14.3b. They are based on the concentric contours.

For the first one, the beam parameters have been tuned to finally have the same volume energy as the "Melt" theme. This theme is called CC SE for "Concentric Contours with Same Energy". However it needs much more time to melt a layer.

The theme "CC SESP" follows the concentric contours path with different parameters. The new parameters allow a melting with the same volume energy and the same volume power than the "Melt" theme. This theme is called CC SESP for "Concentric Contours with Same Energy Same Power".

14.2.2 Results

Vertical struts have been created with the three different themes. Their geometry can be observed in figure 14.4. For each strut, a longitudinal view allows the visualization of the size of the strut and the comparison with the designed one. The other view is a top view that shows the projection of the pores (in red).

Qualitatively, the theme CC SE seems to lead to largely porous parts (figure 14.4b). The pores are no longer spherical but exhibit an elongated shape. Some of the pores are

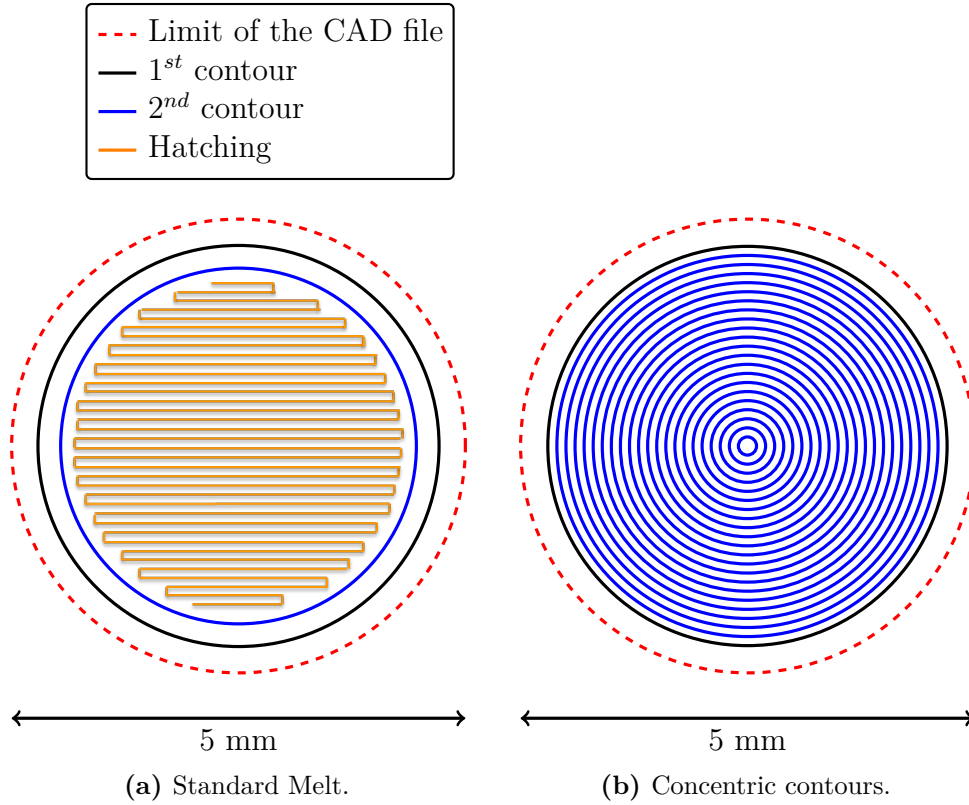


Figure 14.3 Scheme of the melting path at a random layer for a vertical 5 mm-diameter strut with the standard "Melt" theme and the modified one.

		Melt	CC SE	CC SESP
1st Contour	Offset [mm]	0.29	0.3	0.3
	Speed [mm/s]	340	470	2100
	Current [mA]	4	2.4	7.9
2nd Contour	Offset [mm]	0.25	0.1	0.1
	Speed [mm/s]	800	470	2050
	Current [mA]	10	2	8.35
Hatching	Offset [mm]	0.1		
	Speed [mm/s]	4530		
	Current [mA]	15		
Global	Volume Energy [J/m^3] (14.1)	$4.2 \cdot 10^{10}$	$4.3 \cdot 10^{10}$	$4.2 \cdot 10^{10}$
	Time for a layer [s]	$8.3 \cdot 10^{-2}$	$3.6 \cdot 10^{-1}$	$8.3 \cdot 10^{-2}$
	Volume Power [W/m^3] (2.3)	$5.1 \cdot 10^{11}$	$1.2 \cdot 10^{11}$	$5.1 \cdot 10^{11}$

Table 14.2 Parameters values for melting a vertical strut with a 5 mm-diameter for different themes. Red values correspond to reference values that fluctuate during the fabrication depending on Arcam algorithm.

spread in the whole height of the strut. When a pore is created at a given height, it will not be filled at the next layer and the pore will grow as the strut keeps on fabricating.

For the "Melt" theme and the CC SESP, the pores are mainly spherical and the porosity level seems low.

The size accuracy between the manufactured strut and the designed one can be assessed for the different themes. It can be seen that the theme CC SE produces thinner struts.

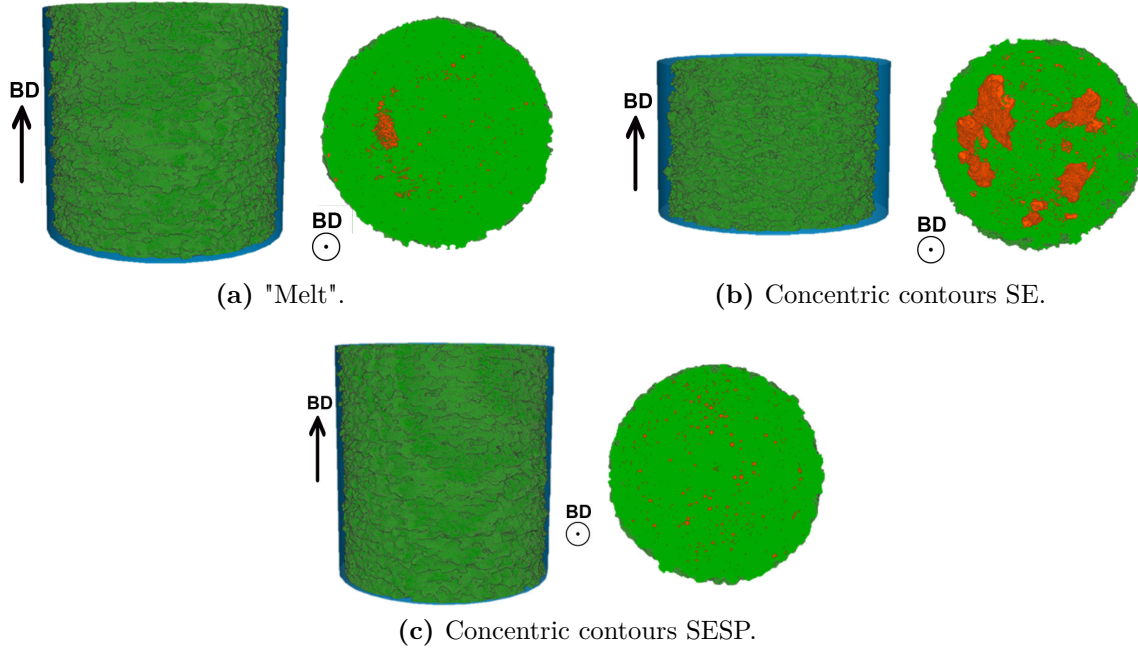


Figure 14.4 Vertical and cross-section views of the 5 mm-diameter vertical struts produced with different themes. The build direction is represented with the black arrows.

This is due to a lower melting power associated to the large pores.

The quantitative results from the 3D images are represented in the table 14.3.

The theme CC SE is largely "porous" (>3%) and exhibits a mechanical equivalent diameter lower than for the "Melt" theme. It can be understood by looking at the process parameters. The fabrication using this theme allows the same volume energy than the "Melt" theme. However it takes a longer time to melt the same surface. Therefore the energy is much more dissipated and do not allow an efficient melting. The necessity to melt with the *same energy* and *same power* is highlighted.

Indeed, when melting using the CC SESP theme, the porosity level remains lower than 0.1% and the mechanical equivalent diameter is similar to the one of the "Melt" theme.

	D_{EQ}^{NUM} [mm]	Porosity [%]	R_a [μm]	R_t [μm]
"Melt"	4.54	0.047	31.4	199.2
Concentric Contours SE	4	3.38	48.6	276.5
Concentric Contours SE SP	4.58	0.031	32.8	235.5

Table 14.3 Results of mechanical equivalent diameter, porosity level, and roughness of 5 mm-diameter vertical struts manufactured with three different process strategies.

In terms of roughness, there is no clear improvement between the "Melt" theme and the "CC SESP" theme. Both themes exhibit a mean arithmetic roughness of 32 μm and a maximum roughness of around 200 μm .

The methodology developed here leads to the same geometry than the standard "Melt" theme.

There is a real need of a thermal simulation of the EBM process that can predict the melted volume and surface irregularities depending on the beam path and parameters. in

this case, the trial-error methodology is not efficient to improve the strut quality.

Summary

In this part, two ways of improving the strut's geometry and surface roughness were investigated:

Improvement through post-treatment:

Two different types of post-treatment were used for improving the surface irregularities of the EBM-processed lattices:

Electro-chemical polishing (ECP) • A solution containing 10 %_{vol} of perchloric acid and 90 %_{vol} of acetic acid was used as an electrolyte for the ECP.

- The current density used for this study was set as the passivation current of 10 mA/cm^2 .
- The ECP was very inhomogeneous within the lattice structure. Internal struts exhibit almost no polishing whereas struts of the external faces of the lattice structures are much more polished.
- The final arithmetic roughness can reach less than 20 μm (starting from a mean roughness of around 40 μm).
- An oxide layer can be formed due to the reaction between the titanium and the acid ions.

Chemical Etching (CE) • The solution for CE consists of 3 %_{vol} HF and 13 %_{vol} HNO_3 . Samples were etched for four hours.

- The CE is much more homogeneous through the lattice structures. The mean roughness of the struts after CE was calculated as 24-26 μm .
- The mechanical properties of lattice structures after CE was assessed and compared with the "raw" properties. The CE reduces the volume of "inefficient" matter. Thus the final Young's Modulus of the etched lattice is similar to the reference Young's modulus for such structure.

Improvement through EBM process strategy:

The process parameters and beam path were tuned to optimize the melting of vertical 1 mm-diameter and 5-mm diameter struts. The aim is to reduce the difference in size between designed struts and fabricated ones.

1 mm-diameter struts The size of a 1 mm-diameter vertical strut was optimized by changing the process strategy.

- Using a thermal simulation, a new contour offset has been set to enlarge the produced strut.
- The produced strut exhibits a mechanical equivalent diameter of $0.84 \mu m$ versus $0.46 \mu m$ when melting with the "Net" theme.

5 mm-diameter struts The beam path of a vertical 5 mm-diameter was adjusted using concentric contours instead of squared beam lines.

- For 5 mm-diameter struts, the beam path has been changed using only concentric contours.
- When melting with the same energy as for the "Melt" theme, large pores appear. They results from a lack of melting due to a large time to melt a layer.
- When melting with the same energy and same power as for the "Melt" theme, the porosity level remains low ($<0.1\%$) but no improvement has been observed compared to the standard "Melt" theme.
- A thermal simulation of the beam path is highly needed to improve the EBM process.

Conclusion and future work

Conclusions

Aim and strategy

The aim of this PhD was to characterize and optimize lattice structures manufactured by Additive Manufacturing using the Electron Beam Melting technology. The problematic has been split into different parts. Firstly, a microstructural and mechanical characterization of the constitutive material allowed the understanding of the inner properties of the struts.

Then, the characterization of struts was focused on 1 mm-diameter struts. The use of X-ray tomography and image analysis was crucial to fully characterize the inner and outer structure of the struts. FFT simulation on the struts images allowed the stiffness prediction of single struts. The produced lattice structures were characterized by uniaxial compression.

A mechanical equivalent diameter was assessed for different strut diameters and orientations. The introduction of this equivalent diameter allows us to take into account the constraints of the EBM process into simulations and mechanical optimization procedures.

Lastly, two ways of improving the strut geometry were investigated: either by post-treatment or by tuning the EBM process strategy.

Main results

Characterization of the constitutive material

The microstructure of thin struts and bulk parts was assessed:

- Both microstructures exhibit a lamellar morphology of the α phase and a preferential orientation of the parent β grains along the build direction.
- Thin struts show a slightly finer parent β grain size than bulk parts. This could lead to a higher hardness for such thin parts.

The same mechanical properties were observed between small struts and larger ones. However, the roughness has a large impact on the ductility of the produced parts.

Oxygen pick up during reuses of the initial powder has been highlighted by elementary analysis. It influences drastically the mechanical properties by reducing the elongation to failure and increasing the yield strength.

An influence of the pore distribution and mode of failure on the ductility of EBM-produced tensile samples has been shown.

Stiffness prediction of lattice structures produced by EBM

- When using standard process parameters, the porosity level remains lower than 0.1%. Pores are spherical and mainly come from the atomization process of the powders.
- The produced struts are systematically thinner than the designed ones. Thus, the produced lattice structures have a lower density than the designed ones.
- Due to large surface irregularities, the struts can be separated into "efficient" and "inefficient" matter. The stiffness of the strut is carried by the "efficient" matter.

-
- By computing the elastic stiffness of the strut, a mechanical equivalent diameter was proposed (D_{EQ}^{NUM}). It is the diameter of a circular cylinder having the stiffness of the strut. It allows to take into account both phenomena: the size discrepancy and the efficient matter.
 - This mechanical equivalent diameter was validated by comparing numerical prediction and experimental data on an octet-truss lattice structure.
 - An analytic value of the mechanical equivalent diameters as a function of the strut orientation (α) and nominal diameter (D_{CAD}) was assessed: $D_{EQ}^{NUM} = f(\alpha, D_{CAD})$.

Mechanical optimization

- The analytic value of mechanical equivalent diameters was used in a FEM simulation to find the optimal orientation of a lattice structure within the process. This optimization of orientation may lead to significant improvements of elastic properties.
- The analytic value of D_{EQ}^{NUM} was also used in a parametric optimization. This "realistic" optimization compute the "true" properties of the lattice at each iteration. It allows to largely improve the distribution of matter by taking into account the manufacturing constraints.

Improvement of strut size and surface morphology

- Electro-Chemical Polishing (ECP) and Chemical Etching (CE) post-treatments were applied on lattice structures. The ECP treatment is not efficient because it exhibits a large inhomogeneity of polishing between the external struts and the struts inside the lattice structure.

On the other side, CE treatment allows an homogeneous reduction of the surface irregularities. It allows a decrease of the "inefficient" matter.

- The use of a thermal simulation of the EBM process has been highlighted for the optimization of process strategies to melt struts with a diameter closer to the nominal one. A trial-and-error methodology did not allow improvement of size or surface roughness.

Future work

Generalization of the concept of "mechanical equivalent diameter"

The mechanical equivalent diameter defined in this work allows us to take into account differences between the input design and the fabricated part for lattice structures: not only differences in size but also differences in mechanical response (concept of inefficient matter).

Through two examples, we have shown the ability to use this equivalent diameter in "in-house" parametric optimization procedures. The developed rules have larger implications. It would indeed be interesting to introduce into commercial codes, similar "response surface" linked to a specific process (Laser or Electron Beam Melting). Some process

constraints should also be introduced: *e.g.* a minimum thickness for trusses, forbidden angles of fabrication, minimum size of cell (for powder removal purpose) *etc.* When not only stiffness properties are concerned, the influence of the orientation of the struts on the microstructure and texture should also be investigated.

The mechanical equivalent diameter defined here refers only to stiffness properties. It is sufficient for some applications (launcher for example). For many others (bio-medical, aeronautics...), **fatigue properties** are of crucial importance. The surface roughness of lattice structures produced by EBM can be critical in this context. A preliminary study on the reduction of the roughness was assessed in this PhD using post-treatments such as Chemical Etching. However, it would be interesting to see the impact of such reduction of roughness on the fatigue characteristics of the structures. The presence of few bulk porosity would lead also to poor properties in fatigue.

A question arises: does exist a critical thickness, a critical bulk porosity under which it is not possible to use lattice structures for parts submitted to cyclic loading?

The approach proposed in this work could be a starting point for such a study.

Application of lattice structures

Lattice structures are of interest for a purpose of weight saving. They can be directly introduced in a design process. They can also emerge from a topological optimization procedure. Some methods (*e.g.* SIMP method [30,31]) define an optimal distribution of matter in terms of "grey levels". These grey levels may correspond, locally, to a given level of mechanical properties (as discussed in the work of Brackett et al. [32]). That means that light-but-stiff structures resulting from topological optimization could be divided into fully dense zones and "lattice" zones [114]. For such configurations, a **conformal implementation** of lattice structures has to be optimized to improve the interface between zones of different density, and especially, between dense zones and "lattice" zones.

In that sense, we developed a software "lattice-creator" that allows one to produce random and periodic lattice structures. The description of the possibilities of the software is detailed in appendix D. It gives the user the possibility to create graded structures as shown in figure 14.5. It is possible to produce a porosity gradient and to fix the bulk part on the dense side of the lattice.

Here again, numerical predictions of the mechanical properties of such structures should take into account the mechanical equivalent diameter, as defined in this work.

When dealing with such "lattice" zones, one has to allow the powder to be removed after the fabrication process. This manufacturing constraint can limit the range of application of "lattice" zones. Anyway, it requires a systematic study. Such a study has been carried out for bulk parts [76], but lacks for lattice structures.

Lattice structures as hosting architecture

The **osseointegration** of prosthesis is critical for improving the performances of the implant. The use of porous zones within a prosthesis can reduce the Young's modulus of the prosthesis and avoid the "stress-shielding" effect which induce an unfavorable stress distribution at the bone-implant interface. This phenomena is due to a large difference of

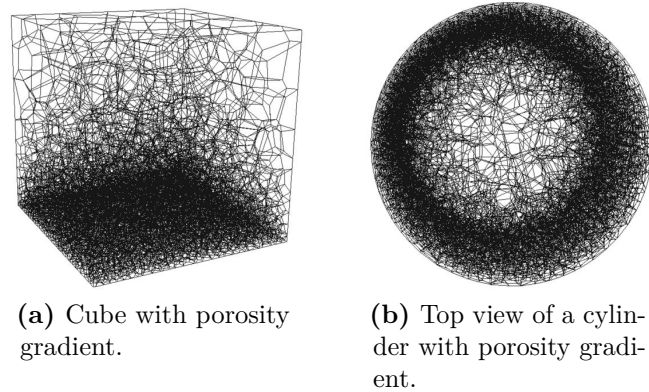


Figure 14.5 Example of structures with porosity gradient obtained using the "lattice-creator" (see appendix D).

stiffness between the prosthesis and the bone. It can damage the bone at the interface with the implant.

Porous zones are also hosting structures for osseous cells. Numerous questions are still open: what is the role of the pore size? what is the role of the surface roughness? do we need monomodal or bimodal distribution of pores? [115]. For sure, to optimize the osseointegration, one need to control perfectly the strut size and pores dimensions. From the results of this PhD, it would be interesting to dig further in this direction.

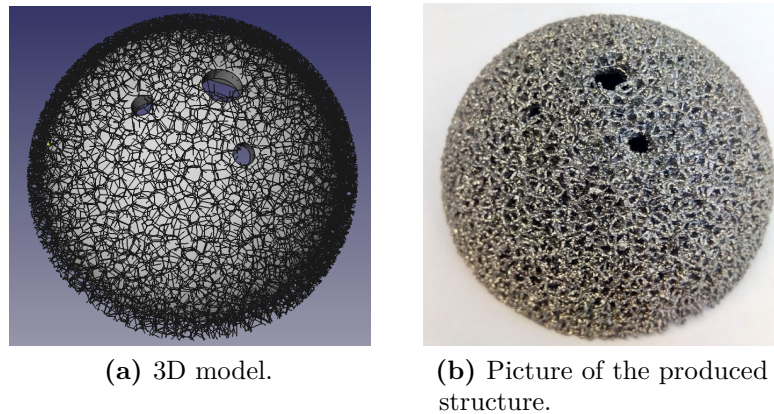


Figure 14.6 Model and produced acetabular cups. The trabecular surface has been obtained using the "lattice-creator" program (appendix D).

An example of an acetabular cup with the surface designed using the "lattice-creator" software is shown in figure 14.6a. The produced cup is shown in 14.6b.

Another way to imagine lattice structures as hosting structures is to use it as one of the constituent of a composite material. More precisely, it is possible to create composites composed of two co-continuous phases. The metal lattice structure would be a skeleton embedded in a "matrix phase" in such a way we can combine the properties of the stiff, rigid lattice structure with the properties of a more deformable "matrix" phase, for example a polymer. A first example will focus on the fabrication of a composite "metal lattice"

filled by a polymeric foam, in order to create a damping structure (Collaborative work with R. Rinaldi, INSA Lyon).

Thermal simulation of the EBM process

The need for predictive tools of the thermal history of the build is an essential milestone towards a better control of the dimensional quality and properties of fabricated parts. Such modeling approach may be of different level of complexity [33,34]. In section 14.1, we have compared a strut fabricated by EBM with the prediction of a simple model currently developed at Grenoble [35].

It is for sure a first step to be continued, at least at the level of small and simple parts such as elementary trusses of different size and orientation, and then at the scale of their assembly. Such development requires alternatively two steps of validation: An "a posteriori" validation, similar to the one done in this work, using for example tomographic analysis or fine roughness calculation, but also (and more complex), an "in situ" validation [116,117]. It is the price to pay to validate numerical simulation, predicting, as a function of the scan strategies, the occurrence of "bad melting", "defects", "porosity" ...



Bibliography

- [1] Mike Ashby. Designing architected materials. *Scripta Materialia*, 68(1):4–7, jan 2013.
- [2] Chris I. Hammetter, Renaud G. Rinaldi, and Frank W. Zok. Pyramidal Lattice Structures for High Strength and Energy Absorption. *Journal of Applied Mechanics*, (c):1–41, 2012.
- [3] Haydn N G Wadley. Multifunctional periodic cellular metals. *Philosophical transactions. Series A, Mathematical, physical, and engineering sciences*, 364(1838):31–68, jan 2006.
- [4] A G Evans, J W Hutchinson, and M F Ashby. Multifunctionality of cellular metal systems. *Progress in Materials Science*, 43(43):171–221, 1999.
- [5] Sriharsha S. Sundarram and Wei Li. The effect of pore size and porosity on thermal management performance of phase change material infiltrated microcellular metal foams. *Applied Thermal Engineering*, 64(1-2):147–154, 2014.
- [6] Carolin Körner, F. Wein, Y. Liebold-Ribeiro, Jan Schwerdtfeger, and Michael Stingl. Combining additive manufacturing with mathematical optimization to realize periodic cellular structures with new properties, 2012.
- [7] V.S. Deshpande, M.F. Ashby, and N.a. Fleck. Foam topology: bending versus stretching dominated architectures. *Acta Materialia*, 49(6):1035–1040, apr 2001.
- [8] J Clerk Maxwell. On the calculation of the equilibrium and stiffness of frames. *Philosophical Magazine Series 4*, 27(182):294–299, apr 1864.
- [9] Lorna J. Gibson and Michael F. Ashby. The Mechanics of Three-Dimensional Cellular Materials. *Proceedings of the Royal Society A: Mathematical, Physical and Engineering Sciences*, 382(1782):43–59, jul 1982.
- [10] G Kooistra, V.S. Deshpande, and Haydn N.G. Wadley. Compressive behavior of age hardenable tetrahedral lattice truss structures made from aluminium. *Acta Materialia*, 52(14):4229–4237, aug 2004.
- [11] Gregory W. Kooistra and Haydn N.G. Wadley. Lattice truss structures from expanded metal sheet. *Materials & Design*, 28(2):507–514, jan 2007.
- [12] H Wadley. Fabrication and structural performance of periodic cellular metal sandwich structures. *Composites Science and Technology*, 63(16):2331–2343, dec 2003.

-
- [13] Douglas T. Queheillalt and H. N G Wadley. Cellular metal lattices with hollow trusses. *Acta Materialia*, 53(2):303–313, 2005.
- [14] Tushar Ramkrishna Mahale. *Electron Beam Melting of Advanced Materials and Structures*. PhD thesis, Graduate Faculty of North Carolina State University, 2009.
- [15] Lawrence E. Murr, S.M. Gaytan, D.A. Ramirez, E. Martinez, J. Hernandez, and Krista Amato. Metal Fabrication by Additive Manufacturing Using Laser and Electron Beam Melting Technologies. *Journal of Material Science & Technology*, 28(1):1–14, 2012.
- [16] Mari Koike, Preston Greer, Kelly Owen, Guo Lilly, Lawrence E. Murr, Sara M. Gaytan, Edwin Martinez, and Toru Okabe. Evaluation of Titanium Alloys Fabricated Using Rapid Prototyping Technologies-Electron Beam Melting and Laser Beam Melting. *Materials*, 4(12):1776–1792, oct 2011.
- [17] Bey Vrancken, Lore Thijs, Jean-Pierre Kruth, and Jan Van Humbeeck. Heat treatment of Ti6Al4V produced by Selective Laser Melting: Microstructure and mechanical properties. *Journal of Alloys and Compounds*, 541:177–185, nov 2012.
- [18] S. Tammam-Williams, H. Zhao, F. Léonard, F. Derguti, I. Todd, and P.B. Prangnell. XCT Analysis of the Influence of Melt Strategies on Defect Population in Ti-6Al-4V Components Manufactured by Selective Electron Beam Melting. *Materials Characterization*, 102:47–61, feb 2015.
- [19] Adnan Safdar and LY Wei. Microstructures of electron beam melted (EBM) bio-material Ti-6Al-4V. *Materials Research Society Symposium Proceedings*, 1132:4–9, 2009.
- [20] Adnan Safdar. *A Study on Electron Beam Melted Ti6Al4V*. PhD thesis, Faculty of Engineering, Lund University, 2012.
- [21] Joakim Karlsson, Torsten Sjögren, Anders Snis, Håkan Engqvist, and Jukka Lausmaa. Digital image correlation analysis of local strain fields on Ti6Al4V manufactured by electron beam melting. *Materials Science and Engineering: A*, 618:456–461, nov 2014.
- [22] A. Safdar, L.-Y. Wei, A. Snis, and Z. Lai. Evaluation of microstructural development in electron beam melted Ti-6Al-4V. *Materials Characterization*, 65(D1d):8–15, mar 2012.
- [23] Nikolas Hrabe and Timothy Quinn. Effects of processing on microstructure and mechanical properties of a titanium alloy (Ti-6Al-4V) fabricated using electron beam melting (EBM), Part 2: Energy input, orientation, and location. *Materials Science and Engineering: A*, 573:271–277, mar 2013.
- [24] L.E. Murr, E.V. Esquivel, S.a. Quinones, S.M. Gaytan, M.I. Lopez, E.Y. Martinez, F. Medina, D.H. Hernandez, E. Martinez, J.L. Martinez, S.W. Stafford, D.K. Brown, T. Hoppe, W. Meyers, U. Lindhe, and R.B. Wicker. Microstructures and mechanical properties of electron beam-rapid manufactured Ti6Al4V biomedical prototypes compared to wrought Ti6Al4V. *Materials Characterization*, 60(2):96–105, feb 2009.

- [25] V. Juechter, T. Scharowsky, R.F. Singer, and C. Körner. Processing window and evaporation phenomena for Ti-6Al-4V produced by selective electron beam melting. *Acta Materialia*, 76:252–258, sep 2014.
- [26] Alphons a. Antonysamy. *Microstructure , Texture and Mechanical Property Evolution during Additive Manufacturing of Ti6Al4V Alloy for Aerospace Applications*. PhD thesis, University of Sheffield, 2012.
- [27] Haijun Gong, Khalid Rafi, Thomas Starr, and Brent Stucker. The Effects of Processing Parameters on Defect Regularity in Ti-6Al-4V Parts Fabricated By Selective Laser Melting and Electron Beam Melting. In *International Solid Freeform Fabrication Symposium - An Additive Manufacturing Conference*, pages 424–439, 2013.
- [28] J. M. Oh, B. G. Lee, S. W. Cho, S. W. Lee, G. S. Choi, and J. W. Lim. Oxygen effects on the mechanical properties and lattice strain of Ti and Ti-6Al-4V. *Metals and Materials International*, 17(5):733–736, 2011.
- [29] R.I Jaffee and H. M. Burte. Critical review. In *Titanium science and technology*, pages 1665–1693. 1973.
- [30] Ole Sigmund. On the Design of Compliant Mechanisms Using Topology Optimization. *Mechanics of Structures and Machines: An International Journal*, 25(October 2012):493–524, 1997.
- [31] O. Sigmund. A 99 line topology optimization code written in matlab. *Structural and Multidisciplinary Optimization*, 21(2):120–127, 2001.
- [32] D Brackett, I Ashcroft, and R Hague. Topology Optimization For Additive Manufacturing. pages 348–362, 2011.
- [33] P Peyre, P Aubry, R Fabbro, R Neveu, and a Longuet. Analytical and numerical modelling of the direct metal deposition laser process. *Journal of Physics D: Applied Physics*, 41(2):025403, 2008.
- [34] 3DSIM. <http://3dsim.com/>.
- [35] Nicolas Beraud. PhD thesis in progress. 2016.
- [36] John W.C. Dunlop and Peter Fratzl. Multilevel architectures in natural materials. *Scripta Materialia*, 68(1):8–12, jan 2013.
- [37] Y. Brechet and J.D. Embury. Architected materials: Expanding materials space. *Scripta Materialia*, 68(1):1–3, jan 2013.
- [38] P. K. Mallick. *Fiber-Reinforced composites. Materials, Manufacturing and Design*. Taylor & Francis Group, crc press edition, 2007.
- [39] M F Ashby. The properties of foams and lattices. *Philosophical transactions. Series A, Mathematical, physical, and engineering sciences*, 364(1838):15–30, jan 2006.
- [40] H.X. Zhu, J.F. Knott, and N.J. Mills. Analysis of the elastic properties of open-cell foams with tetrakaidecahedral cells. *Journal of the Mechanics and Physics of Solids*, 45(3):319–343, mar 1997.

-
- [41] Sahab Babae, Babak Haghpanah Jahromi, Amin Ajdari, Hamid Nayeb-Hashemi, and Ashkan Vaziri. Mechanical properties of open-cell rhombic dodecahedron cellular structures. *Acta Materialia*, 60(6-7):2873–2885, apr 2012.
- [42] V. S. Deshpande, N A Fleck, and M F Ashby. Effective properties of the octet-truss lattice material. *Journal of the Mechanics and Physics of Solids*, 49:1747–1769, 2001.
- [43] R Lakes. Foam structures with negative poisson’s ratio. *Sciences*, 235:1038–1040, 1987.
- [44] Li Yang, Ola Harrysson, Harvey West, and Denis Cormier. Compressive properties of Ti-6Al-4V auxetic mesh structures made by electron beam melting. *Acta Materialia*, 60(8):3370–3379, may 2012.
- [45] Juan Carlos Álvarez Elipe and Andrés Díaz Lantada. Comparative study of auxetic geometries by means of computer-aided design and engineering. *Smart Materials and Structures*, 21(10):105004, oct 2012.
- [46] J. Dirrenberger, S. Forest, D. Jeulin, and C. Colin. Homogenization of periodic auxetic materials. *Procedia Engineering*, 10:1847–1852, 2011.
- [47] Luc Salvo, Guilhem Martin, Mathieu Suard, Ariane Marmottant, Rémy Dendievel, and Jean-Jacques Blandin. Processing and structures of solids foams. *Comptes Rendus Physique*, 15(8-9):662–673, nov 2014.
- [48] Russell Goodall, Ariane Marmottant, Luc Salvo, and Andreas Mortensen. Spherical pore replicated microcellular aluminium: Processing and influence on properties. *Materials Science and Engineering: A*, 465(1-2):124–135, sep 2007.
- [49] Y. Conde, J.-F. Despois, R. Goodall, A. Marmottant, L. Salvo, C. San Marchi, and A. Mortensen. Replication Processing of Highly Porous Materials. *Advanced Engineering Materials*, 8(9):795–803, sep 2006.
- [50] T. A. Schaedler, A. J. Jacobsen, A. Torrents, A. E. Sorensen, J. Lian, J R Greer, L Valdevit, and W B Carter. Ultralight Metallic microlattices. *Science*, 334(6058):962–5, nov 2011.
- [51] Benjamin Vayre, Frédéric Vignat, and François Villeneuve. Metallic additive manufacturing: state-of-the-art review and prospects. *Mechanics & Industry*, 13(2):89–96, may 2012.
- [52] Kaufui V. Wong and Aldo Hernandez. A Review of Additive Manufacturing. *ISRN Mechanical Engineering*, 2012:1–10, 2012.
- [53] William E. Frazier. Metal Additive Manufacturing: A Review. *Journal of Materials Engineering and Performance*, 23(6):1917–1928, apr 2014.
- [54] Erhard Brandl, Christoph Leyens, and Frank Palm. Mechanical Properties of Additive Manufactured Ti-6Al-4V Using Wire and Powder Based Processes. *IOP Conference Series: Materials Science and Engineering*, 26:012004, dec 2011.

- [55] Erhard Brandl, Vesselin Michailov, Bernd Viehweger, and Christoph Leyens. Deposition of Ti-6Al-4V using laser and wire, part I: Microstructural properties of single beads. *Surface and Coatings Technology*, 206(6):1120–1129, dec 2011.
- [56] H. P. Tang, M. Qian, N. Liu, X. Z. Zhang, G. Y. Yang, and J. Wang. Effect of Powder Reuse Times on Additive Manufacturing of Ti-6Al-4V by Selective Electron Beam Melting. *Jom*, 67(3):555–563, feb 2015.
- [57] N Béraud, F Vignat, F Villeneuve, and R Dendievel. New trajectories in Electron Beam Melting manufacturing to reduce curling effect. In *Proceedings of the 47th CIRP Conference on Manufacturing Systems*, volume 00, pages 0–5, 2014.
- [58] Eric Jones, Christopher Sutcliffe, and Robin Stamp. Laser-produced porous structure, 2006.
- [59] Taek Bo Kim, Sheng Yue, Ziyu Zhang, Eric Jones, Julian R. Jones, and Peter D. Lee. Additive manufactured porous titanium structures: Through-process quantification of pore and strut networks. *Journal of Materials Processing Technology*, 214(11):2706–2715, nov 2014.
- [60] Greet Kerckhofs, Grzegorz Pyka, Maarten Moesen, Simon Van Bael, Jan Schrooten, and Martine Wevers. High-Resolution Microfocus X-Ray Computed Tomography for 3D Surface Roughness Measurements of Additive Manufactured Porous Materials. *Advanced Engineering Materials*, 15(3):153–158, mar 2013.
- [61] S. Van Bael, G. Kerckhofs, M. Moesen, G. Pyka, J. Schrooten, and J.P. Kruth. Micro-CT-based improvement of geometrical and mechanical controllability of selective laser melted Ti6Al4V porous structures. *Materials Science and Engineering: A*, 528(24):7423–7431, sep 2011.
- [62] Bartłomiej Wysocki, Wojciech Swieszkowski, and Krzysztof Jan Kurzydłowski. Porous Titanium Scaffold Fabrication For Bone Tissue Engineering By SLM (Selective Laser Melting) Method. In *DDMC 2014*, pages 2–5, Berlin, 2014. Fraunhofer.
- [63] Peter Heintl, A. Rottmair, Carolin Körner, and Robert F. Singer. Cellular Titanium by Selective Electron Beam Melting. *Advanced Engineering Materials*, 9(5):360–364, may 2007.
- [64] O. Cansizoglu, O. Harrysson, D. Cormier, H. West, and T. Mahale. Properties of Ti-6Al-4V non-stochastic lattice structures fabricated via electron beam melting. *Materials Science and Engineering: A*, 492(1-2):468–474, sep 2008.
- [65] L E Murr, S M Gaytan, F Medina, H Lopez, E Martinez, B I Machado, D H Hernandez, L Martinez, M I Lopez, R B Wicker, and J Bracke. Next-generation biomedical implants using additive manufacturing of complex, cellular and functional mesh arrays. *Philosophical transactions. Series A, Mathematical, physical, and engineering sciences*, 368(1917):1999–2032, apr 2010.
- [66] Timothy J. Horn, Ola L.a. Harrysson, Denis J. Marcellin-Little, Harvey a. West, B. Duncan X. Lascelles, and Ronald Aman. Flexural properties of Ti6Al4V rhombic dodecahedron open cellular structures fabricated with electron beam melting. *Additive Manufacturing*, 1-4:2–11, 2014.

-
- [67] S J Li, Q S Xu, Z Wang, W T Hou, Y L Hao, R Yang, and L E Murr. Influence of cell shape on mechanical properties of Ti-6Al-4V meshes fabricated by electron beam melting method. *Acta biomaterialia*, 10(10):4537–47, oct 2014.
- [68] E. Hernández-Nava, C.J. Smith, F. Derguti, S. Tammas-Williams, F. Léonard, P.J. Withers, I. Todd, and R. Goodall. The effect of density and feature size on mechanical properties of isostructural metallic foams produced by additive manufacturing. *Acta Materialia*, 85:387–395, feb 2015.
- [69] S. McKown, Y. Shen, W.K. Brookes, C.J. Sutcliffe, W.J. Cantwell, G.S. Langdon, G.N. Nurick, and M.D. Theobald. The quasi-static and blast loading response of lattice structures. *International Journal of Impact Engineering*, 35(8):795–810, aug 2008.
- [70] M Jamshidinia, F Kong, and R Kovacevic. The Numerical Modelling of Fatigue Properties of a Biocompatible Dental Implant Produced by Electron Beam Melting (EBM). In *International Solid Freeform Fabrication Symposium*, pages 791–804, 2013.
- [71] M. Jamshidinia, L. Wang, W. Tong, and R. Kovacevic. The Bio-Compatible Dental Implant Desined by Using Non-Stochastic Porosity Produced by Electron Beam Melting (EBM). *Journal of Materials Processing Technology*, mar 2014.
- [72] S.J. Li, Lawrence E. Murr, X.Y. Cheng, Z.B. Zhang, Y.L. Hao, R. Yang, F. Medina, and R.B. Wicker. Compression fatigue behavior of Ti-6Al-4V mesh arrays fabricated by electron beam melting. *Acta Materialia*, 60(3):793–802, feb 2012.
- [73] D.a. Ramirez, L.E. Murr, S.J. Li, Y.X. Tian, E. Martinez, J.L. Martinez, B.I. Machado, S.M. Gaytan, F. Medina, and R.B. Wicker. Open-cellular copper structures fabricated by additive manufacturing using electron beam melting. *Materials Science and Engineering: A*, 528(16-17):5379–5386, jun 2011.
- [74] F.a. List, R.R. Dehoff, L.E. Lowe, and W.J. Sames. Properties of Inconel 625 mesh structures grown by electron beam additive manufacturing. *Materials Science and Engineering: A*, 615:191–197, oct 2014.
- [75] Lawrence E. Murr, Shujun Li, Yuxing Tian, Krista Amato, Edwin Martinez, and Frank Medina. Open-Cellular Co-Base and Ni-Base Superalloys Fabricated by Electron Beam Melting. *Materials*, 4(4):782–790, apr 2011.
- [76] Benjamin Vayre. *Conception pour la fabrication additive , application à la technologie EBM*. PhD thesis, Université Grenoble-Alpes, 2014.
- [77] Hazman Hasib, Ola L.a. Harrysson, and Harvey a. West. Powder Removal from Ti-6Al-4V Cellular Structures Fabricated via Electron Beam Melting. *Jom*, 67(3):639–646, feb 2015.
- [78] Lawrence E. Murr, Edwin Martinez, S.M. Gaytan, D.A. Ramirez, B.I. Machado, P.W. Shindo, J.L. Martinez, F. Medina, J. Wooten, D. Ciscel, U. Ackelid, and R.B. Wicker. Microstructural Architecture, Microstructures, and Mechanical Properties for a Nickel-Base Superalloy Fabricated by Electron Beam Melting. *Metallurgical and Materials Transactions A*, 42(11):3491–3508, jun 2011.

- [79] L.E. Murr. Metallurgy of Additive Manufacturing: Examples from Electron Beam Melting. *Additive Manufacturing*, pages 2–15, dec 2014.
- [80] Carolin Körner, Harald Helmer, Andreas Bauereiß, and Robert F. Singer. Tailoring the grain structure of IN718 during selective electron beam melting. *MATEC Web of Conferences*, 14:08001, aug 2014.
- [81] Jan Schwerdtfeger and Carolin Körner. Selective electron beam melting of Ti-48Al-2Nb-2Cr: Microstructure and aluminium loss. *Intermetallics*, 49:29–35, jun 2014.
- [82] Yves Combres. *Métallurgie et recyclage du titane et de ses alliages*, 1997.
- [83] G. Lutjering and J. C. Williams. *Titanium*. Springer, 2007.
- [84] T. Ahmed and H.J. Rack. Phase transformations during cooling in $\alpha+\beta$ titanium alloys. *Materials Science and Engineering: A*, 243(1-2):206–211, mar 1998.
- [85] R K Nalla, B L Boyce, J P Campbell, J O Peters, and R O Ritchie. Influence of Microstructure on High-Cycle Fatigue of Ti-6Al-4V : Bimodal vs . Lamellar Structures. *Metallurgical and Materials Transactions A*, 33(March):899–918, 2002.
- [86] Cyril Cayron. ARPGE: A computer program to automatically reconstruct the parent grains from electron backscatter diffraction data. *Journal of Applied Crystallography*, 40(6):1183–1188, 2007.
- [87] S. S. Al-Bermani, M. L. Blackmore, W. Zhang, and I. Todd. The Origin of Microstructural Diversity, Texture, and Mechanical Properties in Electron Beam Melted Ti-6Al-4V. *Metallurgical and Materials Transactions A*, 41(13):3422–3434, aug 2010.
- [88] Alphons a. Antonysamy, Philip B. Prangnell, and Jonathan Meyer. Effect of Wall Thickness Transitions on Texture and Grain Structure in Additive Layer Manufacture (ALM) of Ti-6Al-4V. *Thermec*, 706-709:205–210, jan 2012.
- [89] F J Gil, M P Ginebra, J M Manero, and J A Planell. Formation of alpha-Widmanstätten structure: effects of grain size and cooling rate on the Widmanstätten morphologies and on the mechanical properties of Ti6Al4V alloy. 329:142–152, 2001.
- [90] Charlotte De Formanoir de la Cazerie. Study of the Microstructure and Mechanical Properties of Electron Beam Melted Ti-6Al-4V for Aeronautic Applications. Technical report, Université Libre de Bruxelles, Bruxelles, 2013.
- [91] ASTM. Standard Test Methods for Tension Testing of Metallic Materials. E8-04, 2004.
- [92] Rafi H Khalid, N V Karthik, Thomas L Starr, and Brent E Stucker. Mechanical property evaluation of Ti-6Al-4V parts made using Electron Beam Melting. pages 526–535, 2012.
- [93] Mattias Svensson. Material properties of EBM- Manufactured Ti6Al4V & Ti6Al4V Eli Under Raw and Hip Conditions. Technical report, 2009.

-
- [94] Li Yang, Ola Harrysson, Harvey West, and Denis Cormier. Modeling of uniaxial compression in a 3D periodic re-entrant lattice structure. *Journal of Materials Science*, 48(4):1413–1422, sep 2012.
- [95] Rafidah Hasan, Robert Mines, and Peter Fox. Characterization of selectively laser melted Ti-6Al-4V microlattice struts. *Procedia Engineering*, 10:536–541, 2011.
- [96] Chunze Yan, Liang Hao, Ahmed Hussein, and David Raymont. Evaluations of cellular lattice structures manufactured using selective laser melting. *International Journal of Machine Tools and Manufacture*, 62:32–38, 2012.
- [97] Sang-in Park, David W. Rosen, and Chad E. Duty. Comparing mechanical and geometrical properties of lattice structure fabricated using Electron Beam Melting. In *Solid Freeform Fabrication Proceedings*, volume 1, pages 1359–1370, 2015.
- [98] Sang-in Park, David W Rosen, Seung-kyum Choi, and Chad E Duty. Effective mechanical properties of lattice material fabricated by material extrusion additive manufacturing. *Additive Manufacturing*, 1-4:12–23, 2014.
- [99] Vincent Boulos, Vincent Fristot, Dominique Houzet, Luc Salvo, P Lhuissier, and P Lhuissier Investigating. Investigating performance variations of an optimized GPU-ported granulometry algorithm. In *18th International European Conference on Parallel and Distributed Computing*, 2012.
- [100] J. C. Michel, H. Moulinec, and P. Suquet. A computational scheme for linear and non-linear composites with arbitrary phase contrast. *International Journal for Numerical Methods in Engineering*, 52(12):139–160, sep 2001.
- [101] R R Boyer, G Welsch, and E. W. Collings. *Materials Properties Handbook: Titanium Alloys*. Materials Park, asm intern edition, 1994.
- [102] Scott R Johnston, Marques Reed, Hongqing V Wang, and David W Rosen. Analysis of Mesostructure Unit Cells Comprised of Octet-truss Structures.
- [103] Toufik Kanit, Franck N’Guyen, Samuel Forest, Dominique Jeulin, Matt Reed, and Scott Singleton. Apparent and effective physical properties of heterogeneous materials: Representativity of samples of two materials from food industry. *Computer Methods in Applied Mechanics and Engineering*, 195(33-36):3960–3982, jul 2006.
- [104] Kasem Theerakittayakorn and Pruettha Nanakorn. Periodic boundary conditions for unit cells of periodic cellular solids in the determination of effective properties using beam elements. In *The 2013 World Congress on Advances in Structural Engineering and Mechanics (ASEM13)*, pages 3738–3748, 2013.
- [105] Dieter Kraft. Algorithm 733 : TOMP - Fortran Modules for Optimal Control Calculations. *ACM Transaction on Mathematical software*, 20(3):262–281, 1994.
- [106] Dieter Kraft. A software package for sequential quadratic programming. Technical report, Deutsche Forschungsanstalt fuer Luft- und Raumfahrt e.V. (DLR), Wessling (Germany). Inst. fuer Dynamik der Flugsysteme, Koeln, 1988.

- [107] Grzegorz Pyka, Greet Kerckhofs, Jan Schrooten, and Martine Wevers. The effect of spatial micro-CT image resolution and surface complexity on the morphological 3D analysis of open porous structures. *Materials Characterization*, 87:104–115, jan 2014.
- [108] Grzegorz Pyka, Andrzej Burakowski, Greet Kerckhofs, Maarten Moesen, Simon Van Bael, Jan Schrooten, and Martine Wevers. Surface Modification of Ti6Al4V Open Porous Structures Produced by Additive Manufacturing. *Advanced Engineering Materials*, 14(6):363–370, jun 2012.
- [109] Grzegorz Pyka, Greet Kerckhofs, Ioannis Papantoniou, Mathew Speirs, Jan Schrooten, and Martine Wevers. Surface Roughness and Morphology Customization of Additive Manufactured Open Porous Ti6Al4V Structures. *Materials*, 6(10):4737–4757, oct 2013.
- [110] M Rinner, J Gerlach, and W Ensinger. Formation of titanium oxide films on titanium and Ti6Al4V by O₂-plasma immersion ion implantation. *Surface and Coatings Technology*, 132(2-3):111–116, 2000.
- [111] Jin-Woo Park, Youn-Jeong Kim, Je-Hee Jang, Tae-Geon Kwon, Yong-Chul Bae, and Jo-Young Suh. Effects of phosphoric acid treatment of titanium surfaces on surface properties, osteoblast response and removal of torque forces. *Acta biomaterialia*, 6(4):1661–70, apr 2010.
- [112] Dawei Gong, Craig a. Grimes, Oomman K. Varghese, Wenchong Hu, R. S. Singh, Zhi Chen, and Elizabeth C. Dickey. Titanium oxide nanotube arrays prepared by anodic oxidation. *Journal of Materials Research*, 16(12):3331–3334, 2001.
- [113] Y. X. Leng, J. Y. Chen, Z. M. Zeng, X. B. Tian, P. Yang, N. Huang, Z. R. Zhou, and P. K. Chu. Properties of titanium oxide biomaterials synthesized by titanium plasma immersion ion implantation and reactive ion oxidation. *Thin Solid Films*, 377-378:573–577, 2000.
- [114] Pierre-Thomas Doutre. *PhD thesis in progress*. PhD thesis, 2017.
- [115] Jacqueline M. Cordell, Michelle L. Vogl, and Amy J. Wagoner Johnson. The influence of micropore size on the mechanical properties of bulk hydroxyapatite and hydroxyapatite scaffolds. *Journal of the Mechanical Behavior of Biomedical Materials*, 2(5):560–570, 2009.
- [116] Emmanuel Rodriguez, Francisco Medina, David Espalin, Cesar Terrazas, Dan Muse, Chad Henry, Eric Macdonald, Ryan B Wicker, El Paso, Lockheed Martin, and Aeronautics Company. Integration of a Thermal Imaging Feedback Control System in Electron Beam Melting. *International Solid Freeform Fabrication Symposium - An Additive Manufacturing Conference*, (Figure 1):945–961, 2012.
- [117] Jorge Mireles, Cesar Terrazas, Francisco Medina, Ryan Wicker, and El Paso. Automatic Feedback Control in Electron Beam Melting Using Infrared Thermography. In *International Solid Freeform Fabrication Symposium - An Additive Manufacturing Conference*, pages 708–717, 2013.

- [118] J.C. Michel, H. Moulinec, and P. Suquet. Effective properties of composite materials with periodic microstructure: a computational approach. *Computer Methods in Applied Mechanics and Engineering*, 172(1-4):109–143, 1999.
- [119] H. Moulinec and P. Suquet. A numerical method for computing the overall response of nonlinear composites with complex microstructure. *Computer Methods in Applied Mechanics and Engineering*, 157:69–94, 1997.

Appendices

Appendix A

FFT simulation of heterogenous media

Introduction

In this work, the use of a fast-Fourier transform software allows the direct use of pixelized 3D images as input for the mechanical properties computation of single struts built by EBM.

This appendix aims at presenting some theoretical aspects of the FFT using CraFT. The theory presented here comes mainly from publications by Suquet, Moulinec and Michel [100, 118, 119]

local problem

From a 3D image composed of two phases x_1 and x_2 , the aim of the homogenization procedure is to compute the overall stress and strain Σ, E and thus the effective behavior from the local constitutive relations of each phases:

$\sigma(x) = C(x) : \varepsilon(x)$	Constitutive relations
$\varepsilon(x) = \frac{1}{2}(\nabla u(x) + \nabla^t u(x))$	Compatibility
$div(\sigma) = 0$	Equilibrium
$\langle \varepsilon \rangle = E, \langle \sigma \rangle = \Sigma$	
$u^* = u - E.x$ periodic, $\sigma.n$ anti-periodic	Boundary Conditions

where C is the stiffness tensor, E is the macroscopic strain and σ, ε, u are the local stress, strain and displacement fields. The symbol $\langle . \rangle$ denotes a mean value.

Iteration scheme

To compute the homogeneous properties of a reference medium, Moulinec and Suquet ([119]) introduced an iterative scheme to solve the local problem. The aim is to establish the relation between the local strain at iteration $i+1$ and the local strain at iteration i . To simplify the calculations, the relation is computed in the Fourier space. The constitutive

law are obtained in the real space and the strain field is calculated in the Fourier space. Both are computed iteratively until convergence of fields.

Convergence criterion. Convergence is reached when both criteria are fulfilled:

1. The modulus of the divergence of the stress field is lower than a given value (equilibrium is fulfilled):

$$\|div(\sigma)\| = \sqrt{\sum_{\xi} |\xi \cdot \hat{\sigma}(\xi)|^2} < \zeta \quad (\text{A.1})$$

2. The loading conditions are verified at each step:

In the case of prescribed macroscopic stress (our case), the iterative scheme is:

$$E^{i+1} = E^i + C^0 : (\Sigma - \langle \sigma^i \rangle) \quad (\text{A.2})$$

The criterion is : $\frac{\|\Sigma - \langle \sigma^i \rangle\|}{\|\Sigma\|} < \eta$.

Choice of the accuracy for the convergence criterion

The choice of the accuracy value for the convergence of the FFT simulation can largely influence the result of the simulation and the time to convergence. A study has been made on the vertical strut with a 1 mm diameter to investigate this parameter. It has been chosen that the accuracy for the divergence of stress and loading conditions will be equal: $\zeta = \eta$.

Figure A.1 shows the variation of the time to convergence and the numerical equivalent diameter as a function of the accuracy value. For poor accuracy value, the computational time is low (<1 min) but the value of the computed diameter fluctuates. For values lower than 10^{-3} , the results of the FFT calculation converges (black rectangle). However, computational time keeps on increasing.

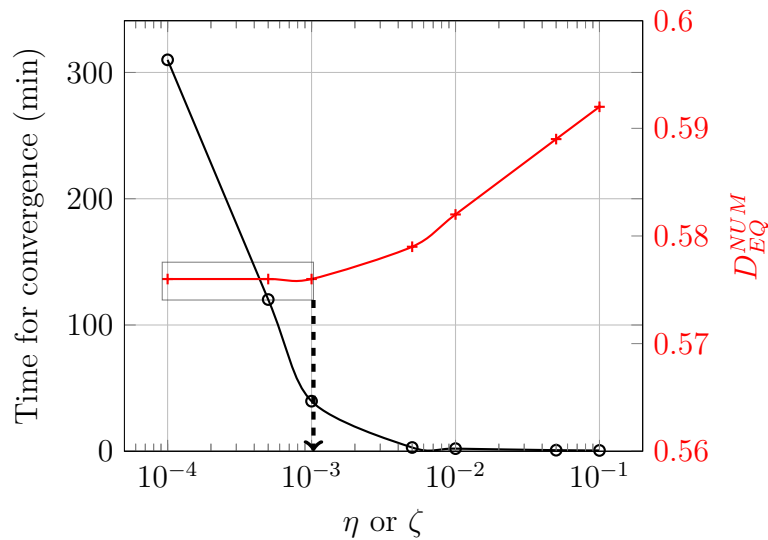


Figure A.1 Influence of the desired accuracy of convergence on the simulation time and numerical result

For that purpose, the value for the accuracy parameter is set as 10^{-3} .

Appendix B

Detailed example of Periodic Boundary Conditions for the beam simulation

The PBC relies on applying kinematic conditions to corresponding points from opposite sides. We detail here how to apply such PBC on the octet-truss unit cell for a Timoshenko beam simulation of the uniaxial tensile test along the x direction. The formalization of the FEM code CAST3M is used.

Generalities on PBC

As mentioned in the manuscript, the PBC are formulated by applying a displacement field \underline{u} on the border δV such as :

$$\underline{u}(\underline{x}) = \underline{\underline{E}}^0 \cdot \underline{x} + \underline{u}'(\underline{x}) \quad \forall x \in \delta V, \quad (\text{B.1})$$

where $\underline{\underline{E}}^0$ is a macroscopic deformation tensor and $\underline{u}'(\underline{x})$ is a periodic displacement field. Its period is equal to the length of the unit-cell (L in figure B.1). For two opposite points (\underline{x}^+ and \underline{x}^-) separated by the period L, the following relation can be established:

$$\begin{aligned} \underline{u}(\underline{x}^+) - \underline{u}(\underline{x}^-) &= \underline{\underline{E}}^0 \cdot (\underline{x}^+ - \underline{x}^-) + \underbrace{(\underline{u}'(\underline{x}^+) - \underline{u}'(\underline{x}^-))}_{=0} \\ &= \underline{\underline{E}}^0 \cdot L. \end{aligned} \quad (\text{B.2})$$

Application on the octet-truss structure

The structure of interest is the octet-truss structure (see figure B.1).

The macroscopic strain corresponds to an uniaxial tensile test. The macroscopic strain tensor can be written in the form:

$$\begin{bmatrix} E_x^0 & 0 & 0 \\ 0 & 0 & 0 \\ 0 & 0 & 0 \end{bmatrix} \quad (\text{B.3})$$

If $F_{\bar{x}} = \{\text{P1}; \text{P2}; \text{P3}; \text{P4}; \text{P5}\}$ and $F_{\bar{x}}^+ = \{\text{P1B}; \text{P2B}; \text{P3B}; \text{P4B}; \text{P5B}\}$, the kinematic relations for opposite points in the x direction are computed as:

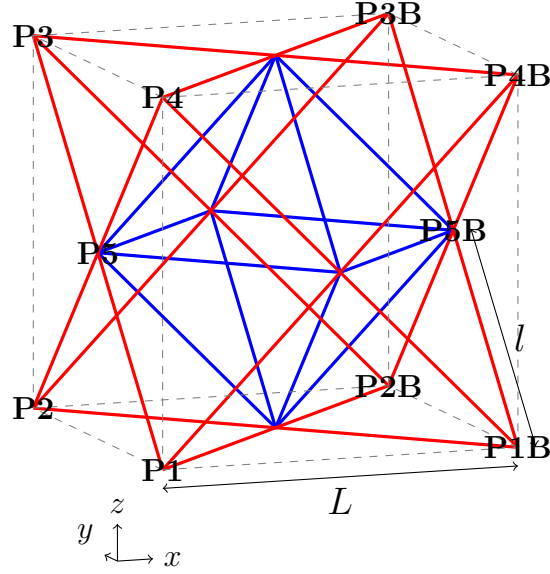


Figure B.1 Octet-truss unit cell composed of 36 struts. The dashed lines represent the bounding box.

$$\begin{aligned}
 u_x(F_X^+) - u_x(F_X^-) &= E_x^0 \cdot L \\
 u_y(F_X^+) - u_y(F_X^-) &= 0 \\
 u_z(F_X^+) - u_z(F_X^-) &= 0.
 \end{aligned}$$

Similarly to the F_X^+ and F_X^- sides, the kinematic relations for the other sides are:

$$\begin{aligned}
 u_x(F_Y^+) - u_x(F_Y^-) &= 0 \\
 u_y(F_Y^+) - u_y(F_Y^-) &= 0 \\
 u_z(F_Y^+) - u_z(F_Y^-) &= 0.
 \end{aligned}$$

$$\begin{aligned}
 u_x(F_Z^+) - u_x(F_Z^-) &= 0 \\
 u_y(F_Z^+) - u_y(F_Z^-) &= 0 \\
 u_z(F_Z^+) - u_z(F_Z^-) &= 0.
 \end{aligned}$$

Within the CAST3M code, the relative displacements are fixed using the "RELA" and "DEPI" operators:

```

RIG1='RELA' 'UX' FXP -'UX' FXM ;
RIG2='RELA' 'UY' FXP -'UY' FXM ;
RIG3='RELA' 'UZ' FXP -'UZ' FXM ;
RIG4='RELA' 'UX' FYP -'UX' FYM ;
RIG5='RELA' 'UY' FYP -'UY' FYM ;
RIG6='RELA' 'UZ' FYP -'UZ' FYM ;
RIG7='RELA' 'UX' FZP -'UX' FZM ;
RIG8='RELA' 'UY' FZP -'UY' FZM ;
RIG9='RELA' 'UZ' FZP -'UZ' FZM ;

```

```
DEP1='DEPI' RIG1 ( $E_X^0 * L$ ) ;  
DEP2='DEPI' RIG2 0. ;  
DEP3='DEPI' RIG3 0. ;  
DEP4='DEPI' RIG4 0. ;  
DEP5='DEPI' RIG5 0. ;  
DEP6='DEPI' RIG6 0. ;  
DEP7='DEPI' RIG7 0. ;  
DEP8='DEPI' RIG8 0. ;  
DEP9='DEPI' RIG9 0. ;
```

To suppress the rigid body motions, one node of the unit-cell is fixed.



Appendix C

Comments on the relative density calculation

The relative density of a regular octet-truss lattice can be computed easily by considering the volume of the struts divided by the volume of the bounding box. For a unit-cell composed of struts with a length l and a radius r , the first order relative density is expressed as (from [42]):

$$\bar{\rho}^{1st} = 6\pi\sqrt{2}\left(\frac{r}{l}\right)^2 \quad (\text{C.1})$$

This density is an over-estimation of the true density since it counts multiple times the volume of the intersections of beams.

In section 8.3, the relative density used was the "true" relative density ($\bar{\rho}^{true}$) since the calculations were done on an octet-truss composed of volume element. The relative density was then calculated by integration of the volume.

The difference between the first order and true relative density is plotted for a regular octet-truss in figure C.1.

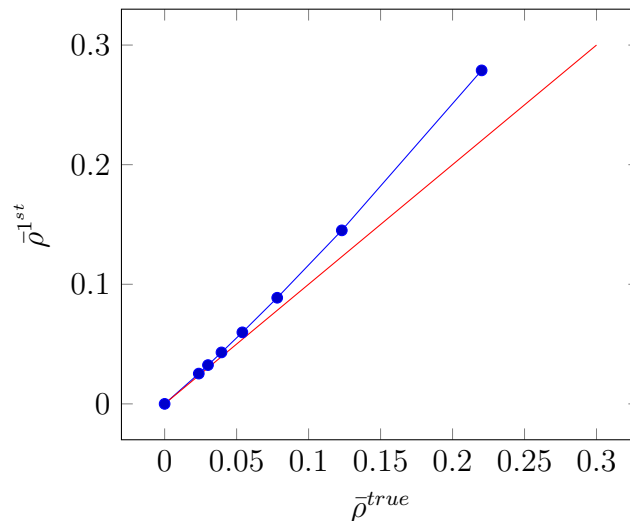


Figure C.1 First order relative density as a function of the true relative density. The red line represents the isovalue.

The first order relative density is really close to the true relative density until 5-10%. For larger densities, the difference between the first order and second order is large since the volume of the node is not anymore secondary.

For 1 mm circular struts, the true density is calculated as :

$$\bar{\rho}^{true} = 6\pi\sqrt{2} \left(\frac{r}{l}\right)^2 - 55 \left(\frac{r}{l}\right)^3 \quad (\text{C.2})$$

In this work, the range of density is lower than 5 % so that the first order density can be used in optimization and simulation procedures. However, when simulating larger densities, the true relative density value should be calculated.

Appendix D

Description of the lattice creator program

The program allows the creation of lattice structures in the wireframe format. This format is composed of points coordinates and connectivity table between the points. It has been written in C and fortran.

A thickness is then assigned to each segment at the end of the procedure.

This program allows the manufacturing of unit-cells for creating periodic structures. It can create also random structures based on the Voronoi tessellation. The third type of structures that can be created is structures with graded porosity.

Periodic structures

Different periodic structures can be created. The unit cells of the structures are represented in figure D.1.

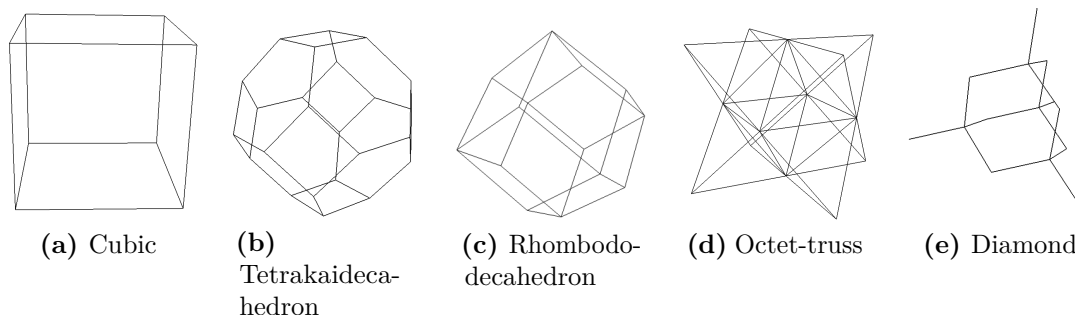


Figure D.1 Example of unit-cell that can be designed.

The program can produce either the unit cells or a repetition of them in a 3D bounding box.

Stochastic structures

The fabrication of stochastic structures relies on the Voronoi tessellation. A set of points (seeds) is specified in space. For each seed there is a corresponding region consisting of all

points closer to that seed than to any other. These regions are called Voronoi cells. The final geometry corresponds to the edges of the Voronoi cells.

It is possible to design monomodal, bimodal or multi-modal random lattices by restraining a particular distance between the seeds. Some examples of monomodal and bimodal distribution of cells are represented in figure D.2.

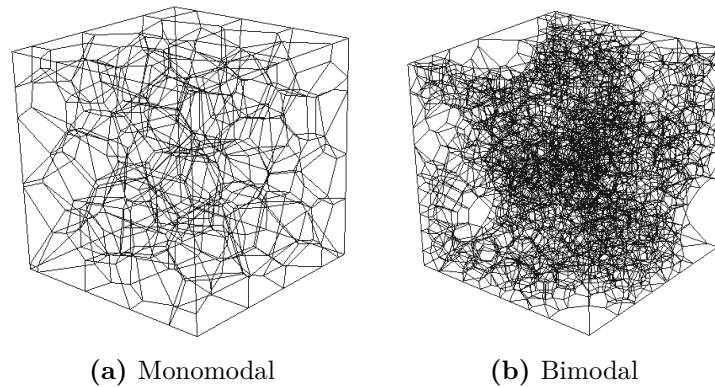


Figure D.2 Example of stochastic lattice structures that can be produced.

Graded structures

For the integration of lattice structures within bulk parts, the density of the lattice should evolve depending on the stress intensity of the zone. For that purpose, graded random lattice structures are promising geometries to fulfill such an application.

Some examples are represented in figure D.3. The graded lattices can be produced either within a cube, a cylinder or a sphere. When looking at the cylinder with a large density at the shell and low density in the core, it looks like human bone. Such a structure could indeed be used in osseointegration.

Output

The output of the program is a VTK file containing the coordinates of the nodes and the connectivity between them. This file can then be processed with a visualization software such as Paraview®. Within this software, one can give a desired diameter to the wireframe structure. The file is saved as a STL file for its manufacturing by the EBM process.

Moreover, the program outputs a file describing the geometry of the produced structure in the CAST3M and COMSOL formats for further beam simulation using these FEM software products.

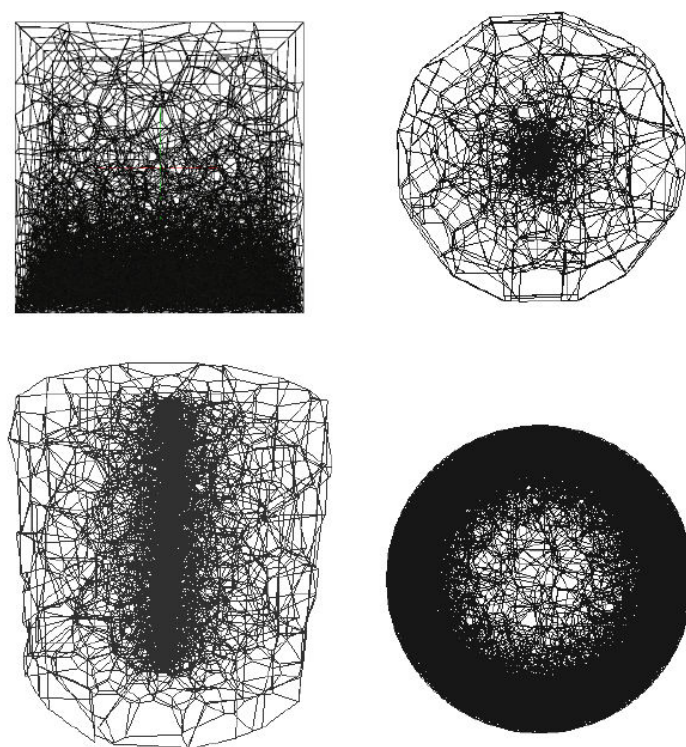


Figure D.3 Example of graded lattice structures that can be produced.



Résumé

Le récent développement de la Fabrication Additive de pièces métalliques permet d'élaborer directement des structures à partir de modèles 3D. En particulier, la technologie "Electron Beam Melting" (EBM) permet la fusion sélective, couche par couche, de poudres métalliques. Elle autorise la réalisation de géométries très complexes mais apporte de nouvelles contraintes de fabrication.

Ce travail se concentre sur la caractérisation géométrique et mécanique de structures treillis produites par cette méthode. Les pièces fabriquées sont comparées au design initial à travers des caractérisations par tomographie aux rayons X. Les propriétés mécaniques sont testées en compression uni-axiale. Pour les poutres de faibles épaisseur, la différence entre la structure numérique et celle fabriquée devient significative. Les écarts au design initial se traduisent pour chaque poutre par un concept de matière mécaniquement efficace. D'un point de vue modélisation, ce concept est pris en compte en remplaçant la poutre fabriquée par un cylindre avec un *diamètre mécaniquement équivalent*. Ce diamètre équivalent est utilisé dans des simulations et optimisations "réalistes" intégrant ainsi les contraintes de fabrication de la technologie EBM.

Différentes stratégies sont aussi proposées pour réduire la proportion de volume "inefficace" et améliorer le contrôle de la taille des poutres, soit en jouant sur les paramètres procédé et les stratégies de fusion, soit en effectuant des post-traitements.

Mots clés : Electron Beam Melting ; Fabrication Additive ; Structures Treillis ; Tomographie aux rayons X ; Simulation Eléments Finis.

Abstract

The recent development of Additive Manufacturing for the fabrication of metallic parts allows structures to be directly manufactured from 3D models. In particular, the "Electron Beam Melting" (EBM) technology is a suitable process which selectively melts a powder bed layer by layer. It can build very complex geometries but brings new limitations that have to be quantified.

This work focuses on the structural and mechanical characterization of lattice structures produced by such technology. The structural characterization mainly rely on X-ray tomography whereas mechanical properties are assessed by uni-axial compression. The geometry and related properties of the fabricated structures are compared with the designed ones. For small strut size, the difference between the designed structure and the produced one is large enough to impact the desired mechanical properties. The concept of mechanical efficient volume is introduced. For the purpose of simulation, this concept is taken into account by replacing the struts by a cylinder with a *mechanical equivalent diameter*. After validation, it has been used into "realistic" simulation and optimization procedures, thus taking into account the process constraints.

Post-treatments (Chemical Etching and Electro-Chemical Polishing) were applied on lattice structures to get rid of the inefficient matter by decreasing the surface roughness. The control of the size of the fabricated struts was improved by tuning the process strategies and parameters.

Keywords: Electron Beam Melting; Additive Manufacturing; Lattice structures; X-ray tomography; Finite Element simulation.